

Dissertation

Cross-Linked Gold Nanoparticle Membranes:
Novel Materials for Electromechanical
Sensors and Actuators

Dissertation zur Erlangung des Doktorgrades
an der Fakultät für Mathematik, Informatik und
Naturwissenschaften

Fachbereich Chemie
Universität Hamburg

vorgelegt von

Hendrik Schlicke

Hamburg
2017

Dissertation

Titel: Cross-Linked Gold Nanoparticle Membranes:
Novel Materials for Electromechanical Sensors
and Actuators

Titel (deu.): Membranen aus vernetzten Gold-Nanopartikeln:
Neuartige Materialien für elektromechanische
Sensoren und Aktuatoren

Eingereicht von: Hendrik Schlicke

Matrikelnummer: 5942970

Email: mail@hendrikschlicke.de

Arbeitsgruppe: Prof. Dr. Horst Weller

Institut: Institut für Physikalische Chemie

Universität: Universität Hamburg

Datum der Einreichung: 29. September 2017

Erstgutachter: Dr. Tobias Vossmeier

Zweitgutachter: Prof. Dr. Alf Mews

Druckfreigabe erteilt: 01. Dezember 2017

Datum der Disputation: 01. Dezember 2017

Prüfungskommission: Prof. Dr. Horst Weller
Prof. Dr. Carmen Herrmann
PD Dr. Tobias Kipp

Diese Arbeit wurde im Zeitraum von Januar 2014 bis September 2017 in der Arbeitsgruppe von Prof. Dr. Horst Weller, im Team von Dr. Tobias Vossmeier, am Institut für Physikalische Chemie, Fachbereich Chemie der Universität Hamburg, durchgeführt.

I List of Publications

The following list contains chronologically ordered peer-reviewed journal articles and conference proceedings published within the framework of this research project as well as a filed patent application. An equal contribution of two authors is denoted by a double-dagger (‡) symbol.

Journal Articles

1. H. Schlicke, D. Battista, S. Kunze, C. J. Schröter, M. Eich, T. Vossmeier, “Free-standing Membranes of Cross-Linked Gold Nanoparticles: Novel Functional Materials for Electrostatic Actuators”, *ACS Appl. Mater. Interfaces* **2015**, *7*, 15123-15128.^[1]
2. H. Schlicke, M. Rebber, S. Kunze, T. Vossmeier, “Resistive pressure sensors based on freestanding membranes of gold nanoparticles”, *Nanoscale* **2016**, *8*, 183-186.^[2]
3. H. Schlicke,[‡] C. J. Schröter,[‡] T. Vossmeier, “Electrostatically driven drumhead resonators based on freestanding membranes of cross-linked gold nanoparticles”, *Nanoscale* **2016**, *8*, 15880-15887.^[3]
4. H. Schlicke, M. Behrens, C. J. Schröter, G. T. Dahl, H. Hartmann, T. Vossmeier, “Cross-Linked Gold-Nanoparticle Membrane Resonators as Microelectromechanical Vapor Sensors”, *ACS Sens.* **2017**, *2*, 540-546.^[4]

Conference Proceedings

1. H. Schlicke, C. J. Schröter, M. Rebber, D. Battista, S. Kunze, T. Vossmeier, “Free-standing Membranes of Cross-Linked Gold-Nanoparticles: Novel Functional Materials for MEMS/NEMS Applications”, *TechConnect Briefs 2016: Advanced Manufacturing, Electronics and Microsystems* **2016**, 83-86.^[5]
2. H. Schlicke, S. C. Bittinger, M. Behrens, M. Yesilmen, H. Hartmann, C. J. Schröter, G. T. Dahl, T. Vossmeier, “Electrostatically Actuated Membranes of Cross-Linked Gold Nanoparticles: Novel Concepts for Electromechanical Gas Sensors”, *Proceedings* **2017**, *1*, 301.^[6]
3. H. Schlicke, C. J. Schröter, G. T. Dahl, M. Rebber, M. Behrens, T. Vossmeier, “Membranes of Organically Cross-Linked Gold Nanoparticles: Novel Materials for MEMS/NEMS Sensors and Actuators”, *2017 IEEE Nanotechnology Materials and Devices Conference (NMDC)*, in press.

Patent Application

1. H. Schlicke, T. Vossmeier, M. Behrens, S. C. Bittinger / CAN GmbH, “Method for detecting an analyte based on the detection of the mechanical properties of a freestanding nanoparticle composite material”, patent application GB1704749.9, filed on March 24, 2017.

II Contents

I	List of Publications	vii
II	Contents	ix
III	List of Symbols and Abbreviations	xiii
III.1	Abbreviations	xiii
III.2	Symbols	xvi
1	Abstract	1
2	Zusammenfassung	5
3	Introduction	9
3.1	Gold Nanoparticles	12
3.1.1	Optical Properties	13
3.1.2	Synthesis	15
3.2	Gold Nanoparticle Composites	17
3.2.1	Fabrication	18
3.2.2	Charge Transport and Resistive Sensing	22
3.2.3	Resistive Strain Sensing	24
3.2.4	Resistive Chemical Sensing	26
3.3	Nanomembranes	31
3.3.1	Fabrication	31
3.3.2	Mechanical Properties and Sensing	34

CONTENTS

3.3.3	Nanomembrane Resonators	39
3.4	Interferometry	49
4	Goal	53
5	Synopsis	55
5.1	Fabrication and Interfacing of Freestanding GNP Membranes	58
5.1.1	Fabrication of GNP Membranes	58
5.1.2	Fabrication of Supporting Microstructures	59
5.1.3	Membrane Transfer	62
5.2	Resistive Pressure Sensing	63
5.2.1	Sensing Principle	64
5.2.2	Sensor Fabrication	67
5.2.3	Probing the Sensor Characteristics	68
5.2.4	Sensitivity	69
5.2.5	Conclusions and Outlook	70
5.2.6	Publication: Resistive Pressure Sensors Based on Freestanding Membranes of Gold Nanoparticles	72
5.3	Electrostatic Actuation of GNP Membranes	77
5.3.1	Working Principle	77
5.3.2	Device Fabrication	79
5.3.3	Device Testing	80
5.3.4	Conclusions and Outlook	81
5.3.5	Publication: Freestanding Membranes of Cross-Linked Gold Nanoparticles: Novel Functional Materials for Electrostatic Actuators	83
5.4	Electromechanical GNP Membrane Resonators	90
5.4.1	Working Principle	90

5.4.2	Device Fabrication	92
5.4.3	Device Testing	93
5.4.4	Conclusion and Outlook	96
5.4.5	Publication: Electrostatically Driven Drumhead Resonators Based on Freestanding Membranes of Cross-Linked Gold Nanoparticles . .	97
5.5	Electromechanical Chemical Sensors	107
5.5.1	Operation and Sensing Principle	107
5.5.2	Sensor Fabrication	110
5.5.3	Sensor Testing	110
5.5.4	Conclusions and Outlook	113
5.5.5	Publication: Cross-Linked Gold-Nanoparticle Membrane Resonators as Microelectromechanical Vapor Sensors	115
6	Unpublished Work and Further Publications	123
6.1	Freestanding Membranes of Gold Nanoparticles Cross-Linked by α, ω -Alkanedithiols: Elasticity as a Function of the Alkane Chain Length .	124
6.1.1	Materials and Preparation Methods	124
6.1.2	X-Ray Diffraction	125
6.1.3	UV/vis Spectroscopy	127
6.1.4	Charge Transport Characterization	128
6.1.5	Transmission Electron Microscopy	129
6.1.6	Elasticity	130
6.1.7	Conclusions and Outlook	133
6.2	Electromechanical Gold Nanoparticle Membrane Resonators: Influence of Geometry and Size on the Vibrational Characteristics	135
6.2.1	Device Fabrication	135
6.2.2	Resonator Characterization	136

CONTENTS

6.2.3	Results	137
6.2.4	Conclusions and Outlook	142
6.3	Further Results	144
6.3.1	Sensor Response Kinetics of GNP Membrane Resonators	144
6.3.2	Quasi-static Deflection of GNP Membranes for Chemical Sensing	148
6.4	Conference Proceeding: TechConnect Nanotech 2016	152
6.5	Conference Proceeding: Eurosensors 2017	157
6.6	Conference Proceeding: IEEE NMDC 2017	162
7	Discussion and Outlook	165
8	Bibliography	169
A	Appendix	183
A.1	Supporting Information	183
A.1.1	Resistive Pressure Sensors Based on Freestanding Membranes of Gold Nanoparticles	184
A.1.2	Freestanding Membranes of Cross-Linked Gold Nanoparticles: Novel Functional Materials for Electrostatic Actuators	201
A.1.3	Electrostatically driven drumhead resonators based on freestanding membranes of cross-linked gold nanoparticles	216
A.1.4	Cross-Linked Gold-Nanoparticle Membrane Resonators as Micro-electromechanical Vapor Sensors	233
A.2	Interferometer Setup	256
A.3	Chemicals and Safety	258
B	Danksagung	265
C	Eidesstattliche Versicherung	267

III List of Symbols and Abbreviations

III.1 Abbreviations

10DT 1,10-decanedithiol

12A 1-dodecylamine

12T 1-dodecanethiol

16DT 1,16-hexadecanedithiol

2D 2-dimensional

2DT 1,2-ethanedithiol

3D 3-dimensional

3DT 1,3-propanedithiol

4DT 1,4-butanedithiol

4M2P 4-methylpentan-2-one

5DT 1,5-pentanedithiol

6DT 1,6-hexanedithiol

8DT 1,8-octanedithiol

9DT 1,9-nonanedithiol

A.D. anno domini

AC alternating current

ADT α, ω -alkanedithiol

AFM atomic force microscopy

AG analyte gas

ALD atomic layer deposition

ANN artificial neural network

AT 1-alkanethiol

III. List of Symbols and Abbreviations

B.C. before christ

BDT 1,4-benzenedithiol

BOE buffered oxide etch

CA cellulose acetate

CMR carcinogenic, mutagenic or toxic to reproduction

CNT carbon nanotube

cP primitive cubic

CVD chemical vapor deposition

DC direct current

DCM dichloromethane

DEG diethylene glycol

DI deionized

DMF *N,N*-dimethylformamide

DNA deoxyribonucleic acid

DT dithiol

EDTA ethylenediaminetetraacetate

EG ethylene glycol

ESI Electronic Supplementary Information

FET field effect transistor

FFT fast Fourier transformation

FWHM full width at half maximum

GHS globally harmonized system

GISAXS grazing incidence small angle X-ray scattering

GNP gold nanoparticle

HDPE high density polyethylene

HOMO highest occupied molecular orbital

- IR** infrared
- IV** current-voltage
- LAN** local area network
- LbL** layer-by-layer
- LDPE** low density polyethylene
- LUMO** lowest unoccupied molecular orbital
- MEMS** microelectromechanical systems
- MOEMS** microoptoelectromechanical systems
- NEMS** nanoelectromechanical systems
- OA** oleylamine
- PCA** principal component analysis
- PCB** printed circuit board
- PDMS** polydimethylsiloxane
- PMMA** poly(methyl methacrylate)
- PS** polystyrene
- PTM** pentaerythritol tetrakis(3-mercaptopropionate)
- QCM** quartz crystal microbalance
- SAM** self-assembled monolayer
- SAXS** small angle X-ray scattering
- SEM** scanning electron microscopy
- SI** Supporting Information
- SIEBIMM** strain-induced elastic buckling instability for mechanical measurements
- SMU** source measure unit
- SPR** surface plasmon resonance
- TCP** transmission control protocol
- TEM** transmission electron microscopy

TMDC transition metal dichalcogenide

UV ultraviolet

UV/vis ultraviolet/visible

VOC volatile organic compound

XRD X-ray diffraction

ZG zero gas

III.2 Symbols

a aperture radius

A area

a_e distance between electrodes

α angle

$A_{m,n}, B_{m,n}, A_{n,m}, B_{n,m}, \tilde{A}_{n,m}, \tilde{B}_{n,m}$ constants

a_x, a_y edge lengths

A_x, A_y amplitudes

B Jones matrix

β tunneling decay constant

β_N tunneling decay constant in reciprocal units of CH₂ group count

b_x, b_y half edge lengths

c phase velocity

c_0 speed of light

C_1, C_2 constants

c_a analyte concentration

d membrane/electrode distance

D particle diameter

- δ interparticle spacing
- e elementary charge
- E modulus of elasticity
- E_a activation energy
- ϵ permittivity
- ϵ_0 vacuum permittivity
- ϵ_1 real part of dielectric function
- ϵ_2 imaginary part of dielectric function
- ε strain
- ϵ_m matrix permittivity
- ϵ_r relative permittivity
- \vec{E} Jones vector
- f frequency
- F force
- f^* normalized frequency
- g gauge factor
- h central point deflection
- J_n n th Bessel function
- k Boltzmann constant
- κ extinction coefficient
- K_H Henry constant
- K_L Langmuir constant
- l length
- L crystalline domain size
- λ wavelength
- m, n mode numbers

III. List of Symbols and Abbreviations

N integer

ν Poisson ratio

ω angular frequency

p partial pressure

P pressure

ϕ phase angle

Q quality factor

r, θ polar coordinates

R resistance

R_C radius of curvature

R_{GNP} gold nanoparticle radius

x_{analyte} analyte molar fraction

ρ mass density

ρ_A areal mass density

$\left(\frac{\Delta R}{R_0}\right)_{\text{sat}}$ Langmuir saturation response

R_{\square} sheet resistance

s arc length

S sensitivity

σ stress, conductivity

σ_0 pre-stress, preexponential factor (conductivity)

t time

T temperature

T_0 tension

τ decay time

θ diffraction angle

ϑ angle

t_m membrane thickness

V voltage

V_{NP} nanoparticle volume

w deflection in z direction

W, \tilde{W} vibrational normal mode

$\xi_{n,m}$ m th root of the n th order Bessel function

x, y, z cartesian coordinates

Y biaxial modulus

1 Abstract

Composites of organically cross-linked gold nanoparticles (GNPs) represent a novel material class with tunable optical and electronic properties as well as the ability to sorb analyte molecules. Their perturbation-sensitive tunneling-based charge transport mechanism renders these materials interesting for sensing applications. While most studies on these materials were performed after depositing them as films onto supporting substrates, the preparation and characterization of freestanding membranes with nanoscale thicknesses were reported more recently. For the design of novel hybrid microelectromechanical systems (MEMS) and nanoelectromechanical systems (NEMS) with respect to sensing applications it is of great interest to couple the mechanical properties of these membranes to their electronic properties and sorption capabilities.

This thesis summarizes different projects, including the first reports on the coupling of electronic and mechanical properties of freestanding GNP membranes in novel types of micro- and nanoelectromechanical sensors and actuators. Further, the tunability of the GNP membranes' conductivity and mechanical properties by variation of the linker molecules was demonstrated. The projects can be grouped into four topics, i.e., pressure sensing, electrostatically driven actuators and resonators, chemical sensing, and mechanical characterization.

In the first project, the fabrication of a resistive pressure sensor exploiting the electromechanical characteristics of a 1,6-hexanedithiol (6DT) cross-linked GNP membrane is investigated. Here, the membrane was employed both as diaphragm and strain sensitive transducer. The sensor consisted of a microstructure, suitable to monitor the resistance of a 55 nm thick freestanding GNP membrane, which sealed a cuboid microcavity featuring a $500 \times 40 \mu\text{m}^2$ aperture. Variations of the environmental pressure induced bulging and strained the membrane, going along with significant resistance changes. The device showed a high resistive sensitivity of $\sim 1 \times 10^{-4} \text{ mbar}^{-1}$. Further, a geometric model was developed approximating the sensor's transfer function. By fitting the model to the experimental data, a gauge factor of $g \sim 7$ was determined.

The second project provides the first demonstration of the direct electrostatic actuation of freestanding GNP membranes using DC voltages. Here, microstructures featuring cylindrical cavities, supporting freestanding 6DT cross-linked GNP membranes with diameters of $\sim 200 \mu\text{m}$, were fabricated. The structures were equipped with electrodes at the bottom of the cavities, closely below the membranes, forming capacitive devices. When biasing the electrode-membrane pairs with DC voltages in the range of $\pm 40 \text{ V}$, electrostatic forces deflected the membranes by up to $\sim 1 \mu\text{m}$. The comparison of the experimentally observed voltage-deflection relations to a theoretical model suggested that the deflection behavior of the membranes was governed by their pre-stress, with values in the low MPa range. Electrostatic actuation is a versatile principle for coupling electronic

signals to motion/deflection of micro- and nanoscopic elements in MEMS/NEMS and can, in the case of GNP membranes, be used for various purposes, such as the fabrication of microoptoelectromechanical systems (MOEMS) or electromechanical sensors.

Two further projects focus on micro-/nanoelectromechanical resonators based on free-standing 6DT cross-linked GNP membranes with facile electrostatic excitation. It was demonstrated that circular or rectangular freestanding membranes with lateral dimensions in the tens of micrometer range show resonant vibrations in the high kHz to low MHz range and quality factors of up to ~ 2000 when operated in vacuum (10^{-1} to 10^{-2} mbar). An experimental setup was assembled, providing excitation of these devices by AC voltage signals and optical deflection read-out using laser interferometry. Experimentally observed resonance spectra and mode shapes were in good agreement with the model of a tense membrane, with negligible bending stiffness, oscillating in vacuum.

GNP membrane resonators and actuators are highly interesting devices for chemical sensing. As demonstrated in the fifth project, sorption of analyte molecules induces variations of the membranes' mechanical properties, resulting in pronounced shifts of the fundamental resonance frequency of GNP membrane resonators. A microelectromechanical chemical sensor is reported, consisting of a circular, 120 μm sized 6DT cross-linked GNP membrane. Using electrostatic excitation and interferometric deflection read-out, the resonance frequency of the device was monitored while exposing it to toluene, 4-methylpentan-2-one (4M2P), 1-propanol and water vapors under reduced pressure (~ 20 mbar). For example, fundamental frequency downshifts of up to $\sim 5\%$ were measured when dosing the sensor with toluene vapor at a partial pressure of ~ 20 Pa. It was further observed that sensors with GNP membranes tightly sealing microcavities display somewhat retarded responses to analyte exposure, compared to sensors featuring freestanding membranes on open structures. A continuative study, presently in progress, shows that this effect is presumably based on retarded analyte diffusion through the GNP membranes. Hence, due to different permeabilities of different analytes, the response times can potentially be used as a metric for analyte recognition.

A subsequent project aimed at the demonstration of microelectromechanical chemical sensing employing GNP membranes actuated by DC voltages. Like the resonance frequencies, the quasi-static voltage-deflection relation of an electrostatically actuated GNP membrane is influenced by the sorption-induced changes of its mechanical properties and can therefore also be used as sensing signal. This sensing principle is advantageous for detecting analytes under ambient conditions, as the deflections of quasi-statically actuated membranes may be slow and are hence not prone to damping. The novel transduction concepts discussed in this thesis can be employed in combination with conventional chemiresistive sensing using GNP membranes, to provide input for multivariable sensing applications.

Eventually, freestanding membranes of GNPs cross-linked by different α, ω -alkanedithiols (ADTs) were investigated regarding their elastic properties utilizing bulge testing. It was observed that the elastic modulus of the materials could be adjusted in the range between ~ 3 to ~ 10 GPa when decreasing the ADT chain length from 10 to 4, respectively. The

variation of the ADT chain length went along with changes in the materials' optical and electronic properties. This finding underlines the tunability and optimization possibility of GNP/ADT composites' properties for various applications, as addressed within this thesis.

2 Zusammenfassung

Kompositmaterialien aus organisch vernetzten Gold Nanopartikeln (GNPn) stellen eine neuartige Materialklasse dar. Neben einstellbaren optischen und elektronischen Eigenschaften weisen die Materialien die Fähigkeit auf Analytmoleküle aufzunehmen. Der Ladungstransport durch derartige Materialien basiert auf Tunneleffekten und ist daher sehr empfindlich gegenüber äußeren Einflüssen. Dies macht GNP-Kompositmaterialien interessant für Anwendungen in der Sensorik. In einem Großteil der bisherigen Forschungsarbeiten an GNP-Kompositen wurden diese in Form von Filmen, die zuvor auf Substraten abgeschieden wurden, untersucht. Die Herstellung und Charakterisierung von freistehenden GNP-Membranen mit Schichtdicken im Nanometerbereich wurde dagegen erst vor Kurzem demonstriert. Durch die Kopplung der mechanischen Eigenschaften solcher Membranen mit ihren elektronischen Eigenschaften, sowie ihrer Fähigkeit Analytmoleküle aufzunehmen, ergeben sich interessante Möglichkeiten zur Herstellung neuartiger, hybrider mikro- und nanoelektromechanischer Systeme (MEMS und NEMS) für Sensoranwendungen.

Die vorliegende Arbeit fasst verschiedene Projekte zusammen, in denen unter anderem erste Anwendungen von freistehenden GNP-Membranen in neuartigen mikro- und nanoelektromechanischen Sensoren und Aktuatoren demonstriert wurden. Des Weiteren wurde die Einstellbarkeit der elektronischen und mechanischen Eigenschaften der Komposite durch Variation der Vernetzungsmoleküle gezeigt. Die Projekte können in vier übergeordnete Themenbereiche aufgeteilt werden. Diese umfassen Drucksensorik, elektromechanische Aktuatoren und Resonatoren, chemische Sensorik, sowie die mechanische Charakterisierung der GNP-Membranen.

Im ersten Projekt wurden die elektromechanischen Eigenschaften einer 55 nm dicken, 1,6-hexandithiol-(6DT-)vernetzten GNP-Membran für die Herstellung eines neuartigen resistiven Drucksensors genutzt. Hierbei erfüllte die GNP-Membran zwei Funktionen. Zum einen verschloss sie eine mikrostrukturierte quaderförmige Kavität mit einer $500 \times 40 \mu\text{m}^2$ großen Öffnung, und trennte diese von der Umgebung. Änderungen des Umgebungsdrucks führten somit zu einer Auslenkung der Membran. Zum anderen wurde die resistive Dehnungssensitivität des Materials genutzt, um die aus der Auslenkung resultierende Dehnung der Membran als Widerstandsänderung zu erfassen. Der Drucksensor zeigte eine hohe resistive Sensitivität von $\sim 1 \times 10^{-4} \text{ mbar}^{-1}$. Weiterhin wurde ein geometrisches Modell zur Abschätzung der Transferfunktion des Sensors entwickelt. Bei Anwendung des Modells auf die experimentellen Daten wurde eine gute Übereinstimmung festgestellt. Weiterhin konnte ein k-Faktor der Membran von $g \sim 7$ ermittelt werden.

Das zweite Projekt umfasst die erste Demonstration der direkten elektrostatischen Aktuierung freistehender GNP-Membranen mit Gleichspannungen. Hierzu wurden Mikrostrukturen mit zylindrischen Kavitäten (Durchmesser: $\sim 200 \mu\text{m}$) hergestellt, welche von 6DT-

vernetzten Membranen überspannt wurden. Weiterhin enthielten die Mikrostrukturen Elektroden auf der Unterseite der zylindrischen Kavitäten, in geringem Abstand unter den freistehenden Membranen. Durch das Anlegen von Gleichspannungen im Bereich von ± 40 V zwischen den Elektroden und Membranen entstanden elektrostatische Kräfte, welche die Membranen bis zu ~ 1 μm auslenkten. Durch den Vergleich der experimentell ermittelten Spannungs-Auslenkungsbeziehungen mit einem theoretischen Modell konnte gezeigt werden, dass das Ansprechverhalten der Membranen durch ihre mechanische Vorspannung bestimmt wurde, die im niedrigen MPa-Bereich lag. Elektrostatische Aktuierung ist ein verbreitetes und vielseitig anwendbares Prinzip zur Kopplung elektronischer Signale mit Bewegungen und Auslenkungen mikro- und nanoskopischer Elemente in MEMS/NEMS. Im Falle der GNP-Membranen könnte das Prinzip für verschiedene Anwendungen genutzt werden, wie etwa zur Herstellung von mikrooptoelektromechanischen Systemen (MOEMS) oder elektromechanischen Sensoren.

Zwei weitere Projekte befassen sich mit mikro-/nanoelektromechanischen Resonatoren aus freistehenden, 6DT-vernetzten GNP-Membranen. Es wurde gezeigt, dass kreisförmige und rechteckige freistehende Membranen mit lateralen Größen von mehreren zehn Mikrometern resonante Oszillationen im hohen kHz bis niedrigen MHz-Bereich zeigen. Weiterhin ergaben sich Gütefaktoren von bis zu ~ 2000 , wenn die Resonatoren im Vakuum (10^{-1} bis 10^{-2} mbar) betrieben wurden. Im Rahmen dieser Arbeit wurde ein experimenteller Aufbau entworfen, mit dem derartige Resonatoren mittels elektrostatischer Anregung angetrieben, und resultierende Oszillationen der Membranen mittels Laserinterferometrie verfolgt werden konnten. Die beobachteten Resonanzspektren und Schwingungsmoden der Resonatoren konnten mit dem Modell einer gespannten, freistehenden Membran mit vernachlässigbarer Biegesteifheit im Vakuum beschrieben werden.

Resonatoren und Aktuatoren aus GNP-Membranen stellen äußerst interessante Systeme für die chemische Sensorik dar. Im fünften Projekt dieser Arbeit wurde gezeigt, dass die Sorption von Analytmolekülen zu Änderungen der mechanischen Eigenschaften der GNP Membranen führt. Hieraus resultierten Verschiebungen der fundamentalen Resonanzfrequenz der Resonatoren. Ein mikroelektromechanischer chemischer Sensor, basierend auf einem kreisförmigen, elektrostatisch angeregten 6DT-vernetzten GNP-Membranresonator mit einem Durchmesser von 120 μm wurde vorgestellt und mittels interferometrischer Schwingungsmessung ausgelesen. Der Resonator wurde unter reduziertem Druck (~ 20 mbar) betrieben und Prüfgasen mit verschiedenen Konzentrationen von Toluol, 4-Methylpentan-2-on, 1-Propanol und Wasser ausgesetzt. Dies resultierte z.B. in einer Abnahme der Grundfrequenz des Resonators von ~ 5 % bei einer Beaufschlagung mit Toluoldampf mit einem Partialdruck von 20 Pa. Weiterhin wurde gezeigt, dass die Sensorantwort von Membranen, die auf Mikrokavitäten abgeschieden wurden und diese vollkommen abschlossen, im Gegensatz zu der von Membranen die von beiden Seiten für die Prüfgase zugänglich waren, deutlich verzögert ist. Eine derzeit andauernde Untersuchung deutet darauf hin, dass diese verzögerte Sensorantwort geschlossener Resonatoren durch Diffusion der Analytmoleküle durch die Membranen verursacht wird. Aufgrund unterschiedlicher Permeabilitäten verschiedener Analytmoleküle kann diese Verzögerung potentiell als Merkmal für die Identifikation von Analyten genutzt werden.

In sich anschließenden Projekt wurde gezeigt, dass mit Gleichspannungen quasi-statisch aktivierte GNP-Membranen ebenfalls als chemische Sensoren genutzt werden können. Neben Resonanzfrequenzen von GNP-Membranresonatoren wird auch die Spannungs-Auslenkungsbeziehung von GNP-Membranaktuatoren durch sorptionsinduzierte Veränderungen ihrer mechanischen Eigenschaften beeinflusst. Die Nutzung der Spannungs-Auslenkungsbeziehung als chemisches Sensorsignal hat speziell bei Messungen unter ambienten Bedingungen den Vorteil, dass die quasi-statische Auslenkung, im Gegensatz zu hochfrequenten Oszillationen, bei Raumdruck nicht gedämpft wird. Die in dieser Arbeit vorgestellten neuartigen Sensorkonzepte können in Verbindung mit konventionellen GNP-membranbasierten Chemiresistoren in multivariaten Sensorsystemen kombiniert werden.

Schließlich wurden die elastischen Eigenschaften von GNP-Membranen, die mit α,ω -Alkandithiolen (ADT) unterschiedlicher Kettenlänge vernetzt wurden, mittels Bulge-Experimenten untersucht. Es wurde gezeigt, dass eine Einstellbarkeit des Elastizitätsmoduls zwischen ~ 3 und ~ 10 GPa durch die Verkürzung der ADT-Kettenlänge von 10 auf 4 erreicht werden kann. Die Variation der ADT-Kettenlänge geht ebenfalls mit einer Änderung der optischen und elektronischen Eigenschaften der Komposite einher. Die in diesem Projekt getätigten Beobachtungen unterstreichen die Möglichkeiten, die Eigenschaften von GNP-Kompositmaterialien für spezifische Anwendungen, wie z.B. der in dieser Arbeit beschriebenen Nutzung in MEMS und NEMS, anzupassen.

3 Introduction

Human beings own different sensory receptors — transducers collecting information from their surrounding or interior and propagating them as electric stimuli to the central nervous system.^[7] Sensing enables perception and subsequent reaction, e.g. to environmental changes. The five traditionally recognized senses were firstly listed by Aristotle^[8] and encompass the ability to hear (auditory perception), see (vision), taste (gustation), smell (olfaction) and touch (cutaneous sensation).^[7] By far, this traditional listing is non-exhaustive as humans can also i.a. sense temperature, balance, motion, vibration and pain. Furthermore, our bodies are equipped with a multitude of other sensory receptors.^[8] The ability to sense grants the capability to interface with the environment and other individuals, which enables human life and makes it enjoyable.

Today, the demand for new technologies drives the development of an increasing number of devices and machines, fulfilling a broad variety of tasks in the fields of science, health care, medicine, communication, transportation, environmental monitoring, entertainment and many more. Several of these devices are designed for the direct interaction with humans, or to monitor and — when appropriate — react to external events, environmental conditions, changes of their orientation in space, or other physical parameters. As data acquisition, processing and evaluation are commonly based on analog and digital electronic circuitry, these entities have to be transduced into electronic signals, i.e., currents or voltages. The need for transducers fulfilling this task — electronic analogs of the human sensory receptors — has lead to intensive research and development in the field of sensors. As of today, a broad plurality of sensors is commercially available and implemented into everyday life devices, e.g., smartphones, cars, fitness gadgets or portable health care devices. To return to the traditional human senses, these are roughly represented by electronic analogs such as microphones (auditory perception), photodetectors/pixel sensors (vision), electrochemical sensors/electronic tongues (gustation), gas and vapor sensors/electronic noses (olfaction), and touch/strain sensors (cutaneous sensation). Furthermore, electronic sensors enable the detection of physical quantities which cannot be readily sensed by the human body, such as magnetic fields, electromagnetic radiation in a broad frequency range and many more. A variety of these sensors are elaborate and perform with high sensitivity, precision and selectivity or even specificity, while the development of others is still in its infancy.

Many sensors are based on microelectromechanical systems (MEMS). Generally, electromechanical systems are mechanical elements coupled to electronic circuitry via electromechanical transducers. While input transducers perform actuation, i.e., the translation of electronic signals into mechanical stimuli, output transducers sense mechanical stimuli and convert them into electronic signals.^[9] Materials and processes of microelectronics enabled the development of lithographic processes for the production of microscopic electromechanical systems, provoking the use of the term MEMS.^[9] Since their commercialization in the 1970s, MEMS have grown to a technology being outstandingly

successful in providing high performance sensors, available in high volumes and at low unit prices.^[10] The onset of silicon-based MEMS sensors was related to accelerometers and pressure sensors, which became widespread as they fulfilled the qualifications for automotive environments.^[11] Here, they were used especially in safety-critical systems like airbags and brakes, as well as in engine management systems.^[11] Since 2009 the MEMS sensor market experiences a noticeable growth, fueled by their use in consumer electronics, such as smartphones. These applications require small-sized, ultra-low current and ultra-low price MEMS.^[11] Examples for such sensors in mobile devices are microphones, accelerometers and gyroscopes for position/orientation sensing, or pressure sensors, which are utilized e.g. for altitude sensing or — in combination with other devices — for delivering weather forecasts.^[10] The use of MEMS in consumer electronics surpassed the automotive market share in 2012.^[11,12] In 2018 the MEMS market is expected to exceed 12 billion USD, covering the application fields of consumer and mobile electronics, automotive technologies, data processing, industry, medical electronics, military and civil aerospace, and wired communications.^[12]

Research and development continuously aim at the fabrication of sensors employing novel materials and transduction methods to achieve higher sensitivities and selectivities. Following the trend in commercial transistor electronics, MEMS feature sizes are being decreased, reaching the nanometer scale. Devices employing functional components in this size regime are often referred to as nanoelectromechanical systems (NEMS).^[9,13] The recent advances in nanotechnology provide novel classes of nanostructured materials and makes use of different phenomena or structural characteristics observable at nanoscopic length scales.^[13] Hence, besides the fabrication of MEMS and NEMS using conventional, well-established silicon-based technologies^[10] novel (nano-)materials have been introduced for the fabrication of functional hybrid MEMS/NEMS components.

While on the one hand one-dimensional materials such as carbon nanotubes (CNTs) are investigated, e.g. as resonators with high mass sensitivity,^[14,15] on the other hand freestanding nanomembranes recently attracted considerable attention. Different materials such as graphene,^[16–29] the transition metal dichalcogenides (TMDCs),^[30–36] black phosphorous,^[37] nanometer thin carbon nanomembranes^[38–41] or composite structures based on nanoparticles^[1–4,42–48] are currently being studied regarding their mechanical properties, resonance behavior and potential applications, i.a. in sensing and signal processing.

This work focuses on the characterization of freestanding membranes consisting of dithiol (DT) cross-linked gold nanoparticles (GNPs) with nanoscale thicknesses, and the exploration of their potential applications in MEMS/NEMS devices. Originating from their nanostructure, GNP-based composite materials, which can be fabricated from solutions of colloidal GNPs via facile ink-based procedures,^[49–52] offer unique and tunable structural, optical,^[52–54] and electronic properties.^[52,53,55–57] These led to demonstrations of applications e.g. as resistive strain sensors^[50,58–61] or — due to their ability to sorb analyte molecules — chemiresistors,^[51,53,60,62–67] i.e., resistive sensors for the detection of analytes in the liquid or gas phase. In the vast majority of such (sensing) devices, the GNP composites were employed as thin films deposited onto wafers, glass or flexible materials, such as polymers. However, the fabrication of freestanding GNP composite membranes,

supported by microstructures, enables coupling of their unique electronic and optical properties to their mechanical characteristics. This interplay gives rise to a multitude of interesting features, which can be employed in new types of hybrid MEMS/NEMS.

In the first part of this work, a novel type of resistive pressure sensor with high sensitivity is introduced.^[2] The sensor comprises an α, ω -alkanedithiol (ADT) cross-linked GNP composite membrane as functional component, acting both as diaphragm and strain sensitive transducer. To the best of our knowledge, this is the first report of a pressure sensor utilizing the electromechanical properties of a freestanding nanoparticle membrane to achieve a direct resistive signal read-out.

The second part of this work embodies the first demonstration showing the direct electrostatic actuation of a conductive GNP membrane.^[1] Electrostatic actuation is a common principle in MEMS and NEMS,^[9] and a versatile method for deflecting or translating mobile components of such systems by the application of an electronic signal. The demonstrated capability of electrostatic actuation enables advanced applications and investigations, as outlined in the following parts of this thesis.

The third study covers the demonstration of electrostatically driven drumhead resonators of ADT cross-linked GNP membranes.^[3] Here, electrostatic actuation with alternating current (AC) voltages was employed to drive resonant oscillations of freestanding GNP membranes. Such drumhead resonators are promising candidates for different sensors, as their resonance frequencies can be influenced by changes in their environment.

The latter is endorsed in the fourth part of this work.^[4] The project provides the first demonstration of an electrostatically driven GNP membrane resonator acting as a chemical sensor for volatile organic compounds (VOCs). A pronounced shift of the resonator's fundamental resonance frequency under exposure to toluene, 1-propanol, 4-methylpentan-2-one (4M2P) and water was measured. Its operating mode represents a novel transduction mechanism for the detection of chemical vapors or gases using GNP composites.

Further, yet unpublished studies aiming at the mechanical characterization of GNP membranes cross-linked by different DTs, a deepened investigation of the resonance behavior of GNP/ADT membranes, and additional experiments regarding chemical sensing using freestanding GNP membranes are described.

The following section provides an overview on the scientific context, the current state of knowledge and a résumé of the underlying theory regarding the different aspects of this work. First, the synthesis and characteristics of GNPs are described, followed by a section highlighting the fabrication, charge transport properties and related sensing applications of GNP composites. Afterwards, freestanding nanomembranes, studies into their electromechanical properties, their resonance behavior and sensing applications are described. As this research project involved the design and assembly of a measurement setup utilizing an interferometer for device characterization, eventually the basics of the interferometric measurements are introduced.

3.1 Gold Nanoparticles

Since ancient times, the element gold, with its pretty shiny yellow appearance, attracted the interest of mankind. The extraction of gold started in the 5th millennium before christ (B.C.) near Varna (Bulgaria).^[68] Since then, gold became probably the most prominent noble metal for the fabrication of artworks, decoration and jewelry, and a valuable trading good. Furthermore, due to its high electrical conductivity and stability against corrosion, bulk gold and gold coatings play a crucial role in the electronics industry.^[69,70] Typical applications include corrosion-resistant contact platings, bond wires in semiconductor packages, hybrid circuits, solderable coatings for printed circuit boards (PCBs), gold based solders, and metal layers on semiconductors acting as conductor tracks and contact pads. Another large fraction of gold is used for dental crowns, bridgework, porcelain enamel onlays and inlays, due to its biocompatibility.^[69] However, due to its comparably high price, other materials such as palladium and platinum are often preferred over gold, especially in cases where the requirements for chemical resilience are lower.^[69]

The properties of many bulk substances have been studied extensively in solid state physics and materials science and are believed to be well understood.^[71] With the rise of nanotechnology, the characterization of materials with dimensions on the 1 to 100 nm scale became more and more popular. Nanometer scale matter consists of collections of molecules or atoms, whose properties are neither those of their individual constituents nor those of the corresponding bulk substances.^[71] Different effects arise and — depending on the material class — lead to the observation of unique phenomena and enable new applications. To name a prominent example, there is the quantum size effect observed when shrinking semiconductor (e.g. CdSe) particles to the nanoscale. Due to the confinement of charge carriers in small particles, this effect yields the tunability of the electronic band gap without changing the materials composition, just by variation of the particle size.^[72–75] In another example, magnetic nanoparticles, such as particles from iron oxides, show magnetic properties that are different from the respective bulk material when reaching a certain nanoscale dimension in the order of the magnetic domain size. They commonly show superparamagnetism, i.e., they behave like strong paramagnets.^[76] Furthermore, noble metal (especially gold) nanoparticles show interesting electronic and optical effects, which are described in the following.

The interesting properties and expected applications of such nanoscale objects resulted in driving considerable research efforts concerning their fabrication. While on the one hand *top-down* approaches, such as photo- or electron beam lithography as well as etching or ablation processes are being pushed to produce smaller structures with increasing precision and higher throughput, on the other hand *bottom-up* approaches based on chemical syntheses starting from molecular precursors and yielding colloidal solutions of nanoparticles are being investigated.^[77] Up to now an enormous diversity of scientific studies has been published, including protocols for the synthesis of nanostructures from a large variety of materials and with well controlled sizes and shapes.

Within the library of available nanomaterials, GNPs have a special standing. Among

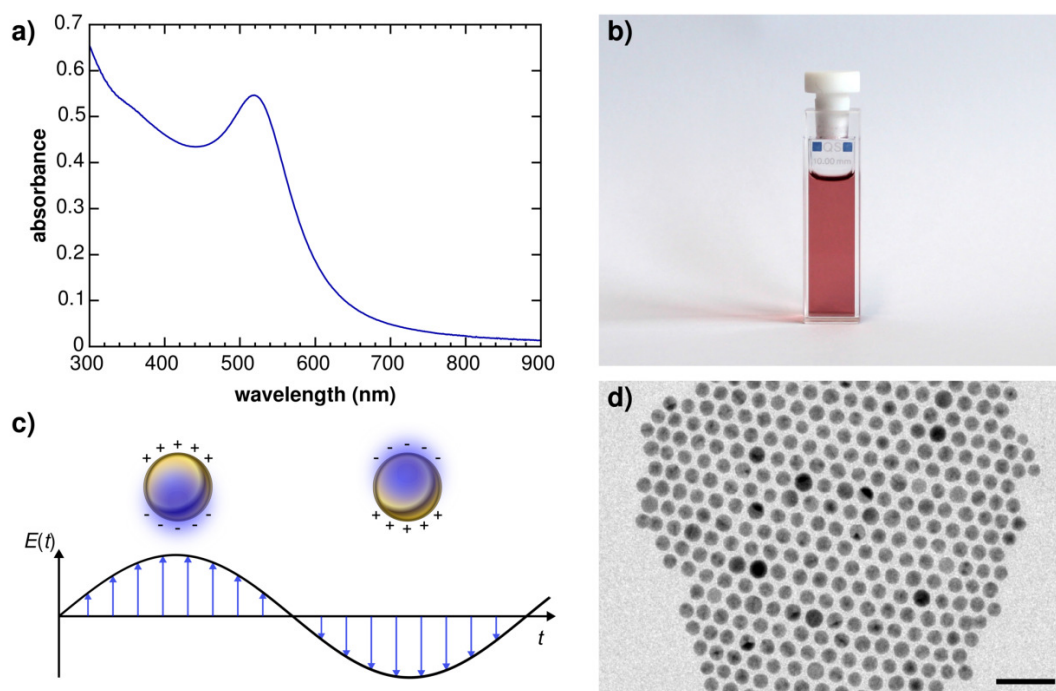


Figure 3.1: a) Absorbance spectrum of the GNP solution depicted in figure part b. The SPR absorption peak at $\lambda \sim 520$ nm is clearly visible. b) Photograph of a cuvette, containing a solution of GNPs in hexane. c) Schematic showing coherent oscillations of a GNP's conduction band electrons in the electric field of incident light. A dipolar oscillation is shown, as significantly contributing to the optical properties of small GNPs ($\lambda \ll D$). d) Transmission electron micrograph of the GNP sample depicted in figure part b. Sample preparation was performed by drop-casting a volume of the dispersion onto a carbon-coated TEM substrate. Scale bar: 20 nm.

metal nanoparticles, they are the most stable.^[68] Still, the interesting surface chemistry of gold allows the controlled exchange of ligands,^[68] and the decoration of the particles with small or complex molecules. In the latter case, these can be e.g. biomolecules such as deoxyribonucleic acid (DNA) functionalized with thiol groups to bind to the GNPs via the formation of strong gold-sulfur bonds.^[78,79] By combining batches of GNPs functionalized with different, complementary DNA strands, it was even possible to prepare specifically designed arrangements of GNPs.^[80] Due to their unique surface chemistry and interesting optical features, gold nanoparticles provide a rich platform for biological detection^[81] as well as medical diagnosis and therapy.^[82] The formation of gold-sulfur bonds can also be exploited for the fabrication of cross-linked GNP networks, as targeted in this work and described in section 3.2.1.

3.1.1 Optical Properties

In contrast to bulk gold, GNPs show a pronounced absorption band that is commonly located in the visible spectral range (cf. figure 3.1a), leading to an intensive red appearance of their solutions.^[83] A photograph of a cuvette containing a dilute GNP solution in hexane is depicted in figure 3.1b. Figure part 3.1d provides a transmission electron micrograph

of the respective gold colloids drop-casted onto a carbon-coated transmission electron microscopy (TEM) substrate. Their impressive appearance caused people to deploy gold colloids for aesthetic purposes and arts. An example is the pigment “Purple of Cassius”,^[84] which was used to give glass a ruby-red coloration or to stain enamel, chinaware, and silk fabric.^[83] Another prominent example of the early artistic use of gold/silver^[85] nanoparticles in glass is the Lycurgus cup (4th century A.D.), appearing green in daylight (reflected light), but red under illumination from the inside (transmission).^[68,83]

The underlying physics of these optical phenomena were explained much later. The origin of the characteristic absorption band of GNPs (see the spectrum in figure 3.1a) is the surface plasmon resonance (SPR). As schematically depicted in figure 3.1c this resonance is based on the coherent oscillation of the free conduction band electrons. Upon exposing GNPs to light, the incident electromagnetic waves are able to interact with their conduction band electrons leading to polarizations. The resulting displacement of the electron density with respect to the positively charged GNP cores leads to a restoring force and hence, oscillations of the electrons.^[83] When the wavelength of the incident light matches the SPR frequency, strong absorption of the electromagnetic radiation can be observed, displayed by the characteristic absorption band in the GNPs’ absorption spectra.

In 1908 Gustav Mie described this phenomenon by solving Maxwell’s equations for spherical particles with the appropriate boundary conditions.^[68,83,86] Mie’s theory describes the particles’ extinction coefficient as the summation over all electric and magnetic multipole oscillations contributing to the absorption and scattering of the interacting electromagnetic field.^[87] In the case of small particles with the diameter D being significantly smaller than the incident wavelength $D \ll \lambda$ only the dipolar term is assumed to contribute to the absorption. In this quasi-static regime, the extinction coefficient κ for N particles of volume V_{NP} can be described following equation 3.1.^[83,87]

$$\kappa = 9N \frac{\omega}{c_0} \epsilon_m^{3/2} V_{\text{NP}} \frac{\epsilon_2(\omega)}{[\epsilon_1(\omega) + 2\epsilon_m]^2 + \epsilon_2(\omega)^2} \quad (3.1)$$

Here, ω denotes the angular frequency of the incident light, and c_0 the speed of light. $\epsilon(\omega) = \epsilon_1(\omega) + i\epsilon_2(\omega)$ is the complex, frequency-dependent dielectric function of the particle material and ϵ_m represents the dielectric constant of the medium surrounding the particles, which is assumed to be frequency-independent.

The dipole approximation described by the above equation does not give any particle size-dependence of the optical absorption spectrum (except for its linear scaling that is proportional to V_{NP}). This is in contrast to experimental observations. For particles smaller than 20 nm, the plasmon bandwidth is inversely proportional to the particle radius.^[87] A size dependence for the quasi-static regime was introduced by assuming a size-dependent dielectric function $\epsilon(\omega, D)$.^[87]

When GNPs are well-separated, i.e., excluding particle-particle interactions, the optical

response of an N particle system is the N -fold of the individual. This is not anymore the case for particle systems with higher packing densities and hence comparably low interparticle spacings.^[83] The plasmon oscillations of the individual particles result in strongly enhanced near fields, localized at the particle surfaces. The near-fields of adjacent particles are able to interact, leading to a coupled plasmon oscillation and consequently significant changes in the optical spectra. For assemblies or aggregations of GNPs in solution this is observed as a red-shift of the plasmon band.^[88] As the plasmon coupling is distance dependent, the effect can be utilized to detect recognition events of molecules attached to GNPs, as in the above-mentioned biochemical examples.^[78–81]

Jain et al. studied the effect of plasmon coupling on the absorbance spectrum of lithographically fabricated gold nanodisc dimers with varying distances. They found that the fractional plasmon wavelength shift for polarization along the interparticle axis decays nearly exponentially with increasing interparticle gaps, with a decay length that is roughly about 0.2 in units of the particle size for different nanoparticle sizes, metal types, or medium dielectric constants.^[88] Sönnichsen et al. exploited the distance-dependent plasmon coupling effect as “plasmonic ruler” and applied it to study the kinetics of DNA hybridization events.^[89] Absorption spectra of composite films, comprising a multitude of GNPs with different interparticle spacings controlled by coating the individual particles with silica shells, have been studied by Ung et al.^[90] and described using the Maxwell-Garnett effective medium theory.^[91,92]

3.1.2 Synthesis

In 1857, Faraday synthesized GNPs, which he suspected to be smaller than the wavelength of light,^[93] by reducing an aqueous solution of a gold salt, such as sodium chloroaurate, with a solution of phosphorous in CS_2 .^[68,94] Since then, a multitude of research reports has been published, aiming at the synthesis of GNPs having different sizes and shapes, capped with a variety of stabilizing agents or functional ligands. The following paragraphs are restricted to two popular methods, which evolved into standard procedures for GNP fabrication.

One prominent approach for the fabrication of GNPs was introduced by Turkevich et al. roughly a century after Faraday’s report. It involves the reduction of gold salts by citrate in aqueous solutions.^[95] The obtained colloids showed average diameters of approximately 20 nm and were stabilized by citrate molecules.^[68,96] Later, in 1973, Frens reported on the size control of GNPs fabricated following Turkevich’s procedure, yielding GNPs of prechosen diameter between 16 and 147 nm by adjusting the sodium citrate concentration, i.e., the citrate to gold ratio.^[97] Further improvements of the Turkevich method have been made, such as lately by Schulz et al. who achieved narrowing of the size distribution by using citrate buffers instead of a citrate solution to control the pH. Further, the shape uniformity of particles was improved by adding ethylenediaminetetraacetate (EDTA) to the reaction.^[96] The Turkevich method is still commonly used, as the stabilizing citrate shell of the GNPs obtained via this route can readily be exchanged by ligands having a

higher affinity to gold — such as thiols — allowing functionalization of the particles.^[68,96]

Another popular method was introduced by Brust et al.. The Brust-Schiffrin method,^[98] published in 1994, was groundbreaking as it firstly allowed the facile synthesis of thermally and air stable GNPs of reduced dispersity and controlled size.^[68] The group used a two-phase system, consisting of a toluene and a water phase. A phase transfer agent, i.e., tetraoctylammonium bromide, was utilized to transfer dissolved $[\text{AuCl}_4]^-$ anions from the aqueous to the organic phase, where the gold compound was reduced by NaBH_4 in the presence of dodecanethiol ligands. Particles with diameters ranging from 1 to 3 nm, with a maximum in the size distribution at 2.0 – 2.5 nm were observed by TEM characterization. Further, the particles could be handled as simple chemical compounds. They could be dried and afterwards redissolved in different non-polar solvents.^[98]

A modification of the original Brust-Schiffrin method reported by Leff et al., yielding 2.5 – 7.0 nm sized GNPs capped with primary amine ligands is of particular interest for the present work.^[99] As the amine-gold bond is weak compared to the thiol-gold bond,^[53,100,101] the particles easily undergo ligand exchange reactions with thiols. In this work we synthesized GNPs following this method and fabricated networks of cross-linked GNPs by ligand-linker exchange with DTs.

3.2 Gold Nanoparticle Composites

This section gives a survey of nanoparticle composites, focusing on materials consisting of cross-linked GNPs. Besides their fabrication, their charge transport properties and recent studies probing their applications as active materials in different sensors will be highlighted.

The motivations for fabricating solids consisting of nanoparticle assemblies are manifold. Depending on the particle type and the matrix separating the particles such composite materials show — due to their nanoscale morphologies — novel collective properties making them promising candidates for various applications. Further, the composites' properties can be adjusted by tuning the properties of the incorporated nanoparticles and/or by varying the matrix material, enabling the fabrication of tailored materials fulfilling specific requirements.

One example belongs to the field of photonics. Here, arrays of highly ordered or near-range ordered nanoscale (and microscale) particles can behave as photonic crystals^[102] or glasses,^[103] respectively, due to their inherent (periodic) alternation of the refractive index. These materials show interesting optical properties such as a photonic band gap and can be employed to control the propagation of light.

In the field of electronics and optoelectronics, Talapin et al. stated that considering chemically synthesized nanoparticles for such applications, the actual active element of most devices will not be individual nanoparticles but their macroscopic arrays.^[104] Such assemblies of e.g. semiconductor nanoparticles are studied in depth, as they provide an alternative to bulk inorganic semiconductors. While the traditional bulk materials offer superior carrier mobilities, light absorption, thermal- and photostability, they are difficult to form by low-cost processes.^[104] In contrast, semiconductor and metal nanoparticles can be prepared via chemical synthesis yielding their colloidal solutions, which can straightforwardly be deposited onto a variety of substrates by cost-effective ink-based deposition methods. Such methods include spin-coating,^[52,105] drop-casting,^[61] spray coating,^[51,106,107] layer-by-layer self-assembly,^[49,53,60] Langmuir-Blodgett techniques,^[108] ink-jet printing,^[109] and presumably many more. Depending on the method as well as the characteristics of the nanoparticles (size, size dispersity, shape, material), their ligand shell, solvent, and concentration, such depositions yield mono- or multilayered, ordered or disordered nanoparticle composite films of adjustable thickness and lateral dimensions. Employing such deposition techniques, different nanoparticle composite based electronic devices were reported. These include e.g. printed field effect transistors (FETs)^[110] or spray coated solar cells from e.g. PbS^[106] and CuInSe₂^[107] nanoparticles. Many of the listed deposition procedures are not limited to rigid substrates. Hence, deposition of nanoparticles onto flexible substrates is possible, offering the fabrication of flexible electronics. These represent a promising technology and are highly demanded, e.g. for applications in wearable devices.^[111]

In colloidal solutions, inorganic nanoparticles are commonly surrounded by a stabilizing ligand shell. Their initial ligands/surfactants are introduced during the particles' syn-

thesis, to control particle growth and to achieve stabilization of the colloids.^[112,113] The chemical nature of the ligand shell may further alter the particles' characteristics such as their optical properties,^[113,114] provide the particles with solubility in a targeted solvent or equip them with a desired surface functionalization.^[113] However, when depositing nanoparticles, their ligand shells commonly endure the deposition process and form a matrix separating the particles in the resulting composite material. Therefore, the electronic properties of a nanoparticle composite depend not only on the electronic structure of the individual nanoparticles, but are also strongly influenced by their matrix. This circumstance has its assets and drawbacks, depending on the intended application of the material.

On the one hand, for the fabrication of electronic and optoelectronic devices, a high mobility of charge carriers within the active material is often desired.^[115] In this case, a ligand matrix comprising bulky, insulating hydrocarbon chains — as present in frequently used thiols, amines, phosphines, phosphine oxides and phosphonic acids — located between the individual nanoparticles is unfavorable.^[115] Such ligands act as insulators and tunneling junctions, impeding charge carrier transport through the nanocomposite films. Great efforts are made to overcome this burden, e.g. by exchanging the native ligands of the particles with very small molecules such as hydrazine,^[116] or 1,2-ethanedithiol (2DT),^[117] inorganic ligands or cross-linkers,^[115,118] thermally decomposable ligands to enable annealing of the particles,^[119,120] or specifically designed cross-linkers, matching the energy levels of the particles and leading to band-like, enhanced transport.^[115]

On the other hand, GNP composites can be employed for the fabrication of highly sensitive sensors, such as resistive strain sensors or resistive sensors for gases or VOCs (chemiresistors). For these particular applications, the separation of the nanoparticles by organic molecules is crucial, since it provides tunneling junctions as well as a flexible matrix, and allows for sorption of analytes. Small perturbations of this matrix, such as variations in the ligand shell thickness (interparticle distances) or changes in the dielectric characteristics, are reflected by drastic changes of the composite's charge transport capabilities. Hence, the conductivity of GNP composites can act as a sensing signal. As this key feature is essential for some parts of this study, it will be described in detail in the respective sections 3.2.2, 3.2.3, and 3.2.4.

3.2.1 Fabrication

This section gives some examples for substrate-supported GNP composites. The fabrication of freestanding membranes is described in section 3.3.1.

In current literature, many GNP composite materials are reported, differing in various physical parameters. There are GNP assemblies ranging from disordered structures^[48,52,53] to GNP supercrystals and superlattices showing tremendous long-range order.^[65,121,122] Further, GNPs in their assemblies can be covalently cross-linked^[49,52,53,60,123,124] (to different degrees) or be attached to each other just by van-der-Waals interactions.^[65,121,122]

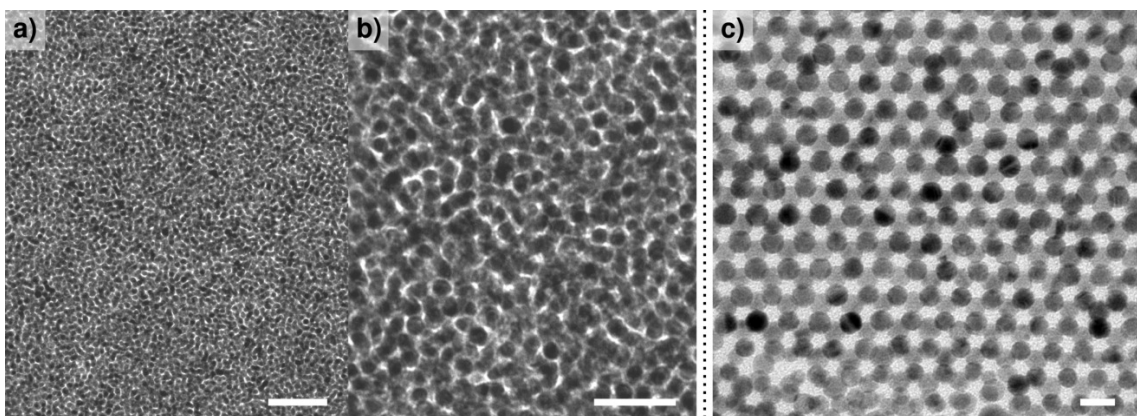


Figure 3.2: Transmission electron micrographs of GNP assemblies. *a)*, *b)* Film of 1,9-nonanedithiol (9DT) cross-linked GNPs (particle diameter: ~ 4 nm, thickness 41 nm) prepared via a LbL-spin-coating based procedure on glass and afterwards transferred to a TEM substrate. Reprinted with permission from [48]. ©2014 American Chemical Society. *c)* Ordered arrangement of OA-stabilized ~ 5.6 nm diameter GNPs formed by assembly at a DEG-air interface and subsequently transferred to a TEM substrate. Courtesy of S. Kunze.^[125] Scale bars: *a)* 50 nm, *b)* 20 nm and *c)* 10 nm.

Figure 3.2c exemplarily shows a transmission electron micrograph of an ordered, multi-layered array of ~ 5.6 nm diameter oleylamine (OA) stabilized GNPs. The structure was assembled at the liquid-air interface of a diethylene glycol (DEG) subphase and subsequently transferred to a carbon-coated TEM substrate. Sandwich-type composites of GNPs embedded between polyelectrolyte layers, fabricated by a layer-by-layer (LbL) spin-coating technique were reported by the Tsukruk group.^[46,54] Generally, different particle sizes, size dispersities and ligand systems were utilized for composite fabrication. A listing of various organically modified metal and alloy nanoparticle systems, specifically used for sensing applications, is provided in a review by Ibañez and Zamborini.^[64] Further, GNP assembly has been conducted on solid substrates such as glass,^[52] silicon wafers^[53] or on various flexible substrates^[61,111].

As mentioned above, the charge transport in GNP composites is strongly dependent on the interparticle matrix. Even though this is crucial for different sensing applications, materials consisting of GNPs capped with long-chain 1-alkanethiols (ATs) or encapsulated within polymers often show extremely low conductivities. This complicates charge transport measurements, as very low currents have to be detected when biasing the samples with reasonable voltages in the 0 – 10 V range. For this study, aiming at the coupling of electronic and mechanical properties of freestanding GNP composites, sheet resistances not exceeding the low $M\Omega$ range are desirable at the given membrane thicknesses of < 100 nm. This is, because of geometrical constraints in freestanding structures, the use of interdigitated electrode structures enabling low resistances at comparably high resistivity is unfavorable. Ideal systems for these purposes are composites of GNPs cross-linked with short DT molecules. Therefore, most experiments described in this work were conducted employing 1,6-hexanedithiol (6DT) cross-linked GNP films and membranes, which showed an acceptable sheet resistance of $R_{\square} \sim 1 M\Omega$ at 55 nm membrane thickness.^[2]

ADT cross-linked GNP composites were firstly reported by Brust et al.. By introducing

ADTs into their synthetic procedure, initially used for the fabrication of AT-stabilized GNPs (see section 3.1.2),^[98] the group observed the formation of GNP clusters which precipitated as an insoluble black solid from their solutions.^[49,55] The group used the precipitated cross-linked GNP composites for the fabrication of pellets and investigated their charge transport properties, as described in section 3.2.2.

Further, Bethell et al. reported a versatile method (LbL self-assembly) for the fabrication of cross-linked GNP films on substrates.^[49] First, a glass substrate was functionalized by treatment with 3-mercaptopropyl-trimethoxysilane. Afterwards, a monolayer of GNPs was attached to the free thiol groups exposed on the substrate surface, by immersion into a solution of “thiol-free” GNPs. These stable solutions of “thiol-free” ~ 8 nm sized GNPs were obtained by omitting the addition of ATs during the particle synthesis. Following a washing step with toluene, the substrate was immersed into a solution of ADT to functionalize the free surface of the GNPs bound to the glass substrate. By a further washing step and a second immersion into the solution of the “thiol-free” GNPs, a second layer of particles was bound on top of the first layer. By repeating these washing/immersion steps with ADT and GNP solutions, multiple particle layers could be deposited. The whole process could conveniently be followed by monitoring the film’s increasing SPR absorption band originating from the deposited GNPs.^[49] The LbL self assembly method was adapted to grow GNP films cross-linked with different dithiol linkers on various functionalized substrates, such as polyethylene,^[58,60] glass or oxidized silicon wafers.^[53,126,127] Here, instead of the “thiol free” GNPs utilized by Bethell et al., GNPs with a 1-dodecylamine (12A) or OA ligand shell, obtained e.g. by synthetic procedures of Leff et al.^[99] or Shen et al.,^[128] respectively, were used. Again, due to the comparably weak amine-gold bond, the ligands were readily stripped and replaced by the strong-binding DT-linkers.^[53]

While the LbL self-assembly method is outstanding for the fabrication of a variety of substrate-supported cross-linked GNP films and yields high degrees of gold-thiol binding,^[53] it has drawbacks when it comes to the fabrication of GNP composites that should later be detached from their initial substrates for the fabrication of freestanding structures. Due to the need for functionalization of the substrate to provide binding sites for the first particle layer, the resulting GNP film is covalently bound to its support. This hinders lift-off and transfer procedures. Also, a relatively high number of time-consuming deposition cycles with several washing steps is necessary for obtaining film thicknesses suitable to fabricate stable, freestanding membranes. Different methods specifically aiming at the fabrication of freestanding GNP membranes are discussed separately in section 3.3.1.

In 2011, our group published a versatile protocol for the rapid fabrication of ADT cross-linked GNP films via a LbL spin-coating method.^[52] This method is discussed in detail in section 5.1.1, as it was extensively employed to fabricate GNP films used in this work. In brief, a concentrated nanoparticle ink containing 3 – 4 nm sized 12A stabilized GNPs in *n*-heptane is applied to a rotating substrate on a spin-coater, leading to the deposition of a particle multilayer. The layer is then cross-linked by depositing ADTs in methanol, with the latter being a non-solvent for the GNPs. By repeating these particle deposition and cross-linking steps, films of several tens of nm thickness can be fabricated within minutes.

Further, as there is no need for a complete immersion of the substrates, only μL volumes of the particle solution are necessary. Films obtained by our LbL spin-coating method show optical and electronic properties which are comparable to those of films obtained by LbL self assembly.^[52] A transmission electron micrograph of a 41 nm thick 9DT cross-linked GNP film, transferred to a carbon coated TEM substrate after fabrication, is depicted in figure 3.2a and b. The film shows a very homogeneous structure on a larger scale, while its disordered, granular nature can be clearly seen at higher magnifications.^[48]

3.2.2 Charge Transport and Resistive Sensing

While the GNPs within a composite material act as conductive cores, the ligand or cross-linker matrix separating the particles forms tunneling barriers for charge carriers. Accordingly, the charge transport behavior can be described by a thermally activated tunneling model, and commonly shows a non-metallic behavior, i.e., an increase in conductivity with increasing temperature.^[55]

The charge transport properties of pellets from small, ligand-stabilized Au₅₅ clusters were investigated by van Staveren et al.^[129] The group observed a temperature-dependent conductivity having a linear dependence of $\ln \sigma$ on $T^{-\frac{1}{2}}$. This is in agreement with earlier studies on granular metals (cermets).^[130] In later studies published in 1995, the charge transport properties of drop-casted films from ligand-stabilized, 1.2 nm sized gold clusters^[56] or of pellets consisting of ADT cross-linked 2.2 nm and 8.0 nm sized GNP composites^[55] were studied by Terrill et al. and Brust et al., respectively. Also within these materials, both groups also observed non-metallic conduction behavior. Here, the temperature dependence of the conductivity σ could be better described^[55] by a simple relation first employed by Neugebauer and Webb for the description of the conduction behavior of evaporated metal films, consisting of a planar array of many discrete metal islands.^[131] This relation (equation 3.2) yields an Arrhenius type T^{-1} temperature dependence of the logarithmic conductivity $\ln \sigma$.

$$\sigma = \sigma_0^\dagger \exp\left(-\frac{E_a^\dagger}{kT}\right) \quad (3.2)$$

Here, σ_0^\dagger is a preexponential factor and E_a^\dagger is the activation energy. Based on the expectation that electron transfer rates decrease exponentially with distance, Terrill et al. proposed a model equation incorporating an exponential tunneling term for including the conductivity's dependence on the interparticle spacing δ (equation 3.3).^[56] The biexponential model was utilized to successfully describe temperature-dependent conductivities of thin films comprising AT stabilized^[56,132] and ADT cross-linked^[53,57,127] GNPs.

$$\sigma(T, \delta) = \sigma_0 \exp(-\beta\delta) \exp\left(-\frac{E_a}{kT}\right) \quad (3.3)$$

Here, σ_0 denotes a preexponential factor and E_a the activation energy. β is the tunneling decay constant.

The second exponential term of the equation describes the above-mentioned temperature dependence. According to the model proposed by Neugebauer and Webb,^[131] and also stated in the granular metal theory by Abeles et al.^[130] E_a is an activation energy for the charge transport, related to the energy cost for the generation of charge carriers, i.e., to remove an electron from a neutral metal particle and to transfer it to another neutral

particle. In the low field regime, the granular metal theory suggests a temperature dependence of the conductivity $\sigma \propto \exp[-2(C/kT)^{0.5}]$, where $C = \delta\beta^\ddagger E_a^\ddagger$ and the activation energy E_a^\ddagger corresponds to:^[57,130]

$$E_a^\ddagger = \frac{e^2}{8\pi\epsilon_r\epsilon_0} \left(\frac{1}{R_{\text{GNP}}} - \frac{1}{R_{\text{GNP}} + \delta} \right) \quad (3.4)$$

R_{GNP} represents the radius of the particles, δ the interparticle spacing and ϵ_r as well as ϵ_0 the relative permittivity of the matrix material as well as the vacuum permittivity, respectively. Brust et al. and Vossmeier et al. used equation 3.4 for the calculation of charge transport activation energies E_a of ADT cross-linked GNP films, assuming an Arrhenius-type activation (cf. equations 3.2 and 3.3). They observed a good agreement with experimentally determined values.^[55,58]

The first exponential of equation 3.3 describes the tunneling of the electrons through the organic matrix between the particles.^[57] Here, β denotes the tunneling decay constant.^[56] When describing GNP composites stabilized or cross-linked with homologous ATs or ADTs, the term was alternatively expressed with respect to the number of methylene (CH_2) units N and a tunneling decay constant β_N in reciprocal units of the methylene group count.^[53,132]

The probability for electrons to tunnel through the matrix is strongly dependent on the molecular structure of the ligands or cross-linkers. ADT cross-linker molecules mainly consist of methylene units, which are considered to act as insulators.^[57] Here, the Fermi level of the metal is located in the gap between the highest occupied molecular orbital (HOMO) and lowest unoccupied molecular orbital (LUMO) of the linker molecule and the side orbitals provide a superexchange pathway for electron transfer.^[57] In this case the conductivity shows a strong exponential dependence on the length of the molecule, i.e. the interparticle distance. In contrast, a weak distance dependence can be observed when the Fermi energy of the metal becomes resonant with molecular orbital energies of the cross-linker.^[57]

For ADT cross-linked GNP films, a tunneling decay constant of $\beta_N = 0.61 \pm 0.1$ was measured.^[53] This is in good agreement with measurements on different ADTs embedded in a monothiol layer on a flat gold surface performed by the Lindsay group, yielding a zero-bias value of $\beta_N = 0.57 \pm 0.03$.^[133] Considerably higher values of $\beta_N = 1.2$ ^[132] and $\beta_N = 0.8 \pm 0.2$ ^[134] were observed for AT capped GNPs and monolayers of AT molecules on gold surfaces, respectively. This observation indicates that cross-linkage of GNPs with ADT cross-linkers enhances the conductivity of the composites.^[53] Its still strong dependence on the cross-linker's alkylene chain length leads to a conductivity increase of roughly one order of magnitude when decreasing the chain length of the cross-linking ADT's backbone by 3 methylene units, as reported by Joseph et al..^[53]

As described in equation 3.3, assuming isothermal conditions, the conductivity of GNP composite films is exponentially dependent on the interparticle spacing δ and the charge

transport activation energy E_a . Considering a GNP composite sensing element with a defined geometry and a baseline resistance R_0 , relative changes of this baseline resistance due to variations in the interparticle spacing $\Delta\delta$ and the activation energy ΔE_a can be conveniently expressed by rearrangement of equation 3.3:^[60,63]

$$\frac{\Delta R}{R_0} = \exp(\beta\Delta\delta) \exp\left(\frac{\Delta E_a}{kT}\right) - 1 \quad (3.5)$$

This resistive sensitivity of GNP composite materials led to substantial efforts, targeting at the investigation of their sensing capabilities, sensing mechanisms, the fabrication of different types of sensors and their potential applications. The two most prominent GNP composite based sensor types — both having direct relevance for studies reported herein — are resistive strain gauges and chemiresistors. Both sensor types and sensing mechanisms will be described in the following two sections.

3.2.3 Resistive Strain Sensing

The strong dependence of the GNP composite's resistance on the interparticle spacing makes the material interesting for the fabrication of strain sensors. Herrmann et al. were the first to report highly sensitive strain gauges of GNP thin-films, fabricated by spray-coating 4-nitrothiophenol functionalized GNPs with an average diameter of ~ 18 nm.^[50] They assessed that the dependence of the charge transport activation energy on the interparticle spacing can be neglected for systems with particles having diameters of $D \sim 10$ nm with spacings of $\delta_0 \sim 1$ nm. Taking into account this approximation, equation 3.5 simplifies to:^[50]

$$\frac{\Delta R}{R_0} = e^{\beta\Delta\delta} - 1 \quad (3.6)$$

Whereat the relative resistance change is governed solely by the exponential tunneling term. The group further provided a model relating the macroscopic strain ε of the composite material to changes in the interparticle spacings $\Delta\delta$, which is described in the following.^[50] Upon application of stress along one direction of the film parallel to the current flow, the film may respond by an elongation of Δl from its initial length l_0 (see figure 3.3a). The resulting strain ε is given by equation 3.7.

$$\varepsilon = \frac{\Delta l}{l_0} \quad (3.7)$$

Approximating the composite as a primitive cubic (cP) packing of GNPs, the length of the composite in one direction can be expressed as $l_0 = N(D + \delta_0)$, where N is the number of particles in the certain direction and δ_0 the initial interparticle spacing. The macroscopic

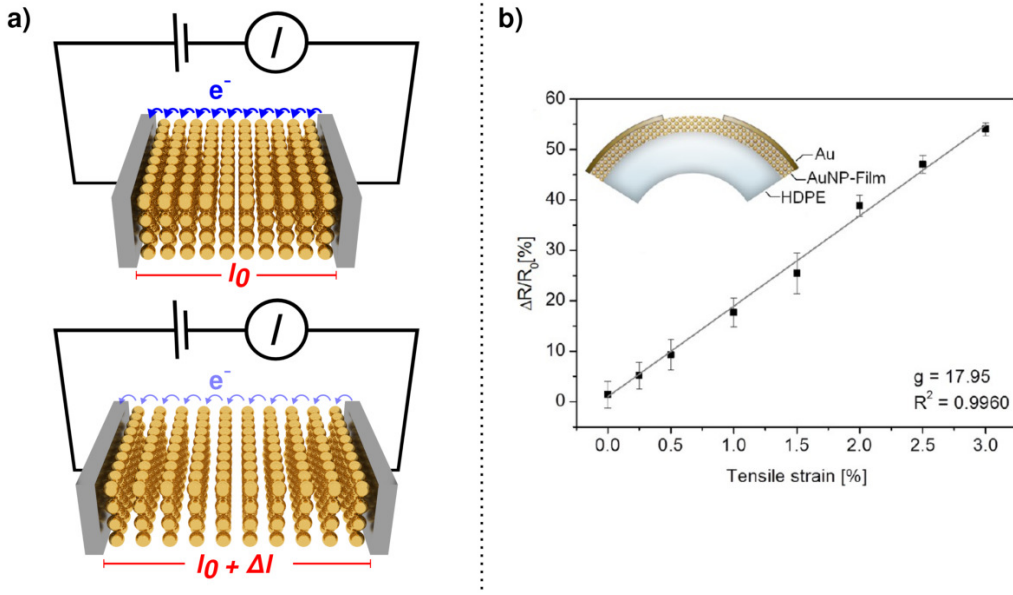


Figure 3.3: a) Effect of strain on a GNP composite's resistance. When subjected to strain, the interparticle spacings δ between GNPs in the composite increase along the strain direction and impede tunneling currents. b) Transfer function of a PTM cross-linked GNP film on HDPE, subjected to strain in a bending test (inset). Reprinted with permission from [60]. ©2012 American Chemical Society.

elongation of the film translates into an increase of the interparticle spacing $\Delta l = N\Delta\delta$, as the organic matrix molecules can be deformed much more easily compared to the GNPs themselves. From these considerations we obtain equation 3.8 relating the interparticle distance change to the macroscopic strain applied to the material.^[50]

$$\Delta\delta = (D + \delta_0)\frac{\Delta l}{l_0} = (D + \delta_0)\varepsilon \quad (3.8)$$

Hence, equation 3.6 can be expressed in terms of strain.^[50]

$$\frac{\Delta R}{R_0} = e^{\beta(D+\delta_0)\varepsilon} - 1 \quad (3.9)$$

Equation 3.9 shows that the resistive response of GNP composite materials to strain is generally non-linear and can be influenced by varying the GNP sizes and initial interparticle distances. However, in the limit of small strains, a linear response characteristic can be derived^[50] by a first order Maclaurin expansion of equation 3.9:

$$\frac{\Delta R}{R_0} = \beta(D + \delta_0)\varepsilon = g\varepsilon \quad (3.10)$$

Here $g = \beta(D + \delta_0)$ is the gauge factor, which is used to characterize the linear sensitiv-

ity of resistive strain gauges. While metal foil based strain gauges typically show gauge factors of $g = 2$, Herrmann et al. observed gauge factors between 50 and 200 in their experiments, which is in agreement with their theoretical estimations yielding values of $g \sim 100$.^[50] Soon after these investigations, Vossmeier et al. reported the fabrication of resistive strain gauges from 9DT cross-linked GNPs via LbL self assembly on low density polyethylene (LDPE) substrates. For these GNP/9DT materials, gauge factors g in the range of 10 to 20 were found via bending tests.^[58] Similar values were observed by Olichwer et al. probing strain gauges based on pentaerythritol tetrakis(3-mercaptopropionate) (PTM) cross-linked GNPs deposited onto high density polyethylene (HDPE). The transfer function of such a sensor is reprinted in figure 3.3b. Regarding the low g values compared to theory and based on scanning electron microscopy (SEM) investigations, the group suggested that structural reorganization, reversible extension of existing cracks and formation of new nanoscale cracks in the film material should be taken into account for a better understanding of the sensing mechanism.^[60] Farcau et al. fabricated arrays of wires formed from GNPs of 18 nm diameter by convective self assembly, having a width in the low micrometer range and thicknesses of one monolayer to few multilayers of particles. The group observed that the strain sensitivity was maximized for GNP wires with monolayer thickness and attributed this observation to particles in the second and upper layers forming conductive bridges between the particles in the lower layer. These interlayer gaps are less affected by strain and in consequence the overall resistance response is reduced.^[59]

With their high gauge factors compared to conventional metal foil based sensors as well as their straightforward ink-based fabrication procedures such as printing, spray-coating, or painting, GNP composite materials are highly interesting materials for sensing strain, leading to ongoing research on this subject. An overview of different nanoparticle based materials used in this regard can be found in a recent review paper by Segev-Bar and Haick.^[111] Still, a disadvantage of GNP based strain gauges is the temperature dependence of their conductivity. As described in equation 3.5 the charge transport shows an Arrhenius-type activation, making strain measurements prone to temperature changes. Such effects could be compensated e.g. by arranging GNP composite based resistors and strain-gauges in a Wheatstone bridge setup or using digital compensation circuits with reference resistors.

3.2.4 Resistive Chemical Sensing

Besides sensing strain, organically stabilized or cross-linked metal nanoparticle composites commonly respond with a resistance change when exposed to VOCs or gases. This effect was first exploited by Wohltjen and Snow,^[51] who demonstrated resistive chemical sensing of toluene, tetrachloroethylene, 1-propanol and water vapors using multilayers of 2 nm sized AT stabilized gold clusters deposited onto interdigitated microelectrodes, using airbrush technique. An exemplary time trace recorded in our lab, showing the relative resistance response of a spin-coated GNP/9DT composite film deposited onto a glass substrate upon exposure to toluene with concentrations ranging between 50 – 10 000 ppm is depicted in figure 3.4b. The measurement was conducted under ambient conditions with

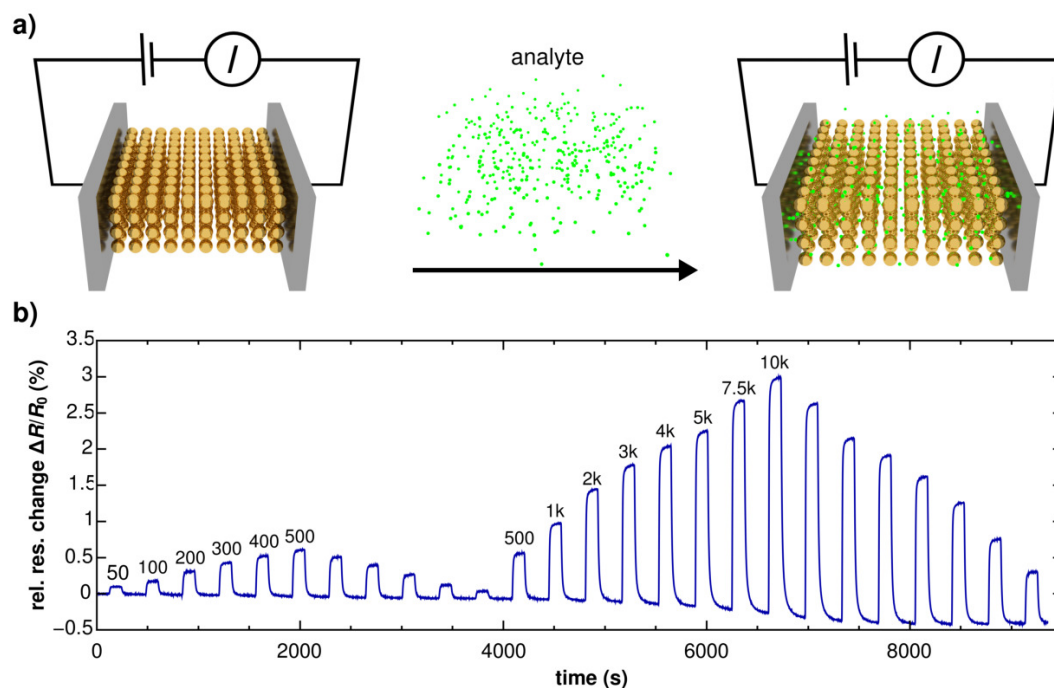


Figure 3.4: a) The sorption of analyte gases or vapors by GNP composites leads to changes of their resistance. On the one hand, resulting swelling of the material leads to an increased interparticle spacing. On the other hand, the analyte molecules influence the permittivity of the organic matrix separating the GNPs. b) Relative resistance change time trace of a GNP/9DT film chemiresistor (thickness: 51 nm), deposited onto a glass substrate, when alternately exposed to nitrogen and nitrogen enriched with varying toluene concentration. The numbers indicate the respective toluene fraction in ppm.

nitrogen acting as carrier gas.

Resistive chemical sensing with GNP composites has been attributed primarily to two effects, which are both based on sorption of analytes within the organic matrix surrounding the GNPs (see figure 3.4a).^[60,63] First, it has been proposed that sorption leads to swelling of the organic matrix, and hence an increase in the interparticle tunneling distances $\Delta\delta$. This should — according to equation 3.5 — lead to an increase in the chemiresistor’s resistance. Second, sorption of analyte should influence the permittivity of the organic matrix ϵ_r . In case of GNP films cross-linked with ADTs, most common analytes have higher dielectric constants than the cross-linker molecules consisting to a large fraction of saturated hydrocarbons. According to the granular metal theory (equation 3.4), an increase in ϵ_r leads to a decrease in E_a , causing a lowered resistivity of the GNP film.^[65]

Several studies are in agreement with the proposed sensing mechanism. Increasing interparticle distances of ordered, AT stabilized GNP films upon sorption of solvent vapor were observed by the Pileni group, using small angle X-ray scattering (SAXS).^[135] Another study by Olichwer et al. correlates the swelling (observed by grazing incidence small angle X-ray scattering (GISAXS)) with the chemiresistive response and sorbed analyte mass (measured by quartz crystal microbalance (QCM) measurements) of similar, ordered, AT stabilized GNP composites.^[65] So far, analogous studies were not conducted on disordered

ADT cross-linked GNP composites, as used in this work, because the determination of interparticle spacings in disordered structures using SAXS is less reliable. Further, in this case, the swelling effect is presumably limited due to the cross-linkage, resulting in lower interparticle distance changes as well as weaker resistive responses.^[53,65,136]

The influence of the matrix permittivity ϵ_r is exemplified in investigations of GNP film chemiresistors, cross-linked with rigid staffane molecules.^[126] These devices showed — in contrast to ADT cross-linked GNP films — even negative relative resistance responses. The sensitivity of these responses increased with increasing analyte permittivity and was dedicated to the reduced ability to swell of the rigidly cross-linked films. Consequently, the permittivity-induced resistance reduction predominated the swelling-induced resistance increase. The permittivity effect was further suspected to influence the responses of chemiresistors consisting of GNP sub-monolayers closely above the percolation threshold. Here it was assumed that swelling was limited due to pinning of the particles to the substrate.^[127]

In summary, there is clear experimental evidence that the two counteracting sorption-induced effects, i.e. the swelling of the material as well as the commonly expected increase in the dielectric constant of the organic matrix, govern the response of GNP based chemiresistors when exposed to VOCs.

Concentration Measurements

The analyte uptake in ADT cross-linked GNP chemiresistors was monitored by QCM measurements and compared to their resistive responses. For 1,16-hexadecanedithiol (16DT) cross-linked films, linear correlations between the analyte concentration within the GNP film $c_{a,\text{film}}$ and the relative resistance change $\Delta R/R_0$ were observed. Further, the relation of $c_{a,\text{film}}$, and hence $\Delta R/R_0$, to the gas-phase analyte concentration c_a was described using a Langmuir isotherm.^[137] In other studies on chemiresistors based on GNP films on glass/silicon substrates, cross-linked with shorter-chain ADTs, the relative resistance response to a given vapor concentration could also be well-described using the Langmuir-isotherm,^[136] while a Langmuir-Henry-isotherm was employed to fit the relative resistance responses of 9DT and PTM cross-linked GNP films on HDPE.^[60] The isotherms are described by equations 3.11 and 3.12, respectively.

$$\frac{\Delta R}{R_0} = \left(\frac{\Delta R}{R_0} \right)_{\text{sat}} \frac{K_L c_a}{1 + K_L c_a} \quad (3.11)$$

$$\frac{\Delta R}{R_0} = \left(\frac{\Delta R}{R_0} \right)_{\text{sat}} \frac{K_L c_a}{1 + K_L c_a} + K_H c_a \quad (3.12)$$

Here, $(\Delta R/R_0)_{\text{sat}}$ denotes the Langmuir saturation response of the sensor, K_L is the Langmuir constant and K_H the Henry constant. While the Langmuir-model takes into account

selective sorption, leading to saturation of the sensor at high analyte concentrations, the Langmuir-Henry model adds a term relating to unspecific, bulk partitioning according to the Henry model.^[60]

By calibrating a GNP composite based chemiresistor it can be further used for concentration measurements. Using samples of an analyte with defined concentrations, the $\frac{\Delta R}{R_0}(c_a)$ relation can be obtained by fitting equation 3.11 or 3.12 to the data.

Analyte Recognition

Besides sensing the concentration of a known analyte molecule, it is essential for various applications to recognize isolated analytes or analyte mixtures as well as single or multiple analytes within analyte mixtures. This is required e.g. for pollutant detection,^[138] in health monitoring and medical diagnosis, aiming at the detection of diseases by analysis of exhaled breath,^[66,139] or in security-related applications, as for the detection of explosives.^[140]

One approach to discriminate analytes is the fabrication of specific sensors. As such a sensor ideally responds solely to one analyte, it is hence capable of recognizing an analyte in a mixture. However, such sensors are very difficult to fabricate and besides, if different analytes should be detected, each needs a respective, specific sensor. Another approach is the usage of an array of sensors that do not react specifically, but have each different selectivities towards the analytes to be discriminated. Here, each analyte or analyte mixture yields an ideally unique response pattern making it distinguishable from other species. Such sensor arrays for detecting analytes in the gas phase were firstly applied by Persaud and Dodd,^[141] trying to mimic the human olfactory system. Consequentially, such arrays were later termed “electronic noses”.^[142] The responses of the sensor arrays can be analyzed by means of multivariate evaluation methods such as principal component analysis (PCA) or artificial neural networks (ANNs).^[143]

For their use in electronic noses, it is crucial to fabricate sensors responding differently to a variety of analytes. The selectivity of GNP composite chemiresistors can be adjusted by varying the composition of the GNP film. By replacing e.g. hydrophobic ADT cross-linkers or AT ligands with more hydrophilic linker molecules or ligands, such as molecules with hydroxyl, carbonyl, amine or carboxyl functions, the sensitivity towards more polar analyte molecules was enhanced, while the sensitivity towards non-polar analyte molecules dropped.^[60,62,64,105] This underlines the importance of analyte solubility in the organic matrix for the respective sensitivity. In a comprehensive review paper,^[64] Ibañez and Zamborini provided a listing of organically-modified metal and alloy nanoparticles used for chemiresistive sensing.

Another approach considered to influence the chemical sensitivity or selectivity of GNP composite chemiresistors is to impose strain on the devices. Yin et al. observed that the resistive response patterns of nanoparticle thin films comprising of 9DT cross-linked 2 nm sized GNPs towards different analytes depend on the amount and direction of strain.^[144]

However, Olichwer et al. also conducted experiments on films of 9DT cross-linked 4 and 9 nm sized GNPs on flexible HDPE substrates and observed a net increase of the sensitivities towards different analytes upon imposing strain on the chemiresistor film, but no significant alteration in the relative response patterns was detected. The sensitivity increase was attributed to an alleviated swelling of the composite due to crack formation, as observed by means of SEM.^[60] Arrays of GNP composite chemiresistors and single-walled CNT networks were used by Haick and co-workers for breath analysis to detect marker molecules corresponding to different diseases.^[66,139] Following a different approach, Zellers and co-workers used a μ GC system for concentrating and separating analyte mixtures before probing them with a detector containing an array of thiol-stabilized GNP chemiresistors. The combination was used for the identification of trichloroethylene^[138] and explosive markers^[140] in a complex mixture of background VOCs.

In view of the investigations conducted in the present work, besides diversifying the selectivities of GNP composite chemiresistors by varying, e.g., their organic matrix material, the exploration of novel transduction methods responding differently to analyte characteristics can be beneficial for enhancing the identification of target analytes. Here, the frequency shifts of GNP membrane based resonators (section 5.5) or their response times (section 6.3.1) as well as their quasi-static deflection responses (section 6.3.2) can be employed as (additional) input parameters for multivariate data analysis targeting at analyte recognition.

3.3 Nanomembranes

In different fields of science, the term “membrane” has different meanings. In this work, the term nanomembrane denotes a freestanding layer of an arbitrary material having a thickness in the sub-micrometer range, which is markedly exceeded by its lateral dimensions. While silicon based materials such as Si, Si₃N₄, SiO₂ are widely used in MEMS/NEMS, this section will cover nanomembranes and devices of more recently explored nanomaterials. The focus is set on nanoparticle composites, while inorganic materials having a layered crystal structure, such as graphene or TMDCs as well as ultrathin carbon nanomembranes are also addressed. First, different methods for the fabrication of freestanding nanomembranes are described and afterwards their mechanical and electromechanical behavior is presented, especially with respect to force sensing and the observation of micro-/nanomechanical resonances.

3.3.1 Fabrication

Inorganic 2D materials. With the rise of graphene following its discovery in 2004,^[145] several studies were conducted on freestanding graphene nanomembranes. They were initiated by Bunch et al., who adapted a peeling technique for the exfoliation of 2-dimensional (2D) crystalline materials.^[146] Graphene was obtained from graphite by rubbing it on thermally oxidized silicon wafers featuring trenches with lateral extensions in the nanometer to low micrometer regime. Thereby, freestanding single- and multilayer sheets spanning the trenches were deposited and further investigated regarding their resonance behavior.^[17] Another procedure for the fabrication of freestanding graphene was used by van der Zande et al.. Graphene was grown on a copper substrate by means of chemical vapor deposition (CVD). After depositing a sacrificial poly(methyl methacrylate) (PMMA) layer on top, the underlying copper substrate could be removed via wet etching. The etchant was exchanged by deionized (DI) water and the graphene/PMMA stack could be scooped out of the liquid with a microstructured substrate. The PMMA-layer being on top was dissolved in dichloromethane and rinsed with acetone and isopropyl alcohol. To obtain freestanding graphene membranes the samples were eventually critical-point dried.^[27]

Also stamp-transfer based methods were utilized for fabricating freestanding membranes of graphene and different TMDCs. Reserbat-Platney et al., Castellano-Gomez et al., and Morell et al. used polydimethylsiloxane (PDMS) sheets to mechanically exfoliate graphene,^[147] MoS₂^[148] and WSe₂,^[34] respectively, and subsequently transfer them onto arrays of microcavities. Also a similar, modified process was used for graphene,^[149,150] MoS₂^[150] and TaSe₂,^[151] wherein in the first step, flakes of the materials were transferred onto the PDMS stamps by mechanical exfoliation using adhesive tape.

Carbon nanomembranes. Freestanding ultrathin carbon nanomembranes with single-molecule thickness were fabricated by Götzhäuser and co-workers.^[152] The group firstly

prepared self-assembled monolayers (SAMs) of molecules, such as thiol-functionalized biphenyls, on gold surfaces. Afterwards the aromatic molecules were cross-linked by means of electron irradiation, leading to cleavage of carbon-hydrogen bonds and the formation of intermolecular carbon-carbon bonds. The films could be released from the gold surface by cleavage of the anchor-group/substrate bond using saturated iodine vapor and subsequent ultrasonic treatment with *N,N*-dimethylformamide (DMF). Besides, SAMs of biphenyl molecules functionalized with trimethoxysilyl anchor-groups were assembled on silicon structures featuring SiN_x windows and cross-linked via electron irradiation. After removal of the silicon nitride layer by HF etching, the freestanding carbon nanomembranes settled to the substrates, spanning the resulting holes. The group further reported an advanced transfer process based on the application of a sacrificial PMMA layer.^[39] Here, following electron irradiation, PMMA was deposited onto a cross-linked SAM assembled on a gold surface. The gold/nanomembrane/PMMA stack was detached from the underlying (mica) substrate, and the gold layer was removed by wet etching. Finally, the nanomembrane was transferred onto a microstructured silicon substrate and the PMMA-layer was dissolved in acetone followed by critical-point drying.^[38,40]

Nanoparticle composite membranes. Different approaches for the fabrication of polymer-encapsulated, ligand-stabilized, and cross-linked nanoparticle composite membranes were reported. One approach implies the lift-off and transfer of nanoparticle composite films initially deposited onto sacrificial substrates. Following detachment, the membranes are transferred to 3-dimensional (3D) supporting structures, featuring recesses or holes, to settle thereon and remain freestanding (cf. figure 3.5a). In 2000, Mamedov et al. reported freestanding LbL assembled films of magnetite nanoparticles. The group assembled a film of polyelectrolytes and 8 – 10 nm sized Fe_3O_4 particles on a sacrificial layer of cellulose acetate (CA) deposited beforehand onto a glass slide. The CA was peeled off together with the nanocomposite and could be dissolved in acetone, retaining the film freely floating in solution. From there, it could be transferred to different substrates.^[153] The principle of using sacrificial layers for film detachment was adapted by different groups, i.a. by Tsukruk and co-workers, who employed it to fabricate freestanding membranes of GNPs sandwiched between polyelectrolyte layers.^[43,46,154] Our group adapted a procedure by Kowalczyk et al.^[155] for lift-off and transfer of ADT cross-linked GNP films from glass substrates without a sacrificial layer.^[52] This approach was also used for membrane fabrication in this work and is described in section 5.1.3. Briefly, a glass substrate coated with a GNP film was floated at the surfaces of a sodium hydroxide solution^[48,52] or pure demineralized water.^[1,2] The solution/solvent was able to intrude between the film and the substrate, leading to delamination. After the glass substrate sank to the bottom of the container, 3D-microstructured substrates were used to skim the membrane from the liquid-air interface.

Other approaches aimed at the direct fabrication of ligand-stabilized or cross-linked GNP films at phase boundaries, such as liquid-air interfaces. Jaeger and co-workers reported the fabrication of freestanding nanoparticle monolayers by spreading nanoparticle suspensions in toluene on water droplets, residing on substrates with pre-fabricated holes.^[156]

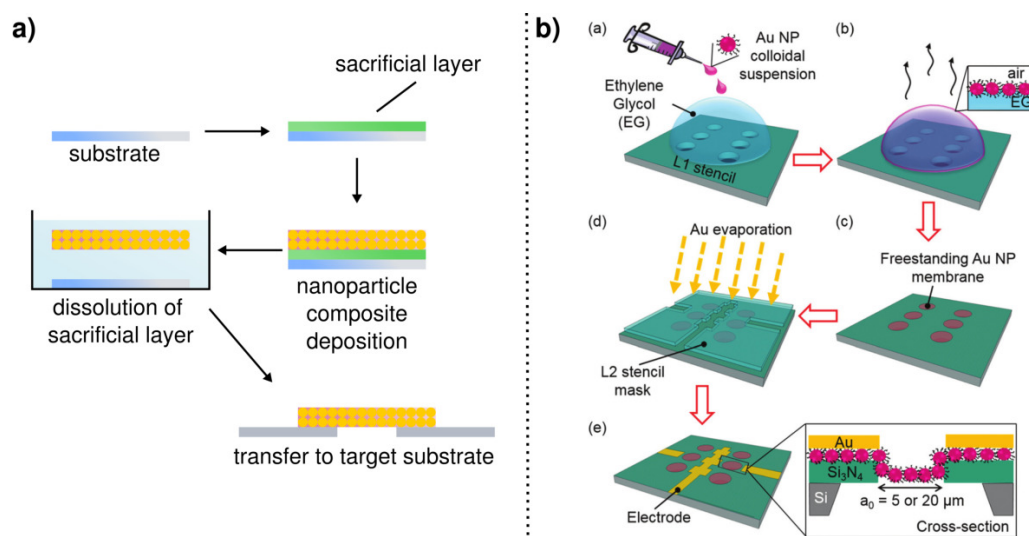


Figure 3.5: Different methods for the fabrication of nanoparticle composite membranes. *a)* A nanoparticle composite film is deposited onto a sacrificial layer, e.g. a polymer layer. The sacrificial layer is dissolved and the film is released from its substrate. Eventually the floating membrane can be transferred and rendered freestanding on a suitable target substrate. *b)* Schematic showing the “droplet-method” for fabricating freestanding membranes on apertures. A GNP suspension is deposited onto the surface of an ethylene glycol (EG) droplet placed on a microstructure. Upon evaporation of the solvent, the particles form a monolayer at the EG-air interface. Upon evaporation of the EG, the GNP monolayer settles on the microcavities. The schematic further shows the fabrication of electrodes via stencil lithography for electronically addressing the GNP monolayer. Reprinted with permission from Ref. [42].

Upon the evaporation of toluene, particle monolayers formed at the surface of the water droplets and draped themselves over the substrates, as the water evaporated. Hereby, they remained freestanding over the holes. This technique was later used in several studies and adapted by other groups (see figure 3.5b).^[42,157–161] Dong et al. reported the organization of highly ordered multicomponent nanoparticle superstructures containing GNPs on liquid surfaces, which could be transferred to holey TEM substrates.^[162] While the above-mentioned procedures yielded non-cross-linked particle membranes, Kosif et al. reported the fabrication of cross-linked structures at the water-air interface, by introducing a catalyst into the water subphase, causing polymerization of suitable ligands capping the GNPs.^[124]

Also, assembly at liquid-liquid interfaces was employed for nanoparticle membrane fabrication.^[163] Le Ouay et al. reported the formation of freestanding nanoparticle membranes in an oil-water mixture. Here, nanoparticles were transported to the interfaces of dichloromethane (DCM) droplets and formed interparticle -Si-O-Si- bonds due to condensation of their mercaptopropyltrimethoxysilane ligands.^[164] Andryszewski et al. demonstrated the fabrication of covalently cross-linked GNP monolayers at the liquid-liquid interface between a hexane and a water phase by the formation of amide bonds between the assembled amine-stabilized GNPs when adding a naphthalene dianhydride derivate.^[123] In the latter cases, freestanding membranes could be obtained by collecting the assembled GNP structures from the phase boundaries using holey TEM substrates.

3.3.2 Mechanical Properties and Sensing

Nanoparticle composites represent novel types of materials, having various potential applications, e.g. in the field of sensing and in flexible electronics. There is hence a significant interest in analyzing their mechanical properties, such as their elasticity, characterized by the elastic modulus E , their ultimate strength, maximum elongation and viscoelastic behavior. Recently, substrate-supported nanoparticle composites were characterized by different techniques, such as nanoindentation.^[165–167] Here, a nanoindenter or an atomic force microscope was used to acquire load-displacement curves by pushing a tip with a defined geometry into a film of the material and retracting it afterwards. From the load-displacement data mechanical characteristics, such as the material’s hardness and elastic modulus E , could be derived using suitable models, e.g. the Oliver-Pharr model.^[168] However, these measurements require material layers having a high thickness compared to the indentation depth, to avoid interferences caused by the underlying substrate.^[48]

The fabrication of freestanding nanocomposite membranes enables probing materials’ characteristics without the influence of an underlying substrate. Further, sensitive responses of ultrathin freestanding membranes to external forces can enable new applications in force and pressure sensing, as well as their use as resonators, which is discussed in detail in section 3.3.3.

Probing Mechanical Properties

Different analytic procedures have been reported for the mechanical characterization of freestanding nanomembranes. The methods commonly involve measurements and interpretations of the materials’ responses to externally applied forces. Frequently used methods include bulge tests, buckling tests as well as indentation experiments.^[169]

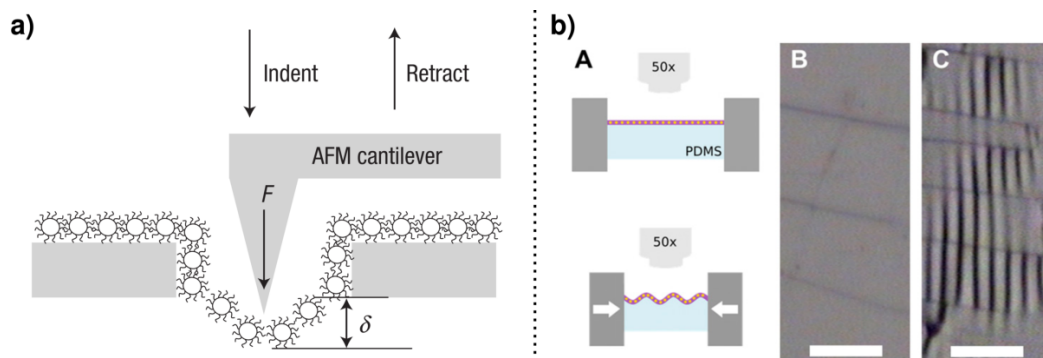


Figure 3.6: a) Schematic showing an AFM based nanoindentation experiment on a freestanding nanoparticle monolayer membrane. A cantilever imposes a force F on the membrane, and F as well as the resulting deflection (here: δ) are measured. Reprinted by permission from Macmillan Publishers Ltd: Nature Materials [156], ©2007. b) **A** Schematic of a buckling test. **B,C** Optical micrographs of a ~ 40 nm film comprised of PS grafted GNPs deposited onto a PDMS substrate, **B** before and **C** after buckling. Scale bars: 10 μm . Reprinted from [170].

Indentation experiments. Besides its wide applicability for imaging, atomic force microscopy (AFM) is a powerful tool for examining mechanical properties of nanoscopic objects.^[169] With regard to freestanding membranes it can be utilized to conduct micro- or nanoindentation measurements. Depending on the size of the freestanding membrane section, an appropriate choice regarding the AFM probe has to be made. While for larger membranes (microindentation) microsphere probes are often selected, preventing the cause of damage to the membrane, nanoprobes can be used for probing smaller membranes (nanoindentation).^[169] During an indentation experiment the probe is used to deflect the freestanding nanomembrane, and a force-displacement curve is acquired. Using suitable models, the mechanical parameters of the membranes can be extracted from the obtained data.^[169] Jaeger and coworkers studied freestanding circular monolayer membranes of 1-dodecanethiol (12T) capped GNPs (cf. figure 3.6a).^[156] For membranes consisting of 5 nm diameter GNPs, spanning micrometer-sized circular apertures, they determined elastic moduli of $E \sim 4$ GPa.^[171] Recently, the group published a report on the thermomechanical response of similar membranes, probed by indentation experiments.^[47]

Buckling Tests. Buckling tests, also referred to as strain-induced elastic buckling instability for mechanical measurements (SIEBIMM),^[172] are another viable technique for probing the mechanical characteristics of nanomembranes. Even though the method does not precisely probe freestanding membranes, it will be included here. The technique involves the transfer of a membrane onto a relatively soft substrate with known elastic modulus and Poisson ratio. A common substrate material is PDMS.^[169,170] During testing, a compressive strain is imposed on the material stack along the substrate axis, leading to microscale buckling of the sample (cf. figure 3.6b). The buckling wavelength λ can be measured using e.g. optical microscopy^[170] or AFM^[169] and used to determine the mechanical properties of the membrane material following equation 3.13.

$$\frac{E}{(1 - \nu^2)} = \frac{3E_s}{(1 - \nu_s^2)} \left(\frac{\lambda}{2\pi t_m} \right)^3 \quad (3.13)$$

Where t_m denotes the membrane thickness, E and ν are the elastic modulus and Poisson ratio of the membrane, respectively, and E_s and ν_s denote the respective characteristics of the substrate. In a recent work, Alivisatos and co-workers used the buckling method to test mechanical parameters of superlattices comprised of polystyrene (PS) grafted GNPs.^[170]

Bulge Tests. Bulge testing represents a versatile method for probing the mechanical characteristics, such as the elastic modulus, the residual stress or the Poisson ratio, of freestanding membranes.^[19,173,174] In this work, bulge testing was employed to investigate the elastic properties of GNP membranes cross-linked using different DTs, which is described in section 6.1. Further, equations for the evaluation of bulge tests^[175] were utilized to describe the deflections of GNP membranes experiencing electrostatic actuation (sections 5.3 and 6.3.2) or acting as functional materials in pressure sensors (section 5.2).

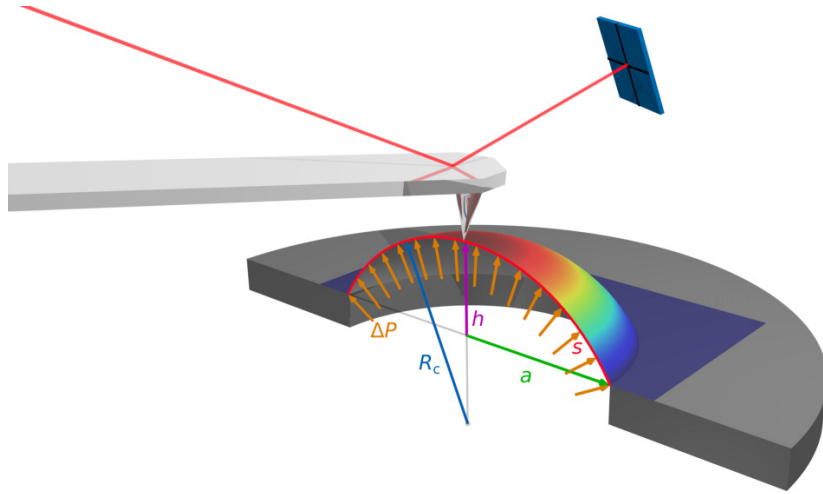


Figure 3.7: Schematic showing a cross-sectional view of a nanomembrane bulged by a pressure difference ΔP , approximated as a spherical cap. Annotations denote the aperture radius a , the bulge's radius of curvature R_c , the central point deflection h as well as the bulge's arc length s . An AFM is utilized to monitor the bulge topography.

For conducting bulge tests, freestanding membranes are deposited onto substrates featuring apertures. In experiments probing nanomembranes, these apertures are commonly circular, square or rectangular shaped and have lateral sizes in the micrometer range. Using a suitable setup, the membranes are loaded with a varying, controlled overpressure from one side, leading to bulging. The resulting deflection can be captured by different means, such as optical microscopy,^[176] interferometry,^[46,177] or AFM.^[38,39,41,48,175]

The simplest implementation of a bulge test^[19] involves a membrane with a pre-stress σ_0 placed onto a circular aperture having a radius a , bulged by applying a varying pressure difference ΔP . The evolving bulge's shape can be approximated as a spherical cap,^[18,173] with a radius of curvature R_c (see figure 3.7). Due to its low thickness t_m compared to the lateral dimensions, the bending stiffness of the bulged nanomembrane can be neglected and only the in-plane stress is taken into account. The biaxial stress σ_t in the membrane can be computed using the standard equation for a thin-walled spherical pressure vessel 3.14.^[19,173]

$$\sigma_t = \frac{\Delta P R_c}{2t_m} \quad (3.14)$$

The biaxial strain ε is derived from the bulge's change in arc length s . In the elastic regime, the biaxial stress and strain are linearly related by the biaxial modulus Y , which is connected to the materials elastic modulus E via the Poisson ratio ν :^[18,173]

$$\sigma_t = Y\varepsilon = \frac{E}{1 - \nu}\varepsilon \quad (3.15)$$

Applying different simplifications, the spherical cap model yields equation 3.16, displaying a relation of the membrane bulge's central point- or peak deflection h to the applied pressure ΔP .^[173]

$$\Delta P(h) = \frac{8Yt_m}{3a^4}h^3 + \frac{4\sigma_0t_m}{a^2}h = \frac{8Et_m}{3(1-\nu)a^4}h^3 + \frac{4\sigma_0t_m}{a^2}h \quad (3.16)$$

The equation can be fitted to experimentally obtained $\Delta P(h)$ datasets and yields the membrane's biaxial modulus as well as its pre-stress as output. While commonly the measured pressure/central point deflection relation $\Delta P(h)$ is used as input for the evaluation, in a recent work,^[48] our group extracted the pressure-dependent radius of curvature $R_c(\Delta P)$ of membrane bulges from AFM profile scans and employed it as input parameter.^[175]

Besides for bulge-tests involving circular freestanding membranes, similar $\Delta P(h)$ relations can be derived for square or high aspect ratio rectangular membranes (equation 3.17).^[175]

$$\Delta P(h) = \frac{C_1\sigma_0t_m}{b_x^2}h + \frac{C_2Et_m}{b_x^4}h^3 \quad (3.17)$$

C_1 and C_2 are constants, which depend on the membrane's geometry. They are $C_1 = 3.393$ and $C_2 = 1/[(1-\nu)(0.8+0.062\nu)^3]$ ^[178] for square membranes ($b_x = b_y$ denote the half edge lengths) as well as $C_1 = 2$ and $C_2 = 4/[3(1-\nu^2)]$ for rectangular membranes exceeding an aspect ratio of $b_y/b_x \geq 4$. Here again b_x and b_y denote the apertures half edge lengths in the two lateral directions.^[175,179]

Tsukruk and co-workers employed bulge tests for analyzing the elastic properties of nanoparticle membranes containing a GNP layer sandwiched between polyelectrolyte multilayers and determined elastic moduli in the range of 5.7 – 9.6 GPa.^[46] Our group conducted bulge tests on 9DT cross-linked GNP membranes utilizing an AFM based deflection read-out. Using the measured central point deflections or the extracted bulges' radii of curvature as input parameters, we obtained values of (2.3 ± 0.3) GPa and (2.7 ± 0.4) GPa for the elastic modulus, respectively.^[48]

Pressure/Force Sensing

Due to their unique mechanical properties, novel nanomaterial membranes are frequently investigated regarding their potential applications as micro- and nanomechanical sensors. While this section focuses on pressure/force sensing, devices based on nanomembrane resonators are discussed separately (section 3.3.3).

Bunch et al. characterized graphene monolayers, representing ultimately (atomically) thin membranes, which sealed the apertures of SiO₂ microcavities. By varying the surrounding

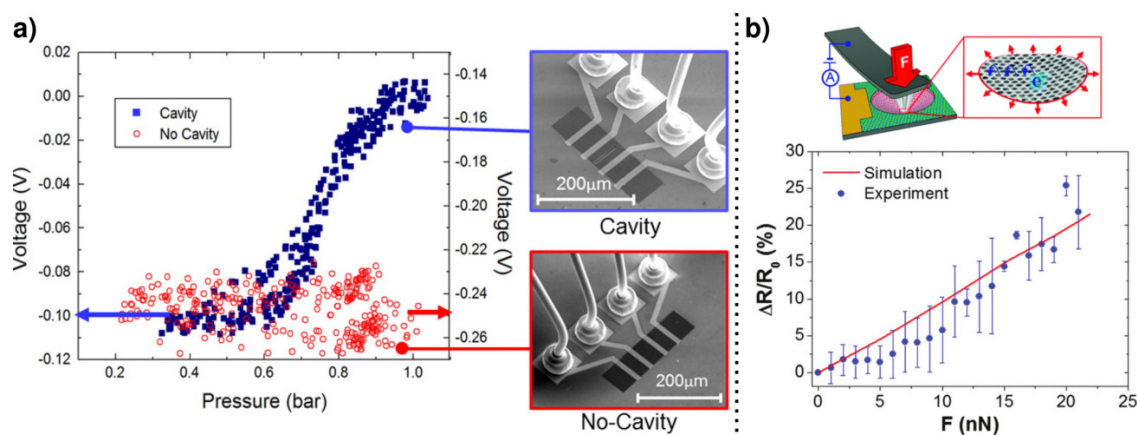


Figure 3.8: a) Scanning electron micrographs of a graphene based pressure sensor. The upper image shows a graphene sheet, addressed by electrodes, sealing an elongated microcavity between the central electrodes. The lower micrograph shows a control device without a microcavity. The graphs depict amplified voltage responses of the devices to pressure, in a Wheatstone bridge arrangement using a pulsed excitation signal and lock-in amplification. Reprinted with permission from Ref [26]. ©2013 American Chemical Society. A further copyright notice regarding the figure is provided in Ref. [180]. b) Experimentally observed and simulated relative resistance responses of a 5 μm diameter freestanding GNP monolayer membrane under point load actuation (see the schematic). Reprinted with permission from [42].

pressure and hence inducing a pressure difference between the microcavity and its exterior, they observed bulging of the membranes, which was imaged by AFM. From the decay times of the bulges the group deduced that graphene is impermeable for different standard gases, including helium. The group envisioned applications for such types of graphene nanomembrane sealed microchambers, e.g. for probing the pressure in small volumes or detecting pressure changes due to chemical reactions.^[18] By recording the conductance of suspended graphene nanomembranes in similar devices, pressure induced resistance changes could be observed upon bulging, as depicted in figure 3.8a. The experiments demonstrated the applicability of these graphene-based devices as resistive pressure sensors.^[26,28,181] Further, Zhu et al. observed piezoelectricity in freestanding MoS_2 monolayer membranes and suggested its use in ultrasensitive sensors and NEMS.^[182]

Nanoparticle composites, especially GNP composite membranes, were investigated in terms of mechanical/pressure sensing. Jiang et al. used bulge testing and indentation experiments to probe the deflection responses of polymer/GNP films.^[43] Based on the experiments they accredited the materials with superior sensitivity as well as a remarkable dynamic range and proposed the use in a new generation of membrane-based acoustic, pressure, chemical and temperature micro-array sensors.^[43] The group later reported on the fabrication of thermo-optical arrays that were employed as Golay-type infrared (IR) microimagers. Here, an array of circular cavities sealed with a GNP nanocomposite membrane was used to resolve the positions of an IR laser spot, by optically monitoring the bulging of the nanomembranes due to thermally induced pressure changes.^[44] However, to the best of our knowledge, no report on employing an electronic read-out for detecting the deflection of GNP nanocomposite membranes existed until our recent publication on pressure sensors,^[2] outlined in section 5.2. We showed that pressure induced mechanical

stress acting on a GNP composite membrane can be read out by simply exploiting its resistive strain sensitivity (c.f. section 3.2.3). This electro-mechanical coupling was also explored in a recent study by Gauvin et al., probing freestanding GNP monolayers using a combination of force spectroscopy and conductive AFM (cf. figure 3.8b).^[42]

3.3.3 Nanomembrane Resonators

Many articles focusing on nanomembranes address their use as NEMS and MEMS resonators. A large fraction of these reports are on graphene and other materials featuring 2D crystal structures, such as TMDCs. In 2007 Bunch et al. reported membrane resonators of single- and multilayer graphene sheets, having fundamental resonance frequencies in the range of 1–170 MHz.^[17] The work was followed by numerous studies employing graphene-based resonators, e.g. for the investigation of their optomechanical properties.^[16] Chen et al. and Singh et al. experimentally determined the thermal expansion coefficient of graphene by measuring a change in the resonance frequency caused by thermally induced changes in membrane tension.^[23,183,184] Further, different applications of graphene based resonators were proposed, including mass sensing.^[23,24] Chen et al. reported the use of a graphene resonator for signal processing and demonstrated a “graphene radio station”, using the resonator as frequency modulator encoding an audio signal in a 100 MHz carrier wave.^[22] Also, materials such as diamond-like carbon,^[185] MoS₂,^[30,33,35] TaO₂,^[151] WSe₂,^[34] and black phosphorous^[37] were later introduced for resonator fabrication. For example, Lee et al. probed the air damping characteristics of atomically thin MoS₂ membrane resonators under varying pressure and suggested the use of the observed relations e.g. for pressure sensing.^[32]

Also amorphous nanomembrane materials were used in NEMS resonators. Zhang et al. reported devices containing ~ 1 nm thick carbon nanomembranes, prepared by electron irradiation induced cross-linking of SAMs, with resonance frequencies in the low MHz range.^[40] The resonance behavior of nanoparticle composite membranes was reported, as in the case of nanoparticle/polymer composite membranes^[46] and ligand-stabilized nanoparticle monolayers.^[45] ADT cross-linked GNP nanomembranes, as firstly introduced for resonator fabrication in this work^[3] (cf. section 5.4), offer tunable mechanical properties and a fairly good and adjustable conductivity that enables direct electrostatic actuation. Further, they can be produced by simple ink-based fabrication schemes and can act as adsorbents, which makes the material applicable for chemical sensing.^[4]

GNP Membrane Vibrations

Depending on their mechanical properties and geometry, there are two limits for the dynamic behavior of sheet-like resonators. While on the one hand it can be governed by their tension/pre-stress (membrane limit), on the other hand their bending stiffness can dominate (plate limit). In a recent work Castellano-Gomez et al. observed the transition from membrane to plate behavior when investigating circular MoS₂ resonators on aper-

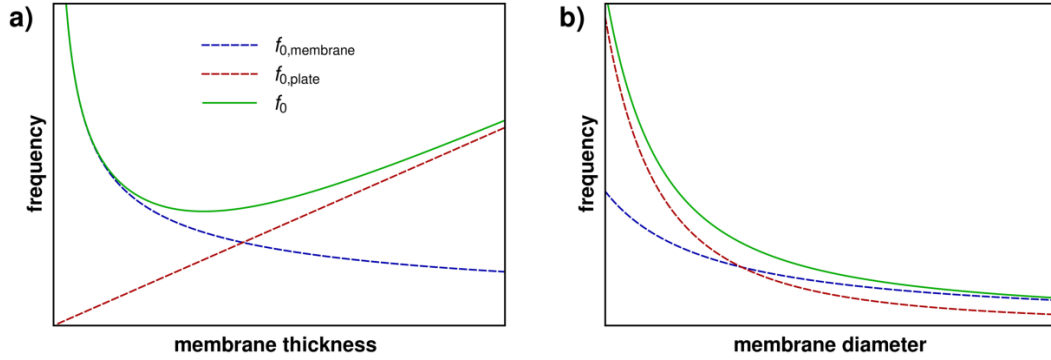


Figure 3.9: Schematic plot of the fundamental resonance frequency of circular sheet resonators, calculated using the membrane model, plate model, as well as a combined model for the cross-over regime. A membrane to plate crossover is visible when a) increasing the membrane thickness t_m or b) decreasing the diameter $2a$.

tures with a diameter ($2a$) of 2 and 3 μm upon increasing the resonator thickness, i.e., the number of MoS_2 layers.^[30]

Within the membrane limit, the fundamental resonance frequency $f_0 = f_{0,1}$ of a circular membrane is governed by the material's tension T_0 or pre-stress σ_0 , the membrane diameter $2a$ and its mass density ρ , as described in equation 3.18.^[30,45,186]

$$f_{0,\text{membrane}} = f_{0,1} = \frac{2.4048}{2\pi a} \sqrt{\frac{\sigma_0}{\rho}} = \frac{2.4048}{2\pi a} \sqrt{\frac{T_0}{\rho t_m}} \quad (3.18)$$

In contrast, the fundamental resonance frequency of a plate-like resonator is given by equation 3.19.^[30]

$$f_{0,\text{plate}} = \frac{10.21}{\pi} \sqrt{\frac{E}{3\rho(1-\nu^2)} \frac{t_m}{4a^2}} \quad (3.19)$$

Here, E denotes the elastic modulus of the sheet material, ν its Poisson ratio and t_m the sheet thickness. The resonance frequency in the cross-over regime can be computed following equation 3.20:^[30]

$$f_0 = \sqrt{f_{0,\text{membrane}}^2 + f_{0,\text{plate}}^2} \quad (3.20)$$

Figure 3.9 schematically depicts the transition of membrane to plate behavior when decreasing the diameter of a resonator (figure part b) or increasing the membrane thickness (figure part a), while keeping the other parameters, including the membrane tension T_0 , constant.

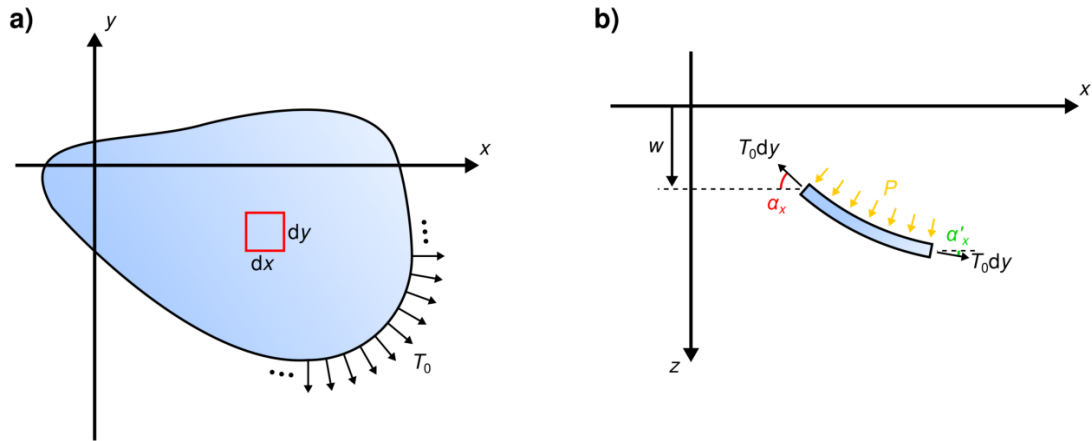


Figure 3.10: a) A membrane under a tensile load T_0 . b) Side view depicting a differential element of the membrane, as outlined in figure part a. The angles α_x and α'_x are drawn between the respective tensile force vectors and the x axis. Adapted from [188].

As discussed in section 6.2, our typically circular GNP membrane resonators, having membrane thicknesses in the tens of nanometer range, diameters of several tens of micrometers, and a pre-stress in the low MPa range, can be well-described using the membrane model.

Waves in Membranes

Membranes are the 2D analogues of strings.^[187,188] They can be described as plates that are subjected to tension, but have a negligible bending stiffness. A drumhead is a well-known example for a membrane.^[187] The following description of membrane motion follows the respective sections in the textbooks of Rao^[187] and Graff.^[188]

To derive the equation of motion for membranes, we begin with a membrane located in the xy plane (figure 3.10a). Across any straight, traversing line, we assume a constant surface tension T_0 per unit length of the line. Further, we assume idealized elastic properties of the membrane, ensuring a constant tension T_0 of the membrane under small deflections from its flat equilibrium position. For the sake of simplicity, we use the areal mass density $\rho_A = \rho t_m$ and the membrane surface tension $T_0 = \sigma_0 t_m$ instead of the corresponding thickness-normalized entities. The coordinate $w(x, y, t)$ denotes the deflection of the membrane in z direction from its equilibrium state at a time t .^[187,188]

We now consider a differential membrane element having the area $dxdy$, as pictured in figure 3.10a. Its mass is approximated as $\rho_A dxdy$ and its inertia force can hence be described by the term 3.21:^[187,188]

$$\rho_A \frac{\partial^2 w}{\partial t^2} dxdy \quad (3.21)$$

Forces of magnitude $T_0 dx$ and $T_0 dy$ act on the sides of the differential membrane element,

3. Introduction

along the y and x direction, respectively. The forces of magnitude $T_0 dy$ acting along the x -direction cause a net force acting in z direction. As visible in figure 3.10b, it can be computed by:^[187,188]

$$- T_0 dy \sin \alpha_x + T_0 dy \sin \alpha'_x \quad (3.22)$$

Approximating $\sin \alpha_x \approx \alpha_x$ as well as $\sin \alpha'_x \approx \alpha'_x$ for small deflections and replacing $\alpha'_x = \alpha_x + \frac{\partial \alpha_x}{\partial x} dx$ yields:

$$- T_0 dy \alpha_x + T_0 dy \left(\alpha_x + \frac{\partial \alpha_x}{\partial x} dx \right) \quad (3.23)$$

An analogous consideration is done regarding the tensile forces $T_0 dx$ acting in y direction, perpendicular to the image plane of figure 3.10b. These two contributions, as well as the force $P(x, y, t) dx dy$ caused by the pressure P are compiled into the membrane equation of motion in z -direction by taking into account the membrane's inertia force (equation 3.21):^[187,188]

$$\begin{aligned} - T_0 dy \alpha_x + T_0 dy \left(\alpha_x + \frac{\partial \alpha_x}{\partial x} dx \right) - T_0 dx \alpha_y + T_0 dx \left(\alpha_y + \frac{\partial \alpha_y}{\partial y} dy \right) \\ + P(x, y, t) dx dy = \rho_A dx dy \frac{\partial^2 w}{\partial t^2} \end{aligned} \quad (3.24)$$

Approximating the angles α_x and α_y as $\frac{\partial w}{\partial x}$ and $\frac{\partial w}{\partial y}$, respectively, the equation simplifies to:^[187]

$$T_0 \left(\frac{\partial^2 w}{\partial x^2} + \frac{\partial^2 w}{\partial y^2} \right) + P(x, y, t) = \rho_A \frac{\partial^2 w}{\partial t^2} \quad (3.25)$$

A description of free membrane vibrations can be obtained by setting the external pressure $P(x, y, t) = 0$:^[187]

$$T_0 \left(\frac{\partial^2 w}{\partial x^2} + \frac{\partial^2 w}{\partial y^2} \right) = \rho_A \frac{\partial^2 w}{\partial t^2} \quad (3.26)$$

The equation can be further expressed as follows, where $\nabla^2 = \frac{\partial^2}{\partial x^2} + \frac{\partial^2}{\partial y^2}$ is the Laplacian operator.^[187]

$$c^2 \nabla^2 w = \frac{\partial^2 w}{\partial t^2} \quad (3.27)$$

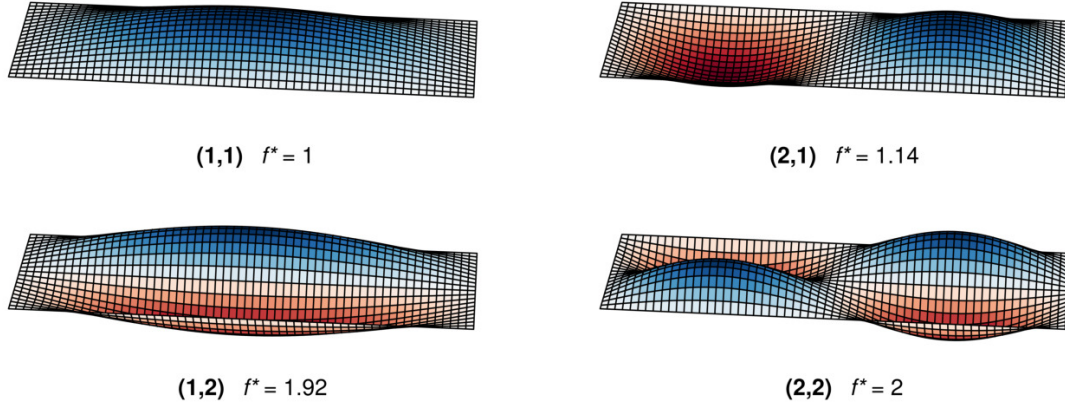


Figure 3.11: Different vibrational modes (m, n) of a clamped, rectangular membrane with $a_x = 150 \mu\text{m}$ and $a_y = 50 \mu\text{m}$. $f^* = f_{m,n}/f_{1,1}$ denotes the relative resonance frequencies with respect to the fundamental resonance mode.

Here, c denotes the phase velocity, which can be written in terms of the areal mass density ρ_A as well as the membrane tension T_0 , or the mass density ρ and the tensile stress/prestress of the membrane σ_0 .

$$c = \sqrt{\frac{T_0}{\rho_A}} = \sqrt{\frac{\sigma_0}{\rho}} \quad (3.28)$$

Normal modes and natural frequencies of rectangular and circular membranes can be analytically described by seeking solutions to the equation of motion in the respective coordinate systems taking into account adequate boundary conditions.

Rectangular membranes. In the case of a clamped, rectangular membrane with its origin at $x = 0, y = 0$ and edge lengths of a_x and a_y in the respective coordinate directions, the following boundary conditions imply a zero deflection at the edges of the membrane at all times:^[187]

$$w(x, 0, t) = w(x, a_y, t) = w(0, y, t) = w(a_x, y, t) = 0 \quad (3.29)$$

Without going into detail regarding the calculus, a set of solutions to the differential equation can be found, with the mode numbers $m \in \mathbb{N} \setminus \{0\}$ and $n \in \mathbb{N} \setminus \{0\}$. The frequency corresponding to a given value of m, n is described by equation 3.30 and the respective normal modes $W_{m,n}$ are given by equation 3.31.^[188]

$$f_{m,n} = \frac{\omega_{m,n}}{2\pi} = c \frac{1}{2} \sqrt{\frac{m^2}{a_x^2} + \frac{n^2}{a_y^2}} \quad (3.30)$$

$$W_{m,n} = \sin\left(\frac{m\pi}{a_x}x\right) \sin\left(\frac{n\pi}{a_y}y\right) \quad (3.31)$$

The estimated mode shapes of four exemplary normal modes of a rectangular membrane with an aspect ratio of $a_y/a_x = 3$ are visualized in figure 3.11. The plots are annotated with the relative natural frequencies of the given modes with respect to the fundamental mode frequency.

The general solution w_g is obtained by the superposition of the particular solutions of the equation of motion:^[188]

$$w_g(x, y, t) = \sum_{n=1}^{\infty} \sum_{m=1}^{\infty} [A_{m,n} \cos(\omega_{m,n}t) + B_{m,n} \sin(\omega_{m,n}t)] W_{m,n} \quad (3.32)$$

Here $A_{n,m}$, $B_{n,m}$ denote constants.

Circular membranes. For the determination of natural frequencies and mode shapes of clamped, circular membranes, calculations are conducted in polar coordinates. In the following the radial and angular coordinate are denoted by r and θ , respectively. Equation 3.27 is hence expressed with the Laplacian operator in polar coordinates (equation 3.34) and gives equation 3.33.^[188]

$$c^2 \nabla^2 w(r, \theta, t) = \frac{\partial^2 w(r, \theta, t)}{\partial t^2} \quad (3.33)$$

$$\nabla^2 = \frac{1}{r} \frac{\partial}{\partial r} \left(r \frac{\partial}{\partial r} \right) + \frac{1}{r^2} \frac{\partial^2}{\partial \theta^2} \quad (3.34)$$

The boundary conditions for a circular membrane clamped at the edge located at its radius a are given by:^[188]

$$w(a, \theta, t) = 0 \quad (3.35)$$

By solving the differential equation a set of normal modes, characterized by mode number tuples $m \in \mathbb{N}^*$ and $n \in \mathbb{N}$ is obtained.^[188] The normal modes are:

$$W_{n,m} = J_n\left(\xi_{n,m} \frac{r}{a}\right) \cos(n\theta), \quad \tilde{W}_{n,m} = J_n\left(\xi_{n,m} \frac{r}{a}\right) \sin(n\theta) \quad (3.36)$$

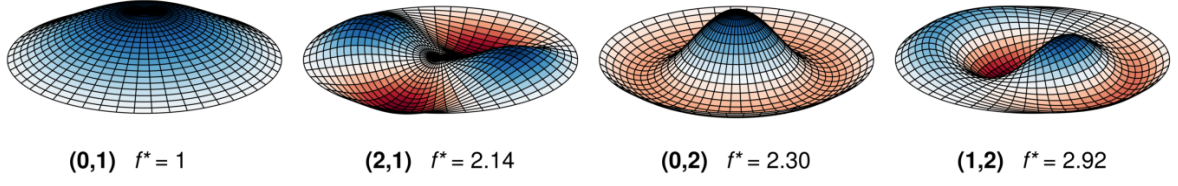


Figure 3.12: Different vibrational modes (n, m) of a clamped, circular membrane. $f^* = f_{n,m}/f_{0,1}$ denotes the relative resonance frequencies with respect to the fundamental resonance mode.

Here, J_n is the n th order Bessel function and $\xi_{n,m}$ represents the m th root of the n th order Bessel function. For a given mode number tuple, the normal modes $W_{n,m}$ and $\tilde{W}_{n,m}$ differ from each other only by an angular rotation of 90° . The natural frequencies of the modes are governed by equation 3.37. ^[45,186]

$$f_{n,m} = \frac{\xi_{n,m}}{2\pi a} c \quad (3.37)$$

The mode shapes of four exemplary normal modes of a circular membrane, annotated with their relative frequencies with respect to the frequency of the fundamental $f_{0,1}$ mode, are depicted in figure 3.12.

Again, the general solution w_g represents a superposition of the normal modes: ^[188]

$$w_g(r, \theta, t) = \sum_{m=1}^{\infty} \left\{ \sum_{n=0}^{\infty} W_{n,m} [A_{n,m} \cos(\omega_{n,m}t) + B_{n,m} \sin(\omega_{n,m}t)] + \sum_{n=1}^{\infty} \tilde{W}_{n,m} [\tilde{A}_{n,m} \cos(\omega_{n,m}t) + \tilde{B}_{n,m} \sin(\omega_{n,m}t)] \right\} \quad (3.38)$$

Where $A_{n,m}$, $B_{n,m}$, $\tilde{A}_{n,m}$, and $\tilde{B}_{n,m}$ are constants.

Excitation of Oscillations and Deflection Read-out

Excitation of Resonators. Resonant oscillations of MEMS/NEMS resonators can be excited by different means. In the following, various actuation methods recently applied to drive nanomembrane resonators are discussed, and other potentially applicable methods are outlined. Figure 3.13 provides schematics depicting different approaches.

Even when no drive is applied, thermal fluctuations at ambient temperatures can lead to *thermal excitation* of resonators, as observed for devices fabricated from layers of black phosphorous^[37] and MoS₂.^[33,35] Kanjanaboos et al. observed thermal excitation of resonators fabricated from freestanding, monolayered nanoparticle membranes.^[45]

In the latter report, the group described further experiments targeting at direct imaging of the membranes' normal modes by scanning the membranes' surfaces using an interferometer. In order to achieve phase-sensitive detection of the membrane motion, an external excitation method was employed using an *external piezo actuator* onto which the freestanding membrane sample was attached (cf. figure 3.14b). The piezo drive signal acted as reference for lock-in amplification of the interferometrically detected deflection signal, enabling the observation of the membrane vibrations' phase shifts. Excitation using external piezoelectric actuators has been employed in numerous studies.^[40,45,161,189,190] However, coupling between the frequency responses of the piezo actuator and the probed resonator structure can play a significant role.^[45]

A further excitation method, as utilized in this thesis is represented by *electrostatic/capacitive actuation*. Here, a counter electrode — often referred to as gate electrode, from FET nomenclature — in proximity to the resonator structure forms a capacitor-like arrangement. Application of AC voltages to this arrangement causes temporally alternating charging and hence alternating electrostatic forces that can drive oscillations. Electrostatic actuation of nanomembrane resonators has been utilized in the cases of graphene,^[17,23] diamond like carbon,^[185] MoS₂ and black phosphorous.^[37]

Another frequently used principle to drive nanomembrane resonators is *photothermal ex-*

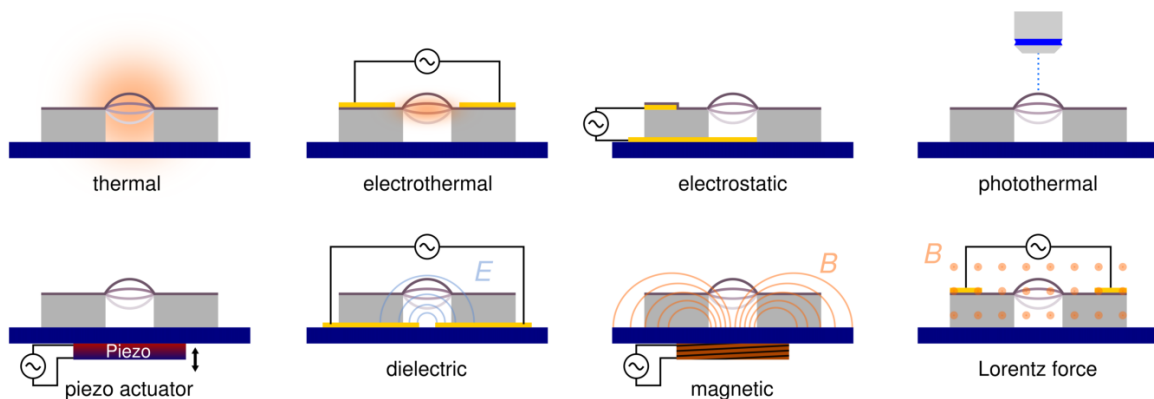


Figure 3.13: Different examples of actuation techniques for MEMS/NEMS resonator excitation.

citation. This technique was theoretically and experimentally investigated by Lammerink et al., focusing on the excitation of resonances of a clamped silicon beam using a modulated argon laser.^[191] The beam was driven by thermal stress, resulting from a thermal distribution induced by the absorbed optical power. Literature gives different examples for nanomembrane resonators driven using this principle, such as TaO₂-based^[151], graphene-based^[17] or MoS₂-based devices.^[30,31] Often photothermal excitation was utilized in setups employing modulated blue excitation lasers with a wavelength of 405 nm, combined with red (e.g. 633 nm HeNe) lasers utilized for interferometric read-out of the membrane deflection (cf. figure 3.14a).^[37]

Besides the latter excitation principles, other excitation methods known in MEMS/NEMS are potentially useful for driving nanomembrane resonators. An actuation method, specifically applied to polymeric actuators,^[192] but presumably transferable to nanomembrane resonators is *dielectric/Kelvin polarization force actuation*. This was demonstrated by Schmid et al. for a dielectric SU-8 resonator, placed over a pair of coplanar electrodes with an applied AC voltage. The resonator is consequentially periodically pulled towards the highest electric field intensity, located over the electrode gap, leading to excitation.^[192–195]

An analogous concept regarding paramagnetic materials in modulated magnetic fields is *magnetic actuation*. Suter et al. reported the fabrication of cantilevers from SU-8, enriched with 5 vol% (18 wt%) of (12.1 ± 3.5) nm sized Fe₃O₄ nanoparticles. Such cantilevers experience forces in inhomogeneous magnetic fields and hence could be excited in an alternating magnetic field induced by a coil driven with alternating currents.^[192,196] The concept should be transferable to nanoparticle composite membranes incorporating superparamagnetic particles.

While the generation of strong, high frequency alternating magnetic fields is challenging, there is an alternative option using static magnetic fields, i.e. *Lorentz force actuation*.^[192,197] By incorporation of conductive pathways forwarding AC currents into resonators, the structures experience a force when placed in a perpendicular, static magnetic field. This Lorentz force can lead to vibrational excitation.^[192]

Electrothermal excitation^[198] was demonstrated for MEMS resonators, such as cantilevers.^[199] Here, a resistive structure is fabricated on the resonator and biased with AC voltages. Resistive heating leads to periodic expansions of the structure and induces a mechanical stimulus driving the resonator.

Read-out. Within the majority of the specified studies focusing on nanomembranes — as well as in this thesis — membrane vibrations were monitored using laser interferometry (cf. figure 3.14a and b). Interferometry is a powerful technique for precisely measuring fast deflection changes on the nano- and picometer scale. The underlying method used in this work is discussed in section 3.4.

For some materials, all-electrical excitation and read-out strategies were reported. This is e.g. the case for graphene-based resonators. Chen et al. employed a high-frequency

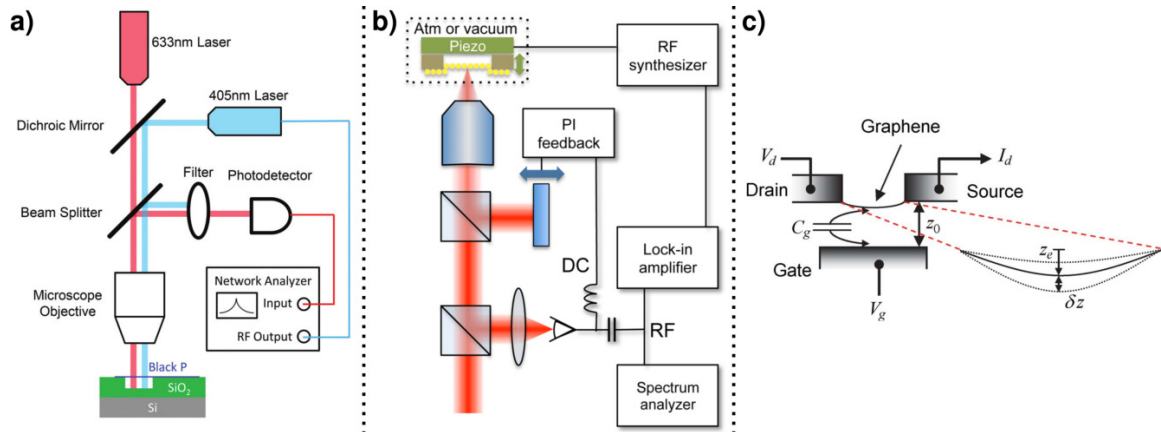


Figure 3.14: a) Schematic showing an experimental setup for photothermally excited black phosphorous resonators using a modulated 405 nm laser and capturing vibrations utilizing a 633 nm laser by means of interferometry. Reproduced from Ref [37] with permission of The Royal Society of Chemistry. b) Experimental setup used for the characterization of GNP monolayer resonators with external piezo actuation as well as interferometric deflection read-out. Reprinted with permission from Ref [45]. ©2013 American Chemical Society. c) Graphene based resonator in a three terminal FET like setup. Due to the dependence of the drain current I_D on the graphene-gate distance change δz , deflections and vibrations can be read out electronically. ©2013 IEEE. Reprinted, with permission, from [21].

mixing approach for actuation and detection of mechanical resonance of graphene sheet resonators. The devices were electronically addressed using a three-terminal, FET like electrode configuration, as depicted in figure 3.14c. While the source and drain electrodes were connected to a freestanding graphene sheet, the Si substrate below the suspended graphene was utilized as gate electrode. They used a downmixing technique, exploiting changes of the graphene layer's conductivity arising under variations of the distance to the gate.^[21–23] Downmixing techniques were also applied for the electrical read-out of MoS₂ resonators' spectra.^[36] In general all-electrical excitation and read-out brings the advantage that no optics are needed, facilitating incorporation of devices into electronic circuitry.

3.4 Interferometry

As discussed in the preceding section, laser interferometry represents a versatile non-contact method for monitoring deflections of MEMS/NEMS components with pico- to micrometer amplitudes. Due to its importance and extensive use within the framework of this thesis, this section provides a description of its basic principles and apparatus implementation. Generally, interferometric distance measurements are based on the superposition of coherent light. The distance information is contained in the phase of the superimposed light waves and can be extracted by interpretation of interference effects.^[200]

The laser interferometer utilized in the measurement setup established within the framework of this thesis is a commercial, modified Michelson type interferometer, incorporated into a technical microscope.^[202] The operational principle was described by Dontsov and is briefly recapitulated here.^[201] The basic optical setup is depicted in figure 3.15. A HeNe laser ($\lambda = 632.8 \text{ nm}$) is coupled into the interferometer head via an optical fiber. This comes with the advantage that the measurement environment is spatially separated from the laser, suppressing thermal influences due to the laser's waste heat.^[201,202]

In the following, light propagation in z direction is considered, see figure 3.15. The angle α denotes the orientation of optical components, whose functional axes are not aligned

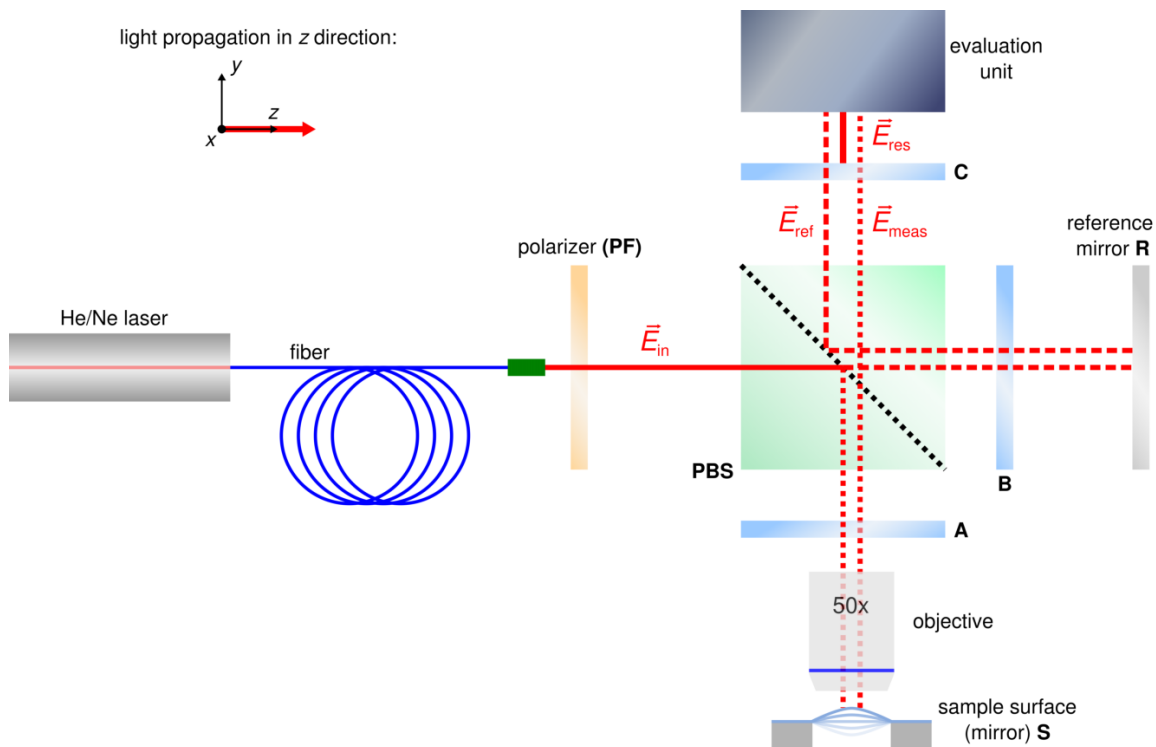


Figure 3.15: Simplified schematic showing the basic principle of the interferometer used in this work for monitoring deflections of the GNP composite membranes. **A**, **B** and **C** represent $\lambda/4$ plates and **PBS** is a polarizing beam splitter. Adapted from [201].

with x or y .

The incoming laser beam first passes a polarizer **PF**, which leads to linearly polarized light, described by the Jones vector in equation 3.39. By adjusting the filter, the fractions A_x and A_y of light being polarized along the x and y axis can be controlled.^[201]

$$\vec{E}_{\text{in}} = \begin{bmatrix} A_x e^{i\phi_E} \\ A_y e^{i\phi_E} \end{bmatrix} \quad (3.39)$$

The polarized beam hits the polarizing beam splitter **PBS**. Here, its x -component is deflected to the measurement arm and passes the $\lambda/4$ plate **A**, causing circular polarization. The circular polarized beam is reflected at the measurement mirror (the sample surface) **S** and passes the $\lambda/4$ plate a second time, changing its polarization to linear, but now along the y axis. Now the beam passes the polarizing beam splitter without being deflected. The phase shift $\Delta\phi_{\text{meas}}$ of this beam fraction \vec{E}_{meas} is proportionally dependent on the measurement arm length l_{meas} .^[201]

$$\phi_{\text{meas}} = \frac{4\pi}{\lambda} l_{\text{meas}} \quad (3.40)$$

The y -polarized fraction of the initial beam \vec{E}_{in} passes straight through the polarizing beam splitter **PBS** into the reference arm. In analogy to the x component, it is circularly polarized by the $\lambda/4$ plate **B**, reflected at the reference mirror **R** and finally linear polarized along the x direction, when passing the $\lambda/4$ plate **B** the second time. The polarization along x leads to complete reflection at the beam splitter. The phase shift of \vec{E}_{ref} is proportional to the reference arm length:^[201]

$$\phi_{\text{ref}} = \frac{4\pi}{\lambda} l_{\text{ref}} \quad (3.41)$$

The Jones vectors of the beam passing through the measurement arm as well as the reference arm can be described utilizing Jones calculus, starting from \vec{E}_{in} and taking into account the Jones matrices of the components in the respective beam paths (table 3.1):^[201]

$$\vec{E}_{\text{meas}} = B_{\text{PBS},y} \cdot B_{\lambda/4} \left(-\frac{\pi}{4} \right) \cdot B_{\text{Mirr}} \cdot B_{\lambda/4} \left(\frac{\pi}{4} \right) \cdot B_{\text{PBS},x} \cdot \vec{E}_{\text{in}} \quad (3.42)$$

$$\vec{E}_{\text{ref}} = B_{\text{PBS},x} \cdot B_{\lambda/4} \left(-\frac{\pi}{4} \right) \cdot B_{\text{Mirr}} \cdot B_{\lambda/4} \left(\frac{\pi}{4} \right) \cdot B_{\text{PBS},y} \cdot \vec{E}_{\text{in}} \quad (3.43)$$

\vec{E}_{meas} and \vec{E}_{ref} show orthogonal linear polarization, disallowing interference. Hence, the $\lambda/4$ plate **C** is adjusted so that circularly polarized beams are formed from both incident

Table 3.1: Jones matrices of different ideal optical components.^[201]

Optical component	Jones matrix (ideal)
PBS (y -plane)	$B_{\text{PBS},y} = \begin{bmatrix} 0 & 0 \\ 0 & 1 \end{bmatrix}$
PBS (x -plane)	$B_{\text{PBS},x} = \begin{bmatrix} 1 & 0 \\ 0 & 0 \end{bmatrix}$
($\lambda/4$ -Plate)	$B_{\lambda/4}(\alpha) = \sqrt{2} \begin{bmatrix} 0.5 + i \cdot (0.5 - \sin^2(\alpha)) & i \cos(\alpha) \sin(\alpha) \\ i \cos(\alpha) \sin(\alpha) & 0.5 - i \cdot (0.5 - \sin^2(\alpha)) \end{bmatrix}$
Mirror	$B_{\text{Mirr}} = \begin{bmatrix} -1 & 0 \\ 0 & 1 \end{bmatrix}$
Polarizer	$B_{\text{PF}}(\alpha) = \begin{bmatrix} \cos^2(\alpha) & \cos(\alpha) \cdot \sin(\alpha) \\ \cos(\alpha) \cdot \sin(\alpha) & \sin^2(\alpha) \end{bmatrix}$

beams.^[201] The vector \vec{E}_{res} of the beam resulting after passing \mathbf{C} is described by equation 3.44. For the sake of simplicity $A_x = A_y = 1$ is assumed.^[201]

$$\vec{E}_{\text{res}} = B_{\lambda/4} \left(\frac{\pi}{4} \right) \cdot \left(\vec{E}_{\text{meas}} + \vec{E}_{\text{ref}} \right) = \begin{bmatrix} -\sin \left(\frac{\pi}{4} + \frac{\phi_{\text{meas}} - \phi_{\text{ref}}}{2} \right) \cdot e^{i \cdot \left[\phi_{\text{E}} + \frac{\pi}{4} + \frac{\phi_{\text{meas}} + \phi_{\text{ref}}}{2} \right]} \\ \cos \left(\frac{\pi}{4} + \frac{\phi_{\text{meas}} - \phi_{\text{ref}}}{2} \right) \cdot e^{i \cdot \left[\phi_{\text{E}} + \frac{\pi}{4} + \frac{\phi_{\text{meas}} + \phi_{\text{ref}}}{2} \right]} \end{bmatrix} \sqrt{2} \quad (3.44)$$

\vec{E}_{res} is a linearly polarized beam, with its polarization angle being linearly dependent on the phase difference between measurement and reference arm:^[201]

$$\Delta\phi = \phi_{\text{meas}} - \phi_{\text{ref}} = \frac{4\pi}{\lambda} (l_{\text{meas}} - l_{\text{ref}}) \quad (3.45)$$

The optical evaluation unit, which is not discussed in detail, provides, after amplification and processing, two signals V_x and V_y to the evaluation electronics, corresponding to the polarization of \vec{E}_{res} . These ideally represent a cosine as well as a sine modulation of the phase shift $\Delta\phi$.^[201] Imaging the signals V_x and V_y as a Lissajous figure, they describe a point on a circle via an angle $\vartheta = \arctan \left(\frac{V_y}{V_x} \right)$. The angle is linearly related to the phase shift and hence, the optical path length difference $l_{\text{meas}} - l_{\text{ref}}$. This relation is used to

3. Introduction

describe sample deflections corresponding to changes in l_{meas} , whereby a full rotation of $\Delta\vartheta = 2\pi$ corresponds to a measurement arm length change of $l_{\text{meas}} = \lambda/2$, assuming a constant l_{ref} .

4 Goal

Composite materials of organically stabilized or cross-linked gold nanoparticles (GNPs) feature unique properties, such as a highly perturbation-sensitive tunneling based charge transport and the ability to sorb analyte compounds. These characteristics render the materials interesting for sensing applications, which was demonstrated in numerous studies on strain sensing and chemical sensing using the materials as film coatings on supporting substrates.

More recently, the fabrication of GNP composite membranes with nanoscale thickness was reported. Combining the mechanical properties of such freestanding nanomembranes with the electronic properties and sorption capabilities of GNP composites is of great interest, as it enables the fabrication of novel micro- and nanoelectromechanical sensors and actuators. The aim of this thesis is to demonstrate and to evaluate different applications arising from this coupling. Therefore, α, ω -alkanedithiol (ADT) cross-linked GNP membranes should be characterized and employed as functional elements in prototypical micro- and nanoelectromechanical devices fulfilling different tasks:

1. Pressure Sensing

The first part of this thesis aims at the fabrication of GNP membrane based pressure sensors. Due to their charge transport mechanism, GNP composites show strong resistance changes when subjected to strain. Hence, freestanding GNP membranes should be employed as sensitive transducers in resistive pressure sensors.

2. Electrostatic GNP Membrane Actuation and Resonance

Electrostatic actuation is a widely used principle to translate electronic signals into motion/deflection of micro- and nanoscopic structures. The second part of this study aims at the fabrication of electrostatic GNP membrane actuators and their characterization. Further, electrostatic actuation should be used to excite resonant oscillations of freestanding GNP membranes.

3. Microelectromechanical Chemical Sensing

GNP composites are able to sorb analyte molecules from the gas phase. Analyte sorption presumably influences the mechanical characteristics of GNP membranes. Hence, sorption-induced effects on the response characteristics of GNP membrane actuators and resonators should be probed, and the application of such devices as electromechanical chemical sensors should be evaluated.

4. Material Characterization.

Composites from ADT cross-linked GNPs are materials with tunable properties, which can be adjusted by the choice of the linker molecule. The goal of a further study is investigating the influence of the ADT cross-linker chain length on the elasticity of the composite material.

5 Synopsis

This thesis summarizes different studies regarding the electromechanical properties of free-standing, organically cross-linked GNP membranes with thicknesses in the 10 to 100 nm range and their potential applications as functional materials in MEMS/NEMS. This section presents four projects, which have been completed, summarized and published in international peer-reviewed scientific journals. For two further projects, manuscripts are in preparation and will be submitted to peer-reviewed journals soon. The latter projects as well as additional unpublished studies are outlined in section 6. The major projects are schematically pictured in figure 5.1, highlighting their topical areas as well as the links between them.

The first project, outlined in section 5.2 with the respective publication reprinted in section 5.2.6, aimed at the utilization of GNP membranes as novel functional materials, acting both as diaphragms and resistive transducers in a new type of pressure sensor. To the best of our knowledge this work represents the first report on pressure sensors utilizing the pronounced resistive strain sensitivity and elasticity of a bare, freestanding nanoparticle membrane. This work is related to earlier studies, employing bulge testing to probe the elastic properties of GNP membranes,^[48] and probing the charge transport characteristics of freestanding GNP/ADT membranes.^[52]

The second project provides the first demonstration of electrostatic actuation of a GNP composite membrane. Electrostatic actuation is a versatile principle widely used in present-day MEMS and NEMS, for translating electronic signals into motion. In the context of this work, which is summarized in section 5.3 with the respective publication reprinted in section 5.3.5, we reported the deflection of a conductive, cross-linked GNP membrane by applying a direct current (DC) electric field. The study forms the basis for further projects, including as the third project of this thesis.

Within the third project, outlined in section 5.4 with the respective publication reprinted in section 5.4.5, electrostatic actuation was employed to excite vibrational resonances of freestanding, cross-linked GNP membranes. As we observed in the foregoing project, GNP membranes deposited onto lithographically fabricated microcavities were tense, i.e., they show a pre-stress which governs their deflection behavior when applying electrostatic forces. This pre-stress also enables the use of the membranes as resonators, exhibiting resonant oscillations at distinct resonance frequencies. Utilizing electrostatic actuation with AC voltages, i.e., alternating electric fields and forces, these resonant oscillation modes can be excited and visualized by means of laser interferometry. GNP membrane resonators are promising candidates for the fabrication of sensitive electromechanical sensors, as demonstrated in a successive project.

The fourth project, summarized in section 5.5 with the respective publication reprinted in

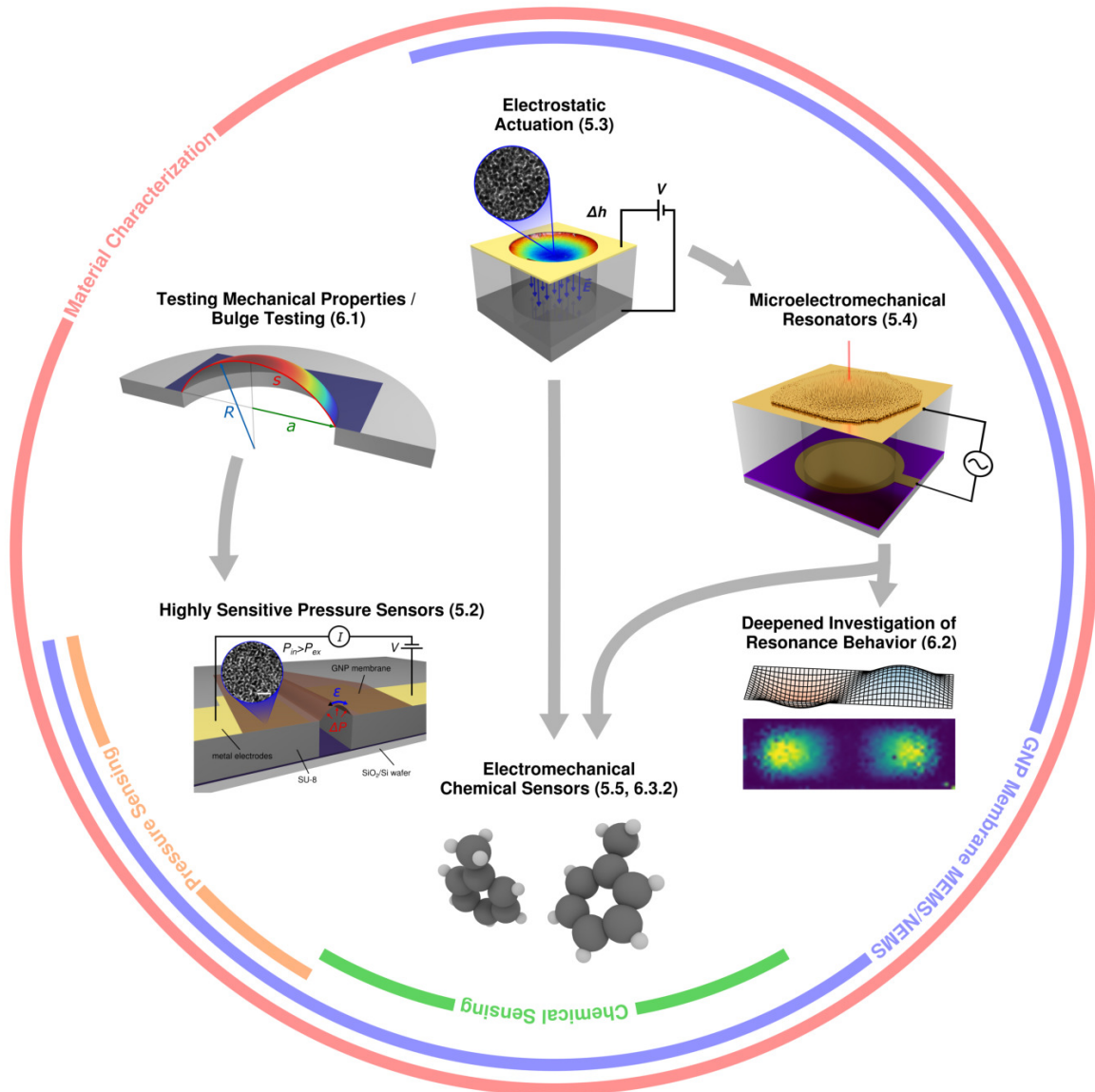


Figure 5.1: Schematic summarizing the major projects included in this thesis. Numbers denoted in parentheses refer to the respective sections in this thesis.

section 5.5.5, closes the circle back to sensing and aimed at the fabrication of electromechanical chemical sensors using freestanding GNP membrane resonators. Connecting to the previous project, oscillations of freestanding GNP membranes were electrostatically excited under reduced pressure, and their fundamental resonance frequencies were continuously monitored. Pronounced resonance frequency shifts were observed when exposing the resonators to vapors of toluene, 4M2P, 1-propanol and water. We assigned the high sensitivity of the resonance frequencies to analyte vapor exposure to sorption-induced changes of the mechanical properties (e.g. pre-stress or modulus of elasticity) of the composite material. The findings of this project as well as of an additional study described in section 6.3.2, targeting the use of quasi-statically actuated GNP membranes as chemical sensors, formed the basis for the patent application GB1704749.9 “Method for detecting

an analyte based on the detection of a change of the mechanical properties of a free-standing nanoparticle composite material” disclosing novel chemical sensors based on this sensing principle.

The results of two further projects are currently being summarized and prepared for submission and publication. The first of these projects, outlined in section 6.1, focuses on the structural and mechanical characterization of freestanding GNP membranes, cross-linked using ADTs of different alkane chain lengths and 1,4-benzenedithiol (BDT). The elasticity of these membranes was probed using AFM based bulge tests,^[38,39,41,175] as used in an earlier work.^[48] The experiments reveal a non-linear dependence of the membranes’ modulus of elasticity on the length of the ADT alkane backbone. This agrees with the assumption that the flexible elastic matrix comprising the GNPs is governing the mechanical properties of the composites. Further, our measurements suggest potential fusion of GNPs to a certain degree when cross-linked with shorter ADTs.

The second, yet unpublished project, summarized in section 6.2, deepens the characterization of resonators fabricated from 6DT cross-linked GNP membranes. Circular resonators with a broad variety of diameters as well as rectangular resonators were investigated and experimentally determined resonance frequencies as well as mode shapes were compared to theory.

The following section 5.1 presents an overview on the basic procedures established for the fabrication of freestanding GNP membranes, as repeatedly applied in subsequently discussed projects, with slight modifications.

5.1 Fabrication and Interfacing of Freestanding GNP Membranes

To study their electromechanical properties and potential applications, prototypical devices employing ADT cross-linked GNP composite membranes as functional materials were fabricated. Each device consisted of a microstructure, suitable to support and electronically address a freestanding GNP membrane, and the membrane itself deposited on top of this structure.

In a first step, the GNP composite materials were deposited as thin films onto sacrificial substrates via spin-coating. Second, microstructures fulfilling specific requirements for the different projects were fabricated. The microstructures had cavities or trenches that could be spanned by the membranes to render them freestanding. Further, they were equipped with electrodes adjacent to the microcavities, either directly connected to the membranes, or in close proximity to the membranes in order to impose electrostatic forces. Lithographic procedures for the fabrication of such microstructures were developed within the framework of this thesis. Finally, a transfer process was employed, enabling the detachment of the membranes from their initial substrates and subsequent deposition onto the microstructures. While the geometric design of the devices as well as the methods and experimental procedures for their characterization were defined by the requirements of the individual projects, the membrane and microstructure fabrication steps as well as the transfer process were similar. Hence, the latter are outlined in the following and only briefly picked up in the respective project sections.

5.1.1 Fabrication of GNP Membranes

In 2011 our group reported a spin-coating procedure for the facile and time efficient fabrication of composite films comprised of ADT cross-linked GNPs.^[52] Compared to conventional layer-by-layer self-assembly,^[49,53] which is time- and solvent-consuming due to several intermediate immersion and washing steps, the spin-coating method enables the fabrication of comparable GNP films with thicknesses in the tens of nanometer range within a few minutes instead of several hours. Further, no covalent binding of the films to the substrates is necessary, which is advantageous for their detachment and transfer onto other substrates.^[52] While the spin-coated and layer-by-layer self-assembled films show overall comparable optical properties and charge transport behavior, recent experiments outlined in section 6.1 suggest that the spin-coating method potentially leads to more pronounced particle fusion, especially when applying shorter ADT cross-linkers. The spin-coating process is schematically summarized in figure 5.2a. Initially, a glass substrate was cleaned and continuously rotated at a constant rate. After pre-treatment with a solution of an ADT, $\sim 3 - 4$ nm sized, amine-stabilized GNPs were deposited by applying their respective solution in *n*-heptane. Afterwards, a methanolic solution of the ADTs was deposited two times onto the substrate, leading to stripping of the GNPs' amine ligands

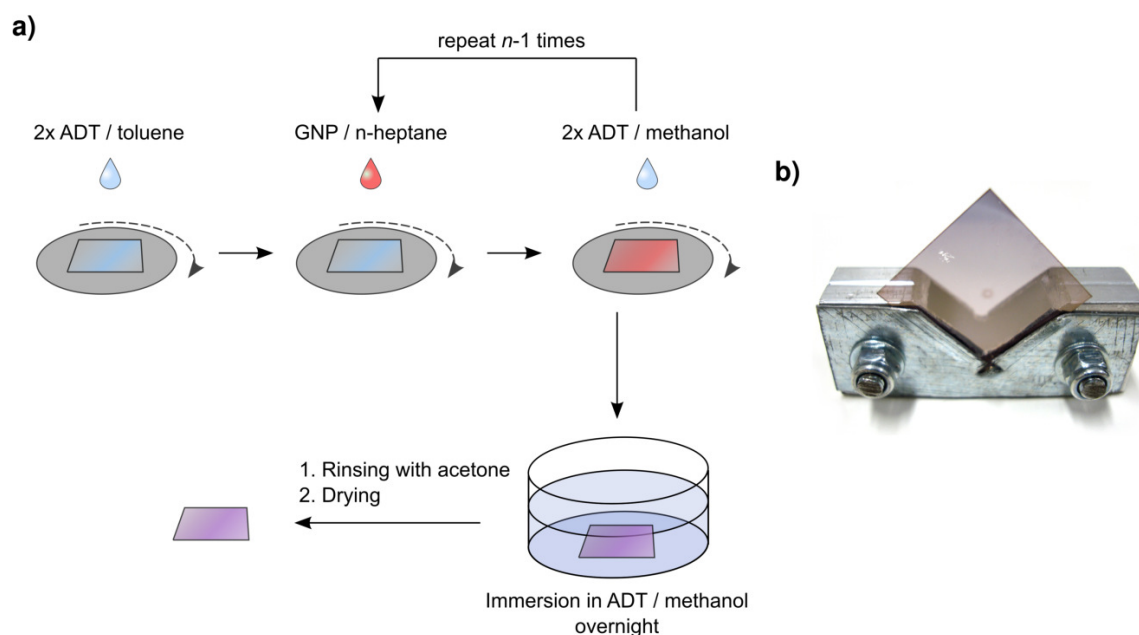


Figure 5.2: a) Schematic of the spin-coating based deposition procedure for ADT cross-linked GNP membranes. Adapted from [52]. ©2011 IOP Publishing. Reproduced with permission. All rights reserved. b) Photograph of a glass substrate coated with a GNP membrane placed in a sample holder.

and cross-linking of the particles with ADTs. The deposition and cross-linking steps represent one deposition cycle. By multiple repetitions of this cycle, desired composite film thicknesses in the 10 – 100 nm range were obtained.^[52] Following the spin-coating process, the samples were immersed in the methanolic ADT solution overnight to finalize the ligand exchange, and eventually rinsed in acetone and dried. An exemplary photograph of a glass substrate coated with a GNP film, placed in a sample holder, is depicted in figure 5.2b.

5.1.2 Fabrication of Supporting Microstructures

For the fabrication of freestanding GNP membranes, the GNP films initially fabricated on glass substrates were transferred onto 3D microstructures featuring cylindrical, cuboid, trapezoidal, or trench-like cavities with lateral sizes in the range of tens to hundreds of micrometers and depths up to $\sim 40 \mu\text{m}$. Different options exist for the fabrication of such microstructures.

In the first place, silicon-based technologies are widely used. Advanced etching processes, such as the Bosch process^[203] exist for creating cavities, trenches and through holes in silicon wafers. Further, anisotropic wet etching of silicon using KOH solutions is a widespread technique for achieving defined recesses.^[204,205] Even though the use of silicon has different advantages over the use of polymeric materials for microstructure fabrication, such as its rigidity and insensitivity towards solvents, there are also some drawbacks concerning the applicability for experiments conducted in this work. Fabrication of cylindrical

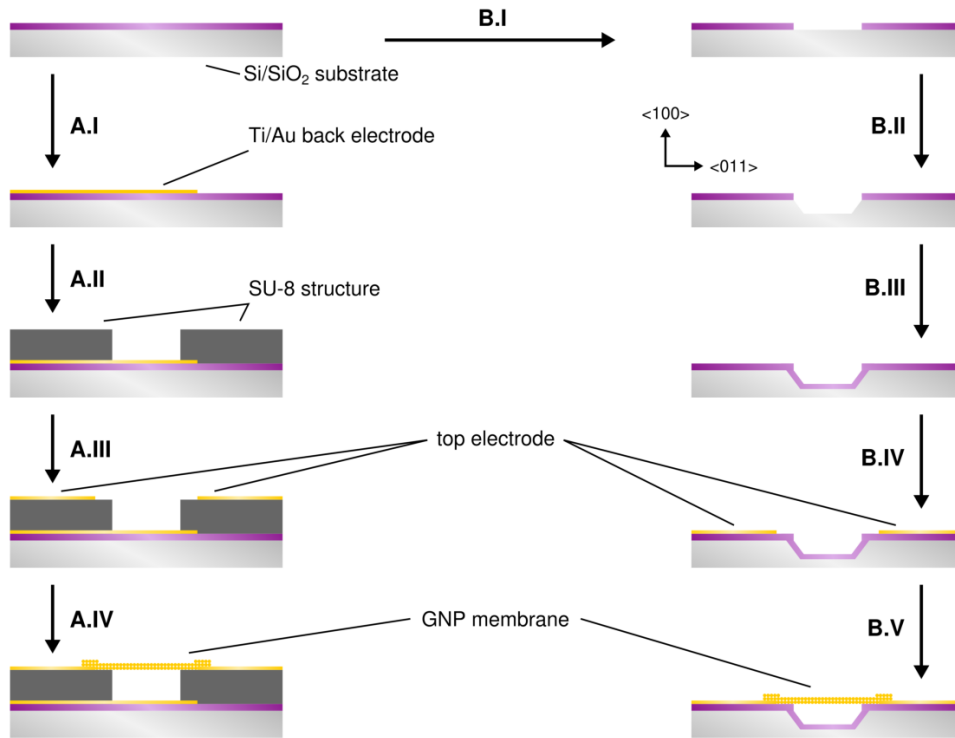


Figure 5.3: Schematic of the SU-8 based (**A** steps) and silicon-based (**B** steps) microstructure fabrication procedure starting with a thermally oxidized silicon substrate. **A.I:** Deposition of back electrodes. **A.II:** Fabrication of the SU-8 microcavity structure. **A.III:** Deposition of top electrodes. **A.IV:** Transfer of the GNP membrane. **B.I:** Etching of the SiO₂ layer. **B.II:** Anisotropic etching of silicon. **B.III:** Thermal SiO₂ growth. **B.IV:** Deposition of top electrodes. **B.V:** Transfer of the GNP membrane.

or cuboid cavities with straight, vertical walls is hardly possible by silicon wet etching. Besides, silicon is a semiconductor with a conductivity that is strongly dependent on the dopant level. Hence, for transport measurements, the etched silicon structure has to be isolated from the GNP membrane and electrodes, e.g. by growing a silicon dioxide layer. Further, it is not straightforward to create an individual, externally addressable electrode at the bottom of a top-down etched cavity, as required by experiments involving a back electrode for imposing electrostatic forces on the freestanding membrane section. Here, the whole silicon wafer containing the cavities could simply be used as an electrode, but this implies a large parasitic capacitance located in the areas where the electrodes and the membrane are directly placed on the thin silicon dioxide layer separating them from the silicon (see figure 5.3, bottom right structure). Nevertheless, in the fourth project outlined in this synopsis, aiming at the fabrication of GNP membrane based chemical sensors, such silicon-based structures were employed for control experiments because of their insensitivity towards organic vapors. Still, the majority of 3D microstructures used to support freestanding membranes in the following projects was fabricated from SU-8, a non-conductive^[206,207] negative tone epoxy photoresist. Due to its simplicity and flexibility, the SU-8 based fabrication process proved to be well-suited for the experiments conducted. The SU-8 as well as silicon-based fabrication routes are schematically depicted in figure 5.3.

SU-8 Based Microstructure Fabrication. The fundamental steps of the SU-8 based microstructure fabrication are depicted in figure 5.3 (**A** steps). SU-8 was deposited onto silicon or thermally oxidized silicon wafers using standard spin-coating and baking steps. The thickness of the SU-8 layer, governing the depth of resulting microcavities, could be adjusted by choosing from different SU-8 formulations featuring varying viscosities, and/or adjusting the spin-coating rotational rates. The resist was further exposed to ultraviolet (UV) light through a patterned photomask featuring the microcavity geometry, post-exposure-baked and developed, to remove non-cross-linked SU-8 in unexposed areas, including the microcavities. Afterwards, the SU-8 layers were hard baked to achieve further cross-linking of the structure (**A.II**). As the SU-8 layer is fabricated on top of the substrate, the fabrication of electrodes at the bottom of the cavities with conductive pathways to external contact pads routed below the SU-8 layer is straightforward. As depicted in figure 5.3 (**A.I**) such metal structures were optionally fabricated on thermally oxidized silicon wafers prior to the SU-8 layer deposition via standard photolithography. To electronically address the freestanding membrane sections spanning the microcavities, gold electrodes were fabricated on top of the SU-8 layer in proximity to the microcavities by a lift-off process. Here, the SU-8 structures as well as the optional, underlying back electrodes were covered with a sacrificial negative photoresist layer. Using photolithography, this resist layer was removed in the distinct areas on the SU-8 surface, where electrodes were to be deposited. Afterwards a metal (commonly gold) layer was deposited by thermal evaporation, directly onto the SU-8 structure in the resist-free areas and on top of the resist layer everywhere else. Finally, in the lift-off step, the remaining photoresist was removed together with the overlying excessive gold layer, leaving the desired, structured electrodes on top of the SU-8 layer (**A.III**).

Silicon-Based Microstructure Fabrication. The silicon-based fabrication route is schematically depicted in figure 5.3 (**B** steps). Here, sections of the oxide layer of a thermally oxidized silicon wafer substrate were removed using buffered hydrofluoric acid (buffered oxide etch (BOE))^[205] after protecting the the remaining oxide sections using a photolithographically structured photoresist mask (**B.I**). Afterwards, a KOH solution was employed to anisotropically etch the underlying silicon substrate. In this step, the previously structured silicon dioxide layer acts as an etch mask. KOH solutions show strongly different etch rates for the crystalline facets of silicon. As the etch rate of $\{111\}$ facets is up to several hundred times^[204,205] slower than those of other facets, they are preferentially formed during etching and the etch process yields defined trapezoidal cavities or trenches in $\{100\}$ oriented silicon wafers (**B.II**). To avoid direct electrical contact between the GNP membranes and the silicon substrate, the microstructures were further oxidized by heating them to $\sim 1000^\circ\text{C}$ in air for several hours (**B.III**). Finally, top electrodes for electrically addressing the GNP membranes were deposited and structured via a lift-off process, as in the case of the SU-8 fabrication route described above (**B.IV**).

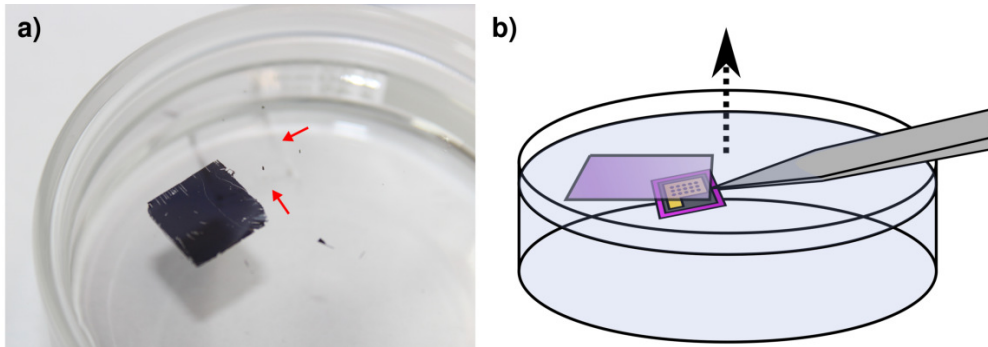


Figure 5.4: a) GNP membrane floating at the water-air interface after detachment from the initial glass substrate (indicated by the red arrows). b) Schematic of the skimming process used to transfer the GNP membranes to 3D microstructures.

5.1.3 Membrane Transfer

As reported in earlier works by our group,^[48,52] GNP membranes were detached from their initial substrates and transferred onto 3D microstructures by a flotation process. The glass substrates supporting the GNP films were floated on demineralized water. After several hours or days, the substrates were carefully immersed into the aqueous phase, while the GNP membranes remained free-floating at the liquid-air interface, as depicted in figure 5.4a. Subsequently, the membranes were skimmed from the interface using the microstructures (figure 5.4b). The samples were then allowed to dry and the GNP membranes settled on top of the microstructures, spanning their microcavities. Alternatively, in the case of the device described in section 6.3.2, the Langmuir-Schaefer technique was employed to transfer a floating GNP membrane to a microstructure.

Currently other transfer techniques, such as stamp transfer and contact printing are investigated in our group and successfully applied. Similar techniques were employed to fabricate freestanding membranes of other nanomaterials (cf. section 3.3.1), e.g. layers of graphene,^[147,149,150,190] MoS₂,^[148,150] WSe₂,^[34] TaSe₂,^[151] or black phosphorus.^[37] These transfer techniques are expected to be more reliable than the flotation process and to improve the control over mechanical parameters of the membranes, such as their pre-stress. Also, contact printing and stamp based processes can presumably be incorporated in large-scale fabrication lines and are therefore promising for approaching industrial production schemes.^[208]

5.2 Resistive Pressure Sensing

Over the past years, substrate-supported films of ligand-stabilized or cross-linked nanoparticles have been studied extensively as resistive strain sensors.^[50,58–60,111,209] As described in the introductory section, such composite materials are well suited for this application since their tunneling based charge transport mechanism is highly sensitive to strain. On the other hand, several research groups — including ours — studied the mechanical properties of freestanding nanoparticle membranes, e.g. of ordered monolayers of monothiol-stabilized GNPs,^[156,159] DNA-capped GNPs,^[210] polymer/GNP composite membranes^[43,176] or dithiol cross-linked multilayered, disordered GNP membranes.^[48] Generally speaking, in these experiments, which are summarized in section 3.3.2, membranes were deposited onto micrometer sized apertures and probed by imposing mechanical stress. The deflection response of the membranes was observed via a suitable detection technique. Using an appropriate model, mechanical characteristics of the materials could be derived from the collected data. Such studies were experimentally conducted e.g. by bulge testing, i.e., application of an overpressure to the back side of the membranes and subsequent observation of their resulting deflection by optical means^[43,46,176] or AFM.^[38,39,41,175] Other studies involved indentation experiments. In these experiments, the deflections resulting from forces applied by cantilever tips were measured using an AFM.^[47,156,159]

However, by the time of our publication,^[2] coupling electronic and mechanical properties of freestanding GNP composite membranes, e.g. by monitoring changes in their resistance when imposing mechanical stress/strain had not been reported. These experiments are highly interesting, as they enable probing the electromechanical properties of the membrane without a perturbing substrate. In many previous experiments addressing the strain sensitivity of GNP composites, these materials were coated as films onto flexible substrates. The structures were subjected to bending, imposing strain on the nanoparticle film. Here, the mechanical properties of the test structures are dominated by their flexible carrier substrates, also hindering — if not circumventing — recognition of failure of the composite coating, e.g. by crack formation.^[60] In contrast, rupture of isolated, freestanding membranes can readily be observed. Besides aiming at the investigation of material characteristics, resistance changes of freestanding nanoparticle membranes in response to mechanical loading can be employed as a sensor signal, leading to novel resistive sensing devices, such as highly sensitive electromechanical pressure sensors. While nanocomposite membranes were proposed as functional materials for pressure sensors earlier,^[43] optical techniques such as interferometry were utilized for readout so far, similar as in common bulge tests. Exploiting the resistance change of a cross-linked GNP membrane as sensor signal enables a facile pressure readout using simple circuitry without expensive and complex microscope optics, which lack the ability to be incorporated in small, cheap and mass-produced devices.

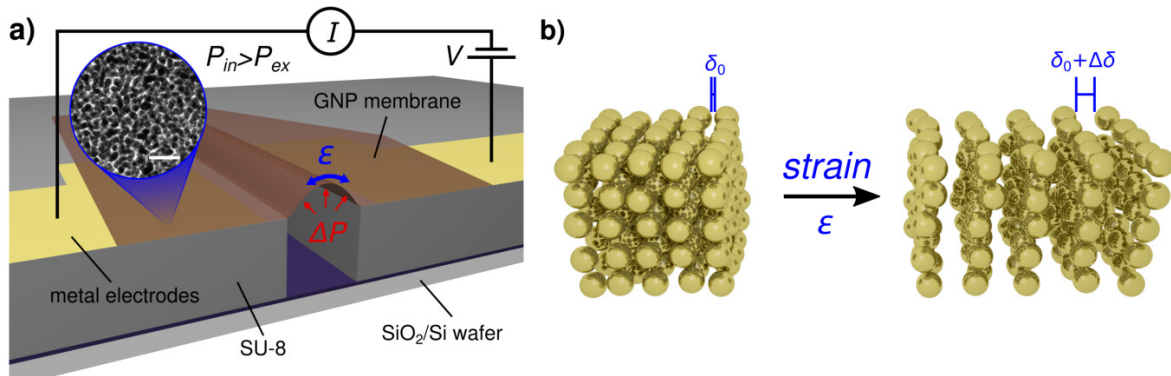


Figure 5.5: a) Schematic view showing the cross-section of a GNP membrane based pressure sensor. The inset shows a transmission electron micrograph of a 6DT cross-linked GNP membrane. Scale bar: 25 nm. Adapted from Ref. [2] with permission from The Royal Society of Chemistry. b) Schematic illustrating the impact of strain on the interparticle distances in GNP composites (simplified).

5.2.1 Sensing Principle

The working principle of our pressure sensor, schematically depicted in figure 5.5a, is that of a gauge pressure sensor sealed at atmospheric pressure.^[211] A GNP membrane seals a microcavity and acts as diaphragm, i.e., as a barrier (ideally hermetically) separating the cavity volume from the exterior. Upon variation of the external pressure P_{ex} , the pressure difference between the latter and the pressure in the cavity volume P_{in} induces a force acting on the membrane. This results in bulging and strain ε , which again leads to a change of the interparticle distances. Because of the membranes' charge transport mechanism (cf. section 3.2.3), a strain-induced interparticle distance increase results in a decreased conductivity and can simply be monitored by measuring the resistance of a membrane section. Hence, the resistance of such a sensing element is correlated to the external pressure P_{ex} . It is expected that the resistance has its minimum value when P_{ex} equals the pressure present in the microcavity P_{in} and increases upon increasing or decreasing P_{ex} , leading to inward or outward bulging of the membrane, respectively.

Modeling the Sensor Transfer Function

A simple model was developed for approximating the sensor's transfer function. In the case of our sensor, the long dimension a_y of the freestanding membrane considerably exceeds its short dimension a_x (see figure 5.7). Upon bulging the membrane by applying a pressure difference, its strain along the long y direction can therefore be neglected in the central region,^[175] where the membrane's resistance along its short direction x is monitored. The pressure dependence of the membrane's deflection can be described by approximating the bulged membrane as a cylindrical cap formed above the aperture. An equation relating the center deflection (height of the cylindrical cap) h with the applied pressure difference is given by equation 5.1.^[175]

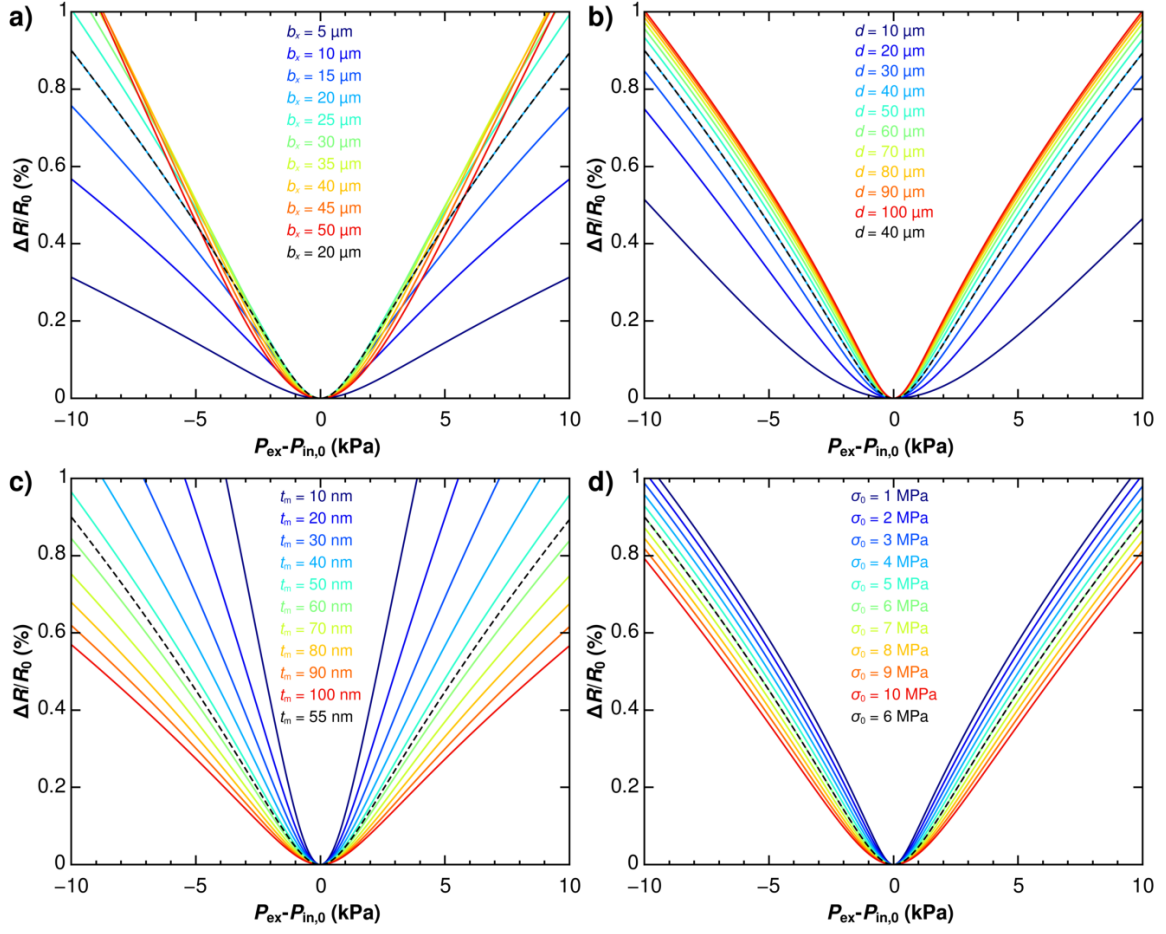


Figure 5.6: Estimated sensor transfer functions obtained under variation of a) the half microcavity width b_x while maintaining a constant a_e/b_x -ratio, b) the microcavity depth d , c) the membrane thickness t_m , and d) the membrane pre-stress σ_0 . For each plot, all other parameters were set to the default values denoted in the text.

$$\Delta P = P_{\text{in}} - P_{\text{ex}} = \frac{C_1 \sigma_0 t_m}{b_x^2} h + \frac{C_2 E t_m}{b_x^4} h^3 \quad (5.1)$$

Here, ΔP is the pressure difference between the external pressure P_{ex} and the pressure within the cavity volume P_{in} , $b_x = a_x/2$ is the half width of the aperture, t_m is the membrane thickness, and E and σ_0 are the elastic modulus and the pre-stress of the freestanding membrane, respectively. In the case of rectangular membranes exceeding an aspect ratio a_y/a_x of 4, which applies in our case, $C_1 = 2$ and $C_2 = 4/[3(1 - \nu^2)]$, with ν being the Poisson ratio of the membrane material.^[175] Due to the small microcavity volume, the change of its internal pressure ΔP_{in} , caused by the volume change upon deflection of the membrane, has to be taken into account. Equation 5.2 describes the relation of the external pressure P_{ex} and the membrane deflection h , assuming an initial microcavity pressure of $P_{\text{in},0}$. The microcavity depth is denoted by d .

$$P_{\text{ex}}(h) = P_{\text{in},0} \frac{2db_x}{2db_x + \frac{\arctan\left(\frac{h}{b_x}\right)(h^2 + b_x^2)^2 + b_x h(h^2 - b_x^2)}{2h^2}} - \frac{C_1 \sigma_0 t_m}{b_x^2} h - \frac{C_2 E t_m}{b_x^4} h^3 \quad (5.2)$$

Considering the estimated cylindrical cap geometry of the membrane bulge, the strain of the membrane ε in direction of the cavity width was derived by computing the variation of its arc length, calculated as a function of the center deflection h . Finally, assuming overall small strains, a linear resistance response to the membrane's strain $\frac{\Delta R}{R_0} = g\varepsilon$ was assumed (cf. section 3.2.3). Based on these constraints, the relative resistance change $\frac{\Delta R}{R_0}$ can be described using equation 5.3.

$$\frac{\Delta R}{R_0}(h) = \frac{2h^2}{3b_x^2} g \frac{2b_x}{a_e} \quad (5.3)$$

Here, g denotes the membrane's gauge factor and a_e is the distance between the electrodes. The distance between the electrodes was commonly larger than the aperture width $2b_x$, i.e., the electrodes were placed in a certain distance to the aperture's edges. This has to be taken into account, as the measurement current passes through inactive (not bulged) membrane sections, causing a higher baseline resistance R_0 with respect to the resistance change ΔR originating from the freestanding, bulged membrane section. A detailed derivation of the model is provided in the Electronic Supplementary Information (ESI) of the respective publication, reprinted in section A.1.1, page 184ff.

Figure 5.6 depicts the estimated sensor transfer functions obtained under variation of different device parameters, obtained by parametric plots of $\frac{\Delta R}{R_0}(h)$ against $[P_{\text{ex}} - P_{\text{in},0}](h)$. If not otherwise specified, a cavity depth $d = 40 \mu\text{m}$ and width $2b_x = 40 \mu\text{m}$, electrode spacing $a_e = 80 \mu\text{m}$, membrane thickness $t_m = 55 \text{ nm}$, membrane elastic modulus $E = 6 \text{ GPa}$, Poisson ratio $\nu = 0.33$, pre-stress $\sigma_0 = 6 \text{ MPa}$ and gauge factor $g = 7$ were assumed. Further, the initial pressure in the microcavity was assumed to be ambient ($P_{\text{in},0} = 1 \times 10^5 \text{ Pa}$). The data indicate that the sensor response is stronger for thinner membranes and membranes having a lower pre-stress, as lower pressure differences are needed to bulge the membranes to the same extent (in terms of change in arc length). Increasing the aperture width (while assuming a constant a_e/b_x ratio) leads to a slight increase in sensitivity until a maximum of sensitivity would be reached. However, widening of the cavity complicates the fabrication of larger-scale defect-free freestanding membranes. Reducing the distance between the electrodes and the cavity edges (ideally to zero, i.e. $a_e = 2b_x$) would give maximum sensitivity, as in this case the measurement current would pass no inactive (not bulged) membrane sections. Lowering the microcavity volume by reducing the cavity depth lowers the sensor response, as the pressure change in the microcavity upon bulging becomes more pronounced.

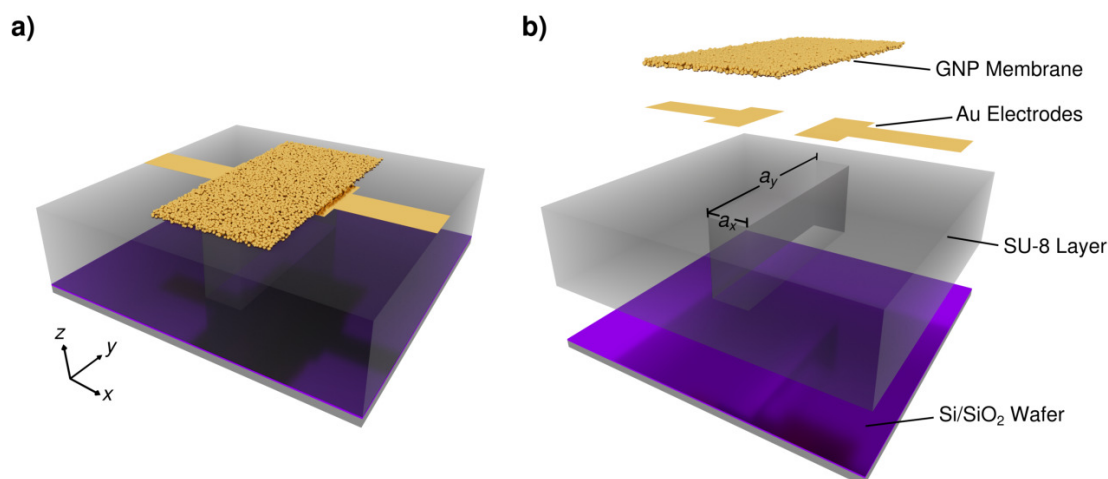


Figure 5.7: a) Schematic depiction of the GNP membrane based pressure gauge. b) Exploded view of the device, showing the substrate, the SU-8 layer featuring a lithographically fabricated microcavity, the electrode layer and the GNP membrane.

5.2.2 Sensor Fabrication

The pressure sensor investigated in this work is schematically depicted in figure 5.7. It consists of a microelectrode structure, fabricated following a multi-step photolithographic process, and a GNP membrane.

The 55 nm thick, 6DT cross-linked GNP film was deposited onto a glass substrate following our standard spin-coating based procedure,^[52] using GNPs with a size of (3.5 ± 0.7) nm, as described in section 5.1.1. The film was thoroughly characterized regarding its optical properties (ultraviolet/visible (UV/vis) spectroscopy), thickness (AFM) and conductivity (current-voltage (IV) measurements). It showed a typical conductivity of 0.1 S cm^{-1} . Details on the film properties are provided in the respective ESI, reprinted in the appendix, section A.1.1, page 184ff.

Besides, the supporting microstructure, featuring a microcavity suitable to act as support for the membrane and as a gas reservoir was fabricated. The structure was equipped with electrodes, to measure the resistance of the freestanding membrane section. A representative scanning electron micrograph of an exemplary structure is depicted in figure 5.8a. The fabrication process for these types of structures was established within the framework of this thesis and is delineated in summarized 5.1.2. In brief, a layer of SU-8 was deposited onto a thermally oxidized silicon wafer. Using photolithographic techniques, a cuboid microcavity, featuring a width of $\sim 40 \mu\text{m}$ and a length of $\sim 500 \mu\text{m}$ was integrated in this layer. The depth of this cavity was governed by the SU-8 layer thickness, which was $\sim 40 \mu\text{m}$. In a second photolithography step, two opposing metal electrodes were fabricated, adjacent to the long sides of the cavity as visible in figures 5.7 and 5.8a.

To finalize the pressure sensor, the substrate-supported GNP film was transferred onto the microstructure as described in section 5.1.3. To this end, it was floated on demineralized

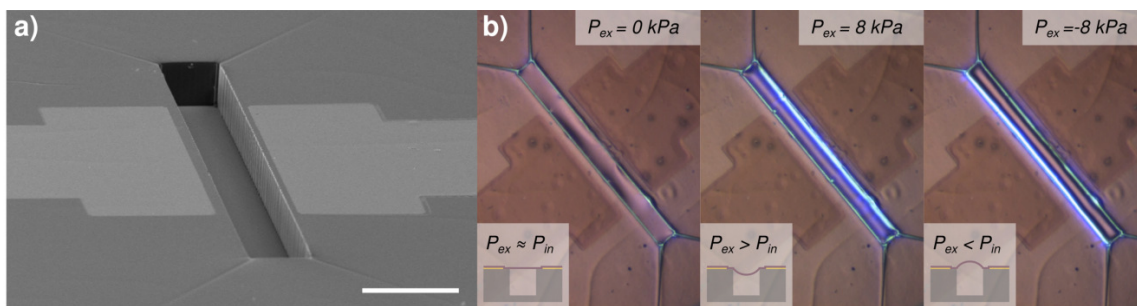


Figure 5.8: a) Scanning electron micrograph of an exemplary 3D microstructure featuring a microcavity and proximal metal electrodes, as used for pressure sensor fabrication. Scale bar: 100 μm . b) Optical micrographs of the pressure sensor investigated in this study, placed in a pressure test cell under varying external pressure loading. Adapted from Ref. [2] with permission from The Royal Society of Chemistry.

water and after an incubation period of up to two days, the membrane could be detached from its glass substrate by careful immersion of the latter into the aqueous phase. The membrane remained free-floating at the liquid-air interface and was skimmed using the microstructure and then allowed to dry. Figure 5.8b depicts optical micrographs of the finalized pressure sensor investigated in this study.

5.2.3 Probing the Sensor Characteristics

The GNP membrane based pressure sensor was mounted onto a PCB and the microelectrodes were electrically contacted using silver paint. The PCB was placed into a custom-built test cell, equipped with a commercial pressure sensor, a periphery suitable to adjust the pressure, and feedthroughs for electrically connecting the sample to measurement hardware. The GNP membrane based pressure sensor was connected to a source measure unit (SMU) and a constant bias of 1 V was applied. The resulting current through the GNP membrane was monitored to observe resistance changes upon variations of the pressure. The pressure within the test cell (external pressure P_{ex}) was varied in the range of $-10 \text{ kPa} < \Delta P_{\text{ex}} < 10 \text{ kPa}$ with respect to atmospheric pressure $P_{\text{ex},0}$, which is also supposed to be the initial microcavity pressure ($P_{\text{in},0}$). Positive as well as negative deviations of the cell pressure led to bulging of the membrane, as clearly visible in figure 5.8b, which is depicting optical micrographs acquired while setting P_{ex} equal, higher and lower compared to atmospheric pressure. Along with bulging, changes in the membrane resistance in a range of up to $\sim 0.7\%$ were observed. This is shown in figure 5.9, illustrating the result of an experiment involving multiple sweeps of the test cell pressure. The experiment demonstrates that our sensor is functional. The dotted red line depicts a fit of our approximate model to the data, taking into account the cavity geometry and the membrane thickness. The elastic modulus $E = 6.0 \text{ GPa}$ of the 6DT cross-linked membrane was obtained by bulge testing (see the ESI, section A.1.1), and a Poisson ratio of $\nu = 0.33$ ^[48] was assumed. The model was fitted to the data by manually adjusting the membrane pre-stress to $\sigma_0 = 6 \text{ MPa}$ and the gauge factor to $g = 7$. Pre-stress in the low MPa range was observed earlier^[1] for 6DT cross-linked GNP membranes deposited onto

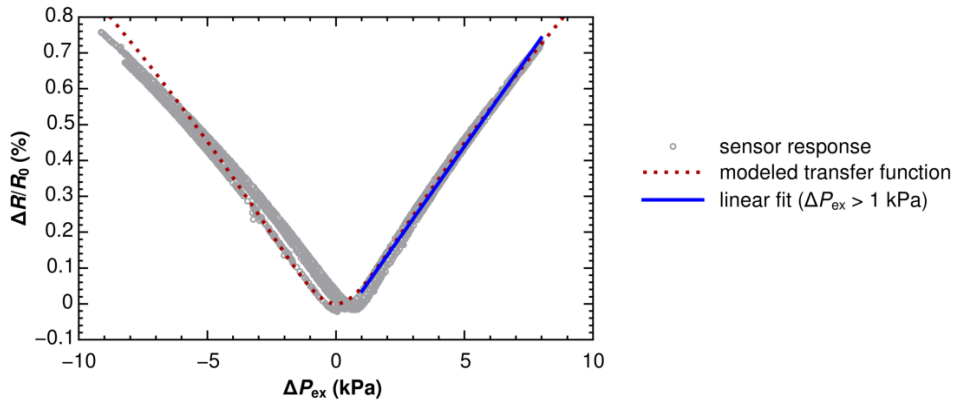


Figure 5.9: Transfer function of the GNP membrane based pressure sensor. The data were acquired by sweeping the test cell pressure P_{ex} while continuously monitoring the resistance of the GNP membrane. The pressure axis denotes the pressure difference ΔP_{ex} between the test cell pressure and ambient. The dotted red curve depicts a fit of our approximate model and the blue line represents a linear fit to the data in the range of $\Delta P_{\text{ex}} > 1$ kPa. Adapted from Ref. [2] with permission from The Royal Society of Chemistry.

SU-8 microcavities, as described in the subsequent project in section 5.3. The good agreement of the experimental data with the simulation indicates that our model is suitable to give a good approximation of the sensor response.

5.2.4 Sensitivity

To determine the sensitivity of our pressure sensor, a linear function was fitted to the response data. A linear fit to the positive pressure region ($\Delta P_{\text{ex}} > 1$ kPa) is plotted as a solid blue line in figure 5.9. The slope of the function describes the pressure sensitivity S_{P} of the sensor in the given pressure range. It is defined as the measured relative change in resistance upon variation of the test cell pressure ΔP_{ex} .

$$S_{\text{P}} = \frac{\Delta \left(\frac{\Delta R}{R_0} \right)}{\Delta (\Delta P_{\text{ex}})} \quad (5.4)$$

Following the procedure described above, a sensitivity of $S_{\text{P}} = 1.01 \times 10^{-4} \text{ mbar}^{-1}$ was determined. Table 5.1, partially adapted from Wang et al.,^[28] lists sensitivities of different recently published MEMS pressure sensors based on graphene, carbon nanotubes as well as silicon-based technologies. Among the devices, our pressure sensor shows a comparably high sensitivity. However, it is to note that the listed values represent sensitivities of the final devices, which do not exclusively depend on the functional materials, but are also influenced by other device parameters, such as the membrane and electrode geometry. In the case of our sensor, it should be taken into consideration that the actual absolute

Table 5.1: Performance comparison table, listing the pressure sensitivities of different MEMS-type pressure sensors. Resistive sensitivities as well as sensitivities of Wheatstone bridge output voltages are listed. Partially adapted from Wang et al.^[28]

Device Structure	Sensitivity S/mbar^{-1}	Reference
GNP membrane diaphragm/transducer	1.01×10^{-4}	this work
Suspended Graphene	2.96×10^{-6}	Smith et al. ^[26]
Graphene on suspended perforated SiN_x membrane	2.8×10^{-5}	Wang et al. ^[28]
Graphene on suspended imperforated SiN_x membrane	6.67×10^{-6}	Zhu et al. ^[29]
Graphene on fixed perforated layer on Si substrate	0.88×10^{-6}	Hurst et al. ^[181]
Polysilicon on suspended polysilicon diaphragm	1.5×10^{-6}	Kalvesten et al. ^[212]
Single-walled carbon nanotube on Al_2O_3 membrane	$\sim 1 \times 10^{-4}$	Stampfer et al. ^[213,214]

pressure difference $|P_{\text{in}} - P_{\text{ex}}|$ acting on the membrane is supposed to be lower than the pressure difference ΔP_{ex} initially set in the test cell (which was used to compute the sensitivity). This is because of the variation of the microcavity volume upon bulging, leading to changes of its internal pressure P_{in} . The resistive sensitivity of the membrane to a pressure difference was hence underestimated. Still, this effect is accounted for in our theoretical model approximating the sensor transfer function (cf. section 5.2.1).

5.2.5 Conclusions and Outlook

In this project we demonstrated the first application of a GNP membrane in a pressure sensor, acting both, as diaphragm and strain-sensitive transducer with facile resistive readout. The sensor showed an impressive sensitivity, which is presumably due to the flexibility and comparably high gauge factor of the GNP membrane. However, considering our theoretical model we estimated a gauge factor of $g = 7$ for the 6DT cross-linked GNP composite material, which is slightly below values for 9DT cross-linked GNP films on flexible substrates, ranging between 10 and 20.^[58] In the literature gauge factors reaching up to ~ 200 were reported for GNP composites.^[50] We suggest that gauge factors higher than observed in this study — and hence an increased pressure sensitivity — can be achieved by incorporation of larger GNPs (see section 3.2.3). Further, by reducing the membrane thickness, stronger deflections due to applied pressure differences are expected, again improving the device sensitivity. The order of the GNPs in the membrane materials should also influence the gauge factor, as disordered membranes are able to respond to stress more easily by local rearrangements, microcrack formation and local relaxation, impairing the interparticle distance changes leading to resistivity increase. Regarding substrate-supported GNP strain gauges, Farcau et al. observed the highest sensitivities for monolayered GNPs.^[59] Hence, the use of monolayered GNP membranes could also be favorable. Recently, a study on electromechanical sensing in freestanding monolayered GNP membranes was published by Gauvin et al.. The group reported gauge factors of 109 ± 21 and 78 ± 17 for $20 \mu\text{m}$ and $5 \mu\text{m}$ diameter circular membranes (particle size: 7 nm), respectively, by probing them using AFM force spectroscopy and conductive AFM simul-

taneously.^[42] Thus, by these adjustments it should be possible to improve the sensitivity of the device.

While the flexibility and strain sensitivity of GNP composite membranes is favorable for the device sensitivity, one drawback concerning the use as diaphragms in MEMS/NEMS pressure sensors is their permittivity for vapors and gases.^[171] Especially in the case of sealed pressure sensors this attribute leads to equilibration of pressure between the exterior and the reservoir over time, compromising the detection of slow pressure changes and the stability of the measurements. Current studies in our group address the reduction of the composites' permeability for gases and vapors, e.g. by introducing diffusion barrier layers. Potential candidates could be alumina layers deposited by atomic layer deposition (ALD). Such layers were employed as gas barriers for enhancing the reliability of GNP based strain gauges by protecting them from influences of humidity.^[209]

In conclusion, this project highlights the potential of nanoparticle composites as functional materials in novel MEMS and NEMS pressure sensing devices.

5.2.6 Publication: Resistive Pressure Sensors Based on Freestanding Membranes of Gold Nanoparticles

Reprinted from “Resistive pressure sensors based on freestanding membranes of gold nanoparticles”, H. Schlicke, M. Rebber, S. Kunze, T. Vossmeier, *Nanoscale* **2016**, *8*, 183-186^[2] with permission from The Royal Society of Chemistry.

The corresponding ESI is reprinted in section A.1.1, pages 184ff.



Cite this: *Nanoscale*, 2016, **8**, 183

Received 7th October 2015,
Accepted 28th November 2015

DOI: 10.1039/c5nr06937h

www.rsc.org/nanoscale

Resistive pressure sensors based on freestanding membranes of gold nanoparticles†

Hendrik Schlicke, Matthias Rebber, Svenja Kunze and Tobias Vossmeier*

In this communication the application of gold nanoparticle membranes as ambient pressure sensors with electromechanical signal transduction is demonstrated. The devices were fabricated by sealing microstructured cavities with membranes of 1,6-hexanedithiol cross-linked gold nanoparticles, which were electrically contacted by metal electrodes deposited on both sides of the cavities. Variations of the external pressure resulted in a deflection of the membranes and, thus, increased the average interparticle distances. Therefore, the pressure change could easily be detected by simply monitoring the resistance of the membranes.

Due to their tunable electronic, mechanical and optical properties, freestanding membranes of gold nanoparticles (GNPs) capped with monofunctional ligands, interlinked with bi- or multifunctional molecular cross-linkers or embedded in polymer matrices are promising candidates for the application as functional materials in micro- and nanoelectromechanical systems (MEMS/NEMS). In contrast to conventional silicon based MEMS/NEMS requiring elaborate multi-step lithographic fabrication schemes, noble metal nanoparticle composites can be fabricated and deposited by cost-effective procedures such as spin-coating, ink-jet printing,^{1,2} stamping³ and are compatible with a broad variety of rigid or flexible substrate materials.

Recently, a series of MEMS/NEMS applications was demonstrated by several research groups. Kanjanaboos *et al.* demonstrated the fabrication of microscale drumhead resonators from freestanding monolayers of monothiol-capped GNPs with resonance frequencies in the MHz range.⁴ Tsukruk and co-workers reported the fabrication of Golay type IR microimagers based on nanocomposite GNP/polymer membranes deposited on microcavities.⁵ The group also presented the application of freestanding membranes of polymer-encapsulated GNPs as

pressure gauges.⁶ However, optical readout techniques of the membrane deflection were applied in all cases. More recently, we reported on the first electrostatic actuator based on a free-standing membrane of alkanedithiol (ADT) cross-linked GNPs.⁷

GNP membranes cross-linked using dithiols offer the ability to adjust the conductivity over several orders of magnitude.^{8,9} Using shorter-chain ADTs, fairly good conductivities can be achieved. Analogously to thin films of monothiol-capped GNPs deposited on flexible substrates,¹⁰ the charge transport through assemblies of ADT cross-linked GNPs is sensitive to strain, directly affecting the interparticle distances and impeding tunnel currents. Based on this behavior, the applicability of substrate supported dithiol cross-linked GNP films as sensitive strain gauges with gauge factors G_s of 10–20 was demonstrated.^{11,12}

Previously, freestanding membranes of highly ordered GNP monolayers were fabricated and their remarkable elastic properties were probed by AFM indentation measurements.^{13,14} Si *et al.* reported the fabrication of freestanding monolayer sheets from Au@Ag nanocubes, which could be lithographically milled into nanoribbons or folded into 3d origami.¹⁵ In a recent study¹⁶ we reported on the fabrication of freestanding 1,9-nonanedithiol (9DT) cross-linked GNP membranes on circular apertures (~100 μm diameter) and the characterization of their viscoelastic properties by AFM micro-bulge tests.¹⁷ The Young's modulus was measured in the low GPa range and it was demonstrated that these membranes withstand pressure loadings of several kPa, corresponding to a biaxial stress of tens of MPa.¹⁶ These mechanical properties together with their electric conductivity make crosslinked gold nanoparticle membranes interesting functional materials for MEMS/NEMS applications.

In this communication we present the fabrication of resistive pressure gauges employing a 1,6-hexanedithiol (6DT) cross-linked GNP membrane as strain sensitive transducer. To the best of our knowledge, this is the first report on sensors utilizing the unique electromechanical properties of a free-standing nanoparticle membrane to enable a direct and simple resistive signal readout.

Institute of Physical Chemistry, University of Hamburg, Grindelallee 117, 20146 Hamburg, Germany. E-mail: tobias.vossmeier@chemie.uni-hamburg.de;
Fax: +49 40 42838 3452; Tel: +49 40 42838 7069

† Electronic supplementary information (ESI) available. See DOI: 10.1039/c5nr06937h

For fabricating the sensor devices, GNP membranes were deposited onto 3d microstructures featuring rectangular cavities, typically of $\sim 40\ \mu\text{m}$ in width and $\sim 500\ \mu\text{m}$ in length. The microstructures were prepared from SU-8, a negative tone photoresist commonly used for the fabrication of MEMS structures,^{18,19} using standard photolithography on thermally oxidized silicon wafers (oxide thickness 300 nm). The depth of the cavities ($\sim 40\ \mu\text{m}$) could be trimmed by varying the resist layer thickness. In proximity to the long sides of the cavities, gold or platinum electrodes ($\sim 40\ \text{nm}$ thickness) were deposited for measuring the resistance of the freestanding membrane sections. A schematic showing the device architecture is presented in Fig. 1a. Fig. 1b shows a SEM image of the microcavity prepared in SU-8 resist with proximal metal electrodes, before depositing the nanoparticle membrane. A detailed description of the microstructure fabrication process is provided in the ESI†

6DT cross-linked GNP membranes were fabricated by spin-coating a heptanoic solution of GNPs (diameter $(3.5 \pm 0.7)\ \text{nm}$) and a methanolic solution of 6DT alternately onto a glass substrate, as reported earlier.²⁰ The resulting GNP films showed a typical conductivity of around $0.1\ \text{S cm}^{-1}$.⁷ Thicknesses of the films were measured by atomic force microscopy (AFM).²⁰ A TEM image revealing the granular structure of the 6DT cross-linked GNP membrane is shown as inset in Fig. 1a. See the ESI† for a representative absorbance spectrum, a current-voltage (I - V) measurement, and an AFM scan of the substrate supported GNP film used for device fabrication.

Following deposition, the cross-linked GNP films were transferred from their initial substrates by floating them on demineralized water.²⁰ After an incubation period of up to two days at ambient conditions, the membranes could easily be lifted off their glass substrates by carefully immersing the latter into water. Doing this, the membranes detached from the substrates and remained floating at the liquid-air interface. Subsequently, the electrode microstructures were used to skim the membranes from the water surface. While the samples were allowed to dry, the membranes settled to the 3d structures and remained freestanding over the rectangular cavities. The substrates were then fixed onto custom-designed printed circuit boards, contacted and transferred to a custom-built pressure cell. A Keithley 2601A source measure unit was employed to source a constant voltage of 1 V across the device and to measure the resulting current. The pressure cell was equipped with a cascade of valves, suitable for applying pressure transients in a range of $\pm 10\ \text{kPa}$, relative to ambient pressure. As reference sensor a digital pressure gauge (Sensor-technics HDIM100DBF8P5) was connected to the cell. Details of the setup can be found in the ESI.†

Fig. 1c shows the optical micrograph of a device with a 6DT cross-linked GNP membrane (55 nm thickness) spanning the rectangular microfabricated cavity. Also the gold electrodes ($\sim 300\ \mu\text{m}$ width, $\sim 80\ \mu\text{m}$ distance), covered by the membrane are clearly recognized. An initial resistance of 259 k Ω was determined for this device, corresponding to a sheet resistance of $R_s = 0.95\ \text{M}\Omega$. Compared to conventional metal foil strain

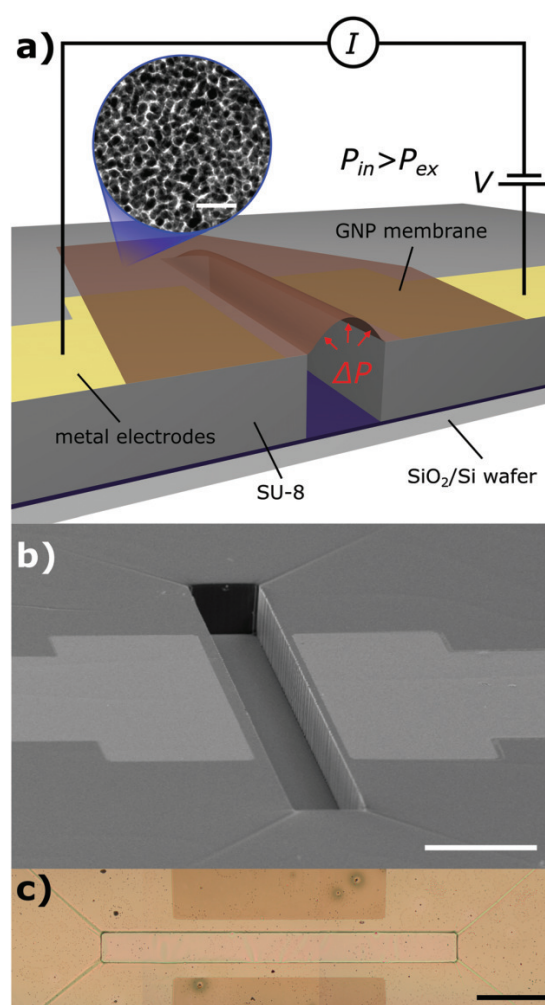


Fig. 1 (a) Schematic showing a cross-sectional view of a GNP membrane based pressure sensor. The GNP membrane is sealing the cavity microstructured into SU-8 photoresist. Electrodes deposited onto the SU-8 layer are used to monitor the membrane's resistance under applied pressure loading. The inset shows a TEM image of a 1,6-hexanedithiol cross-linked GNP membrane (scale bar: 25 nm). (b) SEM image of a microcavity with proximal metal electrodes prior to membrane deposition. Scale bar: 100 μm . (c) Optical micrograph of a 6DT cross-linked GNP membrane deposited onto a 3d electrode microstructure. Scale bar: 100 μm .

gauges the significantly higher resistance of GNP based transducers allows for operating the devices under lower power dissipation.¹⁰ Additionally, it is straightforward to adjust the sheet resistance for specific device requirements because the resistivity of cross-linked GNP films can be tuned over several orders of magnitude by varying the size^{8,9,20} and structure²¹ of the cross-linker.

The application of positive pressure transients of up to 8 kPa resulted in pressure differences between the cavity and the

exterior, causing an inward deflection of the freestanding membrane. Movements of the membrane could clearly be observed using a microscope camera (Fig. 2a, middle). A movie

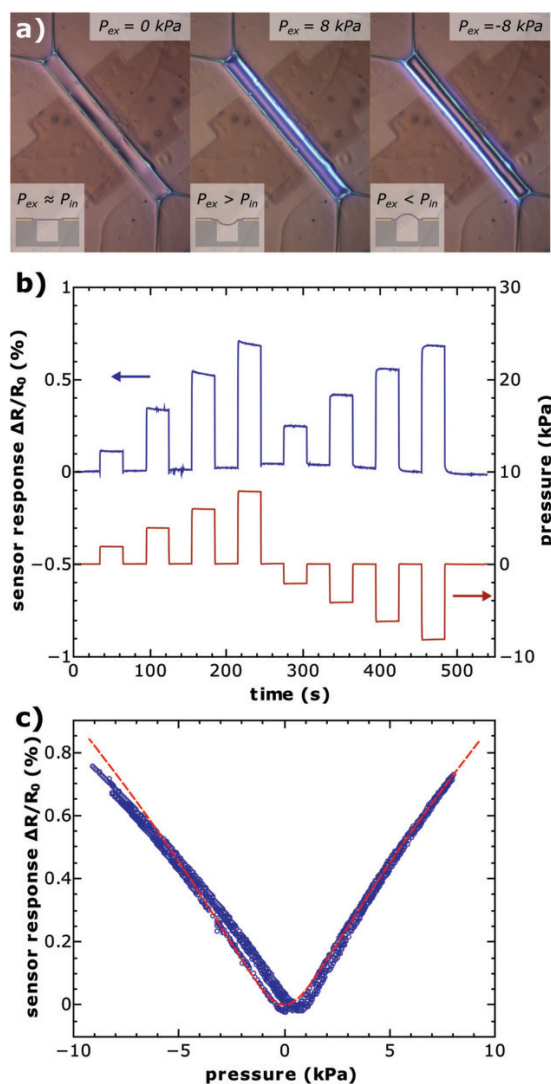


Fig. 2 (a) Optical micrographs of a pressure gauge fabricated from a 6DT cross-linked GNP membrane placed in a pressure cell under an external pressure loading of (left) 0 kPa, (center) 8 kPa and (right) -8 kPa (relative to the ambient pressure). The deflections of the membrane inwards and outwards the rectangular microcavity are observable by the reflections of the non-centered incident microscope illumination on opposite sides of the bulge. (b) Pressure transients (0 to ± 8 kPa) applied to the device (red) and resulting resistance changes relative to the baseline resistance R_0 (blue). (c) Transfer function of the device relating the applied external pressure to the measured resistance change. An estimate of the transfer function, which is based on the membrane's mechanical properties, the dimensions and geometry of the device, and a gauge factor G_s of 7, is depicted as dashed red line. Details to the underlying calculation are provided in the ESI.†

showing the periodical deflections of the nanoparticle membrane induced by the repeated pressure loadings shown in Fig. 2b can be found in the ESI.† The deflection of the membrane was accompanied by an increase in resistance as shown by the response transients in Fig. 2b. When negative external pressures of up to -8 kPa (relative to ambient) were applied again pressure differences between the cavity and the exterior were established. In this case the freestanding membrane showed outward deflections while remaining attached to the SU-8 layer surrounding the cavity (Fig. 2a, right). As expected, the device responded with a similar increase in resistance (up to $\sim 0.7\%$) for positive and negative applied pressures (see Fig. 2b), especially in the higher pressure range, resulting from similar strain experienced by the membrane in both cases, inward and outward deflection. It is to note that the device remained functional over the course of the study of several weeks.

Fig. 2c shows the sensor's transfer curves obtained by repeatedly sweeping the external pressure and continuously monitoring the current at an applied voltage of 1 V. Corresponding resistance and pressure time series can be found in the ESI.† The sensor displayed an almost linear response for the positive and negative external pressure branch. A slight offset of the response curve's minimum is observed and is attributed to a slight difference between the initial cavity pressure and the ambient pressure.

The response of the pressure sensor was estimated by taking into account the mechanical properties of 6DT cross-linked GNP membranes obtained by AFM bulge tests (ESI.†).⁷ Using this data and the device geometry, an estimate of the bulge height of the membrane in response to the applied pressure loading as well as the resulting strain could be calculated. Taking into account a constant gauge factor G_s of 7 and a residual membrane stress of 6 MPa (values in the MPa range are common for freestanding GNP membranes^{7,16}), resulted in estimates of the sensor responses which are, within the given pressure range of ± 8 kPa, very similar to the experimental data. This is clearly seen in Fig. 2c, which shows the calculated transfer function (dashed red line) in very good agreement with the experimental response curve. A detailed description of the calculation as well as simulations regarding the influences of different device parameters on the sensor's response characteristics are provided in the ESI.†

In summary, we presented the first prototype of a resistive pressure sensor based on a freestanding membrane of gold nanoparticles. A sensor response of up to $\sim 0.7\%$ was obtained for pressure changes in a range of ± 8 kPa. The measured sensor responses were found in good agreement with a simple approximate model relating the applied external pressures to the membrane strain, and assuming a gauge factor G_s of 7, similar as observed for substrate supported strain gauges based on 9DT cross-linked GNP coatings.¹¹ According to previous findings reported for strain gauges based on GNP assemblies, it should be possible to enhance the sensitivity of the presented pressure sensor by the following adjustments: first, it was demonstrated that the resistive strain sensitivity of sub-

strate-supported GNP films increased with decreasing thickness and was highest for monolayer films. This finding was attributed to the 2d confinement of conduction paths in the case of the monolayer film.²² Additionally, as shown by our model calculation provided in the ESI,† decreasing the membrane thickness increases the device's sensitivity because thinner membranes are bulged more heavily than thicker ones at a given pressure. Second, an increase of the nanoparticle size is assumed to increase the sensitivity, because the gauge factor of nanoparticle based resistive strain gauges scales with the particle diameter, as deduced from a simple geometric model.¹⁰ Third, the order of the particles in a freestanding membrane is expected to influence the strain sensitivity. Compared to a highly ordered GNP membrane a disordered membrane responds to stress more easily by local rearrangements, microcrack formation and local relaxation rather than by homogeneous changes in the interparticle distances.²³ Taken together, ultimate sensitivities should be achievable by employing membranes consisting of a single, highly ordered monolayer of relatively large GNPs. This, however, will require reducing the device's dimensions in order to avoid collapse of the membrane and to enable electrode aspect ratios allowing for practical resistance measurements. Additionally, we note that by applying a more elaborate capacitive readout of the membrane deflection, it should be possible to determine the direction of the pressure variation with respect to the internal cavity pressure.

Acknowledgements

The work of H. S. is supported by a scholarship of the Joachim Herz Foundation. T. V. acknowledges financial support by the German Research Foundation (DFG), grant number VO698/3-1. Furthermore we thank Stefan Werner for transmission electron microscopy measurements.

References

- 1 S. Fuller, E. Wilhelm and J. Jacobson, *J. Microelectromech. Syst.*, 2002, **11**, 54–60.
- 2 E. S. Park, Y. Chen, T.-J. K. Liu and V. Subramanian, *Nano Lett.*, 2013, **13**, 5355–5360.
- 3 B. Kowalczyk, M. M. Apodaca, H. Nakanishi, S. K. Smouk and B. a. Grzybowski, *Small*, 2009, **5**, 1970–1973.
- 4 P. Kanjanaboos, X.-M. Lin, J. E. Sader, S. M. Rupich, H. M. Jaeger and J. R. Guest, *Nano Lett.*, 2013, **13**, 2158–2162.
- 5 C. Jiang, M. E. McConney, S. Singamaneni, E. Merrick, Y. Chen, J. Zhao, L. Zhang and V. V. Tsukruk, *Chem. Mater.*, 2006, **18**, 2632–2634.
- 6 C. Jiang, S. Markutsya, Y. Pikus and V. V. Tsukruk, *Nat. Mater.*, 2004, **3**, 721–728.
- 7 H. Schlicke, D. Battista, S. Kunze, C. J. Schröter, M. Eich and T. Vossmeier, *ACS Appl. Mater. Interfaces*, 2015, **7**, 15123–15128.
- 8 Y. Joseph, I. Besnard, M. Rosenberger, B. Guse, H.-G. Nothofer, J. M. Wessels, U. Wild, A. Knop-Gericke, D. Su, R. Schlögl, A. Yasuda and T. Vossmeier, *J. Phys. Chem. B*, 2003, **107**, 7406–7413.
- 9 M. Brust, D. J. Schiffrin, D. Bethell and C. J. Kiely, *Adv. Mater.*, 1995, **7**, 795–797.
- 10 J. Herrmann, K. H. Müller, T. Reda, G. R. Baxter, B. Raguse, G. J. J. B. De Groot, R. Chai, M. Roberts and L. Wiczorek, *Appl. Phys. Lett.*, 2007, **91**, 183105.
- 11 T. Vossmeier, C. Stolte, M. Ijeh, A. Kornowski and H. Weller, *Adv. Funct. Mater.*, 2008, **18**, 1611–1616.
- 12 M. Segev-Bar and H. Haick, *ACS Nano*, 2013, **7**, 8366–8378.
- 13 W. Cheng, M. J. Campolongo, J. J. Cha, S. J. Tan, C. C. Umbach, D. A. Muller and D. Luo, *Nat. Mater.*, 2009, **8**, 519–525.
- 14 K. E. Mueggenburg, X.-M. Lin, R. H. Goldsmith and H. M. Jaeger, *Nat. Mater.*, 2007, **6**, 656–660.
- 15 K. J. Si, D. Sikdar, Y. Chen, F. Eftekhari, Z. Xu, Y. Tang, W. Xiong, P. Guo, S. Zhang, Y. Lu, Q. Bao, W. Zhu, M. Premaratne and W. Cheng, *ACS Nano*, 2014, **8**, 11086–11093.
- 16 H. Schlicke, E. W. Leib, A. Petrov, J. H. Schröder and T. Vossmeier, *J. Phys. Chem. C*, 2014, **118**, 4386–4395.
- 17 A. Turchanin, A. Beyer, C. T. Nottbohm, X. Zhang, R. Stosch, A. Sologubenko, J. Mayer, P. Hinze, T. Weimann and A. Götzhäuser, *Adv. Mater.*, 2009, **21**, 1233–1237.
- 18 E. H. Conradie and D. F. Moore, *J. Micromech. Microeng.*, 2002, **12**, 368–374.
- 19 H. Lorenz, M. Despont, N. Fahrni, N. LaBianca, P. Renaud and P. Vettiger, *J. Micromech. Microeng.*, 1997, **7**, 121–124.
- 20 H. Schlicke, J. H. Schröder, M. Trebbin, A. Petrov, M. Ijeh, H. Weller and T. Vossmeier, *Nanotechnology*, 2011, **22**, 305303.
- 21 J. M. Wessels, H.-G. Nothofer, W. E. Ford, F. von Wrochem, F. Scholz, T. Vossmeier, A. Schroedter, H. Weller and A. Yasuda, *J. Am. Chem. Soc.*, 2004, **126**, 3349–3356.
- 22 C. Farcau, H. Moreira, B. Viallet, J. Grisolia, D. Ciuculescu-Pradines, C. Amiens and L. Ressler, *J. Phys. Chem. C*, 2011, **115**, 14494–14499.
- 23 N. Olichwer, E. W. Leib, A. H. Halfar, A. Petrov and T. Vossmeier, *ACS Appl. Mater. Interfaces*, 2012, **4**, 6151–6161.

5.3 Electrostatic Actuation of GNP Membranes

Sensors and actuators are closely related, as both terms name transducers acting in opposite directions. Sensors monitor systems, and respond to chemical or physical stimuli such as heat, light, pressure or mechanical input (such as position, motion, deflection and strain) with electronic output (e.g. resistance, capacitance, voltage or current changes). In contrast, actuators perform vice versa, which commonly involves translating electronic signals into motion.^[9] Many devices also combine different functionalities, e.g. MEMS or NEMS incorporating sensing output transducers, which detect the response to a force induced by an actuating input transducer. While the first project made use of GNP membranes by utilizing their resistive strain sensitivity to electronically monitor deflection/pressure, the second project, described in the following, aimed at the fabrication of GNP membrane based actuators.

Electrostatic actuation is a versatile and established principle frequently used in MEMS and NEMS, utilized for deflecting or moving microscopic and nanoscopic structural elements.^[9,17,23,37,185,192,215] Herein we show that the concept of electrostatic actuation can be applied to freestanding nanoparticle composite structures, which is a further step towards their integration into MEMS/NEMS, enabling links to new applications, as demonstrated in consecutive projects described in this thesis.

5.3.1 Working Principle

The structure of an electrostatic GNP membrane actuator as investigated in this work is schematically depicted in figure 5.10a. The device can be viewed as a parallel plate capacitor having one fixed plate (the counterelectrode represented by the wafer), and one flexible, mobile plate (the freestanding GNP membrane suspended over a microcavity). Upon applying a voltage between the wafer and the membrane, both are oppositely charged. This induces an attractive electrostatic force that is governed by the applied voltage as well as the membrane-counterelectrode distance d . The force acts against a restoring force caused by the structural rigidity of the GNP membrane and to some extent deflects the flexible membrane into the microcavity, towards the wafer (see the sketch in figure 5.10e).

Modeling the Device Response

We developed a simple model describing the membrane deflection under varying voltage loading. The model assumes a constant, homogeneous electric field between the membrane and the counter-electrode, i.e., only small deflections of the membrane with respect to the initial distance to the wafer are considered. In this case, the electrostatic force per unit area F/A as a function of voltage V can be described by equation 5.5.

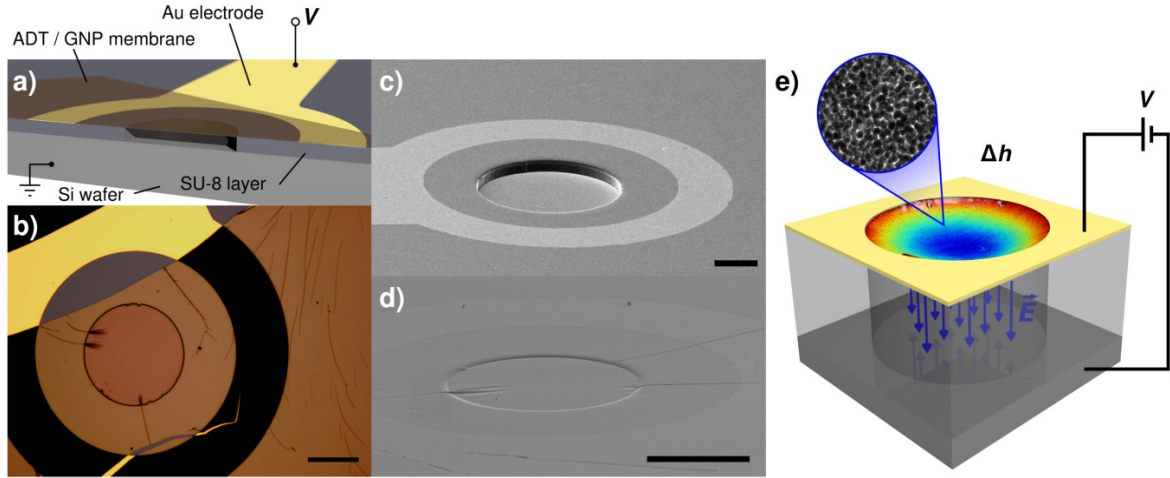


Figure 5.10: a) Schematic showing a cross-sectional view of a GNP membrane based electrostatic actuator. b) Optical micrograph of a representative GNP membrane based electrostatic actuator. Scale bar: 100 μm . c) Scanning electron micrograph of a 3D microelectrode structure, as used as support for the GNP membranes to obtain the electrostatic actuator devices. Scale bar: 60 μm . d) Scanning electron micrograph of a readily fabricated electrostatic actuator, featuring a 6DT cross-linked GNP membrane spanning the microcavity. Scale bar: 100 μm . e) Sketch depicting the working principle of a GNP membrane based electrostatic actuator. The inset shows a transmission electron micrograph of a cross-linked GNP membrane. Reprinted with permission from Ref. [1]. ©2015 American Chemical Society.

$$\frac{F}{A} = \frac{\epsilon V^2}{2d^2} \quad (5.5)$$

Here, ϵ is the permittivity of the gas (air) within the microcavity and d is the distance between the membrane and the wafer.

The central point deflection h of a membrane spanning a circular aperture can be related to the pressure difference ΔP acting on the membrane by equation 5.6, implying some constraints and simplifications. This equation is frequently used for the evaluation of bulge tests (cf. section 3.3.2).^[48,173]

$$\Delta P(h) = \frac{8Yt_m}{3a^4}h^3 + \frac{4\sigma_0 t_m}{a^2}h \quad (5.6)$$

Here, a is the aperture radius, Y is the membrane's biaxial modulus that is related to the material's elastic modulus E via the Poisson ratio ν by $Y = E/(1 - \nu)$,^[173] and σ_0 is the membrane pre-stress. Assuming small deflections of several hundreds of nanometers for circular, $\sim 200 \mu\text{m}$ sized membranes, we expect them to show a low curvature. Hence, the membrane's surface normals (in whose directions the force resulting from an applied pressure difference would act) show only little angular deviation from the field lines of an assumed homogeneous electric field induced by the application of a voltage between the almost flat membrane and the counter electrode. Hence, for our approximate model,

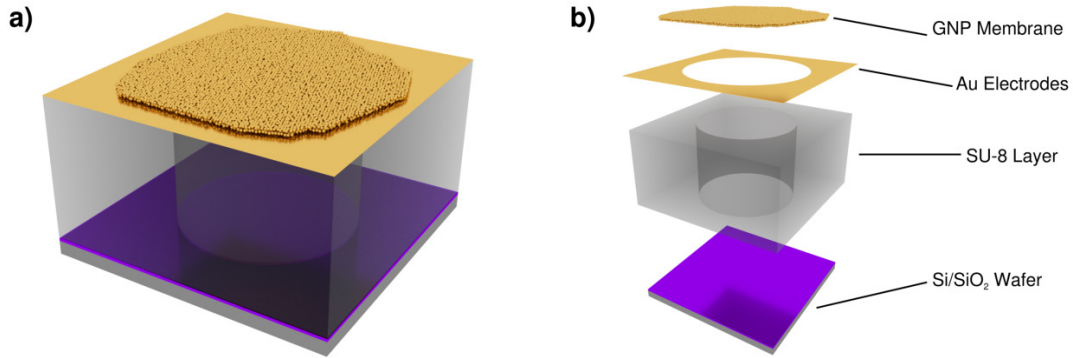


Figure 5.11: Schematic depicting the material layer composition of an electrostatic GNP membrane actuator. a) Sketch of the final device. b) Exploded view.

we assume that the electrostatic force per area given by equation 5.5 leads to similar deflections of the membrane as a pressure difference ΔP , within the limits of the above constraints. Consequently, we replace the pressure difference ΔP (in equation 5.6) by the electrostatic force per area F/A to yield equation 5.7.

$$\frac{\epsilon V^2}{2d^2} = \frac{8Yt_m}{3a^4}h^3 + \frac{4\sigma_0 t_m}{a^2}h \quad (5.7)$$

It is to note, that the electrostatic force per unit area observed in our experiments was small in comparison to common pressures applied during bulge testing^[48] and hence led to rather small deflections. Therefore, the second term on the right hand side of equation 5.7, relating to the pre-stress of the membrane and having a linear contribution of h , considerably dominates the first term having a cubic dependency on the central point deflection.

5.3.2 Device Fabrication

The structure of a device as investigated in this project is schematically depicted in figure 5.11, and a cross-sectional view is provided in figure 5.10a. Its fabrication process is very similar to the procedure used for GNP membrane based pressure sensors in the foregoing project and was introduced in section 5.1.

First, an SU-8 layer featuring cylindrical microcavities with a diameter of $\sim 200 \mu\text{m}$ was fabricated by means of photolithography on a doped silicon wafer, optionally equipped with a thermal oxide layer (see figure 5.11). As the membrane acts as one electrode in a capacitor-like setup with the doped wafer substrate acting as counterelectrode, a single electrode, placed on top of the SU-8 layer and in proximity to the edge of the microcavity is sufficient to charge the membrane and achieve a functional device. Hence, a structured gold electrode was deposited utilizing the aforementioned lift-off process.

As described in section 5.1.1, 6DT cross-linked GNP membranes were fabricated following

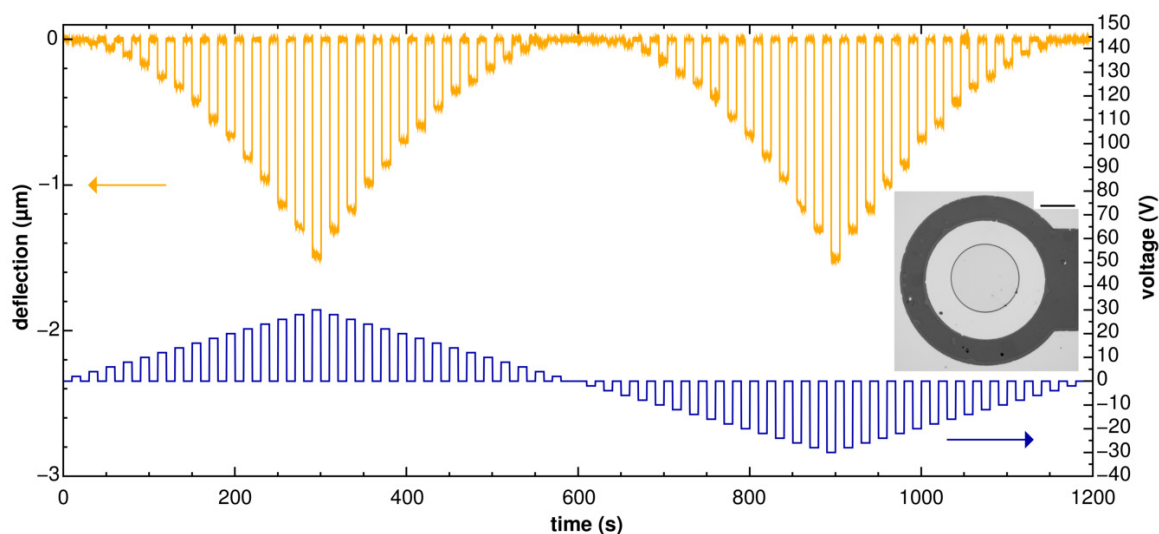


Figure 5.12: Baseline corrected, interferometrically measured central point deflection transients of a 6DT cross-linked GNP membrane actuator (membrane thickness: 33 nm, membrane diameter: $\sim 200 \mu\text{m}$), excited with pulses of varying voltages. The inset shows an optical micrograph of the respective device. Scale bar: $100 \mu\text{m}$. Reprinted with permission from Ref. [1]. ©2015 American Chemical Society.

our layer-by-layer spin-coating process, and thoroughly characterized (see the respective Supporting Information (SI) document in section A.1.2, page 201*ff*). For membrane fabrication, different GNP batches with average diameters of $(3.5 \pm 0.5) \text{ nm}$, $(3.5 \pm 0.8) \text{ nm}$ and $(3.6 \pm 0.6) \text{ nm}$ were used. The obtained GNP films had thicknesses ranging from 29 to 45 nm and showed conductivities of $\sim 0.1 \text{ S cm}^{-1}$.

Following their deposition, the membranes were detached from their initial glass substrates by flotation on water, transferred and deposited onto the microstructures by skimming as described in section 5.1.3. After drying, the membranes settled on the microstructures, remaining freestanding over the microcavities. The distance between the membranes and the wafer counter-electrodes was defined by the SU-8 layer thickness, ranging from $\sim 8 \mu\text{m}$ to $\sim 15 \mu\text{m}$ for different devices investigated in this study.

5.3.3 Device Testing

The functionality of the devices was tested by different means. On the one hand, contact mode AFM was used to track motions of the freestanding membranes using a cantilever. Further, two complementary optical techniques, i.e., confocal microscopy and laser interferometry were applied to monitor the membrane deflection under varying voltage loading. Detection by optical means has the advantage that no mechanical contact to the membrane is necessary, which might impose forces on the device and perturb the measurements. Figure 5.12 exemplarily depicts a baseline-corrected deflection time trace observed using laser interferometry when biasing a 33 nm thick, $\sim 200 \mu\text{m}$ diameter GNP membrane, freely suspended in $7.6 \mu\text{m}$ distance to its counter electrode with varying voltage pulses of

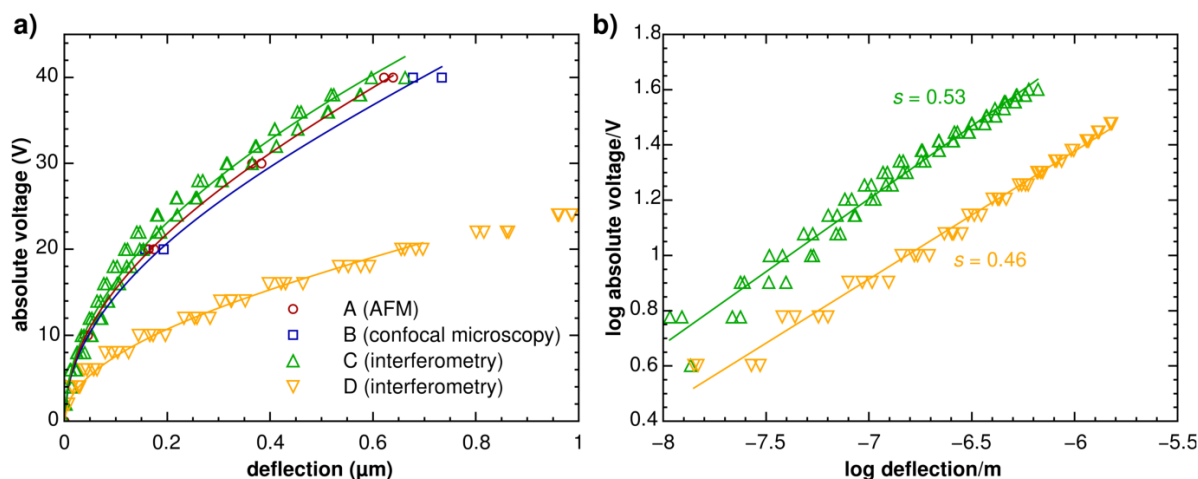


Figure 5.13: a) Voltage-deflection $V(h)$ relations determined for four different GNP membrane actuators using different methods, as indicated. The orange triangles depict datapoints extracted from the interferometric measurement depicted in figure 5.12. b) log-log plot of selected $V(h)$ datasets with linear fits. The fits are annotated with the respective slopes s . Reprinted with permission from Ref. [1]. ©2015 American Chemical Society.

up to ± 30 V. The resulting deflection transients clearly indicate the functionality of the device.

Using AFM, confocal microscopy and laser interferometry, voltage-deflection relations were determined for a total of four devices by measuring the membrane central point deflections at different applied voltages. The results of these experiments are depicted in figure 5.13. Each dataset was fitted using our model (equation 5.7), setting all geometric constraints and leaving the membrane pre-stress σ_0 the only free fit parameter. The fits yielded membrane pre-stress values in the low MPa range, which are typical for membranes comprised of organically capped GNPs^[159] or taut membranes of cross-linked GNPs.^[48] Double logarithmic plots of two $V(h)$ datasets illustrated in figure 5.13b yielded approximately linear relations. Corresponding linear fits to the data showed slopes of ~ 0.5 , indicating a relation between voltage and deflection approximately scaling with $V \propto h^{1/2}$ or $V^2 \propto h$. This underlines the dominant role of the second term in equation 5.7, implying that the membrane deflection in the given voltage range is governed by the membrane pre-stress.

5.3.4 Conclusions and Outlook

Within the project outlined in this section we demonstrated the ability to actuate conductive nanoparticle composite membranes in an electric field screened by a fixed counter electrode. The application of this versatile principle to nanoparticle composite membranes marks another important step towards their integration into MEMS and NEMS devices and forms the basis for further applications and the following projects enclosed in this work.

Microscopic structural elements, deflected by the application of electrostatic forces play a prominent role in microoptoelectromechanical systems (MOEMS). MOEMS represent a rich enabling technology, created in the 1990s by the combination of microoptics and MEMS.^[215] Examples of MOEMS device are micro mirrors and scanners, tiltable micro-fabricated mirrors with a lateral size in the micrometer range. The orientation of these mirrors can be adjusted by electrostatic forces, and their deflection can be used to direct incident light. Such devices play a significant role in display technology or optical switching in telecommunication.^[13,216,217] Returning to our GNP membrane based electrostatic actuator, it is of potential interest to couple the optical properties of GNP membranes, which are in the visible wavelength range dominated by plasmonics, to electronically induced mechanical motion or strain. One could also imagine a device, similar as presented in this study, wherein electrostatic forces are used to accurately tune the distance, and hence the optical path length between a semitransparent, partially reflective nanoparticle composite membrane and a reflective back electrode to control interference effects. Such effects were observed by Cartamil-Bueno et al. for graphene sheets, freely suspended closely above a reflective silicon wafer. They proposed an interference-based colorimetry technique to monitor pressure-induced deflections of the graphene membranes and further suggested applications as interferometric modulator displays.^[20]

Besides potential applications in optics, the response of GNP composite materials to electrostatic forces could be used to probe their mechanical properties, or to monitor changes of the latter caused by variations in the environment. Within the fourth project summarized in this chapter, as well as in an unpublished study described in section 6.3.2, we demonstrate chemical sensors based on this principle.

Another important result of the aforementioned experiments is the conclusion drawn from the voltage-deflection behavior of the electrostatic actuators. Here, the electrostatically induced deflection of GNP membranes deposited onto microcavities is presumably governed by the membrane's pre-stress. This pre-stress should in turn also make the membranes behave as drumheads having distinct vibrational modes, observable at their respective resonance frequencies. Electrostatic actuation by AC voltages could potentially be used to impose periodically varying forces on the membranes exciting of such oscillations. These considerations directly connect to the consecutive project described in the next section, covering the investigation of the oscillatory behavior of electrostatically driven GNP membrane based drumhead resonators.

5.3.5 Publication: Freestanding Membranes of Cross-Linked Gold Nanoparticles: Novel Functional Materials for Electrostatic Actuators

Reprinted with permission from “Freestanding Membranes of Cross-Linked Gold Nanoparticles: Novel Functional Materials for Electrostatic Actuators”, H. Schlicke, D. Battista, S. Kunze, C. J. Schröter, M. Eich, T. Vossmeier, *ACS Appl. Mater. Interfaces* **2015**, *7*, 15123-15128.^[1] Copyright ©2015 American Chemical Society.

The corresponding SI is reprinted in section A.1.2, pages 201ff.

Freestanding Membranes of Cross-Linked Gold Nanoparticles: Novel Functional Materials for Electrostatic Actuators

Hendrik Schlicke,[†] Daniela Battista,^{†,‡} Svenja Kunze,[†] Clemens J. Schröter,[†] Manfred Eich,[§] and Tobias Vossmeier^{*,†}

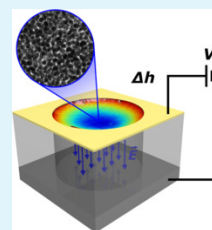
[†]Institute of Physical Chemistry, University of Hamburg, Grindelallee 117, 20146 Hamburg, Germany

[§]Institute of Optical and Electronic Materials, Hamburg University of Technology, Eissendorfer Strasse 38, 21073 Hamburg, Germany

Supporting Information

ABSTRACT: Their tunable electrical, optical, and mechanical properties make freestanding membranes of organically cross-linked gold nanoparticles (GNPs) interesting materials for applications in micro- and nanoelectromechanical systems. Here, we demonstrate the application of α,ω -alkanedithiol-cross-linked GNP membranes as electrostatically driven actuators. The devices were fabricated by depositing these membranes (thickness 29–45 nm) onto cylindrical cavities (diameter $\sim 200\ \mu\text{m}$; depth $\sim 8\text{--}15\ \mu\text{m}$), which were lithographically patterned in a SU-8 resist. Applying voltages of up to $\pm 40\ \text{V}$ across the membrane and the silicon substrate deflected the membranes by several hundreds of nanometers, as measured by atomic force microscopy, confocal microscopy, and interferometry. A simple electrostatic model, which takes into account the membranes' mechanical properties, was used to interpret the experimental data.

KEYWORDS: freestanding, membrane, gold, nanoparticle, MEMS, NEMS, actuator, electrostatic



Composite materials containing metal or semiconductor nanoparticles are of considerable interest for the fabrication of micro- and nanoelectromechanical systems (MEMS/NEMS). Their electronic, magnetic, mechanical, and optical properties can be adjusted and tuned for specific target applications.^{1–6} Further, these materials enable the cost-efficient fabrication of devices via laser writing, printing, and self-assembly techniques on various substrates.^{7–11}

Recently, the mechanical properties of freestanding membranes comprised of ligand-stabilized gold nanoparticles (GNPs),^{12,13} cross-linked GNPs,¹⁴ or polymer/GNP composites¹⁵ have been studied in different laboratories using atomic force microscopy (AFM) indentation or micro bulge tests. These investigations showed that GNP membranes are mechanically surprisingly robust. Furthermore, thermally excited and piezo-driven resonators based on GNP monolayers have been demonstrated, and their possible application as sensors has been proposed.¹⁶ However, electrostatic actuation of such GNP membranes has not been demonstrated, so far, although this mode of actuation is a fundamental and widely used operating principle in MEMS.

The focus of our present work is on composite membranes of alkanedithiol (ADT)-cross-linked GNPs with thicknesses in the 20–100 nm range, which were fabricated via facile layer-by-layer spin-coating. The mechanical stability of these membranes allows for their transfer from their initial substrates onto various 3d microstructures to produce freestanding membranes.¹⁷ This was demonstrated in a recent study, in which we investigated the material's elastic and viscoelastic properties via AFM bulge tests and measured a Young's modulus of $\sim 2.5\ \text{GPa}$ for 1,9-nonanedithiol-cross-linked GNP membranes.¹⁴ In principle, the

unique mechanical, optical, and charge-transport properties of GNP composites can be tuned by adjusting the particle size and shape or the size and structure of the cross-linker. For example, because charge transport in these membranes relies on thermally activated tunneling, the conductivity can be tuned over several orders of magnitude simply by using different length ADT linkers to tune the interparticle distances.^{17–19} By using conjugated dithiocarbamate cross-linkers, it was even possible to yield metallic conductivity.²⁰ In addition, such tuning of the conductivity is accompanied by significant shifts of the plasmon absorbance band in the visible and near-IR spectral ranges. Current studies in our group investigate the influence of the cross-linker's size and structure on the mechanical properties of GNP membranes. Altogether, their tunable electronic, optical, and mechanical properties make GNP membranes a highly promising novel material for MEMS/NEMS applications.

In this study, we present an electrostatic actuator exploiting the flexibility and conductivity of a GNP membrane as a functional material. To the best of our knowledge, this is the first demonstration showing electrostatic actuation of a conductive GNP membrane.

In principle, a freestanding section of a dithiol-interlinked GNP membrane, which acts as one electrode, is brought into close proximity to a silicon wafer representing the back electrode. By application of a potential difference, the elastic

Received: March 27, 2015

Accepted: July 6, 2015

Published: July 6, 2015



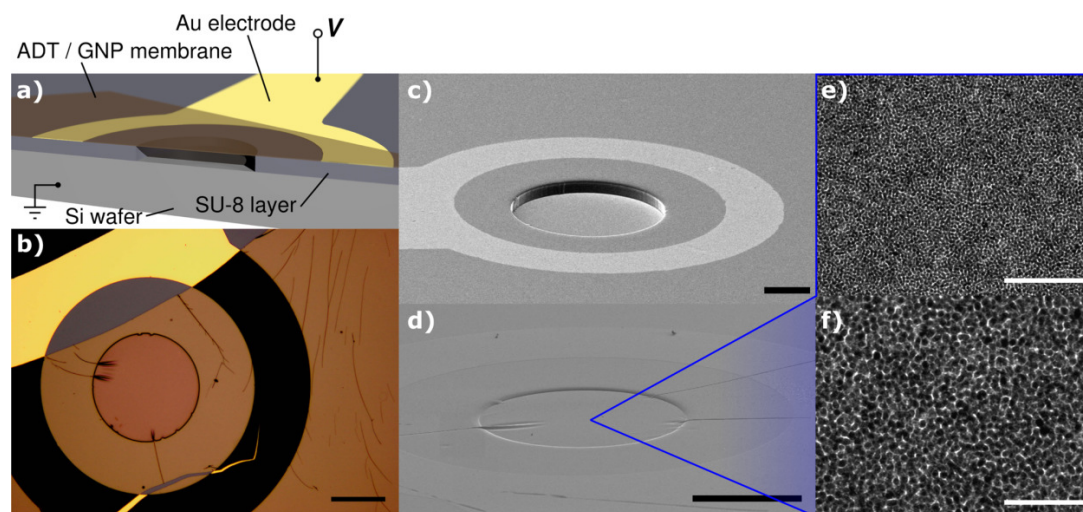


Figure 1. (a) Schematic showing a cross-sectional view of the electrostatic actuator with an ADT-cross-linked GNP membrane deposited onto the ring-shaped top electrode. (b) Representative optical micrograph of such an electrostatic actuator. Scale bar: $100\ \mu\text{m}$. (c) SEM micrograph of the 3d-microstructured SU-8 resist having a cylindrical cavity with a ring-shaped top electrode. Scale bar: $60\ \mu\text{m}$. (d) SEM micrograph of an electrostatic actuator with a deposited 6DT-cross-linked GNP membrane spanning the cylindrical cavity. Scale bar: $100\ \mu\text{m}$. (e and f) Representative TEM micrographs of a 6DT-cross-linked GNP membrane. Scale bars: 100 and 50 nm, respectively.

membrane is deflected toward the latter by electrostatic forces resulting from opposite charging. Figure 1a schematically depicts a cross-sectional view of the electrostatic actuator. A SU-8 layer having a circular cavity equipped with a ring-shaped gold electrode was microfabricated on a doped silicon wafer (Figure 1c), and subsequently an ADT-cross-linked GNP membrane was deposited onto the 3d structure and remained freestanding above the microcavity (Figure 1b,d).

Initially, doped silicon substrates with a native oxide layer (p/B-doped, $1\text{--}10\ \Omega\ \text{cm}$) were used as back electrodes, while in later experiments, doped silicon wafers (n/Sb-doped, $0.005\text{--}0.025\ \Omega\ \text{cm}$; p/B-doped, $<0.005\ \Omega\ \text{cm}$) with a thermally grown oxide layer ($\sim 300\ \text{nm}$) were introduced. The thicker oxide layer enabled better electric insulation and, hence, suppressed parasitic direct-current conductance of the ideally purely capacitive device. Because of the low thickness of the oxide layer, its influence on the overall capacitance of the device is negligible. In the first fabrication step, a layer of SU-8 was deposited onto the back-electrode material by spin-coating. Photoresist layer thicknesses of $\sim 8\text{--}15\ \mu\text{m}$ were obtained by adjusting the spinning frequencies. SU-8 is a nonconductive³ negative-tone photoresist with high chemical and mechanical stability prevalently used for the fabrication of relief structures in MEMS.^{21,22} The SU-8 layer was patterned through standard photolithography, yielding cylindrical cavities with a diameter of $\sim 200\ \mu\text{m}$ and a depth of $\sim 8\text{--}15\ \mu\text{m}$, determined by the layer thickness. In the second step, the ring-shaped electrode structure was prepared on top of the SU-8 relief structure by patterning a sacrificial, second photoresist layer (AZ nLOF 2070) with a negative image of the electrode structure. Afterward, a $\sim 100\text{-nm}$ -thick gold layer was deposited by thermal evaporation and the sacrificial photoresist layer was dissolved, baring the electrode by lifting off the gold layer from resist-coated areas. A ring-shaped electrode geometry around the cavity was chosen because it ensures a constant electrical potential of the freestanding membrane area, even if the membrane should have parasitic electrical contact to the back

electrode somewhere outside the electrode ring (e.g., by unwanted deposition of the membrane at the edges of the substrate). Figure 1c shows a representative example of the 3d electrode structure. The microfabrication process is described in detail in the Supporting Information (SI).

ADT-cross-linked GNP films were prepared via deposition onto glass substrates by alternately spin-coating a heptanoic solution of 1-dodecylamine-stabilized GNPs with an average diameter of $3\text{--}4\ \text{nm}$ and a methanolic solution of the dithiol cross-linker. Upon application of multiples of these deposition cycles, the layer thickness can be adjusted in the range of $20\text{--}100\ \text{nm}$.¹⁷ The GNP films exhibited characteristic UV/vis absorption spectra featuring a pronounced plasmon band and ohmic charge-transport behavior with conductivities of around $0.1\ \text{S}\ \text{cm}^{-1}$.¹⁷ Representative UV/vis spectra and IV data can be found in the SI. Transmission electron microscopy (TEM) micrographs of a $(38 \pm 1)\text{-nm}$ -thick 1,6-hexanedithiol (6DT)-interlinked GNP membrane transferred to a carbon-coated TEM substrate are depicted in Figure 1e,f and reveal the membrane's nanoscale granular morphology. Representative TEM images of the GNPs used for film preparation are provided in the SI.

Following deposition, the GNP films could be detached from their glass substrates by carefully immersing the latter into demineralized water (Millipore, $18.2\ \text{M}\ \Omega\ \text{cm}$), leaving the former floating on the liquid's surface. Afterward, the membranes were transferred to the electrode structures by skimming them off the liquid–air interface. After settling to the relief structure, the freestanding section of the membrane often showed wrinkle patterns, as are visible in Figure 1b. When the optical micrographs of the freestanding membrane sections are compared to those obtained from membranes deposited on circular $100\ \mu\text{m}$ apertures for bulge test experiments in an earlier study, there was no slack observable. The appearance resembled taut membranes, with positive residual stress in the low megapascal range.¹⁴

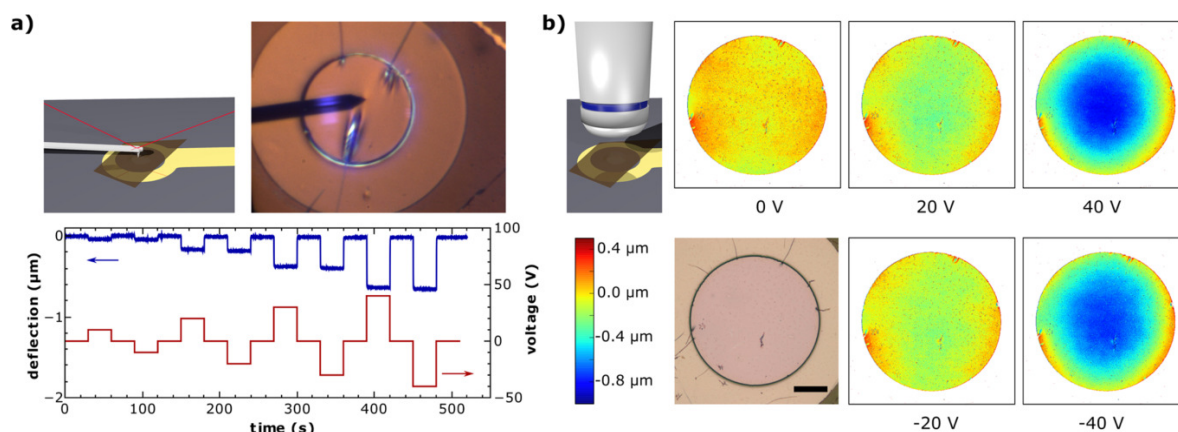


Figure 2. (a) Schematic of the AFM experiment used for probing the deflections of the actuator's 6DT-cross-linked GNP membrane (top, left). Optical micrograph acquired during the AFM experiment (cavity diameter ~ 200 μm ; membrane thickness 45 nm; top, right). Recorded voltage and deflection traces (bottom). (b) Schematic of the actuator investigated by confocal microscopy (top, left). Optical micrograph of a 6DT-cross-linked GNP membrane (29 nm thickness) spanning the actuator's cylindrical cavity (bottom, left). Scale bar: 50 μm . Color-coded deflection maps recorded at different bias voltages as indicated (top and bottom).

Voltages of up to $|V| = 40$ V were applied to the membrane and back electrode to probe the devices' functionality. Figure 2a depicts a schematic and an optical micrograph of a 6DT/GNP-membrane-based actuator (device A) in an AFM setup. As determined by AFM, this membrane had a thickness of 45 ± 1 nm (see the SI).

The deflection of the membrane corresponding to different applied voltages was captured by AFM. As depicted in Figure 2a, an AFM probe (OSCM-PT, $0.5\text{--}4.4$ N m^{-1}) was positioned close to the center on the membrane's surface in contact mode, and the membrane deflection was subsequently measured as a function of time. Voltages between -40 and $+40$ V were applied to the membrane in 30 s pulses, spaced by a 0 V delay of another 30 s. The figure shows time traces of the measured membrane deflection and the voltage applied to the sample. The deflection signal has a rectangular shape with steeply rising and falling edges, indicating a fast and reversible response of the actuator to the voltage signal. It should be noted that the measured deflections show no significant dependence on the bias direction. This is expected because the total charge and, hence, effective force only depend on the absolute value of the applied voltage. When the highest voltage of ± 40 V was applied, the deflection of the membrane was ~ 0.6 μm .

An optical micrograph of another actuator (device B), based on a (29 ± 1) -nm-thick 6DT-cross-linked GNP membrane, is depicted in Figure 2b. The membrane shows fewer defects and wrinkles, and its deflection forced at different voltages was captured using a confocal microscope (Zeiss LSM700). Because this technique is a noncontact method, it is complementary to the AFM characterization, as described above. The obtained topographic images were leveled with respect to the measured height values of the SU-8 layer surrounding the freestanding membrane section and are presented in Figure 2b as color-coded deflection maps. The data indicate a pronounced deflection of the membrane center of ~ 0.2 and ~ 0.7 μm at applied voltages of $|V| = 20$ and 40 V, respectively. As in the AFM experiments, very similar deflections were measured when the bias direction was reversed. These results clearly demonstrate the functionality of the electrostatic actuators

comprising organically cross-linked GNP membranes as active components.

In order to interpret the voltage-dependent deflection of the GNP membranes, we consider the following simple model:

Ideally, the actuator presented in this work can be viewed as a parallel-plate capacitor, with the GNP membrane and the silicon wafer representing the two electrodes. The capacitance of the freestanding membrane section is given by $C = A\epsilon/d$, where A is the freestanding membrane area, d is the distance separating the plates, and ϵ is the permittivity of the dielectric (air). Application of a bias voltage V to the device results in charging of the membrane and back electrode with a charge $|\pm Q| = CV$.

In a first approximation, the force F per unit area acting on the membrane can hence be obtained by taking into account the homogeneous electric field $E = Q/2A\epsilon$ of one electrode screened by the charge density (Q/A) of the second electrode. Implication of the capacitance term for a parallel-plate capacitor yields eq 1.

$$\frac{F}{A} = \frac{Q}{A}E = \frac{Q^2}{2A^2\epsilon} = \frac{C^2V^2}{2A^2\epsilon} = \frac{\epsilon V^2}{2d^2} \quad (1)$$

Assuming a distance of $d = 10$ μm between the membrane and the back electrode, an applied bias voltage of $V = 40$ V, and a permittivity of $\epsilon \approx \epsilon_0$ for air, a force per area of $F/A = 71$ Pa acting on the membrane can be estimated. The force F is assumed to act along the electric field lines, i.e., orthogonal to the membrane's surface, pulling the membrane inward, into the cylindrical cavity.

While the electrostatic pressure acting on the membrane can be estimated by applying the simple electrostatic model outlined above, a relation describing the membrane deflection as a function of the bias voltage is more delicate to find. Here, we use an approach that is commonly applied for the interpretation of bulge test data. Bulge testing is a common procedure to study a material's elastic and viscoelastic properties. When this method is applied, a thin film of the material is deposited onto a substrate with a defined aperture and inflated by the application of varying overpressure. By

analysis of the resulting pressure–deflection data, information on the sample's mechanical properties is obtained.

A simple model describing the relationship between the applied pressure P and the central point deflection h of the bulged circular membrane is given by eq 2.²³ In good agreement with the experimental results,¹⁴ it is based on the assumption of a spherical bulge geometry.

$$P(h) = \frac{8Yt}{3a^4}h^3 + \frac{4\sigma_0 t}{a^2}h \quad (2)$$

In this equation, t is the film thickness, a is the aperture radius, Y is the biaxial modulus of the membrane material, and σ_0 its residual stress, which may be positive or negative for membranes in a taut or slack initial state, respectively. The above equation holds for small deflections ($h \ll a$) and low film thicknesses ($t \ll h$). The former constraint, which is fulfilled for our membranes measuring $\sim 200 \mu\text{m}$ in diameter and showing high nanometer-range deflections when biased with voltages up to 40 V, also implies that the membrane shows a fairly low curvature. Hence, the membrane's surface normals (in whose direction the force caused by an applied pressure would act) show only very little angular deviation from the electric field lines of an assumed homogeneous field applied between the almost flat membrane and the back electrode.

Therefore, we assume that the force per unit area acting on the membrane, originating either from the applied overpressure in a bulge test or from a homogeneous electric field as in the presented actuators, leads—under the above constraints and in a first approximation—to similar deflections. We, hence, replace the overpressure P by the voltage-dependent F/A term given in eq 1.

$$\frac{\varepsilon V^2}{2a^2} = \frac{8Yt}{3a^4}h^3 + \frac{4\sigma_0 t}{a^2}h \quad (3)$$

It should be noted that this model neglects changes in the electric field originating from membrane movement and deformation, which can be significant in the case of larger deflections. Eventually, the above relationship between the applied voltage V and the central-point deflection h is based on several approximations, but it is expected to provide a useful description of increasing membrane deflections with increasing bias voltage, especially in the range of small deflections, with $h \ll d$, $h \ll a$, and $t \ll h$.

Figure 3a shows plots of the $V(h)$ data of actuators A and B depicted in Figure 2. To enable a more detailed analysis of the actuators' voltage–deflection behavior, the functionality of two further devices, C and D, was investigated. For these measurements, which were performed using an interferometric MEMS analyzer (Nanovibration Analyzer NA, SIOS Messtechnik GmbH), the membranes were deflected by applying voltages ranging from 0 to ± 40 V and from 0 to ± 30 V in steps of 2 V, respectively (see the SI). A clear nonlinear dependence is observed with deflections of up to several hundreds of nanometers for all devices. Also, fits of eq 3 to the data sets are depicted as solid lines. For these fits, a biaxial modulus for the 6DT-cross-linked GNP membranes of 8.9 GPa was implied, as determined by AFM bulge test experiments (see the SI). The membrane–wafer distance d was approximated as the SU-8 layer thickness, measured by profilometry or imaging of the SU-8 layer cross section by scanning electron microscopy (SEM), and the thickness t of the respective membrane was determined by AFM (Table 1 and the SI). The only remaining free-fit

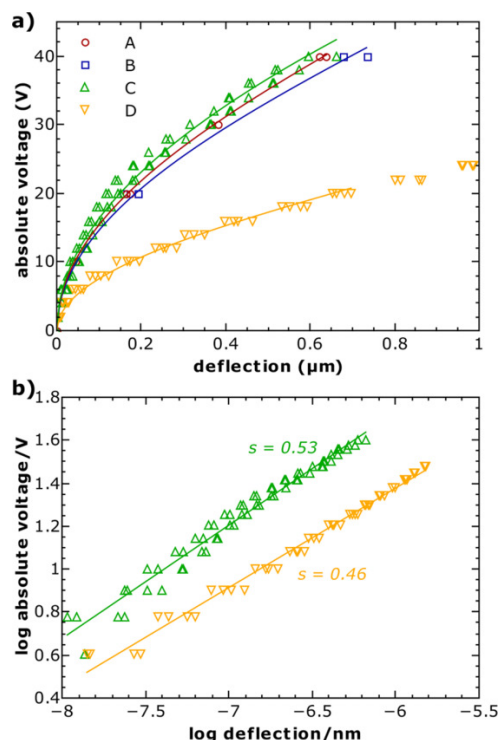


Figure 3. (a) Plots of the voltage–deflection relationship measured for the electrostatic actuator devices A and B shown in Figure 2a,b, as well as devices C and D, measured by interferometry. The solid lines represent fits of eq 3 to the respective data sets. The membranes had a diameter of $\sim 200 \mu\text{m}$; other device parameters are presented in Table 1. (b) log/log plot of the $V(h)$ relationship found for devices C and D with linear fits (s denotes the slope of the fits).

Table 1. Device Parameters of Actuators A–D

device	membrane thickness t / nm	SU-8 thickness d / μm	residual stress σ_0 / MPa
A	45 ± 1	13	3.4
B	29 ± 1	15	3.6
C	$37 \pm <1$	7.7	14
D	$33 \pm <1$	7.6	3.3

parameter was the residual stress σ_0 of the freestanding membrane section. Because our model assumes a constant electric field, it is not applicable for the description of large deflections. Hence, data points with deflections in the range of $>10\%$ of the SU-8 layer thickness d were omitted for the fitting procedure. As seen in Figure 3a, the fit functions are in good agreement with the measured data and returned residual stress values ranging from 3.3 to 14 MPa (Table 1). Residual stress values in the low megapascal range are typical for freestanding membranes comprised of organically capped GNPs¹³ or taut cross-linked GNP membranes¹⁴ investigated previously via AFM nanoindentation or AFM bulge tests. We attribute the deviation of the residual stress value of actuator C to the fabrication process, which involves manual transfer of the membranes onto the 3d-structured substrates. It has been observed previously that the residual stress of cross-linked GNP membranes prepared by this procedure can scatter significantly.¹⁴ As can be deduced from the device parameters listed

in Table 1, the strong deflection of device D compared to devices A and B at a given voltage is mainly due to the smaller electrode distance d . Compared to device C, the stronger response of actuator device D is essentially due to the much lower residual stress σ_0 .

In eq 3, the first term takes into account the response of an initially relaxed membrane, whereas the second term accounts for the residual stress σ_0 . With the parameters of the devices investigated and the maximum deflection considered for the fitting procedure, the residual stress term is about 1 order of magnitude larger than the first term. This dominance is also displayed by the square-root-like curvature of the $V(h)$ plots and is confirmed by plotting the data of devices C and D on a log/log scale (Figure 3b), returning slopes of 0.53 and 0.46, respectively. Thus, our model suggests that the voltage–deflection characteristic is qualitatively dominated by the residual stress of the membranes.

In conclusion, we presented the fabrication of electrostatic actuators based on organically cross-linked GNP membranes. 3d-microstructured ring electrodes were fabricated from SU-8 using standard photolithography, and the GNP films were deposited onto those structures, providing freestanding circular GNP membranes. When biasing the devices with voltages up to $|V| = 40$ V, central-point deflections of several hundreds of nanometers were measured using AFM, confocal microscopy, or interferometry. Qualitatively proving the functionality of these devices, the measured values are also in good agreement with estimations computed using a simple electrostatic model.

Our results highlight the capability of GNP membranes for future applications in MEMS/NEMS devices. Because of their conductive and flexible nature, they offer great potential for the fabrication of electrostatic actuators. By adjustment of the particle sizes as well as the size and structure of the cross-linker, these systems can be tailored regarding their mechanical, electrical, and optical properties to meet specific requirements for given applications. Current investigations aim at the excitation of similar devices by alternating voltage to enable electrostatically driven resonators, which are of interest for the development of ultrasensitive microgravimetric transducers. Here, the membranes' charge-transport mechanism, which is sensitive to strain,^{24–26} could further be exploited for the facile electronic readout of the membranes' resonance frequency, resulting in all-electronic sensing devices.

■ ASSOCIATED CONTENT

● Supporting Information

Characterization of the GNPs and substrate-supported GNP films, a detailed description of the lithographic processing methods and of the mechanical characterization of 6DT/GNP membranes by AFM bulge tests, and optical micrographs as well as voltage and deflection transients recorded during the interferometric measurements of devices C and D. The Supporting Information is available free of charge on the ACS Publications website at DOI: 10.1021/acsami.5b02691.

■ AUTHOR INFORMATION

Corresponding Author

*E-mail: tobias.vossmeier@chemie.uni-hamburg.de.

Present Address

[‡]D.B.: Chemical Sciences and Technologies, University of Milano-Bicocca, Milano, Italy.

Notes

The authors declare no competing financial interest.

■ ACKNOWLEDGMENTS

We thank Ancke Reinert for contributing to this project by device fabrication in the framework of advanced practical research placements as part of her degree program. The work of H.S. is supported by a scholarship of the Joachim Herz Foundation. M.E. acknowledges financial support from the German Research Foundation (DFG) via SFB 986 “M³” (Projects C1 and C2). T.V. acknowledges financial support by the DFG (Grant VO698/3-1).

■ REFERENCES

- (1) Damean, N.; Parviz, B. A.; Lee, J. N.; Odom, T.; Whitesides, G. M. Composite Ferromagnetic Photoresist for the Fabrication of Microelectromechanical Systems. *J. Microelectromech. Syst.* **2005**, *15*, 29–34.
- (2) Jiang, C.; McConney, M. E.; Singamaneni, S.; Merrick, E.; Chen, Y.; Zhao, J.; Zhang, L.; Tsukruk, V. V. Thermo-Optical Arrays of Flexible Nanoscale Nanomembranes Freely Suspended over Micro-fabricated Cavities as IR Microimagers. *Chem. Mater.* **2006**, *18*, 2632–2634.
- (3) Jiguet, S.; Bertsch, A.; Hofmann, H.; Renaud, P. Conductive SU8 Photoresist for Microfabrication. *Adv. Funct. Mater.* **2005**, *15*, 1511–1516.
- (4) Kandpal, M.; Sharan, C.; Poddar, P.; Prashanthi, K.; Apte, P. R.; Ramgopal Rao, V. Photopatternable Nano-Composite (SU-8/ZnO) Thin Films for Piezo-Electric Applications. *Appl. Phys. Lett.* **2012**, *101*, 104102.
- (5) Lucas, T. M.; James, K. T.; Beharic, J.; Moiseeva, E. V.; Keynton, R. S.; O'Toole, M. G.; Harnett, C. K. Wavelength Specific Excitation of Gold Nanoparticle Thin-Films. *Appl. Phys. Lett.* **2014**, *104*, 011909.
- (6) Tsai, K. L.; Ziaei-Moayyed, M.; Candler, R. N.; Hu, W.; Brand, V.; Klejwa, N.; Wang, S. X.; Howe, R. T. Magnetic, Mechanical, and Optical Characterization of a Magnetic Nanoparticle-Embedded Polymer for Microactuation. *J. Microelectromech. Syst.* **2011**, *20*, 65–72.
- (7) Bai, Y.; Ho, S.; Kotov, N. A. Direct-Write Maskless Lithography of LBL Nanocomposite Films and its Prospects for MEMS Technologies. *Nanoscale* **2012**, *4*, 4393–4398.
- (8) Fuller, S.; Wilhelm, E.; Jacobson, J. Ink-Jet Printed Nanoparticle Microelectromechanical Systems. *J. Microelectromech. Syst.* **2002**, *11*, 54–60.
- (9) Yokota, T.; Nakano, S.; Sekitani, T.; Someya, T. Plastic Complementary Microelectromechanical Switches. *Appl. Phys. Lett.* **2008**, *93*, 023305.
- (10) Park, E. S.; Chen, Y.; Liu, T.-J. K.; Subramanian, V. A New Switching Device for Printed Electronics: Inkjet-Printed Microelectromechanical Relay. *Nano Lett.* **2013**, *13*, 5355–60.
- (11) Jung, S.-H.; Chen, C.; Cha, S.-H.; Yeom, B.; Bahng, J. H.; Srivastava, S.; Zhu, J.; Yang, M.; Liu, S.; Kotov, N. A. Spontaneous Self-Organization Enables Dielectrophoresis of Small Nanoparticles and Formation of Photoconductive Microbridges. *J. Am. Chem. Soc.* **2011**, *133*, 10688–10691.
- (12) Mueggenburg, K. E.; Lin, X.-M.; Goldsmith, R. H.; Jaeger, H. M. Elastic Membranes of Close-Packed Nanoparticle Arrays. *Nat. Mater.* **2007**, *6*, 656–660.
- (13) He, J.; Kanjanaboos, P.; Frazer, N. L.; Weis, A.; Lin, X.-M.; Jaeger, H. M. Fabrication and Mechanical Properties of Large-Scale Freestanding Nanoparticle Membranes. *Small* **2010**, *6*, 1449–1456.
- (14) Schlicke, H.; Leib, E. W.; Petrov, A.; Schröder, J. H.; Vossmeier, T. Elastic and Viscoelastic Properties of Cross-Linked Gold Nanoparticles Probed by AFM Bulge Tests. *J. Phys. Chem. C* **2014**, *118*, 4386–4395.
- (15) Jiang, C.; Markutsya, S.; Pikus, Y.; Tsukruk, V. V. Freely Suspended Nanocomposite Membranes as Highly Sensitive Sensors. *Nat. Mater.* **2004**, *3*, 721–728.

- (16) Kanjanaboos, P.; Lin, X.-M.; Sader, J. E.; Rupich, S. M.; Jaeger, H. M.; Guest, J. R. Self-Assembled Nanoparticle Drumhead Resonators. *Nano Lett.* **2013**, *13*, 2158–62.
- (17) Schlicke, H.; Schröder, J. H.; Trebbin, M.; Petrov, A.; Ijeh, M.; Weller, H.; Vossmeier, T. Freestanding Films of Crosslinked Gold Nanoparticles Prepared via Layer-by-Layer Spin-Coating. *Nanotechnology* **2011**, *22*, 305303.
- (18) Joseph, Y.; Besnard, I.; Rosenberger, M.; Guse, B.; Nothofer, H.-G.; Wessels, J. M.; Wild, U.; Knop-Gericke, A.; Su, D.; Schlögl, R.; Yasuda, A.; Vossmeier, T. Self-Assembled Gold Nanoparticle/Alkanedithiol Films: Preparation, Electron Microscopy, XPS-Analysis, Charge Transport, and Vapor-Sensing Properties. *J. Phys. Chem. B* **2003**, *107*, 7406–7413.
- (19) Brust, M.; Schiffrin, D. J.; Bethell, D.; Kiely, C. J. Novel Gold-Dithiol Nano-Networks with Non-Metallic Electronic Properties. *Adv. Mater.* **1995**, *7*, 795–797.
- (20) Wessels, J. M.; Nothofer, H.-G.; Ford, W. E.; von Wrochem, F.; Scholz, F.; Vossmeier, T.; Schroedter, A.; Weller, H.; Yasuda, A. Optical and Electrical Properties of Three-Dimensional Interlinked Gold Nanoparticle Assemblies. *J. Am. Chem. Soc.* **2004**, *126*, 3349–56.
- (21) del Campo, A.; Greiner, C. SU-8: A Photoresist for High-Aspect-Ratio and 3D Submicron Lithography. *J. Micromech. Microeng.* **2007**, *17*, R81–R95.
- (22) Conradie, E. H.; Moore, D. F. SU-8 Thick Photoresist Processing as a Functional Material for MEMS Applications. *J. Micromech. Microeng.* **2002**, *12*, 368–374.
- (23) Small, M. K.; Nix, W. D. Analysis of the Accuracy of the Bulge Test in Determining the Mechanical Properties of Thin Films. *J. Mater. Res.* **1992**, *7*, 1553–1563.
- (24) Olichwer, N.; Leib, E. W.; Halfar, A. H.; Petrov, A.; Vossmeier, T. Cross-Linked Gold Nanoparticles on Polyethylene: Resistive Responses to Tensile Strain and Vapors. *ACS Appl. Mater. Interfaces* **2012**, *4*, 6151–6161.
- (25) Vossmeier, T.; Stolte, C.; Ijeh, M.; Kornowski, A.; Weller, H. Networked Gold-Nanoparticle Coatings on Polyethylene: Charge Transport and Strain Sensitivity. *Adv. Funct. Mater.* **2008**, *18*, 1611–1616.
- (26) Herrmann, J.; Müller, K.-H.; Reda, T.; Baxter, G. R.; Raguse, B.; de Groot, G. J. B.; Chai, R.; Roberts, M.; Wiczorek, L. Nanoparticle Films as Sensitive Strain Gauges. *Appl. Phys. Lett.* **2007**, *91*, 183105.

5.4 Electromechanical GNP Membrane Resonators

Microelectromechanical resonators are essential components of various presently used MEMS and NEMS. They fulfill a wide spectrum of tasks. Microresonators with capacitive transduction, as employed in this study, are used in electrometers, gravimetric sensors, gyroscopes, optical scanners, oscillators, signal filters, strain sensors and vibromotors.^[192] Resonators are also widely used in sensing, as many parameters of resonant systems are affected by external factors, such as temperature,^[218] pressure,^[31,32,219] or exposure to vapors.^[192,220] These variations can therefore go along with alterations in the oscillators' behavior. Hence, resonators can be employed to detect environmental conditions e.g. by changes in one or more of their resonance frequencies, quality factors, or as phase shifts.

Membrane resonators represent one group of microelectromechanical resonator devices. Often they are also referred to as drumhead resonators, due to their similarity with the respective instrument. The devices comprise taut membranes, suspended over microscale apertures, with distinct resonance frequencies related to resonance modes, which can be excited by different means. Recently, various groups reported the fabrication of such resonators using novel layered 2D nanomaterials, such as graphene,^[17,23,27,190] MoS₂,^[30,33,35] or black phosphorus.^[37] Also, nanoparticle composite membranes were investigated regarding their resonance behavior.^[45,46,161] However, in the latter case, excitation was performed by driving oscillations by external piezoelectric drives. In this project, we applied the principle of electrostatic actuation, as described in the foregoing section, to impose periodically alternating electrostatic forces and consequently excite resonant modes of freestanding membranes of 6DT cross-linked GNPs. The resulting oscillations were observed in the time-domain by recording deflection time traces via laser interferometry. From the data, resonant frequencies, amplitude distributions, as well as quality factors were determined and compared to theory.

5.4.1 Working Principle

A schematic of an electrostatically driven GNP membrane resonator is provided in figure 5.14d. The device is very similar to the electrostatic actuator described in the foregoing section and consists of a GNP membrane deposited onto a circular microcavity fabricated in an SU-8 layer, equipped with a top electrode for providing electronic contact to the composite. As in the case of the electrostatic actuator described in the foregoing section, the resonators were excited using electrostatic forces induced by applying voltages between the membrane and a counter electrode. From the figure it is apparent that the devices investigated in this project feature local gold back electrodes at the bottom of the microcavities on the thermally oxidized silicon substrate rather than using the whole conductive silicon wafer itself as counter electrode (as in the case of the actuator device in the foregoing section). This is supposed to result in an overall lower capacitance of the device resulting in higher impedance and lower power consumption when operating the resonator, especially at higher frequencies.

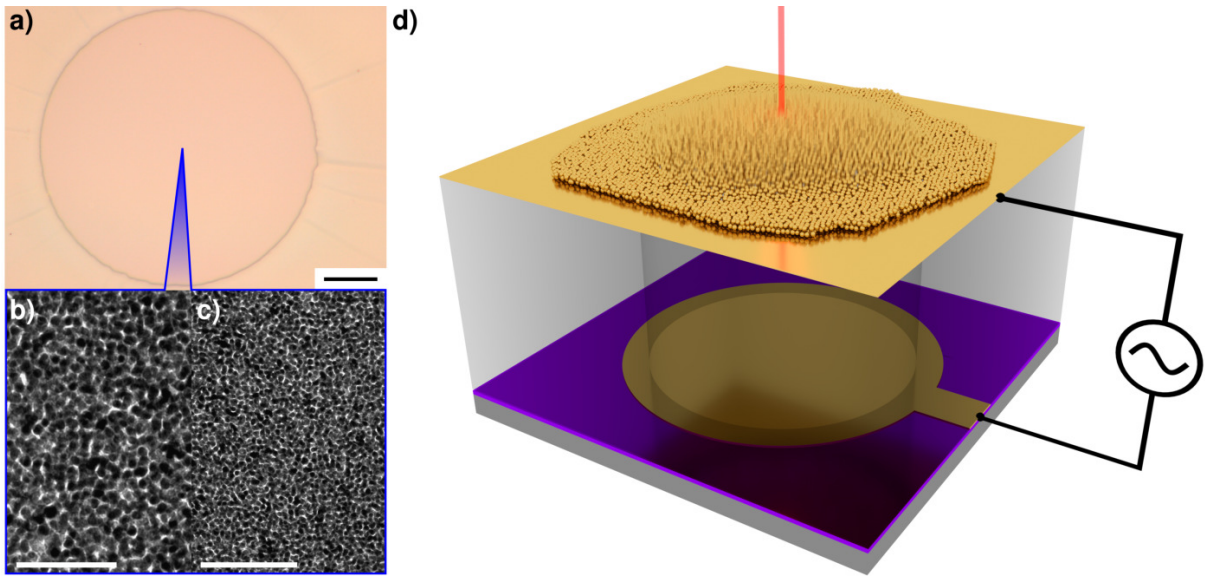


Figure 5.14: a) Optical micrograph of a GNP membrane resonator. The image shows a freestanding 6DT cross-linked GNP membrane spanning a 100 μm diameter circular cavity. Scale bar: 20 μm . b) and c) Representative transmission electron micrographs of a 6DT cross-linked GNP membrane transferred to a carbon-coated TEM substrate. Scale bars: b) 50 nm and c) 100 nm. Adapted from Ref. [2] with permission from The Royal Society of Chemistry. d) Schematic depiction of a GNP membrane resonator with an incident laser beam originating from an interferometer setup. Reprinted with permission from Ref. [4]. ©2017 American Chemical Society.

The theoretical model of a membrane resonator with negligible bending stiffness, operated in vacuum, is described in the introductory section 3.3.3. In brief, the resonance frequencies corresponding to the normal modes of circular membrane resonators under vacuum can be computed following equation 5.8.^[45,186]

$$f_{n,m} = \frac{\xi_{n,m}}{2\pi a} \sqrt{\frac{\sigma_0}{\rho}} \quad (5.8)$$

Here, a denotes the membrane/aperture radius, σ_0 and ρ represent the pre-stress and mass density of the membrane, respectively. $\xi_{n,m}$ is a constant depending on the mode number and is, for circular membranes, represented by the m -th root of the n -th order Bessel function. Hence, a vibrational spectrum of a circular membrane resonator operated in vacuum shows normal modes (n, m) , located at distinct resonance frequencies $f_{n,m}$. Each mode is characterized by nodal lines, laterally traversing the membrane, having ideally zero amplitudes and separating sections of the membrane oscillating with inverse phase. m denotes the radial mode number, being the count of circular nodal lines, including the circumference of the membrane. n denotes the azimuthal mode number, being the count of nodal lines traversing the membrane center.

Besides the resonance frequency, the quality factor Q is another important characteristic of a resonator, describing its damping. It represents the ratio of the energy stored in and dissipated from the oscillator system during the time interval $1/\omega_0 = 1/(2\pi f_0)$.^[221] In

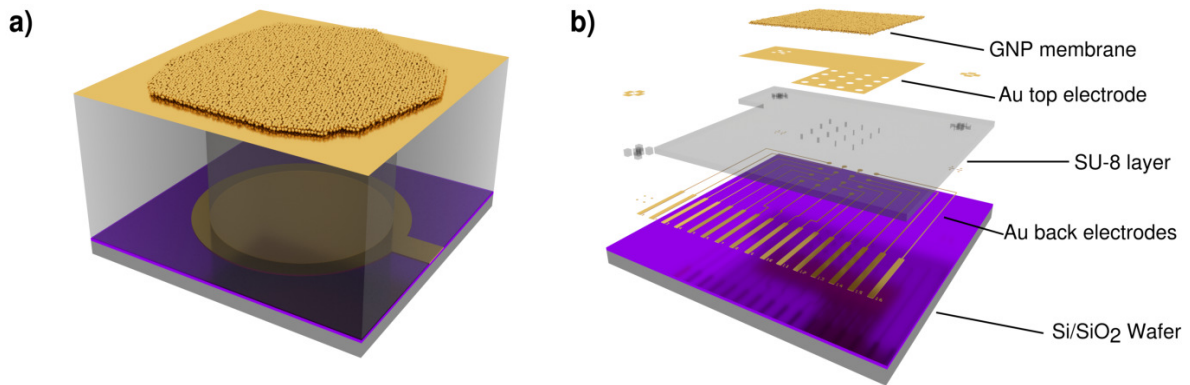


Figure 5.15: a) Schematic showing a single electrostatically driven GNP membrane resonator. b) Exploded view of a 4×4 GNP membrane resonator array.

our study the quality factor was determined by conducting *ring-down* experiments.^[37] In these experiments, the membrane was excited at its fundamental resonance frequency by a burst of the excitation signal. After switching off the excitation signal, the decay or “ring-down” of the oscillation was monitored. Assuming a damped harmonic oscillation, the decay of the oscillation should follow equation 5.9, which was fitted to the respective interval of the experimentally recorded deflection time trace.

$$h(t) = h_0 \sin(2\pi f_0 t + \phi) \exp\left(-\frac{t}{\tau}\right) \quad (5.9)$$

Here h_0 is the initial amplitude at $t = 0$, at the end of the excitation burst, f_0 is the respective resonance frequency, ϕ is the phase of the oscillation and τ represents the exponential decay constant. The quality factor relates to the the product of f_0 and τ .^[37]

$$Q = \pi f_0 \tau \quad (5.10)$$

5.4.2 Device Fabrication

Due to their similarity, the processing route leading to the GNP membrane resonators was very similar to the fabrication process of the GNP membrane based actuators described in the previous section. The only major difference was the deposition of gold counter-electrodes at the bottoms of the microcavities. Further, a sample chip contained an array of 4×4 resonator devices instead of a single actuator. While the resonators shared a common top electrode layer, connecting the membrane to signal ground, each of the 16 resonators integrated in one sample chip had an isolated counter electrode that could be individually addressed. Figure 5.15a schematically shows the structure of a single resonator device as part of an array (exploded view in figure part 5.15b). A photograph as well as a schematic of a complete, readily fabricated wafer chip is depicted in the ESI of

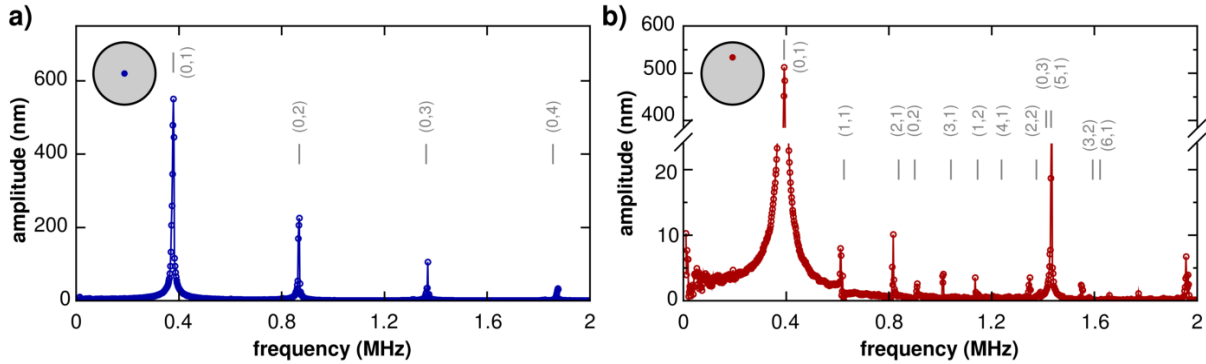


Figure 5.16: Amplitude spectra of a 100 μm diameter 6DT cross-linked GNP membrane resonator (thickness: (38 ± 1) nm) measured a) at its center ($x = 0, y = 0$) and b) at half radius ($x = 0, y = 25 \mu\text{m}$). Vertical gray lines indicate the frequency estimates of higher vibrational modes, based on the fundamental resonance frequency. Adapted from Ref. [2] with permission from The Royal Society of Chemistry.

the respective publication, reprinted in section A.1.3, page 216ff. As described in section 5.1.2, the back electrode structure was first microfabricated onto a thermally oxidized silicon wafer via standard photolithography. A layer of SU-8 was deposited on top of the finalized electrode structure and again photolithographically structured. The final SU-8 structure featured circular microcavities of $\sim 50 \mu\text{m}$ and $\sim 100 \mu\text{m}$ diameter. Following a further photolithographic step, the continuous top electrode, with openings around the microcavities, was deposited and structured onto the SU-8 layer.

Finally, 6DT cross-linked GNP membranes were prepared via spin-coating and transferred onto the microstructures as described in section 5.1. In this project, GNPs with an average diameter of (3.6 ± 0.6) nm were used for membrane fabrication. The membranes had thicknesses ranging between 33 and 52 nm and showed a typical conductivity of 0.1 S cm^{-1} .

5.4.3 Device Testing

One task of the present work was the assembly of a setup for the characterization of GNP membrane based actuators and resonators. The setup consists of a commercial laser interferometer (SIOS Nano Vibration Analyzer NA^[202]) for deflection measurements, a function generator as well as a high voltage amplifier for the generation of drive voltage signals, and a vacuum cell for characterization of the resonator devices under vacuum or reduced pressure. The cell was placed onto a motorized x, y -crosstable to adjust the measurement position. The setup is capable of providing drive voltage signals from DC up to several MHz to the devices while measuring the membrane deflection with a sampling frequency of up to 12.5 MHz. The interferometer enables a maximum z -resolution of deflection measurements of 20 pm.^[202] While the basic theory of interferometry is provided in the theory section 3.4, technical details on the measurement setup are provided in the appendix, section A.2.

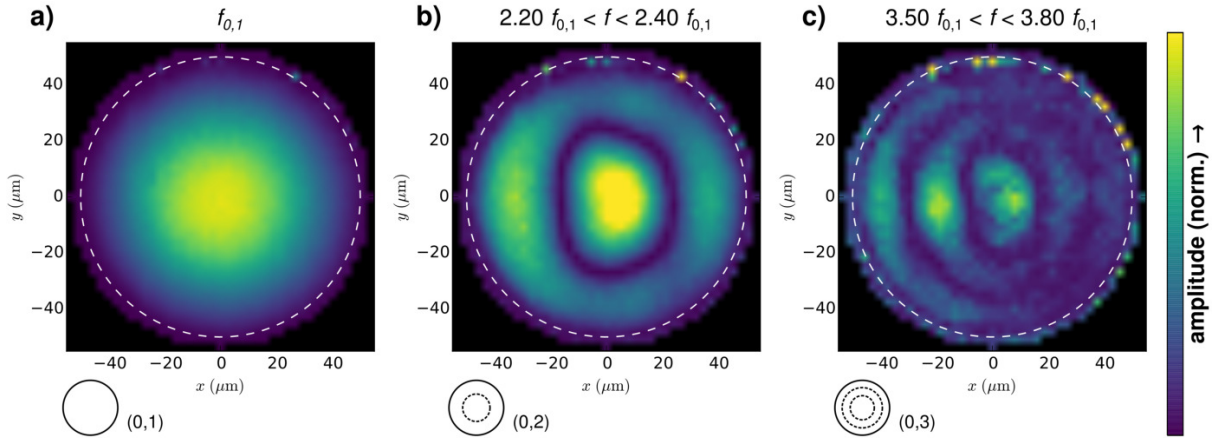


Figure 5.17: False-colored plots, depicting the lateral distribution of maximum vibrational amplitudes of a circular 100 μm diameter GNP membrane resonator. a) , b) , and c) show the maximum amplitudes observed in different spectral regions, as indicated. Adapted from Ref. [2] with permission from The Royal Society of Chemistry.

First, vibrational spectra of a resonator device were recorded under vacuum ($\sim 10^{-1}$ to 10^{-2} mbar), by applying AC voltage signals of varying drive frequency f_d to the membrane and measuring the respective amplitudes of the induced oscillation. Two vibrational spectra of a 100 μm diameter 6DT cross-linked GNP resonator, recorded at its center ($x = 0, y = 0$) and off-center at half radius ($x = 0, y = 25 \mu\text{m}$) are depicted in figure 5.16. Both spectra show a pronounced amplitude maximum slightly below 400 kHz. We designate this peak to the fundamental (0, 1) vibrational mode of the freestanding membrane. The distinct peaks visible in the spectra confirm our working hypothesis assuming that our devices can act as resonators, which can be excited by electrostatic forces. According to the model equation for circular membrane resonators under vacuum (equation 5.8), the frequencies of higher modes can be computed by taking into account the fundamental resonance frequency. Within the two plots, the Gray lines annotated with mode numbers indicate the frequency estimates of higher modes, based on the respective fundamental resonance frequencies. It is to note that when measuring at different positions on the membrane, not all modes can be observed. For example, in the measurement at the membrane center, shown in figure 5.16a, only peaks related to (0, m) modes can be observed, as modes with $n > 0$ have nodal lines with zero amplitudes traversing the membrane center. In contrast, the off-center measurement illustrated in figure 5.16b shows additional peaks, while e.g. the (0, 2) mode, which is expected to show a circular nodal line close to the measurement position almost vanished. In general, there is a good agreement of the experimentally observed vibrational frequencies with the theoretical model.

Using a faster *frequency sweeping* spectrum acquisition method, the fundamental resonance frequencies $f_{0,1}$ of a total of 26 resonator devices, having membrane diameters of either 50 μm or 100 μm , and membrane thicknesses of (34 ± 1) nm or (51 ± 1) nm were determined. In brief, the *frequency sweeping* method (cf. the ESI, section A.1.3, page 216ff) involved the application of a drive frequency f_d swept sine excitation signal to the devices, while simultaneously monitoring their deflection. The recorded deflection time traces showed pronounced oscillations when f_d matched one of their resonance fre-

quencies. Amplitude spectra were obtained by fast Fourier transformation (FFT) of the deflection time traces. The larger, 100 μm diameter resonators showed average resonance frequencies of (336 ± 28) kHz and (376 ± 18) kHz for the thicker and thinner GNP membranes, respectively. Values roughly twice as high, (697 ± 53) kHz and (735 ± 4) kHz, were measured for the smaller resonators and the respective membrane thicknesses. This agrees with theory, which expects a duplication of resonance frequency with a bisection of the resonator diameter (see equation 5.8). The influence of membrane geometry on the resonance behavior was further investigated in a yet unpublished connecting project, outlined in section 6.2. Considering the observed resonance frequencies, we found a minor influence of the membrane thickness, which could be caused by differences in the membrane pre-stress. While the mass density ρ should be constant for membranes of different thicknesses, the pre-stress might depend on the latter. This becomes more clear when expressing the phase velocity $c = \sqrt{\sigma/\rho}$ in terms of areal mass density $\rho_A = \rho t_m$ and membrane tension T_0 (force per unit edge length) $c = \sqrt{T_0/\rho_A}$.^[45] While ρ_A should scale linearly with t_m , T_0 could have a slightly different thickness dependence.

To further substantiate the assignment of the vibrational modes to the peaks in the resonance spectra, an *amplitude mapping* experiment was conducted. Here, vibrational spectra were acquired at varying positions on a 100 μm diameter resonator membrane using the fast *frequency sweeping* acquisition method. Amplitude images were created by plotting the spatial distribution of the maximum oscillation amplitude observed in different spectral ranges, normalized to the fundamental resonance frequency $f_{0,1}$. Three of these plots are depicted in figure 5.17. The plots in figure 5.17a, b and c depict the maximum amplitude distributions at $f_{0,1}$ and in the ranges of $2.20f_{0,1} < f < 2.40f_{0,1}$ and $3.50f_{0,1} < f < 3.80f_{0,1}$, respectively. While no nodal lines (except for the circumference of the resonator) were observed in the case of figure 5.17a — as anticipated for the fundamental resonance mode — figure 5.17b shows one and figure 5.17c two circular nodal lines. This agrees well with the shapes of the vibrational modes $(0, 2)$ and $(0, 3)$ expected in the respective frequency ranges at $f_{0,2} = 2.30f_{0,1}$ and $f_{0,3} = 3.60f_{0,1}$. The results of this *amplitude mapping* experiment confirm our assignment of the vibrational modes shown in the spectra, depicted in figure 5.16.

Finally, *ring-down* experiments, as described in section 5.4.1 were conducted to determine the quality factors of 26 devices. An exemplary experiment is depicted in figure 5.18. After the excitation of a 100 μm diameter resonator with 40 cycles of a sine voltage, the oscillation decay was monitored and fitted using the damped harmonic oscillator model. In the case of this particular device, the fit yielded a resonance frequency of $f_{0,1} = 313$ kHz and an oscillation decay time of $\tau = 1.070$ ms. This corresponds to a quality factor of $Q \sim 1051$. Average quality factors of 1288 ± 416 and 797 ± 183 were determined for resonators with membrane diameters of 100 μm and 50 μm , respectively.

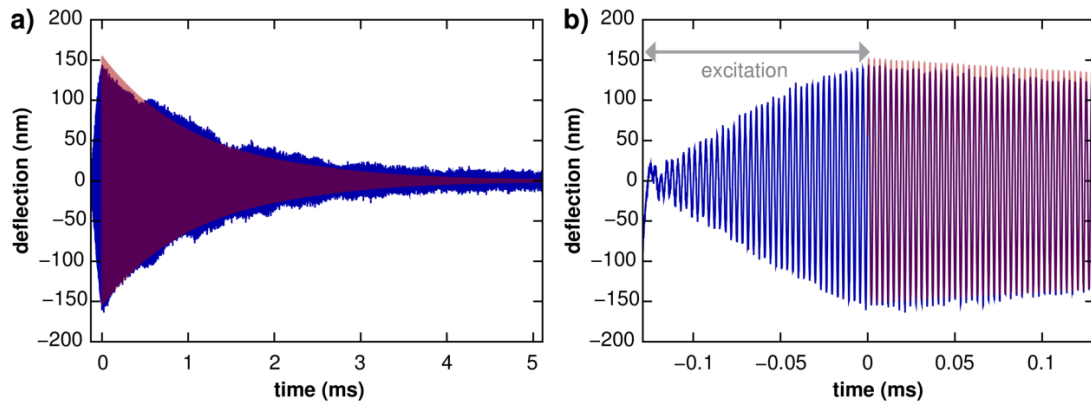


Figure 5.18: *a)* Deflection time trace of a *ring-down* experiment for quality factor determination (blue). The membrane was excited with 40 cycles of a sine voltage signal ending at $t = 0$. The red line represents a fit of the damped harmonic oscillator model to the oscillation decay. *b)* Zoomed-in plot of the excitation interval and the beginning of the oscillation's decay. Adapted from Ref. [2] with permission from The Royal Society of Chemistry.

5.4.4 Conclusion and Outlook

The present study represents a demonstration of electrostatically driven resonators based on GNP/6DT membranes, as well as a thorough characterization of their vibrational behavior. The principle of electrostatic actuation, investigated within the preceding project was utilized to excite oscillations of the freestanding membranes. The experimentally observed spectra and amplitude mappings could be well-described employing the theoretical model of a clamped membrane oscillating in vacuum. A consecutive study, which is subject to publication, is outlined in section 6.2. Within this study the influence of the resonator size on the resonance frequency and quality factor, as well as rectangular resonators are investigated in detail.

The resonators described in this work are of potential interest for the fabrication of sensors. On the one hand, it was demonstrated that resonators could be employed as pressure sensors, by using pressure-dependent changes in resonance frequencies or quality factors as sensing signal.^[32,219] On the other hand, GNP membrane based resonators are promising candidates for the fabrication of chemical sensors, because the material is known to sorb analytes from the gas phase, as described in the theory section 3.2.4. This application is the focus of the following project.

For the application as sensors, an all-electronic readout of spectra is of major interest to eliminate the use of an interferometer and to enable the fabrication of miniaturized devices. Currently, efforts are made to solve this problem, e.g. by implementing a capacitive readout or the utilization of the GNP membrane's resistive strain sensitivity.

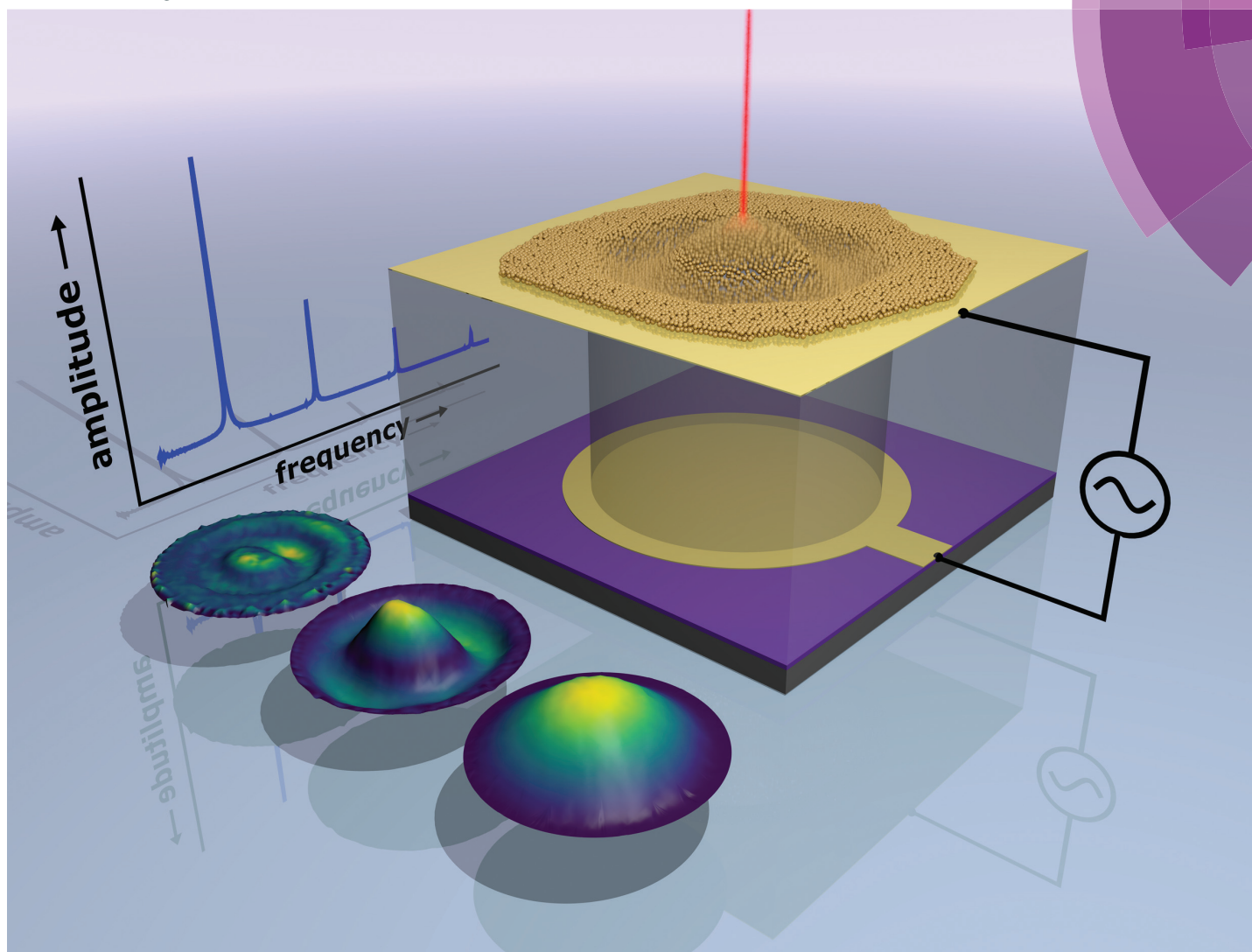
5.4.5 Publication: Electrostatically Driven Drumhead Resonators Based on Freestanding Membranes of Cross-Linked Gold Nanoparticles

Reprinted from “Electrostatically driven drumhead resonators based on freestanding membranes of cross-linked gold nanoparticles”, H. Schlicke, C. J. Schröter, T. Vossmeier, *Nanoscale* **2016**, *8*, 15880-15887^[3] with permission from The Royal Society of Chemistry.

The corresponding ESI is reprinted in section A.1.3, pages 216ff.

Nanoscale

www.rsc.org/nanoscale



ISSN 2040-3364



PAPER
Tobias Vossmeier *et al.*
Electrostatically driven drumhead resonators based on freestanding membranes of cross-linked gold nanoparticles





Cite this: *Nanoscale*, 2016, **8**, 15880

Electrostatically driven drumhead resonators based on freestanding membranes of cross-linked gold nanoparticles†

Hendrik Schlicke,[‡] Clemens J. Schröter[‡] and Tobias Vossmeier^{*}

Freestanding, nanometer-thin membranes of alkanedithiol cross-linked gold nanoparticles represent elastic, mechanically robust and electrically conductive materials, which are interesting for the fabrication of novel nano- and microelectromechanical devices. In this work we present the first electrostatically driven drumhead resonators based on such nanoparticle membranes. These circular membranes have a thickness of 33 to 52 nm, a diameter of either 50 μm or 100 μm , and are equally spaced from their back electrode by ~ 10 μm . Using an interferometric nanovibration analyzer various vibrational modes with resonance amplitudes of up to several 100 nm could be detected when the membranes are excited by applying AC voltages (< 30 V) with drive frequencies of up to 2 MHz. Further, spatial amplitude distributions of different vibrational modes could be imaged. The devices showed fundamental resonance frequencies in the high kHz range and quality factors Q up to ~ 2000 . Finally, vibrational spectra and observed mode patterns could be well interpreted using the theory for a clamped circular membrane with negligible bending stiffness. Our findings mark an important step towards the integration of freestanding gold nanoparticle composite membranes into electromechanical devices with various applications, such as novel types of pressure or mass sensors.

Received 30th March 2016,
Accepted 8th July 2016

DOI: 10.1039/c6nr02654k

www.rsc.org/nanoscale

Introduction

Resonators perform as fundamental device components in numerous microelectromechanical systems (MEMS). Today they are used *e.g.* in accelerometric and gyroscopic sensors. During the last two decades research and development have been focused on shrinking the dimensions of electromechanical devices yielding so-called nanoelectromechanical systems (NEMS) with critical feature sizes in the nanometer range.¹ Accordingly, interest has grown in the incorporation of nanometer-thin freestanding membranes as functional materials into these devices. Current studies demonstrate the applicability of NEMS and MEMS resonators consisting of such membranes for sensing pressure² or small forces and masses with extremely high sensitivity.³

Besides conventional silicon-based materials, novel 2D and 3D thin films are currently being investigated concerning their integration into resonator devices. Lightweight 2D materials

can for example be used for the fabrication of resonators with high resonance frequencies and high mass sensitivities. Bunch *et al.* demonstrated the fabrication of electromechanical resonators based on graphene membranes with thicknesses varying from a single atomic layer up to 75 nm with fundamental resonant frequencies in the range of 1–170 MHz, actuated by electrical or optical modulation.⁴ With amorphous diamond-like carbon another modification of carbon was used for resonator fabrication, recently.⁵ Also black phosphorus⁶ and transition metal dichalcogenides, such as single⁷ or multi-layer⁸ MoS₂ as well as TaO₂,⁹ were integrated as functional materials. Zhang *et al.* reported on resonators fabricated from carbon nanomembranes obtained by self-assembly and subsequent interlinkage of organic molecules.¹⁰

In addition to inorganic and organic materials, freestanding membranes of nanoparticle/organic composites have gained attention during recent years, offering versatile tunability of application specific properties as well as convenient ink-based film fabrication by printing^{11,12} or spin-coating,¹³ and transfer procedures such as microcontact printing.¹⁴ For example, Tsukruk and coworkers reported on the fabrication of gold nanoparticle (GNP)/polymer composite membranes and, using external piezoelectric actuation, analyzed their resonance frequencies which were found in the kHz range.¹⁵ Further, Jaeger and co-workers reported on the fabrication of

Institute of Physical Chemistry, University of Hamburg, Grindelallee 117, 20146 Hamburg, Germany. E-mail: tobias.vossmeier@chemie.uni-hamburg.de;
Fax: +49 40 42838 3452; Tel: +49 40 42838 7069

† Electronic supplementary information (ESI) available. See DOI: 10.1039/C6NR02654K

‡ These authors contributed equally to this work.



freestanding 2D membranes of self-assembled monolayers from monothiol capped gold nanoparticles and demonstrated their application as drumhead resonators with resonance frequencies in the low MHz range. These resonators were also driven by external piezoelectric actuators or thermal excitation.¹⁶

Thin films and membranes consisting of GNP/polymer composites or GNPs stabilized with long-chain monothiols are usually insulating or exhibit rather low electric conductivity. In contrast, fairly good and adjustable conductivities can be achieved by assembling GNPs with short-chain ligands and by cross-linking the particles with short dithiols. So far, however, most work on conductive GNP composites has been mainly focused on substrate-supported thin films and their applications as chemiresistors¹⁷ or resistive strain gauges^{18–21} and investigations of freestanding membranes consisting of such conductive GNP composites have started only recently. In this context, the emphasis of our present work is on freestanding, dithiol cross-linked GNP membranes and their potential applications in various types of MEMS/NEMS devices. Their conductivity²² as well as other properties, *e.g.* elasticity, optical absorption²³ and chemical affinity^{17,20} can be adjusted by the proper choice of linker molecules and particle sizes and shapes. The mechanical stability of dithiol cross-linked GNP films²⁴ allows them to be lifted off their initial substrates and deposited onto a variety of 3D microstructures to produce devices based on freestanding GNP membranes.¹³ For example, in a recently published study we demonstrated the application of freestanding, organically cross-linked GNP membranes as resistive pressure gauges.²⁵ Until now, resonators built from gold nanoparticle composites have been thermally excited or externally driven by piezoelectric actuators. Electrostatic actuation, which is a widespread principle in MEMS and NEMS has not been applied so far. In an earlier study we demonstrated the static deflection of freestanding GNP membranes by applying DC voltages.²⁶ Here, we fabricated and characterized the first electrostatically driven MEMS/NEMS resonators with high *Q* factors based on freestanding membranes of 1,6-hexanedithiol (6DT) cross-linked GNPs. By applying this versatile principle no external piezo actuators are necessary and the fabrication and integration of such devices are significantly simplified.

Experimental

Synthesis of gold nanoparticles

1-Dodecylamine capped GNPs were used for membrane fabrication in this study. The particles were synthesized following a procedure by Leff *et al.*²⁷

Preparation of cross-linked GNP films

6DT cross-linked GNP films were fabricated as described in an earlier publication.¹³ In this study the process was modified with regard to the pre-treatment procedure for the glass substrates. Here, the substrates were treated in an oxygen plasma

(SPI supplies plasma prep II) prior to deposition. Afterwards, the substrates were placed on a spin-coater and rotated at a constant rate of 3000 rpm. Firstly, 100 μL of a 7.4 mM solution of 6DT in toluene were applied to the rotating substrate two times. After this pre-treatment, a GNP layer was deposited by applying 10 μL of the $\sim 90 \mu\text{M}$ GNP stock solution in *n*-heptane to the substrate. Afterwards, 10 μL of a 7.4 mM solution of 6DT in methanol were applied two times in order to cross-link the GNPs. The GNP deposition and cross-linking steps represent one deposition cycle. GNP films investigated in this study were fabricated by applying either 3 (A, B) or 5 (C, D, E) deposition cycles. Between all applications of the solutions, a delay of ~ 30 s was maintained. Eventually, the GNP films were immersed in a methanolic solution of 6DT (7.4 mM) overnight and subsequently rinsed with acetone and dried in a nitrogen flow.

Fabrication of the 3D electrode microstructures

3D electrode microstructures were prepared following a multi-step optical lithography process, similar to that described in detail in our previous work.²⁶ $15 \times 15 \text{ mm}^2$ pieces of a silicon wafer with a 300 nm SiO_2 layer (Addison, $\langle 100 \rangle \pm 0.5^\circ$, CZ-n-Sb, $300 \text{ nm} \pm 5\%$, $0.005\text{--}0.025 \Omega \text{ cm}$) served as substrates. All photolithography steps were carried out under yellow light.

The back electrodes (BEs) were structured by depositing a sacrificial layer of an AZ nLOF 2070_3.5 μm negative photoresist for 60 s with 150 rps using a spin coater (K.L.M. SCC-200). After deposition, the photoresist was soft-baked on a hotplate for 180 s at 100°C . Once the sample had cooled down to ambient temperature, it was irradiated with UV light through a patterned photomask using a Karl Suss MJB-3 mask aligner. The photoresist was baked post exposure for 60 s at 120°C . After the sample cooled down to ambient temperature the photoresist was developed by immersion in an AZ 726 MIF developer (AZ Electronic Materials) for 60 s. The substrate was then rinsed with demineralized water and dried in a nitrogen flow. Onto this sacrificial layer multiple electrode layers were deposited. In order to increase adhesion and to remove the remaining organic material in the resist-free areas the samples were cleaned for 2 min (Harrick Plasma, PDC-002) in an oxygen plasma. Using thermal evaporation (oerlikon leybold vacuum UNIVEX 350-G or Pfeiffer Classic 250 Vacuum Evaporation System), layers of titanium ($\sim 10 \text{ nm}$) and gold ($\sim 40 \text{ nm}$) were deposited onto the sample. In an additional step a carbon layer ($\sim 10 \text{ nm}$) was deposited on top in order to reduce the reflectivity of the electrodes. The carbon evaporation was carried out by applying a current of $>25 \text{ A}$ to a twisted carbon fiber of $\sim 1.5 \text{ cm}$ length and 0.4 g m^{-1} in vacuum. In the following lift-off step the sample was immersed in TechniStrip NI555 (TECHNIC) at 70°C for 10 min. If necessary, the sample was sonicated (Bandelin Sonorex) for a maximum of 10 s to finalize the lift-off. Afterwards the samples were rinsed with acetone and demineralized water and dried in a nitrogen flow.

On top of the BEs a SU-8 2015 (MicroChem) photoresist layer was spin-coated for 60 s at 100 rps. This resulted in a SU-8 layer with a thickness of $\sim 10 \mu\text{m}$. After deposition, the



photoresist was soft-baked for 180 s at 95 °C. Once the sample had cooled down to ambient temperature, it was irradiated with UV light through a patterned photomask and a 360 nm long pass filter (Omega Optical Inc. PL-360 LP). The photoresist was baked post exposure for 240 s at 95 °C. After the sample cooled down to ambient temperature the photoresist was developed by immersion in an mr-Dev600 (Micro Resist Technology) developer for 180 s under agitation. The substrate was then rinsed briefly with a fresh developer and 2-propanol and dried in a nitrogen flow. Finally the sample was hard baked for 20 min on a ramping hot plate starting from 120 °C to 200 °C in the first 10 min. Commonly, the maximum deviation of the SU-8 cavity diameter from the targeted values of 50 μm and 100 μm was in a range of $\pm 2 \mu\text{m}$.

For the top electrode (TE) a sacrificial layer was structured on top of the SU-8 structures. A layer of an AZ nLOF 2070_3.5 μm photoresist was spin-coated for 60 s at 68 rps. After deposition the photoresist was soft-baked for 90 s at 120 °C. Once the sample cooled down to ambient temperature an additional layer of the AZ nLOF 2070_3.5 μm photoresist was spin-coated for 60 s at 68 rps and soft baked for 180 s at 120 °C. The second coating step was conducted to ensure a complete coverage of the 3D structure with the photoresist. Afterwards, UV light exposure was carried out using a patterned photomask. The photoresist was baked post exposure for 60 s at 120 °C. After the sample cooled down to ambient temperature the photoresist was developed by immersion in an AZ 726 MIF developer (AZ Electronic Materials) for 120 s. The substrate was then rinsed with demineralized water and dried in a nitrogen flow. In order to increase adhesion and remove the remaining organic material in the resist-free areas, the samples were cleaned for 2 min (Harrick Plasma, PDC-002) in an oxygen plasma. For the TEs a single gold layer ($\sim 40 \text{ nm}$) was deposited using thermal evaporation. In the following lift-off step the sample was immersed in TechniStrip NI555 (TECHNIC) at 70 °C for $\sim 15 \text{ min}$. If necessary, the samples were sonicated (Bandelin Sonorex) for $\sim 5 \text{ s}$. Finally, the samples were rinsed with acetone and demineralized water and dried in a nitrogen flow.

Results and discussion

Fabrication of resonator devices

Fig. 1a depicts a schematic view of an exemplary device. A GNP membrane was deposited onto a microstructure, spanning a circular microcavity. A gold top electrode, used as the signal ground, makes electrical contact with the membrane. In close proximity below the freestanding membrane another gold (back) electrode is arranged. Application of an AC signal to the latter electrode results in a time-dependent potential difference and hence attractive coulomb forces driving oscillations of the membranes.

The microsystem comprises a layered Ti/Au/carbon back electrode ($\sim 10 \text{ nm}/\sim 40 \text{ nm}/\sim 10 \text{ nm}$, respectively), which was lithographically fabricated on an oxidized silicon wafer

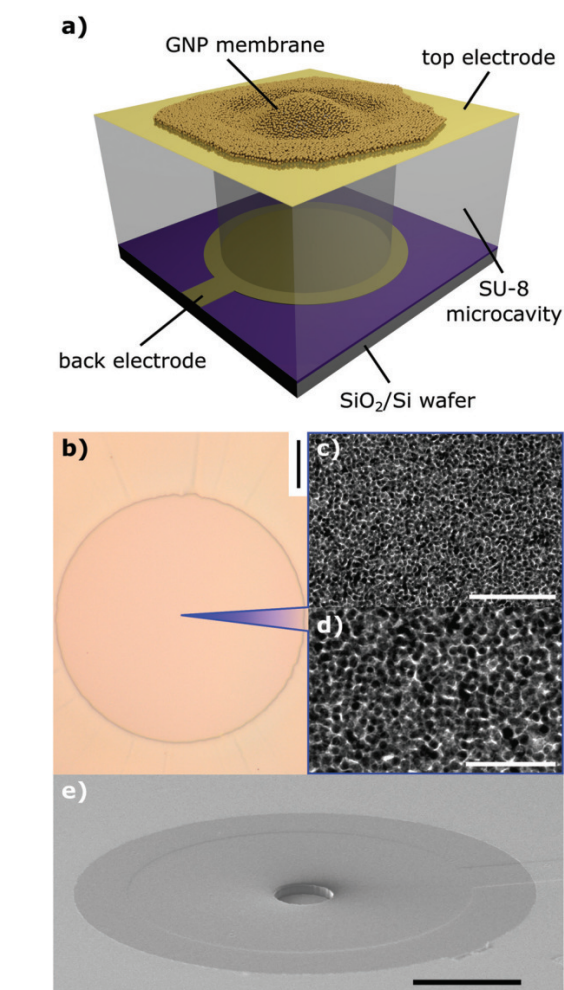


Fig. 1 (a) Schematic of a GNP membrane resonator. (b) An optical micrograph of a device. The image shows a 6DT cross-linked GNP membrane deposited onto a circular 100 μm cavity. Scale bar: 20 μm . (c, d) Transmission electron micrographs of a representative 6DT cross-linked gold nanoparticle membrane transferred to a carbon-coated TEM substrate. Scale bars: (c) 100 nm and (d) 50 nm. (e) A scanning electron micrograph of an electrode substrate featuring a 50 μm wide cavity, as used for resonator fabrication. Scale bar: 100 μm .

(300 nm thermal oxide) by vacuum evaporation and a subsequent lift-off process. Here, the carbon layer yields a lower reflectivity of the electrode, which is favorable for the interferometric measurements conducted in this study (see below). Onto the back electrode, a $\sim 10 \mu\text{m}$ thick layer of SU-8, a non-conductive epoxy photoresist, was deposited *via* spin-coating. Using standard photolithography, cylindrical cavities of 50 μm and 100 μm diameter were structured into the SU-8 layer. In the final lithography step, a top electrode (Au, $\sim 40 \text{ nm}$ thickness) was deposited onto the SU-8 layer and structured by applying a lift-off process, analogously to the fabrication of the back electrode. Each microsystem contains an array of 4×4



devices (see the ESI, Fig. S5†). While the top electrode is continuous, each device features an individual back electrode, which enables addressing the resonators one-by-one. A scanning electron micrograph of an as-fabricated electrode microstructure featuring a 50 μm wide cylindrical cavity is depicted in Fig. 1e.

6DT cross-linked GNP films were fabricated following our standard spin-coating based procedure. Alternately a solution of dodecylamine-capped GNPs (core diameter: 3.6 ± 0.6 nm) in *n*-heptane and a methanolic solution of 6DT were deposited onto glass substrates, as described earlier. By repeating these deposition steps, the thickness of the resulting GNP thin film could be adjusted.¹³ UV/vis absorption spectroscopy of the films showed a typical red shift of the GNP surface plasmon resonance absorption band due to the close packing of the particles in the material. Also the current-voltage characteristics of the films were recorded and ohmic behavior with a conductivity of 0.1 S cm^{-1} was observed, which is in good agreement with earlier studies.^{13,23,26} The thickness of the GNP films was determined by AFM measurements as reported earlier.¹³ See the ESI† for respective absorbance spectra, current-voltage data, topographic AFM data of the as-deposited films, a representative transmission electron micrograph as well as a size histogram of the GNP batch used for film fabrication. Fig. 1c and d show transmission electron micrographs of a GNP membrane transferred to a carbon-coated TEM substrate. The granular structure of the membrane with grain sizes in the nanometer regime can clearly be identified.

Following deposition, the GNP films were lifted off their initial glass substrates by flotation on demineralized water. After a few days the films could be detached from their substrates by careful immersion of the substrates into the aqueous phase making the membranes to free-float at the liquid-air interface. Subsequently, the membranes were skimmed using the electrode microstructures. An optical micrograph of a 6DT cross-linked GNP membrane transferred to a microstructure featuring a 100 μm wide cylindrical cavity is provided in Fig. 1b. The structures were allowed to dry and, thereafter, fixed on custom-designed printed circuit boards and connected by wire bonding.

Vibrational spectra

The fabricated resonator devices were placed into a custom-built vacuum cell (pressure 10^{-1} to 10^{-2} mbar) mounted on an *x,y*-translation stage. Fig. 2 depicts the setup used for device characterization. The membrane actuators were driven by the voltage signal of a function generator (Keysight 33521B) amplified by a high voltage amplifier (Falco Systems WMA-300). Commonly the samples were excited with a sine voltage function $V(t) = V_{\text{DC}} + V_{\text{AC}} \sin(2\pi f_d t)$ in a drive frequency f_d range up to 2 MHz. An offset voltage of $V_{\text{DC}} > V_{\text{AC}}$ was chosen to avoid a change of the bias direction resulting in a force minimum at the zero crossing point as the operating coulomb forces F scale with the square voltage, $F \propto V^2$.²⁶

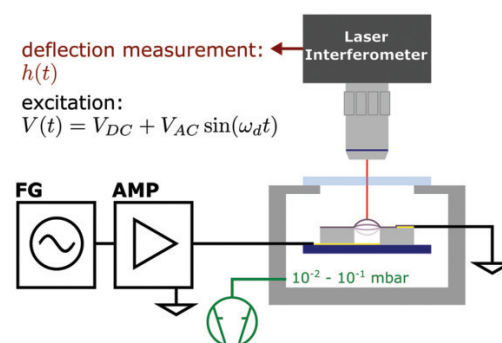


Fig. 2 Schematic of the setup used for electrostatic resonator characterization. A sine voltage signal from a function generator (FG) amplified by a high voltage amplifier (AMP) is used to drive a resonator placed in a custom-built vacuum cell. Deflection time traces are recorded with a laser interferometer.

For standard vibration spectrum acquisition (“frequency scanning” acquisition), membrane deflection time traces $h(t)$ were recorded using an interferometer (SIOS Nanovibration Analyzer NA) at varying excitation frequencies f_d . For each applied frequency, 8192 datapoints were acquired with a sample rate of 12.5 MHz. Due to its measurement principle, the SIOS Nanovibration Analyzer NA enables highly linear deflection measurements. Detailed information on the interferometric measurements are provided in the ESI.† Amplitude spectra $h_0(f_d) = 2|C(f_d)|$ were obtained by computing the magnitude of the vibration’s Fourier component C at the respective drive frequency f_d for each recorded deflection time trace. No deflection of the SU-8 layer was measured in proximity to the freestanding membranes. A detailed summary of the measurement and data processing is provided in the ESI.†

Fig. 3a shows the vibration amplitude spectrum measured in the center ($x = 0, y = 0$, see the inset) of a 6DT cross-linked GNP membrane (thickness: 38 ± 1 nm) spanning a 100 μm cavity, excited with a voltage signal of $V_{\text{AC}} = 5$ V and $V_{\text{DC}} = 15$ V. The spectrum shows a first pronounced peak at a frequency of $f_{0,1} = 379$ kHz with an amplitude of several hundreds of nanometers, which we assign to the fundamental (0,1) vibration of the membrane. For a clamped membrane under tensional stress σ , with a density ρ and negligible bending stiffness, its natural resonant frequencies in a vacuum are expected at distinct frequencies $f_{n,m}$, which can be computed using eqn (1).^{16,28}

$$f_{n,m} = \frac{\xi_{n,m}}{\pi 2a} \sqrt{\frac{\sigma}{\rho}} \quad (1)$$

$\xi_{n,m}$ is a constant depending on the mode number and is represented by the m -th root of the n -th order Bessel function for circular membranes. The mass density of composite membranes of 6DT cross-linked ~ 4 nm sized GNPs was estimated as $\rho = 3.8 \text{ g cm}^{-3}$ by XPS measurements, reported previously.²⁹ Taking into account the aperture radius of $a = 50 \mu\text{m}$, a tensional stress of the membrane of $\sigma = 9.3 \text{ MPa}$ could be



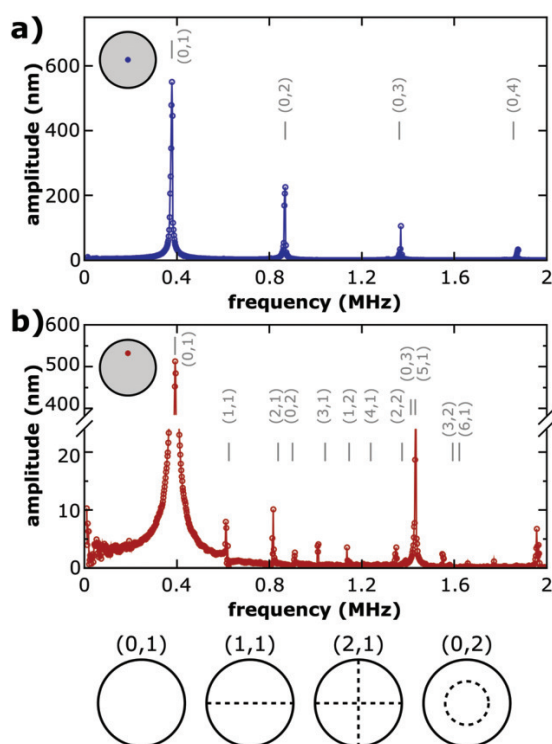


Fig. 3 Amplitude spectra of a 100 μm diameter 6DT cross-linked GNP membrane resonator (thickness: 38 ± 1 nm) measured (a) at its center ($x = 0$, $y = 0$) and (b) off-center ($x = 0$, $y = 25$ μm). The inset schemes depict the approximate position on the membrane surface. Vertical grey lines indicate the estimated frequencies of different vibrational modes of the membrane according to eqn (1). The respective mode numbers are given as (n,m) tuples. Sketches of selected vibrational mode patterns with their characteristic nodal lines are depicted at the bottom of the figure.

extracted. Values in the MPa range compare well with the residual stress values measured for 6DT cross-linked membranes under DC electrostatic deflection.²⁶

Using eqn (1), the frequencies of higher vibrational modes can be estimated by taking into account the $f_{0,1}$ frequency. Vibrational modes (n,m) of circular membranes are characterized by their number of nodal lines separating areas of the membranes with inversely phased oscillations. While the second index m denotes the radial mode number, which is the number of circular nodal lines (including the circumference of the membrane), the first index n denotes the azimuthal mode number, which is the number of nodal lines crossing the center of the membrane. Hence, it is expected that only $(0,m)$ vibrational modes with non-zero amplitudes at the membrane center can be observed as in Fig. 3a. It is clearly visible that the frequencies estimated for $(0,2)$, $(0,3)$ and $(0,4)$ modes agree very well with the spectral positions of amplitude maxima observed in the experiment.

Fig. 3b depicts an amplitude spectrum recorded off-center at the half radius of the resonator membrane. Just like the

amplitude spectrum measured at the membrane center, the off-center spectrum also features a pronounced fundamental resonance peak. However, the peak is slightly shifted to $f_{0,1} = 392$ kHz. In general, we observed slightly shifting resonance peaks when scanning the membrane with the interferometer laser. We attribute this finding to local heating of the membrane due to laser irradiation. Based on the fundamental $f_{0,1}$ resonance frequency, again the frequencies of higher modes were estimated. The spectral positions are depicted as grey vertical lines in Fig. 3b, annotated with respective mode numbers. Most of the estimated mode frequencies agree well with the peak positions found in the experiments.

The fundamental resonance frequencies $f_{0,1}$ of a total of 26 devices were measured using the faster “frequency sweeping” spectrum acquisition method (see the ESI†) applying an excitation voltage signal with $V_{\text{DC}} = 5$ V, $V_{\text{AC}} = 2.5$ V for resonators with a diameter of 100 μm and $V_{\text{DC}} = 10$ V, $V_{\text{AC}} = 5$ V for resonators with a membrane diameter of 50 μm . It is worth noting that changes in the membranes’ tensional stress due to a variation of the offset voltage in the given range did not lead to significant shifts of the fundamental resonance frequency. Further, we did not find evidence for a correlation of the fundamental resonance frequency with the applied drive amplitude within the accuracy of our measurements. See the ESI† for details. In order to study the effect of different membrane thicknesses devices probed in this set of experiments comprised membranes fabricated by applying either three deposition cycles (average thickness $t = 34 \pm 1$ nm) or five deposition cycles (average thickness $t = 51 \pm 1$ nm). For the thicker membranes, fundamental resonance frequencies of 336 ± 28 kHz and 697 ± 53 kHz were found for the larger and smaller resonators, respectively. For the same device dimensions the thinner membranes showed $f_{0,1}$ values of 376 ± 18 kHz and 735 ± 4 kHz. The resonance frequencies of the smaller resonators are approximately twice as high as the resonance frequencies of the larger resonators, as expected by theory (see eqn (1)). Further, on average somewhat higher resonance frequencies were measured for resonators built from thinner GNP membranes. This indicates that tuning of the resonance frequency is possible by adjusting the membrane thickness. Assuming a similar surface tension σt for all membranes, we attribute this finding to the lower mass of the thinner membranes. Further, we assume that the observed scattering of the resonance frequencies can be reduced by optimizing the membrane transfer process, resulting in better control of the membrane tension.

Amplitude mappings

To further confirm the assignment of the resonance frequencies to their vibrational modes, mappings of the membrane vibrations were conducted. The acquisition of amplitude and phase maps was complicated, because the resonance peaks shifted slightly when scanning the laser over the freestanding membrane area. To overcome this problem, vibration spectra were acquired at each mapping position on the membrane by computing fast Fourier transforms (FFTs) of deflection time traces recorded while exciting the samples using frequency



swept sine voltages (“frequency sweeping” acquisition). Deflection amplitude maps were then computed by extracting the peak amplitude in the respective spectral regions. See the ESI† for details on the amplitude mapping procedure. Fig. 4a depicts the spatial amplitude distribution of a 100 μm diameter resonator consisting of a 52 ± 1 nm thick 6DT cross-linked GNP membrane generated by taking into account the first amplitude maximum at $f_{0,1}$ of the spectra recorded at each point. The amplitude distribution shows a maximum at the membrane center which smoothly decreases towards the edges of the membrane. This is expected for the fundamental (0,1) vibration of a clamped membrane. In contrast, Fig. 4b depicts the amplitude maxima found around $\sim 2.3f_{0,1}$, *i.e.* where the (0,2) vibrational mode is expected. A circular nodal line with an amplitude minimum concentrically separating two areas with higher amplitudes is clearly visible. This is characteristic for the (0,2) vibrational mode (see the inset). It is worth noting that the mapping shows a distortion from a perfect circular appearance. This behavior is possibly caused by inhomogeneous local tensioning of the membrane. We assume that such inhomogeneities can be reduced in future by improving the transfer of the membranes onto the microcavities, which is currently carried out manually. Besides, inhomogeneous local heating of membrane sections according to the scan pattern might affect the amplitude images’ symmetry. Plotting the amplitude maxima occurring in the spectral range from $3.50f_{0,1}$ to $3.80f_{0,1}$ yielded the amplitude map shown in Fig. 4c. Here two circular nodal lines can be seen, which are characteristic for the (0,3) vibrational mode, expected at $3.60f_{0,1}$. These results unambiguously confirm the assignment of the resonance modes in the amplitude spectra.

In conclusion, the good agreement of the theoretical and experimental peak positions shows that the membranes’ dynamic behavior in a vacuum can be well-described using the model for a clamped circular membrane with negligible bending stiffness.

Ring down experiments

For determining the resonators’ quality factors Q , ring down experiments were conducted. Here, the resonators were excited at their $f_{0,1}$ resonance frequency by applying a burst of 10 to 80 sine voltage cycles with $V_{\text{DC}} = 5$ V and $V_{\text{AC}} = 2.5$ V for 100 μm membranes. A slightly higher drive signal of $V_{\text{DC}} = 10$ V and $V_{\text{AC}} = 5$ V was used for the smaller 50 μm membrane resonators. Synced with the start of the excitation signal, deflection data $h(t)$ were recorded using the interferometer. After burst excitation, the drive signal was switched off and the ring down of the membrane oscillation was monitored. A modulation of the raw deflection data due to the oscillation of the interferometer’s reference mirror (~ 800 Hz) was removed by Fourier transformation of the $h(t)$ data, elimination of the low-frequency Fourier components (≤ 100 kHz) and back-transformation to the time-domain (see the ESI†). Afterwards, the ring down of the oscillation was fitted using eqn (2), which describes a damped harmonic oscillator.

$$h(t) = h_0 \sin(2\pi f_{\text{res}} t + \phi) \exp\left(-\frac{t}{\tau}\right) \quad (2)$$

Here, h_0 is the initial amplitude of the oscillation and ϕ denotes the phase. As indicated by eqn (3), the quality factor Q is calculated from the decay time of the oscillation τ and the oscillators resonance frequency f_{res} , extracted as parameters of the fit.⁶

$$Q = \tau \pi f_{\text{res}} \quad (3)$$

The exemplary ring down data shown in Fig. 5 were obtained by investigating a 100 μm diameter 6DT cross-linked GNP membrane resonator excited with 40 sine cycles at a drive frequency of 310 kHz. The blue line depicts the deflection of the membrane, while the red line depicts a fit of eqn (2) to the data, beginning at the end of the excitation interval at $t = 0$.

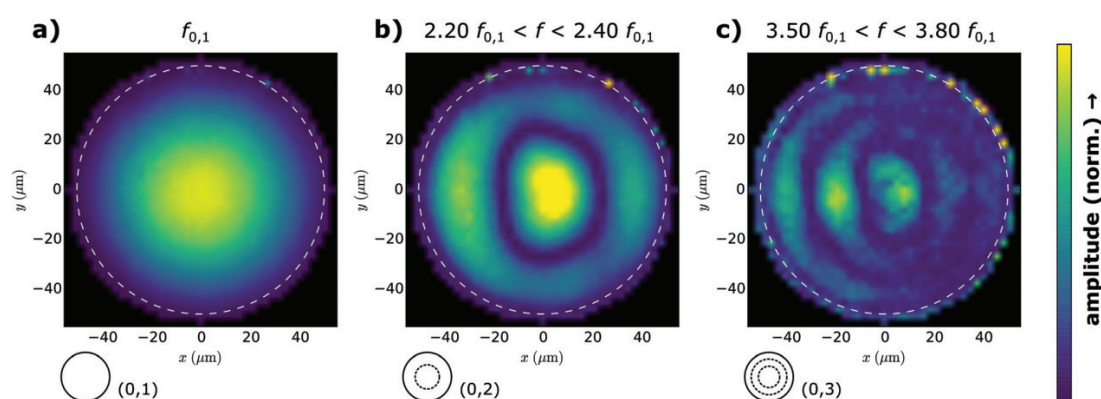


Fig. 4 Amplitude mappings of an electrostatically driven 100 μm diameter GNP membrane resonator. The plots depict the amplitude maxima found in the frequency ranges denoted above the images (a), (b) and (c). The amplitudes are normalized in each image individually. The schemes in the lower left of the plots depict the mode numbers of membrane normal modes which are in good agreement with the observed amplitude patterns. Theoretically, the higher modes shown are expected at resonance frequencies of (b) $f_{0,2} = 2.30f_{0,1}$ and (c) $f_{0,3} = 3.60f_{0,1}$. Dashed white lines depict the outline of the freestanding membrane.



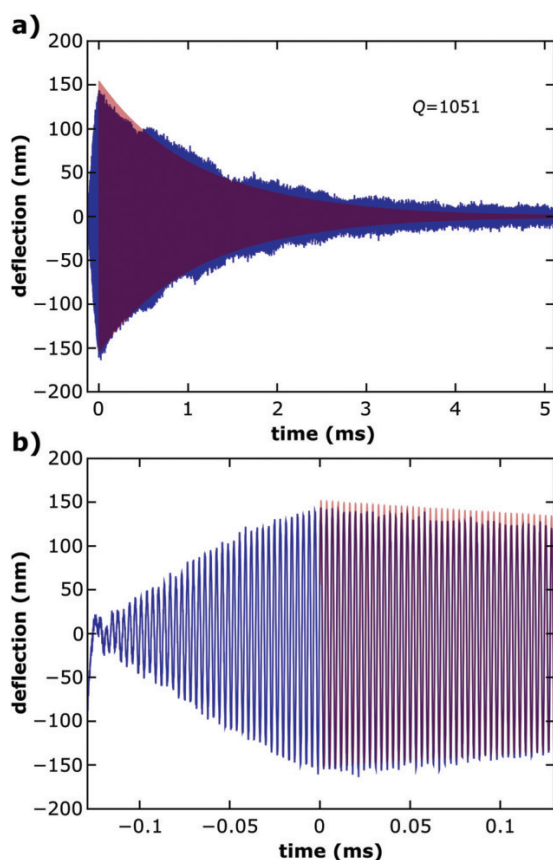


Fig. 5 (a) Measured deflection time trace of a ring-down experiment for quality factor determination (blue). The GNP membrane was excited with 40 cycles of a sine voltage signal ending at $t = 0$ and the subsequent decay of the oscillation was recorded. The red line indicates a fit of the damped oscillator model (eqn (2)) to the deflection data. (b) The zoomed-in plot of the excitation interval and the beginning of the oscillation's decay.

A resonance frequency of $f_{\text{res}} = 313$ kHz and a decay time of the oscillation $\tau = 1.070$ ms were extracted as fit parameters. From these parameters a quality factor of $Q \sim 1051$ could be estimated for the resonator. Furthermore, devices with membrane diameters of 100 μm or 50 μm were investigated and average quality factors of 1288 ± 416 and 797 ± 183 were measured, respectively. A table listing the resonance frequencies and quality factors of all 26 resonators investigated is provided in the ESI.† The average quality factors are higher than the values of up to 500 reported for gold nanoparticle monolayers on ~ 9 μm wide apertures.¹⁶ We attribute this difference to the larger diameters of the membranes used in our study. It is expected that the quality factor of fundamental vibrational modes increases with the ascending membrane diameter due to decreasing dissipation by clamping losses.²⁸ This trend is also confirmed when comparing the values measured for our 50 μm and 100 μm wide resonators.

Conclusions

In summary, we reported the fabrication of electrostatically driven drumhead resonators based on freestanding membranes of organically cross-linked gold nanoparticles. The circular membranes with thicknesses of ~ 34 nm or ~ 51 nm and diameters of 100 μm or 50 μm showed fundamental resonance frequencies in the high kHz range and quality factors up to $Q \sim 2000$ (see the ESI, Table S1†). In resonance, amplitudes of several hundreds of nanometers were measured under excitation with voltages below 30 V. The vibrational modes could be assigned unambiguously to the spectral positions of observed resonances by applying the theory for a clamped circular membrane with negligible bending stiffness.

Currently, our investigations aim at the detailed understanding of the influences of membrane thickness, geometry and size on the resonators' characteristics. Also the effects of external influences, such as pressure variations should be probed. Besides, the interplay of the internal structure of the membranes (cross-linker length, particle size) and their vibrational behavior (resonance frequencies, damping mechanisms) is an objective of our current research efforts. Higher resonance frequencies in the MHz range should be achievable by decreasing the lateral size of the freestanding membranes or their thicknesses. Furthermore, the potential applications of these resonators as pressure or gravimetric molecular sensors with electronic excitation and capacitive or resistive readout of the amplitude spectrum are topics for subsequent research activities.

Acknowledgements

The work of H. S. is supported by a scholarship from the Joachim Herz Stiftung. T. V. acknowledges financial support from the DFG, grant number VO698/3-1. We thank Dr Christian Strelow (University of Hamburg) and Dr Ralf Schüler (SIOS GmbH, Germany) for helpful discussions.

References

- 1 H. G. Craighead, *Science*, 2000, **290**, 1532–1535.
- 2 D. R. Southworth, H. G. Craighead and J. M. Parpia, *Appl. Phys. Lett.*, 2009, **94**, 213506.
- 3 M. Kumar and H. Bhaskaran, *Nano Lett.*, 2015, **15**, 2562–2567.
- 4 J. S. Bunch, A. M. van der Zande, S. S. Verbridge, I. W. Frank, D. M. Tanenbaum, J. M. Parpia, H. G. Craighead and P. L. McEuen, *Science*, 2007, **315**, 490–493.
- 5 M. Tomi, A. Isacson, M. Oksanen, D. Lyashenko, J.-P. Kaikkonen, S. Tervakangas, J. Kolehmainen and P. J. Hakonen, *Nanoscale*, 2015, **7**, 14747–14751.
- 6 Z. Wang, H. Jia, X. Zheng, R. Yang, Z. Wang, G. J. Ye, X. H. Chen, J. Shan and P. X.-L. Feng, *Nanoscale*, 2015, **7**, 877–884.



- 7 A. Castellanos-Gomez, R. van Leeuwen, M. Buscema, H. S. J. van der Zant, G. A. Steele and W. J. Venstra, *Adv. Mater.*, 2013, **25**, 6719–6723.
- 8 J. Lee, Z. Wang, K. He, J. Shan and P. X.-L. Feng, *ACS Nano*, 2013, **7**, 6086–6091.
- 9 S. J. Cartamil-Bueno, P. G. Steeneken, F. D. Tichelaar, E. Navarro-Moratalla, W. J. Venstra, R. van Leeuwen, E. Coronado, H. S. J. van der Zant, G. A. Steele and A. Castellanos-Gomez, *Nano Res.*, 2015, **8**, 2842–2849.
- 10 X. Zhang, R. Waitz, F. Yang, C. Lutz, P. Angelova, A. Götzhäuser and E. Scheer, *Appl. Phys. Lett.*, 2015, **106**, 063107.
- 11 E. S. Park, Y. Chen, T.-J. K. Liu and V. Subramanian, *Nano Lett.*, 2013, **13**, 5355–5360.
- 12 S. Fuller, E. Wilhelm and J. Jacobson, *J. Microelectromech. Syst.*, 2002, **11**, 54–60.
- 13 H. Schlicke, J. H. Schröder, M. Trebbin, A. Petrov, M. Ijeh, H. Weller and T. Vossmeier, *Nanotechnology*, 2011, **22**, 305303.
- 14 B. Kowalczyk, M. M. Apodaca, H. Nakanishi, S. K. Smoukov and B. A. Grzybowski, *Small*, 2009, **5**, 1970–1973.
- 15 S. Markutsya, C. Jiang, Y. Pikus and V. V. Tsukruk, *Adv. Funct. Mater.*, 2005, **15**, 771–780.
- 16 P. Kanjanaboos, X.-M. Lin, J. E. Sader, S. M. Rupich, H. M. Jaeger and J. R. Guest, *Nano Lett.*, 2013, **13**, 2158–2162.
- 17 F. J. Ibañez and F. P. Zamborini, *Small*, 2011, **8**, 174–202.
- 18 J. Herrmann, K. H. Müller, T. Reda, G. R. Baxter, B. Raguse, G. J. J. B. De Groot, R. Chai, M. Roberts and L. Wiczorek, *Appl. Phys. Lett.*, 2007, **91**, 183105.
- 19 C. Farcau, H. Moreira, B. Viallet, J. Grisolia, D. Ciuculescu-Pradines, C. Amiens and L. Rossier, *J. Phys. Chem. C*, 2011, **115**, 14494–14499.
- 20 N. Olichwer, E. W. Leib, A. H. Halfar, A. Petrov and T. Vossmeier, *ACS Appl. Mater. Interfaces*, 2012, **4**, 6151–6161.
- 21 C.-W. Jiang, I.-C. Ni, S.-D. Tzeng and W. Kuo, *Sci. Rep.*, 2015, **5**, 11939.
- 22 M. Brust, D. J. Schiffrin, D. Bethell and C. J. Kiely, *Adv. Mater.*, 1995, **7**, 795–797.
- 23 Y. Joseph, I. Besnard, M. Rosenberger, B. Guse, H.-G. Nothofer, J. M. Wessels, U. Wild, A. Knop-Gericke, D. Su, R. Schlögl, A. Yasuda and T. Vossmeier, *J. Phys. Chem. B*, 2003, **107**, 7406–7413.
- 24 H. Schlicke, E. W. Leib, A. Petrov, J. H. Schröder and T. Vossmeier, *J. Phys. Chem. C*, 2014, **118**, 4386–4395.
- 25 H. Schlicke, M. Rebber, S. Kunze and T. Vossmeier, *Nanoscale*, 2016, **8**, 183–186.
- 26 H. Schlicke, D. Battista, S. Kunze, C. J. Schröter, M. Eich and T. Vossmeier, *ACS Appl. Mater. Interfaces*, 2015, **7**, 15123–15128.
- 27 D. V. Leff, L. Brandt and J. R. Heath, *Langmuir*, 1996, **12**, 4723–4730.
- 28 V. P. Adiga, B. Ilic, R. a. Barton, I. Wilson-Rae, H. G. Craighead and J. M. Parpia, *Appl. Phys. Lett.*, 2011, **99**, 253103.
- 29 Y. Joseph, N. Krasteva, I. Besnard, B. Guse, M. Rosenberger, U. Wild, A. Knop-Gericke, R. Schlögl, R. Krustev, A. Yasuda and T. Vossmeier, *Faraday Discuss.*, 2004, **125**, 77–97.



5.5 Electromechanical Chemical Sensors

The project described in this section loops back to sensing applications of freestanding ADT cross-linked GNP membranes. By taking advantage of electrostatic actuation and resonance excitation investigated in the two preceding studies, the fabrication and performance of a novel type of nanocomposite based electromechanical chemical sensor is reported.

5.5.1 Operation and Sensing Principle

In the preceding section we demonstrated that freestanding GNP membranes can be utilized as microelectromechanical resonators, which are excited by periodically varying electrostatic forces imposed by applying AC voltages. Simplifying, we consider the model of a clamped tense membrane oscillating in vacuum (cf. the introductory section, 3.3.3). The resonance frequencies of such membranes depend on the mode number, geometrical constraints such as the lateral dimensions, and on the phase velocity c .^[186] The phase velocity is equal to the square root of the ratio of membrane's pre-stress σ_0 and density ρ , and for circular membranes proportional to their mode frequencies:

$$f_{n,m} \propto \sqrt{\frac{\sigma_0}{\rho}} \quad (5.11)$$

Similar as in the case of a drum, increasing membrane pre-stress/tension leads to a higher pitch, while increasing the mass density of a membrane drumhead causes lower frequencies.

In the past, organically stabilized and cross-linked GNP films were extensively investigated with respect to their chemiresistive properties and applications (see the introductory section 3.2.4).^[51,60,62–66,105,126,127,136,144,222] The chemiresistive effect is dedicated to sorption of VOCs and gases within the membrane and the resulting swelling (going along with an increase of the interparticle distances / tunneling junctions) as well as changes in the permittivity between the particles.^[60,64] It can also be expected that sorption of analyte species will influence the resonance behavior of freestanding GNP membranes. Figure 5.19 schematically depicts a GNP membrane resonator with interferometric readout, exposed to toluene vapor.

On the one hand, uptake of analyte may have an impact on the mass density ρ of the composite. An increase in the mass density would — considering the model equation 5.11 — lead to decreased resonance frequencies. However, in our experiments described in the following we conducted QCM measurements that revealed a mass uptake in the sub-parts per thousand range at the applied vapor concentrations. Relative mass changes in the parts per thousand range were also observed in literature, even for considerably higher analyte partial pressures and longer-chain monothiol capped non-cross-linked GNP

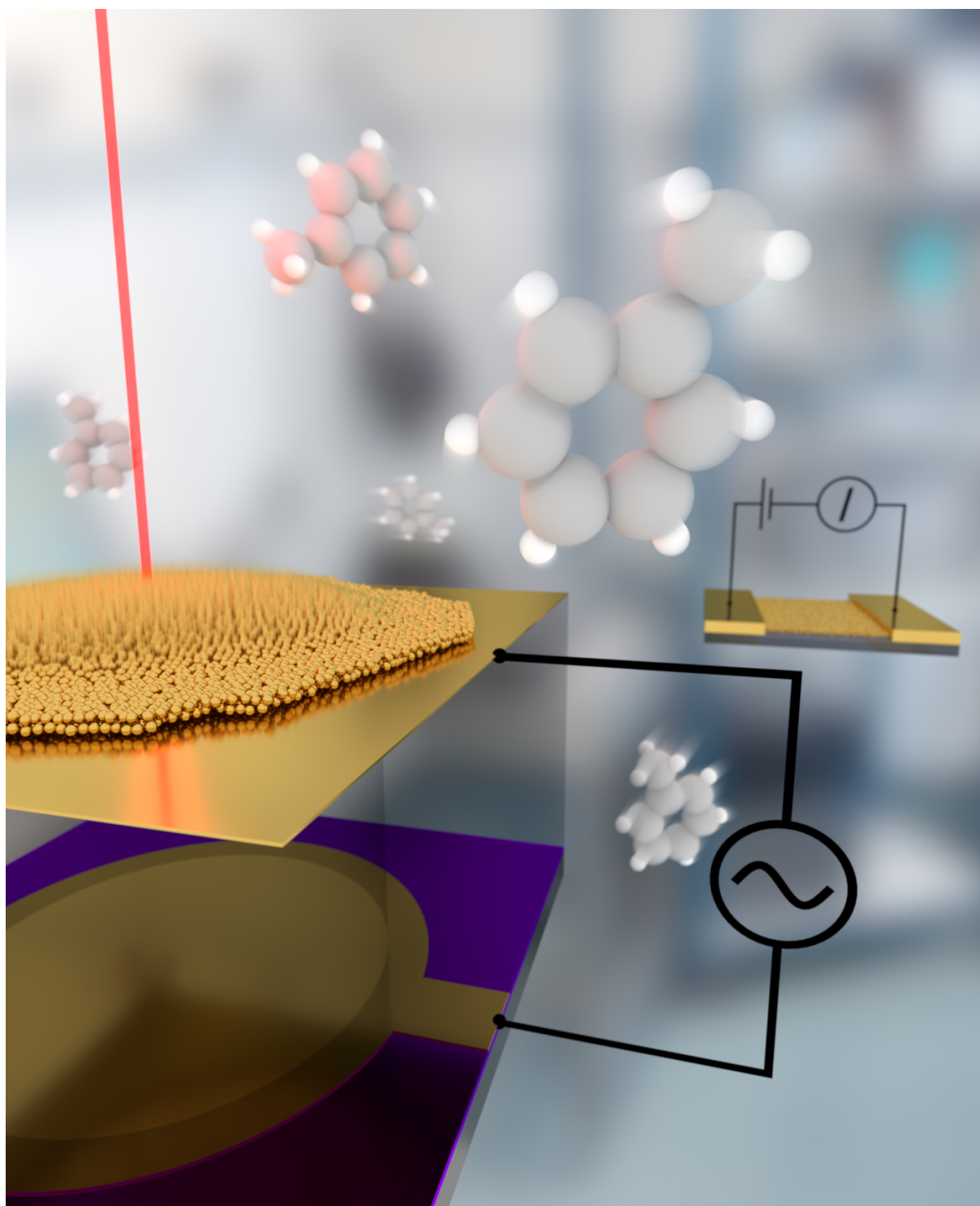


Figure 5.19: Artwork showing a GNP membrane resonator with an incident laser beam originating from an interferometer, surrounded by toluene (analyte) molecules. A conventional GNP thin film chemiresistor is depicted in the background.

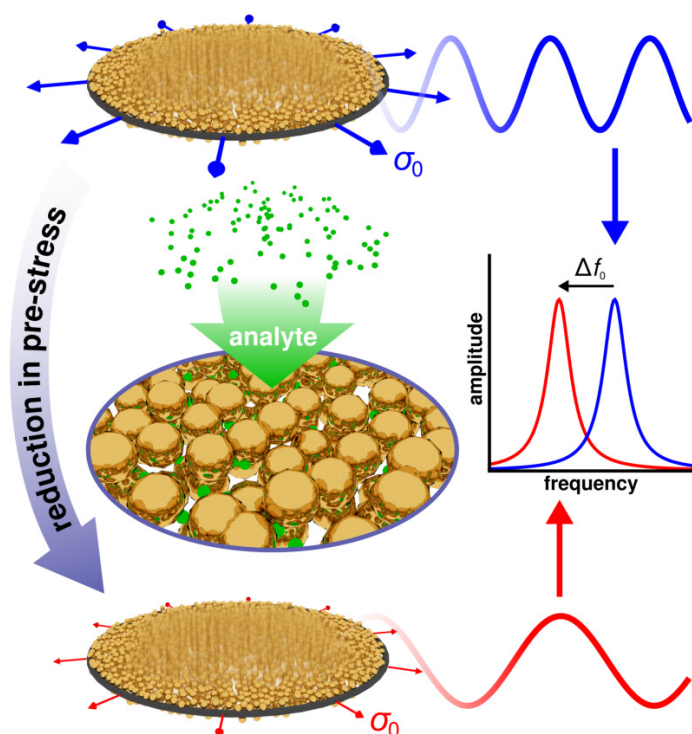


Figure 5.20: Schematic showing the anticipated transduction mechanism of electromechanical chemical sensors based on GNP membranes. Analyte sorption is expected to reduce the membrane pre-stress, resulting in decreasing vibrational mode frequencies. Reprinted with permission from Ref. [4]. ©2017 American Chemical Society.

composites, which are expected to show stronger sorption than their ADT cross-linked analogs.^[65] Considering the approximate model (equation 5.11) and assuming a constant membrane pre-stress, the resonance frequencies of the resonators are expected to change with the inverse of the square root of the relative mass density change $f_{n,m}/f_{n,m,0} = \sqrt{\rho_0/\rho}$. A relative density increase in the parts per thousand range should therefore only result in a minor resonance frequency downshift of $1 - f_{n,m}/f_{n,m,0} < 10^{-3}$. Based on our experiments showing considerably stronger frequency shifts, we conclude that the mass uptake is not playing a dominant role in the transduction mechanism of our sensors.

On the other hand, different studies based on SAXS showed an increase of interparticle distances, i.e., swelling of nanoparticle composites upon exposure to VOCs or water.^[65,135,209] As graphically illustrated in figure 5.20, we expect that the sorption-induced effects causing this swelling presumably reduce the pre-stress σ_0 of the freestanding GNP membrane spanning the microcavity, resulting in decreasing resonance frequencies. Besides the resonance frequencies of GNP membrane resonators, their static deflection behavior under application of DC voltages is dependent on the membranes' pre-stress. This is described in the preceding project (section 5.3), focusing on electrostatic actuation of GNP membranes. Compared to the resonance frequency, the voltage-deflection behavior of such electrostatically actuated membranes is independent of the membranes' mass density (see equation 5.7). In a follow-up study connecting to this project, we therefore conducted experiments comparing changes of a membrane's DC voltage-deflection behavior to changes

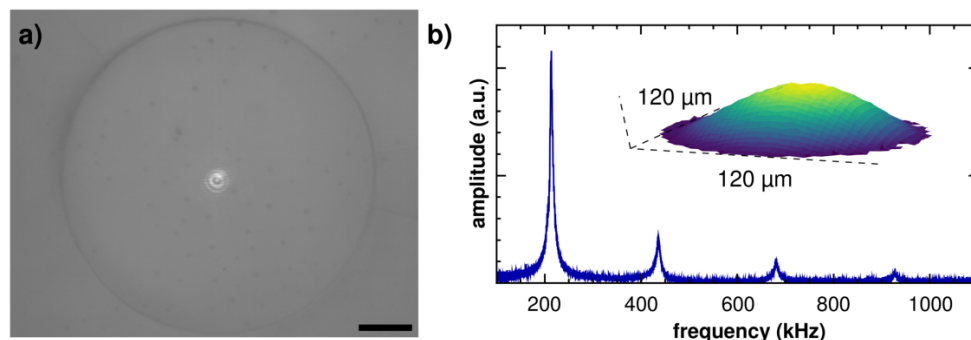


Figure 5.21: *a)* Optical micrograph depicting the 120 μm diameter resonator comprising a 6DT cross-linked GNP membrane, characterized regarding its chemical sensor characteristics. The bright spot in the membrane’s center represents a reflection of the interferometer’s laser. Scale bar: 20 μm . *b)* Vibrational amplitude spectrum of the respective device, acquired under a reduced pressure nitrogen atmosphere (20 mbar). The inset depicts the lateral amplitude distribution at a frequency of ~ 217 kHz. Reprinted with permission from Ref. [4]. ©2017 American Chemical Society.

of their resonance frequencies induced by sorption of analyte species. Both types of experiments yielded similar values and changes of the membrane pre-stress, supporting our assumption that the sensor response is predominantly caused by sorption-induced changes of the membrane’s pre-stress. These additional experiments are described in section 6.3.2, page 148*ff*, and in a recent proceedings paper (section 6.5, page 157*ff*).

5.5.2 Sensor Fabrication

The GNP membrane resonator utilized as electromechanical chemical sensor was essentially similar to the resonator devices described in the preceding section. It consisted of a (44 ± 1) nm thick 6DT cross-linked GNP membrane, spanning a ~ 120 μm diameter circular aperture. The membrane was fabricated using GNPs having an average diameter of (3.4 ± 0.6) nm and showed a typical conductivity of 0.1 S cm^{-1} . A detailed characterization of the membrane and a photograph of the finalized device mounted onto a PCB are provided in the SI, reprinted in section A.1.4, page 233*ff*. An optical micrograph of the membrane is depicted in figure 5.21a.

5.5.3 Sensor Testing

To avoid strong damping resulting in excessive peak broadening of the fundamental resonance mode, the sensing characteristics of the resonator were probed under a reduced pressure nitrogen atmosphere with a total pressure of $P_{\text{abs}} \sim 20$ mbar. Using electrostatic excitation with AC voltages and interferometric deflection readout, the vibrational characteristics of the GNP membrane resonator were probed. Figure 5.21b shows a resonance spectrum of the device. The inset of the figure shows the lateral amplitude distribution observed at frequency of ~ 217 kHz, where the first peak in the resonance spectrum is

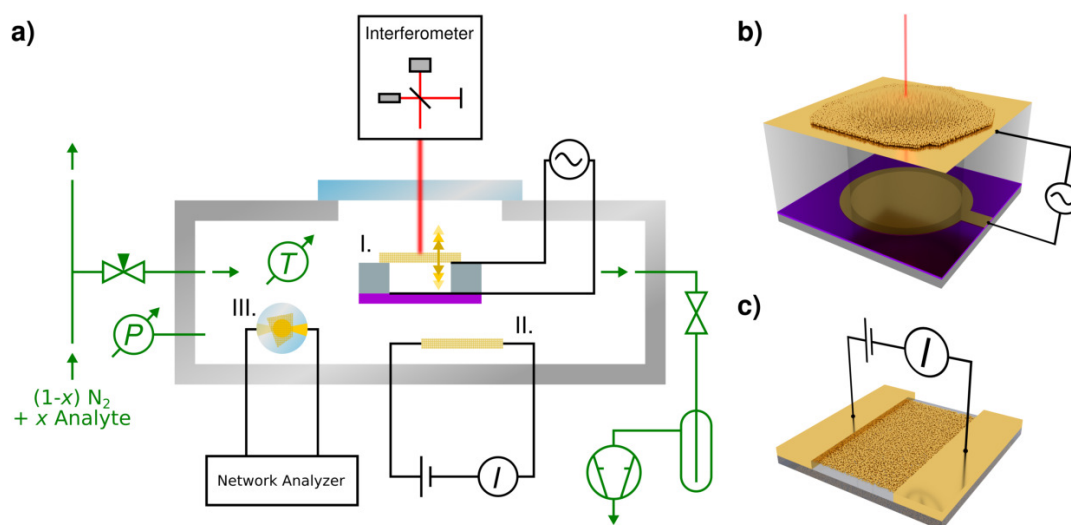


Figure 5.22: a) Schematic depicting the experimental setup for sensor characterization. A GNP membrane based resonator (I), a chemiresistor fabricated from a section of the same GNP film (II.), as well as a QCM loaded with another section of the film (III.), each connected to suitable measurement hardware, were placed into a test cell. The cell was equipped with a pressure and temperature sensor and a periphery capable of introducing different analyte gases at varying total pressures and concentrations. b) Schematic of a GNP membrane resonator. c) Schematic of a GNP film based chemiresistor. Reprinted with permission from Ref. [4]. ©2017 American Chemical Society.

located. The absence of nodal lines with zero amplitude (except for the membrane circumference) and the monotonic radial decay of the amplitude confirm that the first resonance peak in the spectrum corresponds to the fundamental resonance mode. Also, *ring-down* experiments (cf. section 5.4) were conducted and a quality factor of $Q = 45 \pm 1$ was determined for the fundamental resonance mode. This value is significantly lower than values in the 10^2 to 10^3 range observed for similar resonators tested in higher vacuum ($\sim 10^{-1}$ to 10^{-2} mbar) in our previous study. We dedicate this observation to damping caused by the nitrogen present in the test cell. The damping of the resonator further results in broadening of the resonance peaks, as visible in figure 5.21b.

The sensor response characterization was conducted using the interferometer setup with a custom-built test cell, as depicted in figure 5.22a. A detailed description of the interferometer setup is provided in the appendix (section A.2). Besides the GNP membrane resonator (figure 5.22b), the test cell was equipped with a GNP film chemiresistor (figure 5.22c), fabricated from the same 6DT cross-linked GNP composite film, as well as a QCM, coated with another section of the GNP film. The resonator and the additional devices were exposed to the same analyte atmosphere to compare the signals of the resonator and the chemiresistor, and to monitor the mass uptake of the composite using the QCM. A commercial calibration system was utilized to provide a flow of nitrogen gas, enriched with defined molar fractions of analyte vapors x_{analyte} . A portion of this feed was introduced into the test cell via a needle valve, adjusted to maintain a constant, total cell pressure of $P_{\text{abs}} = 20$ mbar. The analyte partial pressures are hence given by $p_{\text{analyte}} = x_{\text{analyte}} P_{\text{abs}}$. The sensor responses were probed by continuously monitoring the fundamental resonance

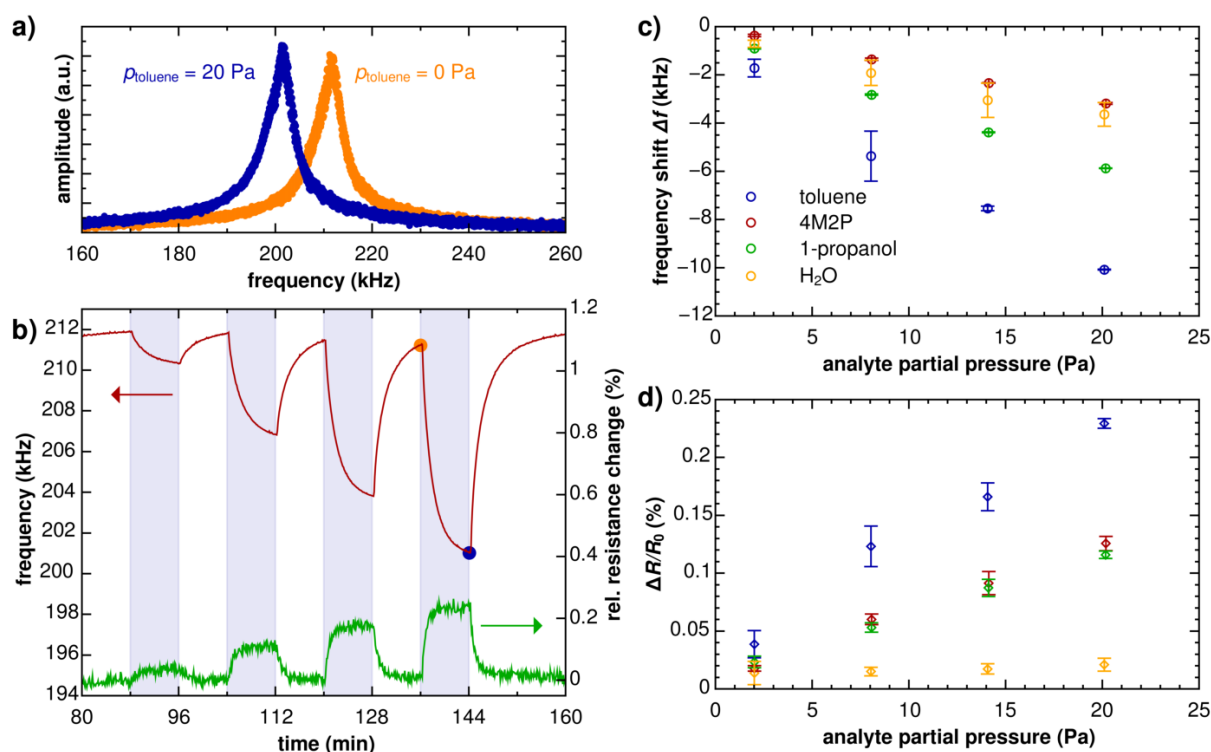


Figure 5.23: a) Plot depicting two spectra showing the fundamental resonance mode of a 120 μm diameter GNP membrane resonator in a 20 mbar nitrogen atmosphere with $p_{\text{toluene}} = 0$ (orange curve) and $p_{\text{toluene}} = 20 \text{ Pa}$ (blue curve). b) Frequency response transients of the GNP membrane resonator, as well as relative resistance change transients of the GNP thin film chemiresistor, when dosed with toluene vapor at partial pressures of $p_{\text{toluene}} = 2, 8, 14$ and 20 Pa . The orange and blue dots mark resonance frequencies determined from the spectra shown in figure part a. c) Frequency shifts of the GNP membrane resonator and d) relative resistance changes of the GNP film chemiresistor observed under exposure to different partial pressures of toluene, 4M2P, 1-propanol and water. Reprinted with permission from Ref. [4]. ©2017 American Chemical Society.

frequency of the resonator, while repeatedly feeding 8 min pulses of analyte gas (AG) containing 1000, 4000, 7000, and 10 000 ppm of the analyte into the test cell, yielding partial pressures of $p_{\text{analyte}} = 2, 8, 14,$ and 20 Pa . The AG applications were spaced by purging with pure nitrogen zero gas (ZG) for 8 min. Four analytes with varying polarities were tested: Toluene, 1-propanol, 4-methylpentan-2-one (4M2P) and water.

Figure 5.23a shows two spectra, as recorded for monitoring the fundamental resonance frequency of the resonator device. The orange and blue curve, recorded during exposure to toluene partial pressure of 0 and 20 Pa, respectively, reveal a clear downshift of the fundamental resonance peak of $\sim 10 \text{ kHz}$ upon exposure to toluene vapor. The two spectra correspond to datapoints of the respective frequency time trace, depicted in figure 5.23b. The time trace clearly shows the changes of f_0 under exposure of the sensor to toluene partial pressures of 2, 8, 14, and 20 Pa. The pronounced downshifts of the resonator's fundamental frequency prove the functionality of our device. As outlined above, the mass uptake of the GNP films observed by the QCM measurements are most likely too small to have major effects on the fundamental resonance frequency. Hence, the frequency

response is presumably due to changes in the membrane pre-stress.

The data in figure 5.23b further show that the response of the sensor does not fully saturate during the 8 min analyte exposure periods. We assign this to the fact that one side of the membrane is exposed to the interior of the microcavity, which is initially filled with pure nitrogen gas. To achieve saturation of the sensor signal, the analyte concentration within the cavity volume has to equilibrate with the exterior, to expose the membrane to the maximum analyte concentration on both sides. This equilibration is however limited by permeation of analyte through the membrane. We assume that this effect dominates the kinetics of the sensor response. This assumption was later substantiated by an experiment, probing the sensing characteristics of a GNP membrane resonator spanning a trench, in a bridge-like geometry. In this case downshifts of the fundamental resonance frequency under exposure to analyte vapors were essentially immediate, as the membrane was exposed directly from both sides. This unpublished study is summarized in section 6.3.1. Interestingly, for the circular resonator investigated here, the transient shapes/kinetics are different for the four analytes, which can be seen in figure 6.11 (section 6.3.1, page 144) and in the time traces of the four measurements, depicted in the respective SI, reprinted in the appendix, page 233ff, section A.1.4. The transient shape (e.g. the saturation time), is likely to depend on the analyte/membrane permeability coefficients and could hence, after calibration, be used as a metric for recognizing an analyte.

Figure 5.23c and 5.23d depict the absolute fundamental frequency shifts of the resonator as well as the relative resistance changes of the chemiresistor, respectively. Overall, the observed frequency and resistance changes show a similar trend, i.e., a more pronounced response to less polar analytes. This is expected, as both sensing mechanisms rely on sorption of the analytes in the composite materials, which is related to the respective partitioning coefficients.^[64] However, while the chemiresistor fails to detect water (cf. the time traces in the SI, appendix, page 184, section A.1.1), the resonator shows clear responses. This can be due to the high analyte permittivity ϵ of water, which has a counteracting effect on the swelling-related response of a GNP based chemiresistor (cf. section 3.2.4). In contrast, it should not significantly influence the response of the GNP membrane resonator. Diverging sensitivities of the resonator and the chemiresistor towards different analytes can be used for analyte discrimination. Here, using a suitable device geometry, it is entirely conceivable to use a single freestanding GNP membrane both, as microelectromechanical and chemiresistive transducer.

5.5.4 Conclusions and Outlook

In this project we demonstrated the application of an electrostatically driven ADT cross-linked GNP membrane resonator as microelectromechanical chemical vapor sensor. The device showed pronounced and reversible downshifts of its fundamental resonance frequency located at ~ 220 kHz by up to $\sim 5\%$ when exposed to different analyte vapors under a reduced pressure nitrogen atmosphere. We proposed a highly sensitive transduction mechanism based on changes of the membrane's pre-stress. The investigations

outlined in this project gave rise to several follow-up studies.

In the case of electrostatically actuated GNP nanocomposites not only the resonance frequency determined by AC actuation can be used as a sensor signal (dynamic measurement) — also the voltage-deflection behavior, i.e., the mechanical response of the composite to applied DC voltages/quasi-static electrostatic forces as shown in section 5.3 can act as a sensor signal (quasi-static measurement, cf. sections 6.3.2, 6.5^[6]). Quasi-static deflection of the membranes has the advantage that it can be easily conducted under ambient conditions, because damping plays no significant role as in the case of vibrational measurements. Even though the resonance frequencies as well as the quasi-static voltage-deflection behavior are both dependent on the membrane pre-stress, the latter is independent of the membrane mass/density (compare eq. 5.11 and 5.7). Hence, these experiments are expected to be able (especially when employing lightweight nanocomposite membranes) to give different response patterns when probing a variety of analytes.

This renders the novel transduction concepts highly interesting for multivariate sensing applications. Both measurement methods (dynamic and quasi-static) can be combined, optionally with additional chemiresistive measurements and evaluation of the above-mentioned response kinetics, to characterize analytes or to provide an input set for PCA or ANN evaluation, targeting at analyte recognition. Using a suitable electrode geometry, it should be possible to conduct the dynamic, quasi-static and chemiresistive measurements on a single freestanding membrane section.

Even more sensors with differing sensitivities and selectivities can be obtained by modification of the membrane's composition, i.e. the introduction of other nanoparticles or cross-linkers showing deviating sorption affinities for analytes.

The results of this project as well as the additional experiments outlined in section 6.3.2 formed the basis for the patent application GB1704749.9, disclosing chemical sensors that detect a sensing signal caused by alterations of a nanocomposite's mechanical properties due to analyte sorption.

5.5.5 Publication: Cross-Linked Gold-Nanoparticle Membrane Resonators as Microelectromechanical Vapor Sensors


Reprinted with permission from “Cross-Linked Gold-Nanoparticle Membrane Resonators as Microelectromechanical Vapor Sensors”, H. Schlicke, M. Behrens, C. J. Schröter, G. T. Dahl, H. Hartmann, T. Vossmeier, *ACS Sens.* **2017**, *2*, 540-546.^[4] Copyright ©2017 American Chemical Society.

The corresponding SI is reprinted in section A.1.4, pages 233ff.

Cross-Linked Gold-Nanoparticle Membrane Resonators as Microelectromechanical Vapor Sensors

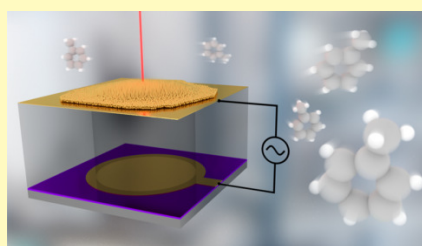
Hendrik Schlicke,¹ Malte Behrens,¹ Clemens J. Schröter,¹ Gregor T. Dahl,¹ Hauke Hartmann,¹ and Tobias Vossmeier^{1*}

Institute of Physical Chemistry, University of Hamburg, Grindelallee 117, 20146 Hamburg, Germany

 Supporting Information

ABSTRACT: We report a novel approach for the detection of volatile compounds employing electrostatically driven drumhead resonators as sensing elements. The resonators are based on freestanding membranes of alkanedithiol cross-linked gold nanoparticles (GNPs), which are able to sorb analytes from the gas phase. Under reduced pressure, the fundamental resonance frequency of a resonator is continuously monitored while the device is exposed to varying partial pressures of toluene, 4-methylpentan-2-one, 1-propanol, and water. The measurements reveal a strong, reversible frequency shift of up to ~10 kHz, i.e., ~5% of the fundamental resonance frequency, when exposing the sensor to toluene vapor with a partial pressure of ~20 Pa. As this strong shift cannot be explained exclusively by the mass uptake in the membrane, our results suggest a significant impact of analyte sorption on the pre-stress of the freestanding GNP membrane. Thus, our findings point to the possibility of designing highly sensitive resonators, which utilize sorption induced changes in the membrane's pre-stress as primary transduction mechanism.

KEYWORDS: gold nanoparticle, freestanding, membrane, MEMS, NEMS, sensor, resonator



A widely used principle for sensing or monitoring chemical, physical, or biological properties and processes is the observation of variations in the oscillatory behavior of optical, electronic, or mechanical resonators. (Electro-)mechanical resonators are often used to detect analytes, i.e., small masses, by monitoring their impact on the resonance frequency. For example, since its first report¹ the quartz crystal microbalance (QCM) evolved into a standard tool for monitoring small mass changes, e.g., during the deposition of thin films via physical vapor deposition (PVD) or in various kinds of sorption and binding studies in physical, chemical, and biological experiments. By shrinking the dimensions of electromechanical resonator systems, involving the reduction of their own mass, extremely high mass sensitivities can be achieved. This was impressively demonstrated by using carbon nanotubes (CNT) as resonators yielding a mass resolution of up to 1.4 zg² at 4 K or even atomic resolution.³ A different class of nano/microelectromechanical resonators is represented by membrane resonators, featuring a freestanding nanometer-thin film under tensional pre-stress, excited by external piezoactuation, electrostatic forces, or laser pulses.

Besides conventional MEMS/NEMS materials such as silicon or silicon nitride, 2D materials like graphene,⁴ MoS₂,^{5,6} or black phosphorus⁷ were used for the fabrication of such membrane resonators. Also, nanometer thin carbon membranes⁸ and composite membranes of alkanethiol-stabilized or polymer-embedded gold nanoparticles (GNPs)^{9,10} with external piezoelectric actuation were investigated regarding their resonance behavior. Such GNP containing membranes were further used

for the construction of highly sensitive pressure sensors,¹¹ or as IR microimagers¹² with optical readout and for electro-mechanical sensing.¹³ Very recently, we demonstrated the fabrication of microelectromechanical drumhead resonators comprising a dithiol cross-linked GNP membrane as oscillator with versatile electrostatic actuation.¹⁴ Thin films of ligand-stabilized or cross-linked GNPs have attracted great interest because their granular nature gives rise to thermally activated tunneling-based charge transport. This implies a strong dependence of the materials' conductivity on the interparticle spacing and the dielectric properties of the organic ligand matrix. As both properties are influenced by sorption of analyte species these composites can be applied as chemiresistors.^{15–17} The affinity of these films and hence their sensitivity to different analytes can be tuned by the choice of the cross-linkers or ligands, e.g., by introducing hydrophobic long-chain α,ω -substituted alkane spacers or more polar linker molecules.^{16,17}

In this work we explore a new approach for vapor/gas sensing using electrostatically driven resonators of cross-linked GNP/dithiol composites. We demonstrate the applicability of drumhead resonators based on freestanding membranes of 1,6-hexanedithiol (6DT) cross-linked GNPs for the detection of volatile compounds in the gas phase. The transduction mechanism of our sensor is schematically depicted in Figure 1. Compared to conventional bulk resonators, which can only

Received: December 21, 2016

Accepted: March 14, 2017

Published: March 28, 2017

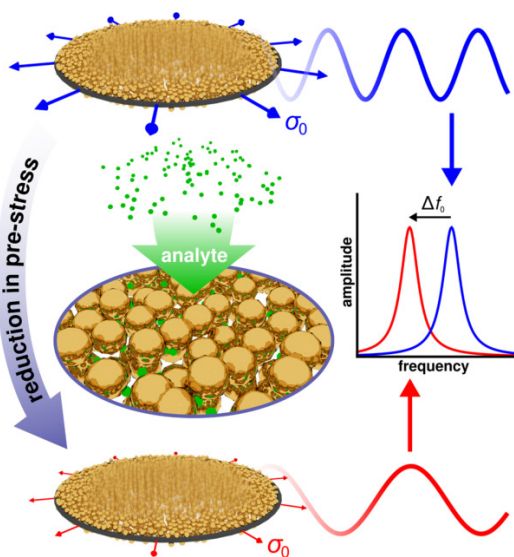


Figure 1. Transduction mechanism of a GNP membrane resonator sensing chemical vapors. Sorption of analyte in the GNP membrane results in reduction of the membrane's pre-stress σ_0 and hence a downshift of the fundamental vibrational resonance frequency Δf_0 .

detect analytes adsorbed on their surface, composites of ligand-stabilized or cross-linked GNPs are permeable¹⁸ and able to sorb analyte molecules within the organic matrix of ligands or cross-linkers. Besides changes of the composite's mass, analyte uptake can cause swelling,^{19,21} which affects the fundamental mechanical properties of the membranes, including their pre-stress and elasticity. As pre-stress is governing the resonance frequency of membrane resonators, its sorption-induced change results in a resonance frequency shift, which is measured as the sensor signal. To study the resonators' response characteristics they were exposed to vapors of toluene, 1-propanol, 4-methylpentan-2-one (4M2P), as well as water under reduced pressure. Monitoring the

amplitude spectra using a laser interferometer revealed strong correlations between the resonance frequencies and the analytes' partial pressures. The resonance frequency shifts were compared to the responses of a chemiresistor prepared from the same cross-linked GNP film. Further, the upper limit of the analyte masses sorbed within the membranes was estimated by QCM measurements. Aside from its utilization for the design of highly sensitive chemical sensors, the new transduction mechanism explored in this study could be employed as a complementary sensing technique, e.g., in combination with conventional GNP based chemiresistors. Because the different transduction mechanisms give rise to distinct sensitivities for different analytes, the resulting response patterns of such sensor arrays could be utilized for enhanced analyte recognition.

RESULTS AND DISCUSSION

The GNP membrane resonators were fabricated as reported in our previous study.¹⁴ A schematic of a device is shown in Figure 2b. The 3D microelectrodes, featuring cylindrical microcavities equipped with a back electrode at their bottom and a top electrode, deposited concentrically around the edge of the upper cavity opening, were lithographically fabricated. Details on the lithographic fabrication procedure are provided in the Supporting Information, pages S-7/S-8. The 6DT cross-linked GNP film was deposited onto a glass slide, following our standard spin-coating based procedure.^{14,22} According to this method, a solution of 1-dodecylamine capped GNPs (average diameter of 3.4 ± 0.6 nm) and a solution of the 6DT cross-linker in methanol were deposited alternately onto the rotating substrate to yield a cross-linked GNP film with a thickness of 44 ± 1 nm. As shown by electron microscopy in our previous work,²³ these GNP films have a disordered granular structure, which should enable the uptake of analyte molecules within the organic matrix formed by the cross-linker. After recording the UV/vis absorbance spectrum, the glass slide coated with the GNP film was cut into four pieces. The first quarter of the film was used for resonator fabrication as described earlier.¹⁴ To transfer the cross-linked GNP film onto the 3D microelectrodes the coated glass substrate was floated

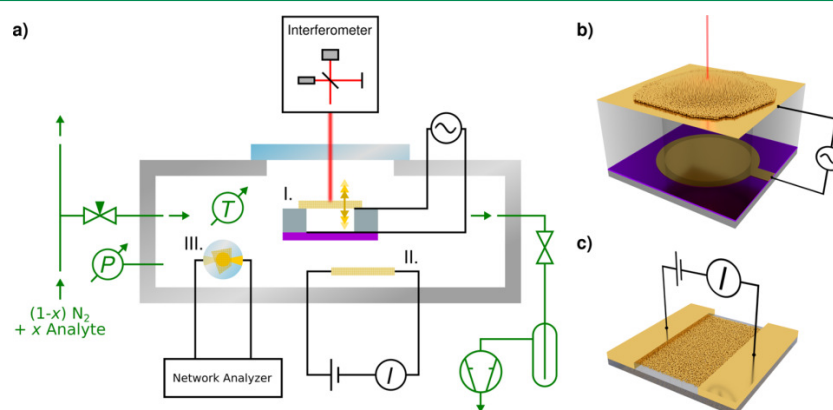


Figure 2. (a) Schematic of the experimental setup. A microelectromechanical GNP membrane resonator with interferometric deflection readout (I), a GNP film based chemiresistor (II), and a quartz crystal microbalance coated with a GNP film (III), each connected to respective suitable readout electronics, were placed into a vacuum cell. The cell was equipped with pressure and temperature sensors and features a periphery that enables the introduction of nitrogen mixed with solvent vapors at defined concentrations. (b) Schematic of a GNP membrane drumhead resonator. (c) Schematic of a chemiresistor based on a GNP film equipped with two electrodes.

on demineralized water, and after several days, the film could be detached by carefully immersing the glass substrate into the aqueous phase, leaving the film free-floating at the liquid–air interface. Using a silicon substrate equipped with the lithographically defined 3D microelectrodes, the floating GNP film was skimmed and formed, after drying, a freestanding membrane as schematically depicted in Figure 2b. For investigating the GNP film's chemiresistive properties, ~100-nm-thick gold electrodes were deposited onto the second glass-supported quarter of the spin-coated GNP film by thermal evaporation.²² A shadow mask was applied during evaporation, yielding a conductive GNP film channel of ~400 μm in length and ~11 mm in width. A schematic of the chemiresistor is depicted in Figure 2c. Changes of the GNP-membrane's mass caused by analyte sorption were estimated by QCM measurements. For this purpose, a section of the GNP film was detached from the third quarter of the coated glass slide and deposited onto the active area of a QCM sensor, as described above for resonator fabrication. The fourth quarter of the as-deposited GNP film was used for film thickness determination using atomic force microscopy (AFM).²² Details on the GNP film properties, including AFM and current–voltage measurements, as well as a UV/vis absorbance spectrum, are provided in the Supporting Information (see pages S-4 to S-6).

A custom-designed vacuum chamber was used to probe the influences of sorbed analytes on the vibrational characteristics, the resistance and mass of the GNP membranes. A schematic of the setup is depicted in Figure 2a. The GNP membrane resonator, the GNP chemiresistor, and the GNP membrane coated QCM were mounted onto a printed circuit board equipped with pins, suitable to attach it to a socket in the vacuum chamber. Photographs of the printed circuit board with the three devices are provided in the Supporting Information, page S-9, Figure S5. The vacuum chamber features electrical feedthroughs, suitable to connect the three devices to external measurement hardware. The electrostatically driven GNP membrane resonator (I) was supplied with a drive signal, provided by a function generator (Keysight 33521B) and amplified by a high-voltage amplifier (Falco Systems WMA-300). Oscillations of the freestanding membrane were monitored using a laser interferometer (Nanovibration Analyzer NA, SIOS GmbH) directed onto the center of the resonator through a glass window. Continuously, amplitude spectra of the GNP membrane resonator were recorded following the "frequency sweeping" acquisition protocol, as described in our earlier work.¹⁴ Here, a frequency f_d swept sine drive signal $V = V_{\text{DC}} + V_{\text{AC}} \sin(f_d 2\pi t)$ with $V_{\text{DC}} = 7.5$ V and $V_{\text{AC}} = 3.75$ V was applied to the resonator, sweeping the frequency in the range from 100 to 450 kHz, which contains the fundamental resonance frequency of the device at approximately 200–250 kHz. During the time of the sweep a deflection time trace was recorded using the laser interferometer (65 536 points, sampling rate 2 MHz) indicating pronounced oscillations when the drive frequency matched the resonance frequency of the device. An amplitude spectrum of the resonator was then computed by Fast Fourier Transformation of the deflection data. Resonance frequencies were extracted by fitting a Lorentzian to the fundamental resonance peak in the frequency range of ± 40 kHz at the spectrum's maximum amplitude point. See the Supporting Information, page S-10, for a detailed description of the spectrum acquisition procedure.

The GNP film chemiresistor (II) was connected to a Keithley 2601A source measure unit, applying a constant 1 V bias and continuously monitoring its resistance by measuring the resulting current flowing through the GNP film. Further, the quartz crystal microbalance (III), loaded with a section of the GNP membrane, was placed into the vacuum chamber and connected to an Agilent E5100A network analyzer to monitor the resonance spectrum of the quartz crystal. The network analyzer was locked onto the falling edge of the phase signal to detect shifts of the resonance frequency. The vacuum chamber was equipped with a digital temperature sensor (DS18B20) and a pressure sensor (oerlikon leybold TTR 101N), which features a MEMS Pirani gauge as well as a membrane piezo pressure sensor. The latter is able to measure the absolute chamber pressure in the given pressure range independently of the gas type present. The outlet of the vacuum chamber was connected to a rotary vane pump via a liquid nitrogen cooling trap. Alternatingly, nitrogen (zero gas, ZG) or an analyte-enriched nitrogen gas mixture (AG) with adjustable molar fractions of analyte x_{analyte} were supplied by a commercial calibration system (MCZ Umwelttechnik CGM 2000) at approximately atmospheric pressure. A portion of this gas mixture was fed to the vacuum chamber's inlet by a needle valve, which was adjusted to yield a constant absolute pressure of $P_{\text{abs}} = 20$ mbar within the vacuum cell. By disconnecting the pump and monitoring the resulting pressure increase, the flow rate of AG/ZG into the vacuum cell of $dV/dt \sim 234$ mL s^{-1} was determined. Hence, the atmosphere in the cell (approximate volume of ~277 mL) was rapidly exchanged. The calibration system was set to alternately provide 8 min AG with molar analyte fractions of $x_{\text{analyte}} = 1000, 4000, 7000,$ and $10\,000$ ppm spaced by an 8 min application of ZG. This procedure yielded alternating analyte partial pressure transients in the vacuum cell of $p_{\text{analyte}} = x_{\text{analyte}} P_{\text{abs}}$.

Figure 3b shows the amplitude spectrum of the 6DT cross-linked GNP membrane resonator, depicted by the optical micrograph in Figure 3a. The spectrum was recorded under ZG atmosphere at 20 mbar using the frequency sweeping method, with $V_{\text{DC}} = 10$ V, $V_{\text{AC}} = 5$ V in the frequency range between 0.01 and 2 MHz, and measured with a 5 MHz deflection sampling rate. The spectrum features distinct peaks, with the lowest observed at a frequency of ~220 kHz. We dedicate this resonance peak to the fundamental oscillation of the freestanding membrane. This is confirmed by amplitude mappings, acquired by recording vibrational amplitude spectra at several positions of the circular freestanding membrane. A 3D map of the amplitude maxima observed at the fundamental resonance frequency of ~217 kHz is depicted in the inset of Figure 3b. The amplitude monotonically decays from the center of the membrane to its edges, confirming the assignment of the fundamental resonance mode. In contrast to earlier experiments conducted in higher vacuum (approximately 10^{-1} to 10^{-2} mbar),¹⁴ the peak positions of the higher vibrational modes could not be straightforwardly described considering the model of an oscillating membrane in vacuum with negligible bending stiffness. We dedicate this observation to the higher pressure affecting the membrane vibration (e.g., by damping) or to inhomogeneities of the freestanding membrane through local stress. The pronounced damping of the membrane's oscillation could also be observed by quality factor Q measurements.^{7,14} Figure 3c shows an exemplary deflection time trace of a ring down experiment for the determination of Q . Here, the resonator was excited with 20 cycles of a sine signal ($V_{\text{DC}} = 10$

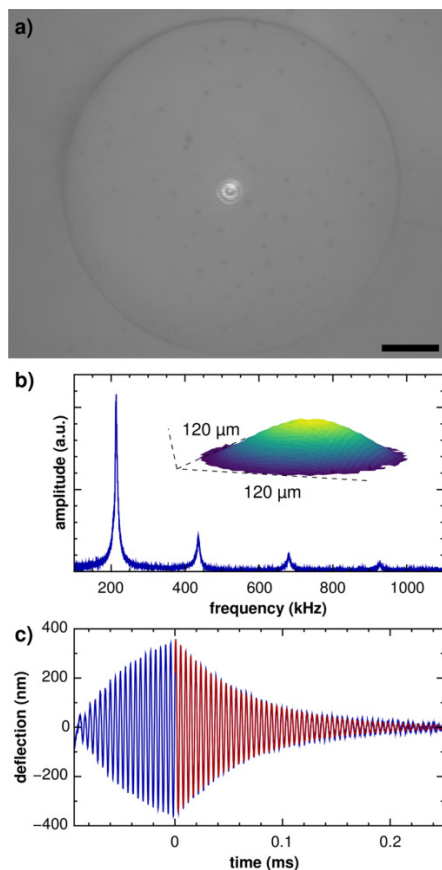


Figure 3. (a) Optical micrograph of the $\sim 120\text{-}\mu\text{m}$ -diameter 6DT cross-linked GNP membrane resonator. The bright spot at the membrane's center represents a reflection of the interferometer's laser. Scale bar: $20\ \mu\text{m}$. (b) Amplitude spectrum of the GNP membrane resonator, measured under 20 mbar nitrogen pressure. The inset depicts the lateral amplitude distribution of the fundamental resonance mode observed at $\sim 217\ \text{kHz}$. (c) Deflection time trace of a ring down experiment conducted under 20 mbar nitrogen pressure with a fit (red line) of the damped harmonic oscillator model.

V , $V_{AC} = 5\ \text{V}$), while simultaneously recording its time-dependent deflection. Afterward, at $t = 0$, the excitation voltage was switched off and the oscillation's decay was recorded. From the data it is clearly visible that the resonator was excited close to saturation and the oscillation quickly decayed after the excitation burst. The oscillation's decay time τ was extracted by fitting the model of a damped harmonic oscillator $h(t) = h_0 \sin(2\pi f_{\text{res}} t + \phi) \exp(-t/\tau)$ to the deflection time trace at $t > 0$ (after the excitation burst) and a quality factor of the resonators fundamental vibrational mode was computed. With five measurements with different excitation burst lengths taken into account (see the Supporting Information, page S-12 to S-14), a quality factor of 45 ± 1 was determined for the resonator investigated in this study. This value is considerably lower than values of several hundreds up to ~ 2000 , determined for comparable resonators in higher vacuum (approximately 10^{-1} to 10^{-2} mbar).¹⁴

To explore the influence of different analyte vapors on the resonator's properties, the calibration system was set to provide

nitrogen mixtures with toluene, 4M2P, 1-propanol, and water. For each analyte, differently concentrated mixtures were fed into the vacuum chamber, yielding analyte partial pressures of up to $\sim 20\ \text{Pa}$. These applications of AG were separated by feeding pure nitrogen gas into the cell. Figure 4a exemplarily depicts the influence of toluene vapor on the vibrational spectrum of the GNP membrane resonator. The measurement reveals a pronounced shift of the fundamental resonance frequency by approximately $10\ \text{kHz}$ (relative shift $\sim 5\%$), caused by the application of toluene with a partial pressure of $p_{\text{toluene}} = 20\ \text{Pa}$. Figure 4b shows the resonance frequency time trace of the respective experiment. It is seen that the magnitude of the frequency shift clearly depends on the applied analyte concentration. During the 8 min transients the frequency shift seems to not fully saturate. This behavior was less pronounced when applying 1-propanol, similar when applying water, and stronger when applying 4M2P vapors. Respective resonance frequency time traces are provided in the Supporting Information (Figures S9 to S12). Further, Figure 4b also depicts the relative resistance change, measured on a second piece of the membrane, as described above. For toluene, the chemiresistor showed a maximum relative resistance increase of 0.23% . Investigations of similar, 6DT cross-linked GNP thin film chemiresistors investigated under ambient pressure showed responses in the same range when loaded with $p_{\text{toluene}} \sim 80\ \text{Pa}$.²⁴

From simultaneous microgravimetric measurements using a $10\ \text{MHz}$ QCM quartz crystal coated with a third section of the GNP membrane only an upper limit of the frequency shifts of $< 2\ \text{Hz}$ could be derived when applying the maximum partial pressure of the different analytes. This is because the transients were strongly superimposed by noise, precluding their individual evaluation (see the time traces in the Supporting Information, Figures S9 to S12). This frequency shift corresponds to an upper limit of mass uptake of $\sim 1\ \text{pg}$ for the freestanding membrane area. The total weight of the freestanding membrane was estimated as $\sim 4.6\ \text{ng}$, taking into account a density of $9.3\ \text{g cm}^{-3}$ for 6DT cross-linked GNP membranes. This value for the density was estimated by a simple geometric approach, approximating the composite as fcc packed gold spheres separated by an edge-to-edge distance of $0.6\ \text{nm}$, as measured for 6DT cross-linked gold nanocomposites by SAXS.²⁵ By using the equation for the fundamental resonance frequency of a clamped circular membrane in vacuum,^{10,14} a rough estimate of the resonator's frequency shift $\Delta f_0 = -23\ \text{Hz}$ was computed for the maximum mass uptake of $\sim 1\ \text{pg}$. Hence, the mass uptake is obviously not exclusively accountable for the comparably high sensitivity of the oscillator's resonance behavior. From earlier experiments, probing the chemiresistive properties of GNP films, it is known that sorption of organic compounds within the organic matrix consisting of alkanethiols or α,ω -alkanedithiols leads to swelling.^{19,26} Consequently, we assume that analyte sorption reduces the membrane's pre-stress, causing a significant decrease of the membrane's resonance frequency and thereby enabling the observed highly sensitive detection of analytes. According to the equation for the fundamental resonance frequency of a circular membrane resonator in vacuum,^{10,14} a fundamental frequency shift of $\Delta f_0 \sim -10\ \text{kHz}$ corresponds to a decrease of the membrane's pre-stress by $\sim 0.97\ \text{MPa}$. With a biaxial modulus of $Y = 8.9\ \text{GPa}$, as measured by bulge tests previously,²⁷ this equates to a decrease in prestrain corresponding to an elongation of the membrane of roughly $\Delta \epsilon = \Delta \sigma / Y =$

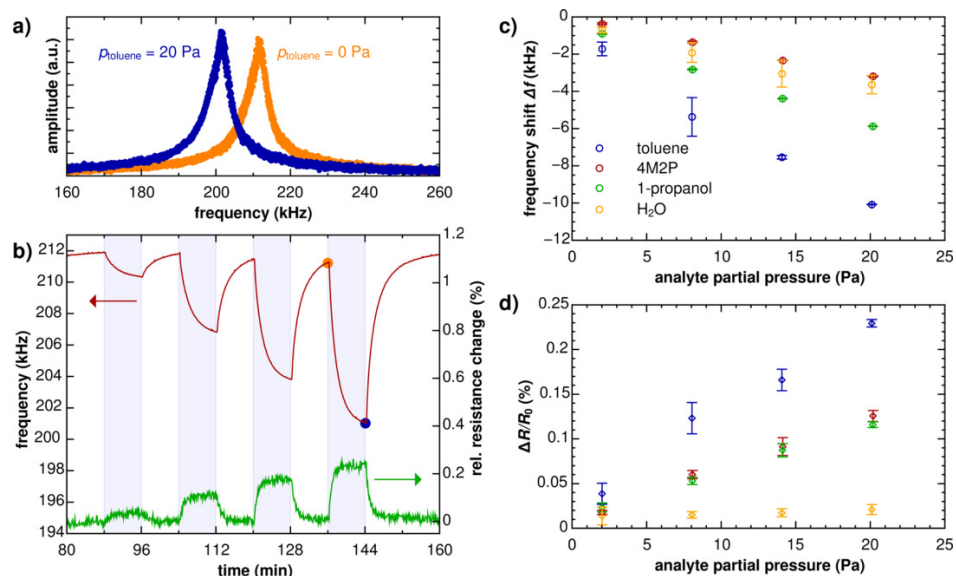


Figure 4. (a) Influence of toluene vapor on the vibrational amplitude spectrum of a 120- μm -diameter 6DT cross-linked GNP membrane resonator. The spectra were acquired at an absolute pressure of 20 mbar and toluene partial pressures of $p_{\text{toluene}} = 0$ (orange curve) and $p_{\text{toluene}} = 20$ Pa (blue curve). (b) Frequency response transients of the GNP membrane resonator (red curve) and resistance response transients of a chemiresistor (green curve) fabricated from the same GNP film, measured when dosing the devices with toluene vapor at partial pressures of 2, 8, 14, and 20 Pa. The orange and blue dots mark the resonance frequencies determined from respective curves shown in (a). (c) Frequency shifts of the GNP membrane resonator under exposure to different partial pressures of toluene, 4M2P, 1-propanol, and water. (d) Corresponding relative resistance changes of the GNP thin film chemiresistor.

0.01%. We note, however, that a sorption-induced lowering of the biaxial modulus would also result in a decrease in pre-stress. Even though this approximate model implies several simplifications, it clearly indicates the strong impact of sorption-induced changes of the membrane's pre-stress on the resonance frequency. The effect of changes in bulk stress of polymeric resonators due to sorption of vapors was studied earlier²⁸ and reported by Schmid et al. for SU-8 microstring resonators exposed to water vapor. They observed decays of the microstrings' resonance frequencies in the tens of percent range when altering the relative humidity of their environment between 3% and 60%.²⁹ In this context, it should be taken into consideration that the SU-8 structure supporting our cross-linked GNP membrane could potentially take up solvent and swell when exposed to vapors. This again may slightly influence the resonator's geometry and, hence, may affect the pre-stress of the GNP membrane. However, we could rule out this possibility by fabricating resonators using structured Si/SiO₂ substrates, i.e., without containing any polymeric resist material. When exposing such a device to toluene vapor similar frequency shifts were observed as in the case of the SU-8 structured devices (see Supporting Information, pages S-20/S-21, Figure S13). Hence, impact of SU-8 swelling on the sensor response can be excluded.

Figure 4c,d depicts the fundamental resonance frequency shifts of the GNP membrane resonator and the relative resistance changes of the GNP membrane observed during the exposure to different analyte vapors and analyte partial pressures. We note that the sensitivities of the resonator and the chemiresistor to toluene, 1-propanol, and water qualitatively show the same trend, i.e., with lower sensitivities for the more polar analytes. This seems reasonable, as both sensing

mechanisms are presumably based on the sorption of the analytes within the organic matrix of the GNP films.

As shown in previous work,¹⁹ the partition coefficient for sorption of an analyte in GNP films is usually governed by the solubility match between the organic ligand matrix and the analyte. Hence, because the 6DT cross-linker is hydrophobic, the partition coefficient for polar analytes, such as water and 1-propanol, is expected to be significantly lower than for hydrophobic molecules, such as toluene. However, while the resistance–time trace recorded when dosing the chemiresistor with water vapor shows almost no measurable signals, the membrane resonator displays measurable frequency shifts (Supporting Information, page S-19, Figure S12). We attribute this finding to the different transduction mechanisms of both types of sensors. In the case of the resonator, already small amounts of sorbed water seem able to decrease the pre-stress of the GNP membrane leading to sizable frequency shifts. In the case of the resistor, two countervailing effects have to be taken into consideration. On the one hand, small amounts of water sorbed within the organic matrix cause some swelling, which leads to increased nanoparticle distances and, thus, should provoke an increase in resistance. On the other hand, water has a high permittivity. Therefore, sorption of water increases the effective permittivity of the organic matrix and this should lead to a decrease of the film's resistance.¹⁹ Thus, in our experiments it seems that in the case of water sorption these two effects cancel each other out, leading to only very faint resistance changes.

While the sensitivities of the chemiresistor toward 1-propanol and 4M2P are comparable, the resonator shows the lowest sensitivity toward 4M2P. However, the different sensitivities of the two sensors for 4M2P are difficult to

compare because the response kinetics for this analyte are very slow and the transients are still far from reaching saturation at the end of vapor exposure (Supporting Information, page S-17, Figure S10).

CONCLUSIONS

In this paper we demonstrated the application of electrostatically driven drumhead resonators comprising freestanding membranes of cross-linked gold nanoparticles for sensing volatile analytes in the gas phase under reduced pressure. The circular resonator investigated in this study was dosed with vapors of toluene, 4M2P, 1-propanol, and water with varying partial pressures. Showing different but overall high sensitivities to the four analytes, frequency shifts of up to ~ 10 kHz, i.e., $\sim 5\%$ of the fundamental resonance frequency, were observed during the exposure to toluene vapor at a partial pressure of 20 Pa. This novel approach of vapor sensing using freestanding GNP membranes can be employed as a complementary method to amend conventional chemiresistive measurements, even in a single device. Next steps involve a comprehensive, systematic study identifying the resonators' sensitivities and tuning their selectivities by varying the membrane's composition. For the targeted application as gas or vapor sensor, measurements at higher or even atmospheric pressure are of great interest. This could potentially be enabled by modifications of the device's geometry and the membrane's pre-stress or utilizing quasi-static deflection methods for extracting mechanical properties of the GNP membranes. A further goal is the facile acquisition of the amplitude spectrum by enabling a full electronic signal readout to replace the interferometer used in our current study.

EXPERIMENTAL SECTION

Synthesis of Gold Nanoparticles. A solution of dodecylamine (12A)-stabilized GNPs in heptane was prepared following the procedure by Leff et al.³⁰ The particles were characterized using transmission electron microscopy (Philips CM 300, operated at 200 kV) and UV/vis spectroscopy (Varian Cary 50). Prior to TEM analysis, a ligand exchange with 1-dodecanethiol (12T) was performed to render the particles stable under TEM conditions.²² The particles had an average diameter of 3.4 ± 0.6 nm. A representative transmission electron micrograph, a histogram of particle diameters, as well as a UV/vis absorbance spectrum are provided in the Supporting Information, Figures S1 and S2.

Fabrication of 6DT Cross-Linked GNP Films. 1,6-Hexanedithiol (6DT) cross-linked GNP films were fabricated following a spin-coating based procedure described in an earlier work,²² with slight modifications.¹⁴ First, glass substrates (borosilicate glass cover slides, 22×22 mm²) were cleaned by sonication in acetone and subsequently rinsed in demineralized water. Afterward, the glass substrates were treated in an oxygen plasma (spi Supplies Plasma Prep II).

6DT cross-linked GNP films were deposited by rotating the substrates at a constant rate of 3000 min⁻¹ on a spin-coater. Initially, 2×100 μ L of a solution containing 7.4 mM 6DT in toluene were deposited. Afterward, 10 μ L of the GNP solution in heptane and 2×10 μ L of a solution containing 7.4 mM 6DT in methanol were applied. The applications of the GNP solution and the methanolic linker solution represent one deposition cycle. For the preparation of the GNP membrane used for resonator fabrication, this deposition cycle was performed four times to achieve the desired film thickness. Between all applications of solutions a time delay of ~ 20 s was kept. Eventually, the films were immersed into the methanolic linker solution overnight, rinsed in acetone, and dried under ambient conditions.

UV/vis absorbance spectra of the GNP films were recorded using a Varian Cary 50 spectrometer and the film thickness was determined by

atomic force microscopy (AFM) using a Digital Instruments Multimode machine, equipped with a Veeco 100 μ m scanner. The conductivity of the films was measured by depositing ~ 100 -nm-thick gold electrodes onto a section of the film using a shadow mask and recording current–voltage data using an Agilent 4156C semiconductor parameter analyzer. A UV/vis absorbance spectrum, topographic AFM scans, and current–voltage data of the substrate-supported GNP film used for resonator fabrication are provided in the Supporting Information, Figures S2, S3, and S4.

Fabrication of 3D Microelectrode Structures and Transfer of GNP Membranes. 3D microelectrode structures were fabricated as described earlier with slight variations.¹⁴ A detailed description of the lithographic fabrication process is provided in the Supporting Information, pages S-7/S-8. GNP membranes were transferred to the structures by flotation of the GNP film coated glass substrates on demineralized water for approximately 3 days. Afterward, the glass substrates were carefully immersed into the water phase and the GNP membranes remained floating at the liquid–air interfaces. The membranes were then transferred onto the microstructures by skimming them from the liquid/air interface.

Electrostatic Excitation and Resonance Frequency Measurements. AC voltages were applied to excite oscillations of the GNP membrane drumhead resonator under different atmospheres. The excitation signal was provided by a Keysight 33521A function generator and amplified by a Falco Systems WMA-300 high voltage amplifier. Deflection time traces of the freestanding membrane were recorded using a SIOS Nanovibration Analyser NA. After setting the absolute cell pressure (20 mbar) with nitrogen (ZG) and adjusting the interferometer laser to the center of the GNP membrane, a delay of ~ 3 h was kept before introducing the analyte gas (AG) and starting the measurement. This was done to minimize drifts of the resonance frequencies, presumably caused by heating of the membrane by the laser until reaching thermal equilibrium or by the equilibration of the initial pressure difference between the resonator cavity and the measurement cell after setting the cell pressure. Detailed descriptions of the data acquisition protocols and data evaluation process are provided in the Supporting Information, pages S-10/S-11.

ASSOCIATED CONTENT

Supporting Information

The Supporting Information is available free of charge on the ACS Publications website at DOI: 10.1021/acssensors.6b00831.

Characterization of the gold nanoparticles and substrate supported GNP films, a detailed description of the lithographic processing and measurement methods, time traces of all chemical sensor experiments, and a control experiment involving a resonator comprising a non-polymeric supporting microstructure (PDF)

AUTHOR INFORMATION

Corresponding Author

*E-mail: tobias.vossmeier@chemie.uni-hamburg.de.

ORCID

Hendrik Schlicke: 0000-0002-6977-4042

Malte Behrens: 0000-0001-5982-5080

Clemens J. Schröter: 0000-0001-9201-6883

Gregor T. Dahl: 0000-0003-2299-9639

Hauke Hartmann: 0000-0002-2912-4862

Tobias Vossmeier: 0000-0001-9738-3826

Notes

The authors declare no competing financial interest.

ACKNOWLEDGMENTS

The work of H.S. is supported by a scholarship of the Joachim Herz Stiftung. T.V. acknowledges financial support by the DFG, grant number VO698/3-1. We thank Sophia Bittinger, who contributed to this study within the framework of her Bachelor thesis, and Katharina Nieswandt, who contributed within the framework of an advanced lab internship.

REFERENCES

- (1) Sauerbrey, G. Verwendung von Schwingquarzen zur Wägung dünner Schichten und zur Mikrowägung. *Z. Phys.* **1959**, *155*, 206–222.
- (2) Lassagne, B.; Garcia-Sanchez, D.; Aguasca, A.; Bachtold, A. Ultrasensitive mass sensing with a nanotube electromechanical resonator. *Nano Lett.* **2008**, *8*, 3735–3738.
- (3) Jensen, K.; Kim, K.; Zettl, A. An atomic-resolution nano-mechanical mass sensor. *Nat. Nanotechnol.* **2008**, *3*, 533–7.
- (4) Bunch, J. S.; van der Zande, A. M.; Verbridge, S. S.; Frank, I. W.; Tanenbaum, D. M.; Parpia, J. M.; Craighead, H. G.; McEuen, P. L. Electromechanical resonators from graphene sheets. *Science* **2007**, *315*, 490–3.
- (5) Lee, J.; Wang, Z.; He, K.; Shan, J.; Feng, P. X. L. High frequency MoS₂ nanomechanical resonators. *ACS Nano* **2013**, *7*, 6086–6091.
- (6) Castellanos-Gomez, A.; Van Leeuwen, R.; Buscema, M.; Van Der Zant, H. S. J.; Steele, G. A.; Venstra, W. J. Single-layer MoS₂ mechanical resonators. *Adv. Mater.* **2013**, *25*, 6719–6723.
- (7) Wang, Z.; Jia, H.; Zheng, X.; Yang, R.; Wang, Z.; Ye, G. J.; Chen, X. H.; Shan, J.; Feng, P. X.-L. Black phosphorus nanoelectromechanical resonators vibrating at very high frequencies. *Nanoscale* **2015**, *7*, 877–884.
- (8) Zhang, X.; Waitz, R.; Yang, F.; Lutz, C.; Angelova, P.; Götzhäuser, A.; Scheer, E. Vibrational modes of ultrathin carbon nanomembrane mechanical resonators. *Appl. Phys. Lett.* **2015**, *106*, 063107.
- (9) Markutsya, S.; Jiang, C.; Pikus, Y.; Tsukruk, V. V. Freely suspended layer-by-layer nanomembranes: Testing micromechanical properties. *Adv. Funct. Mater.* **2005**, *15*, 771–780.
- (10) Kanjanaboos, P.; Lin, X. M.; Sader, J. E.; Rupich, S. M.; Jaeger, H. M.; Guest, J. R. Self-assembled nanoparticle drumhead resonators. *Nano Lett.* **2013**, *13*, 2158–2162.
- (11) Jiang, C.; Markutsya, S.; Pikus, Y.; Tsukruk, V. V. Freely Suspended Nanocomposite Membranes as Highly Sensitive Sensors. *Nat. Mater.* **2004**, *3*, 721–728.
- (12) Jiang, C.; McConney, M. E.; Singamaneni, S.; Merrick, E.; Chen, Y.; Zhao, J.; Zhang, L.; Tsukruk, V. V. Thermo-Optical Arrays of Flexible Nanoscale Nanomembranes Freely Suspended over Micro-fabricated Cavities as IR Microimagers. *Chem. Mater.* **2006**, *18*, 2632–2634.
- (13) Gauvin, M.; Grisolia, J.; Alnasser, T.; Viallet, B.; Xie, S.; Brugger, J.; Ressler, L. Electro-mechanical sensing in freestanding monolayered gold nanoparticle membranes. *Nanoscale* **2016**, *8*, 11363–11370.
- (14) Schlicke, H.; Schröter, C. J.; Vossmeier, T. Electrostatically driven drumhead resonators based on freestanding membranes of cross-linked gold nanoparticles. *Nanoscale* **2016**, *8*, 15880–15887.
- (15) Wohltjen, H.; Snow, A. W. Colloidal Metal-Insulator-Metal Ensemble Chemiresistor Sensor. *Anal. Chem.* **1998**, *70*, 2856–2859.
- (16) Olichwer, N.; Leib, E. W.; Halfar, A. H.; Petrov, A.; Vossmeier, T. Cross-linked gold nanoparticles on polyethylene: Resistive responses to tensile strain and vapors. *ACS Appl. Mater. Interfaces* **2012**, *4*, 6151–6161.
- (17) Ibanez, F. J.; Zamborini, F. P. Chemiresistive sensing with chemically modified metal and alloy nanoparticles. *Small* **2012**, *8*, 174–202.
- (18) He, J.; Lin, X. M.; Chan, H.; Vuković, L.; Král, P.; Jaeger, H. M. Diffusion and filtration properties of self-assembled gold nanocrystal membranes. *Nano Lett.* **2011**, *11*, 2430–2435.
- (19) Olichwer, N.; Meyer, A.; Yesilmen, M.; Vossmeier, T. Gold nanoparticle superlattices: correlating chemiresistive responses with analyte sorption and swelling. *J. Mater. Chem. C* **2016**, *4*, 8214–8225.
- (20) Joseph, Y.; Krasteva, N.; Besnard, I.; Guse, B.; Rosenberger, M.; Wild, U.; Knop-Gericke, A.; Schlögl, R.; Krustev, R.; Yasuda, A.; Vossmeier, T. Gold-nanoparticle/organic linker films: self-assembly, electronic and structural characterisation, composition and vapour sensitivity. *Faraday Discuss.* **2004**, *125*, 77–97.
- (21) Wan, Y.; Goubet, N.; Albouy, P.-A.; Schaeffer, N.; Pileni, M.-P. Hierarchy in Au Nanocrystal Ordering in a Supracrystal: II. Control of Interparticle Distances. *Langmuir* **2013**, *29*, 13576–13581.
- (22) Schlicke, H.; Schröder, J. H.; Trebbin, M.; Petrov, A.; Ijeh, M.; Weller, H.; Vossmeier, T. Freestanding films of crosslinked gold nanoparticles prepared via layer-by-layer spin-coating. *Nanotechnology* **2011**, *22*, 305303.
- (23) Schlicke, H.; Battista, D.; Kunze, S.; Schröter, C. J.; Eich, M.; Vossmeier, T. Freestanding Membranes of Cross-Linked Gold Nanoparticles: Novel Functional Materials for Electrostatic Actuators. *ACS Appl. Mater. Interfaces* **2015**, *7*, 15123–15128.
- (24) Joseph, Y.; Besnard, I.; Rosenberger, M.; Guse, B.; Nothofer, H.-G.; Wessels, J. M.; Wild, U.; Knop-Gericke, A.; Su, D.; Schlögl, R.; Yasuda, A.; Vossmeier, T. Self-Assembled Gold Nanoparticle/Alkanedithiol Films: Preparation, Electron Microscopy, XPS-Analysis, Charge Transport, and Vapor-Sensing Properties. *J. Phys. Chem. B* **2003**, *107*, 7406–7413.
- (25) Schröder, J. H. Herstellung und Charakterisierung von Schichtsystemen aus Gold-Nanopartikeln. Dissertation, Universität Hamburg, 2012.
- (26) Joseph, Y.; Peic, A.; Chen, X.; Michl, J.; Vossmeier, T.; Yasuda, A. Vapor Sensitivity of Networked Gold Nanoparticle Chemiresistors: Importance of Flexibility and Resistivity of the Interlinkage. *J. Phys. Chem. C* **2007**, *111*, 12855–12859.
- (27) Schlicke, H.; Rebber, M.; Kunze, S.; Vossmeier, T. Resistive pressure sensors based on freestanding membranes of gold nanoparticles. *Nanoscale* **2016**, *8*, 183–186.
- (28) Boisen, A.; Dohn, S.; Keller, S. S.; Schmid, S.; Tenje, M. Cantilever-like micromechanical sensors. *Rep. Prog. Phys.* **2011**, *74*, 036101.
- (29) Schmid, S.; Kühne, S.; Hierold, C. Influence of air humidity on polymeric microresonators. *J. Micromech. Microeng.* **2009**, *19*, 065018.
- (30) Leff, D. V.; Brandt, L.; Heath, J. R. Synthesis and Characterization of Hydrophobic, Organically-Soluble Gold Nanocrystals Functionalized with Primary Amines. *Langmuir* **1996**, *12*, 4723–4730.

6 Unpublished Work and Further Publications

This chapter summarizes the results of two projects, which are currently being prepared for publication. The first section (6.1) describes a project aiming at the mechanical characterization of freestanding GNP membranes, cross-linked with different chain-length ADT molecules as well as 1,4-benzenedithiol (BDT). The elasticity of these membranes was determined utilizing bulge tests with AFM based deflection readout.

Within the second section 6.2, the characterization of electrostatically driven resonators comprising freestanding 6DT cross-linked GNP membranes of different sizes and geometries is reported. This project connects to the related publication outlined in the synopsis, section 5.4 and reprinted in section 5.4.5.

Further, additional results as well as three conference proceedings articles are included. Section 6.4 contains a proceedings article, describing our advances in device fabrication and characterization of GNP membrane pressure sensors and electrostatic actuators. The article relates to a talk held in May 2016 at the TechConnect Nanotech 2016 conference in Washington, DC, USA.

Section 6.5 contains a proceedings article, summarizing the novel concepts for electromechanical chemical sensing using GNP membrane resonators and actuators, as discussed in sections 5.5 and 6.3.2, respectively.

The applications of GNP membrane based MEMS and NEMS for pressure (section 5.2) and chemical sensing (section 5.5) are outlined in a further conference proceeding, related to a talk scheduled in October 2017 at the IEEE Nanotechnology Materials and Devices Conference (NMDC) 2017 in Singapore.

6.1 Freestanding Membranes of Gold Nanoparticles Cross-Linked by α, ω -Alkanedithiols: Elasticity as a Function of the Alkane Chain Length

Hendrik Schlicke,[‡] Svenja Kunze,[‡] Elisabeth W. Leib, Maik Finsel, Clemens J. Schröter, Tobias Vossmeier

[‡]Contributed equally to this study.

Composite materials comprised of DT cross-linked GNPs feature interesting optical and electronic properties, which can be tuned by the choice of different GNP sizes or variation of the molecular structure and length of the DT cross-linker molecules. These properties, as well as their dependence on the aforementioned parameters were extensively studied throughout recent years.^[49,52,53,55,57] Besides their optical and electronic properties, also mechanical and electromechanical properties of GNP composites are believed to strongly depend on the material composition. From an engineering perspective, potential applications of novel materials in NEMS/MEMS devices, as proposed in the foregoing projects, require substantial knowledge of tunable (electro-)mechanical characteristics of the materials for appropriate device design and to enable fabrication methods, such as contact printing or roll-to-toll processing. On the other hand, from a basic science perspective, the characterization of these properties is essential for the understanding of structure-property relations.

6.1.1 Materials and Preparation Methods

The following section summarizes a yet unpublished study addressing the structural and mechanical properties of GNP membranes, cross-linked with different DTs, i.e., 1,3-propanedithiol (3DT), 1,4-butanedithiol (4DT), 1,5-pentanedithiol (5DT), 1,6-hexanedithiol (6DT), 1,8-octanedithiol (8DT), 1,9-nonanedithiol (9DT), 1,10-decanedithiol (10DT), as well as 1,4-benzenedithiol (BDT). Structural characterization of the composite materials was performed by TEM, AFM and X-ray diffraction (XRD). Further, optical (UV/vis absorption) and charge transport (temperature dependent conductivity) properties were studied. The elasticity of the membranes was analyzed using an AFM based bulge test method, as it was used for the characterization of 9DT/GNP composites in our earlier study.^[48]

To this end, GNP films, cross-linked with different chain-length ADTs and BDT were deposited onto glass substrates and XRD sample carriers by spin-coating,^[52] as described in section 5.1.1. Five batches of 12A-stabilized GNPs and the eight different DTs were applied for film preparation. The average diameters of the gold nanoparticles used in this study are provided in table 6.1. The thicknesses t_m of all GNP films, ranging between

Table 6.1: Average GNP diameters used for film fabrication.

GNP batch	diameter D /nm
GNP1	3.4 ± 1.0
GNP2	3.9 ± 0.5
GNP3	3.8 ± 0.7
GNP4	4.0 ± 0.6
GNP5	4.0 ± 0.7

21 nm and 51 nm, were determined by AFM. While optical and electronic investigations, as well as XRD were conducted using these samples supported by their original substrates, the films were detached and transferred to carbon coated TEM substrates or metal substrates featuring $\sim 100 \mu\text{m}$ sized circular apertures for TEM analysis or bulge testing, respectively. Film detachment and transfer was conducted similarly as described in section 5.1.3. However, in this study, 5 out of 35 film samples were floated on diluted sodium hydroxide solution ($\sim 0.1 - 0.4 \text{ M}$), which was exchanged by DI water after detachment of the films, and before skimming them from the liquid-air interface. Also, in this study detachment of the films was not forced. Rather than actively immersing the glass substrates into the aqueous phase to force the detachment of the GNP films, they were floated on the aqueous phase for up to three days until detachment from the glass substrates occurred by itself.

6.1.2 X-Ray Diffraction

In an earlier study,^[52] GNP/ADT composite films were analyzed by means of XRD to identify possible aggregation and fusion of the GNPs incorporated in the materials during the deposition process. X-ray diffractograms were evaluated with respect to peak widths, to assess crystalline domain sizes using the Scherrer method.^[223] It was observed that GNP composite films, fabricated following the spin-coating method and using 9DT as cross-linker, showed similar peak widths and hence similar crystalline domain sizes as a drop-casted sample of as-prepared GNPs. In contrast, drop-casted GNPs treated with methanol (which is used as solvent for the DTs within the spin-coating process), omitting the addition of a DT, showed significantly narrower XRD signals. This observation was indicative for particle fusion.^[52] However, we note that the absence of XRD peak narrowing is not evident for the absence of non-epitaxial particle fusion or aggregation, as this would not lead to the formation of larger coherent crystalline domains.

Figure 6.1 shows exemplary X-ray diffractograms of GNP composites cross-linked using 4DT and 10DT, as well as a drop-casted sample of GNP-1 (used for fabrication of the respective films). Qualitatively, the diffraction data are similar for all samples, except for variations in the signal-noise ratio presumably caused by varying amounts of material deposited onto the sample carriers. The Scherrer equation^[223] (equation 6.1) was utilized to compute crystalline domain sizes from the full width at half maximum (FWHM) of the

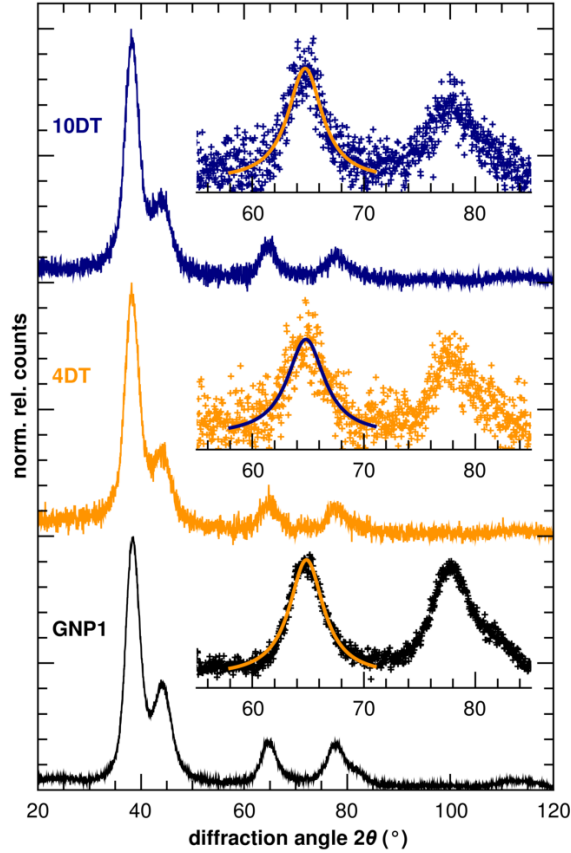


Figure 6.1: X-ray diffractograms of 4DT and 10DT cross-linked GNP films deposited via spin-coating. Further, an X-ray diffractogram of a drop-casted sample of the GNP batch (GNP1) used for composite fabrication is shown as reference. Insets depict additional X-ray diffractograms of the 55 to 85° 2θ range, with Lorentzians fitted to the gold (220) reflection.

Table 6.2: Peak positions and FWHM of the (220) reflections, as well as calculated crystalline domain sizes of GNP films cross-linked by different ADTs and 12A-stabilized GNPs (GNP1) drop-casted from the stock solution.

sample/ADT	peak position $2\theta_{(220)}/^\circ$	peak FWHM $\Delta(2\theta)/^\circ$	crystalline domain size L/nm
GNP1	64.8	3.74 ± 0.07	2.79
4DT	64.8	3.59 ± 0.14	2.90
6DT	64.7	3.73 ± 0.14	2.80
8DT	64.8	3.35 ± 0.12	3.11
9DT	64.7	3.87 ± 0.13	2.70
10DT	64.7	3.43 ± 0.11	3.04

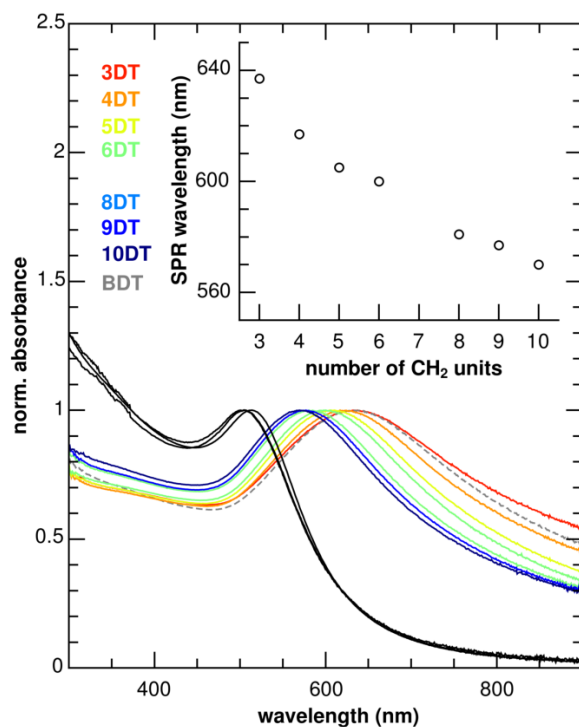


Figure 6.2: UV/vis absorbance spectra of GNP composite films, cross-linked using different DTs. The spectra are normalized to the absorbance at the SPR maximum. The inset shows the SPR peak wavelength plotted against the length of the ADT cross-linker. Spectra of the diluted GNP stock solutions are depicted as black lines.

(220) reflections, extracted by fitting Lorentzians to the diffraction data (see the insets in figure 6.1).

$$L = \frac{\lambda}{\Delta(2\theta) \cdot \cos \theta_{(220)}} \quad (6.1)$$

Here, $\lambda = 0.154$ nm denotes the X-ray wavelength, $\Delta(2\theta)$ is the FWHM, $\theta_{(220)}$ represents the diffraction angle at the peak maximum and L is the crystalline domain size. Values of 2.8, 2.9 and 3.0 nm were determined for the GNP-1, 4DT and 10DT samples, respectively. For further samples, cross-linked by 6DT, 8DT and 9DT, similar values were observed (see table 6.2). Because these samples as well as the GNPs deposited from the stock solution showed only little deviations of L , which are supposedly within the experimental error, XRD shows no indication of particle fusion or aggregation with increased crystallographic domains.

6.1.3 UV/vis Spectroscopy

UV/vis spectroscopy is a powerful technique for the characterization of isolated GNPs, e.g. in solution, as well as their composites. The SPR absorption band of GNPs critically

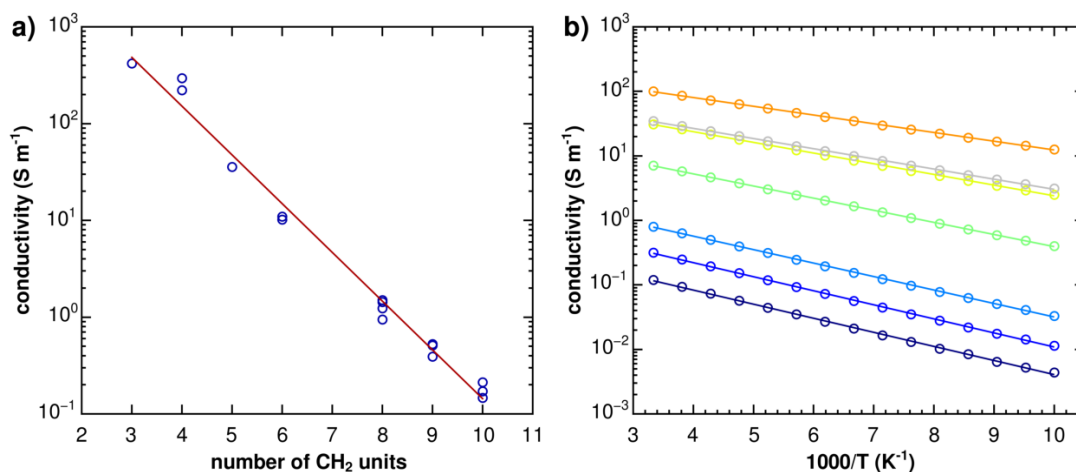


Figure 6.3: a) Room-temperature conductivities of GNP films cross-linked using ADTs with different chain length. b) Arrhenius plots showing the conductivities of GNP film samples cross-linked using 4DT \circ , 5DT \circ , 6DT \circ , 8DT \circ , 9DT \circ , 10DT \circ , as well as BDT \circ . Charge transport activation energies determined from linear fits to the data (solid lines) are denoted in table 6.3.

depends on the surrounding of the particles, especially on interparticle distances, and yields valuable information on the GNP/DT composites' nanostructure. Figure 6.2 depicts UV/vis absorbance spectra of GNP films cross-linked with ADTs having 3 to 10 methylene units as well as films cross-linked with BDT. Further, the absorbance spectra of the GNP batches used for film fabrication are included as reference. All spectra are normalized to the absorbance measured at the SPR peak. The strong red-shift of the films' SPR peaks with respect to the spectra of the isolated GNPs in solution is due to the markedly reduced interparticle distances in the films. The high density of particles leads on the one hand to a change in their dielectric environment. Such effects were theoretically described using the Maxwell-Garnett effective medium theory^[91,92] and confirmed experimentally.^[90] On the other hand, at very short interparticle distances plasmon coupling becomes significant and leads to strong red-shifts of the SPR band.^[88] The inset of the figure shows a plot of the SPR absorbance maximum wavelengths against the respective length of the ADTs. The graph clearly reveals a gradual drop of the SPR wavelength with an increasing length of the ADT. This result evidences that the average interparticle distances are governed by the length of the ADTs. Besides, it was observed that GNP films treated with BDT and 3DT show an SPR maximum in a comparable wavelength range.

6.1.4 Charge Transport Characterization

Charge transport through GNP composites is governed by a thermally activated tunneling processes. Therefore, the conductivity of these materials dramatically decreases with increasing interparticle distance (section 3.2.2). Figure 6.3a shows room-temperature conductivities of several GNP films cross-linked with different ADT cross-linkers plotted on a log-scale against their alkane chain length. The plot exhibits an approximately linear relation, as expected taking into account the biexponential model for conductivity

Table 6.3: Conductivities at 300 K as well as transport activation energies E_a determined for GNP/DT composites from charge transport measurements at varying temperature.

Linker	$\sigma_{300\text{K}}/(\text{S cm}^{-1})$	E_a/meV
4DT	1.0	27
5DT	3.1×10^{-1}	33
6DT	7.1×10^{-2}	37
8DT	8.0×10^{-3}	41
9DT	3.2×10^{-3}	43
10DT	1.2×10^{-3}	43
BDT	3.4×10^{-1}	31

(cf. section 3.2.2) and assuming only minor influence of interparticle distance changes on the transport activation energy E_a . The observed linker dependence of the conductivity also suggests that the interparticle distances are determined by the choice of the ADT cross-linker, indicating that no major fusion or aggregation of nanoparticles within the composite has taken place.

Additionally, low-temperature charge transport measurements were conducted in a temperature range between 100 and 300 K. Figure 6.3b shows Arrhenius plots of conductivities for the differently cross-linked GNP films. The linear, monotonically decreasing graphs confirm the non-metallic charge transport behavior and the Arrhenius type activation, as suggested by the biexponential model. The figure further shows that GNP films cross-linked using BDT exhibit similar charge transport behavior as the 5DT cross-linked films. Table 6.3 summarizes the conductivities measured at 300 K, as well as charge transport activation energies extracted from linear fits to the data. The measured conductivities are in good agreement with values from earlier reports on GNP/ADT composite films.^[52,53] However, in the case of 6DT and 9DT cross-linked films, the observed activation energies are somewhat lower than values determined for layer-by-layer self-assembled samples.^[53] This could be due to differences in the particle sizes or particle size distributions.

6.1.5 Transmission Electron Microscopy

To gain insight into the composites' nanostructure, TEM was conducted. For this purpose, GNP membranes were transferred onto carbon-coated TEM substrates. Representative transmission electron micrographs of composites cross-linked with 4DT, 10DT and BDT are depicted in figure 6.4. The images show a quite homogeneous appearance on a larger scale, and clearly reveal the disordered, granular structure of the films at higher magnifications. We reported similar observations for 9DT^[48] and 6DT^[1] cross-linked films in earlier studies. However, the micrographs indicate a more coarse granularity for membranes cross-linked with shorter chain-length ADTs. These larger features may point to a partial aggregation of the particles. This observation is in contrast to the above-mentioned XRD experiments. However, we note that the quantitative analysis of interparticle dis-

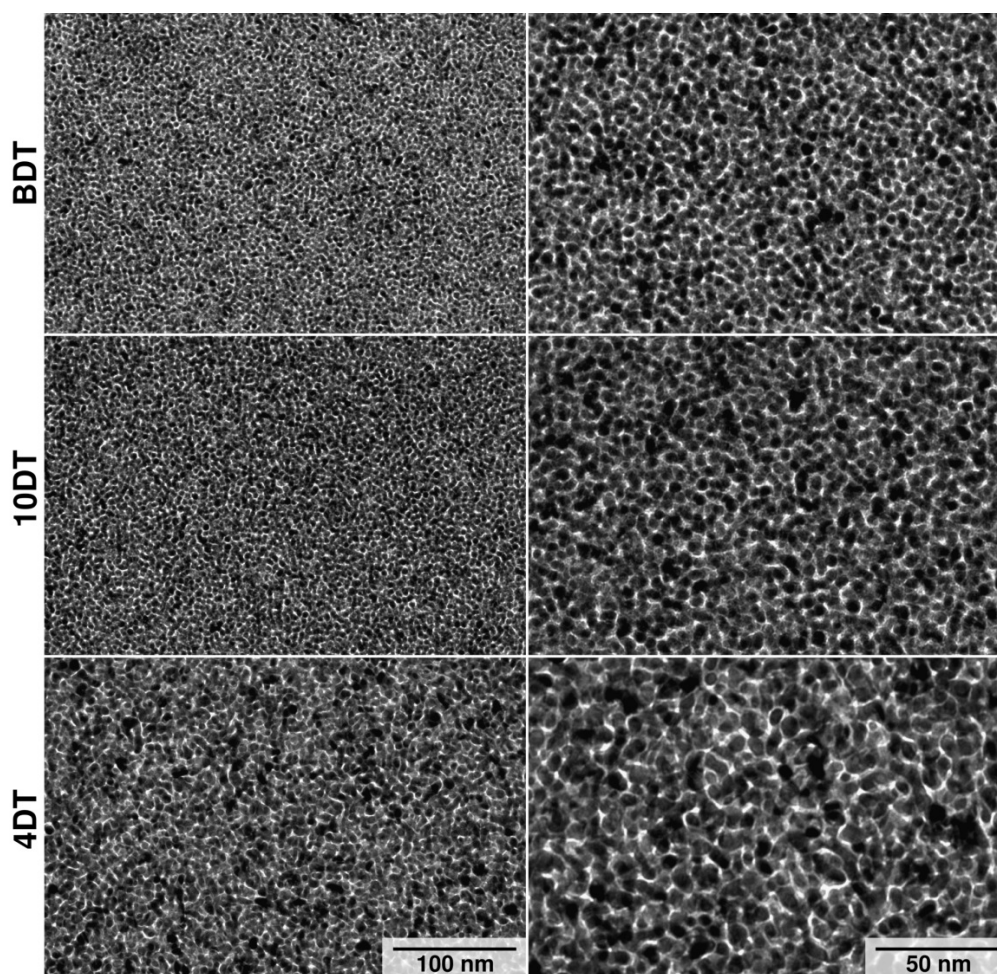


Figure 6.4: Transmission electron micrographs of GNP membranes cross-linked with different DTs, transferred to TEM substrates. The rows show the differently cross-linked samples as indicated, while the columns depict different magnifications.

tances and particle sizes from the TEM images is not possible, due to the disordered, multilayered structure of the films. Further, the effects of the different ADT chain length on the overall appearance of the transmission electron micrographs is hard to predict. Interestingly, images of GNP films cross-linked using BDT are very similar to micrographs of the longer-chain 10DT cross-linked films, even though they reveal optical and electronic properties rather resembling those of films cross-linked using shorter chain ADTs.

6.1.6 Elasticity

Recently, we used bulge tests with AFM deflection readout to determine the elastic and viscoelastic properties of 9DT cross-linked GNP membranes.^[48] In this project, we applied the technique to study the influence of the ADT crosslinker's chain length on the GNP membranes' elastic properties. For the bulge tests GNP membranes were deposited onto substrates featuring $\sim 100\mu\text{m}$ diameter circular apertures. The samples were mounted

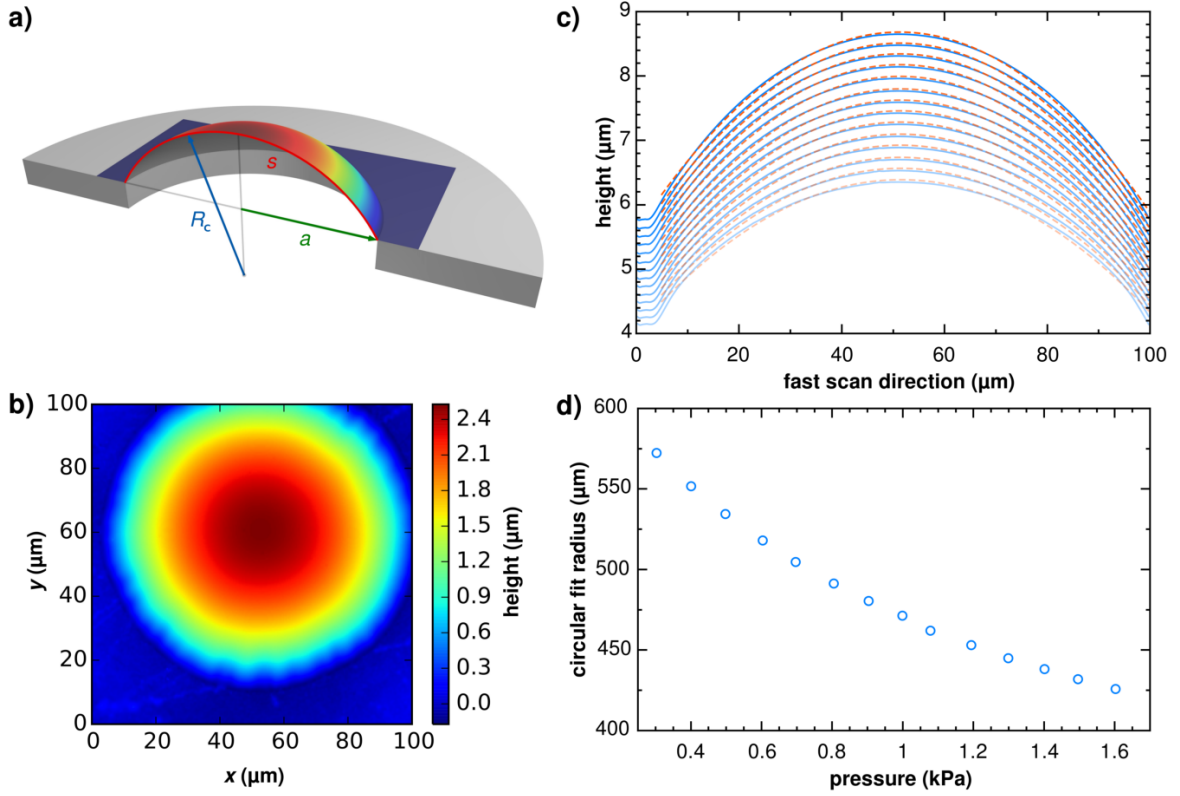


Figure 6.5: a) Schematic depicting a cross-sectional view of a bulged membrane approximated as a spherical cap. The drawing is annotated with quantities relevant for data analysis, i.e. the bulge radius of curvature R_c , the aperture radius a as well as the bulge arc length s . b) Topographical AFM *full scan* of a GNP/8DT membrane (thickness: (44 ± 2) nm), placed onto a ~ 100 μm aperture and bulged with a nitrogen overpressure of ~ 0.7 kPa. c) *Line profile* scans of the latter sample, acquired at overpressures ranging from 0.3 to 1.6 kPa. d) Plot of the bulge radius of curvature with respect to the applied nitrogen overpressure, extracted from the data shown in figure part c.

onto a custom-built sample holder. Nitrogen overpressure, monitored by digital pressure sensors, was applied to the back side of the membranes. For various membrane samples, *full scans*, imaging the majority of the resulting membrane bulge, as well as *line profiles*, representing deflection profiles traversing the membrane center were acquired using AFM. *Line profiles* were recorded at varying applied overpressure in the range of 0.1 to 1.6 kPa and their topography was correlated with respective overpressures to compute the elastic properties of the membranes.

Figure 6.5b visualizes a topographic AFM scan of an 8DT cross-linked GNP membrane placed on a circular aperture and loaded with an overpressure of ~ 0.7 kPa. The membrane bulge reached a height of ~ 2.4 μm with respect to the surrounding substrate. *Line profiles* of the sample, acquired at overpressures ranging from 0.3 to 1.6 kPa are depicted in figure 6.5c. The data were analyzed using a geometric model, approximating the membrane bulges as spherical caps.^[48,173] A schematic, cross-sectional view of a bulged membrane, annotated with quantities relevant for data analysis is provided in 6.5a. Circles were fitted to the *line profiles* (see dashed orange lines in figure 6.5c) using a least-squares algorithm to obtain the pressure-dependent radius of curvature R_c of the membrane bulges (figure

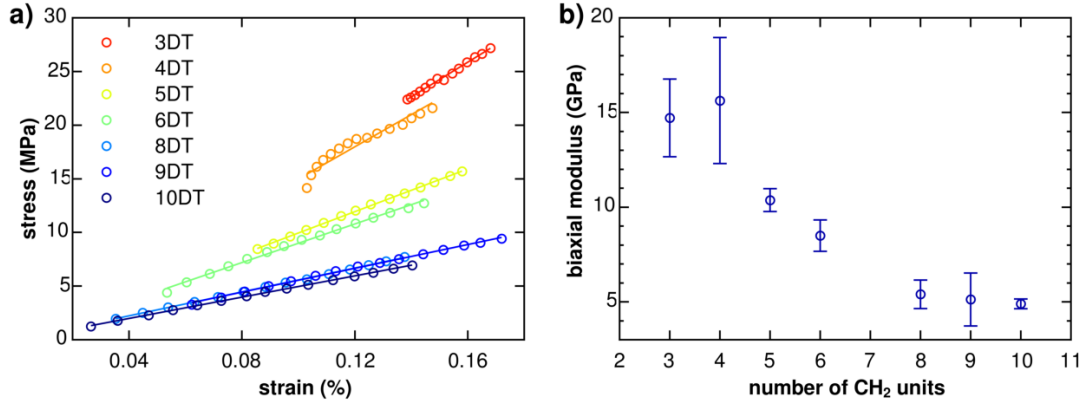


Figure 6.6: *a)* Diagram depicting the biaxial stress-strain relations of representative GNP/ADT composite membranes, measured by AFM bulge tests. Solid lines denote slope fits to the data. *b)* Averaged biaxial moduli of GNP/ADT membranes, obtained by bulge testing several membrane samples cross-linked using ADTs of different chain length.

6.5d). Considering the equation for a thin-walled spherical pressure vessel (eq. 6.2), the bulge radius R_c , the membrane thickness t_m , and the differential pressure ΔP , the tangential biaxial stress σ_t acting on the membranes was computed. The thin-walled pressure vessel approximation requires $t_m \ll R_c$, a condition met in all our experiments.

$$\sigma_t = \frac{\Delta P R_c}{2t_m} \quad (6.2)$$

The biaxial tangential strain ε experienced by the membranes was computed taking into account the variation in the bulge arc length s (eq. 6.3), which was determined geometrically from R_c and the aperture radius a , with the latter measured by optical microscopy (eq. 6.4).

$$\varepsilon = \frac{s}{s_0} - 1 \quad (6.3)$$

$$s = 2R_c \arcsin\left(\frac{a}{R_c}\right) \quad (6.4)$$

In equation 6.3, s_0 represents the initial arc length, i.e., the arc length at infinitesimal overpressure, obtained by extrapolation of a $\sigma_t(s)$ plot to $\sigma_t(s_0) = 0$. s_0 was used to estimate the pre-strain $\varepsilon_0 = \frac{2a}{s_0} - 1$ and pre-stress $\sigma_0 = Y\varepsilon_0$ of the membranes. Here, Y represents the biaxial modulus of the composite material. Positive pre-stress values refer to tense membranes, while a negative computed pre-stress or pre-strain is indicative for slack membranes. As observed in an earlier study,^[48] pre-stress values showed pronounced scattering. This was dedicated to the manual and poorly controlled flotation based transfer process and subsequent drying of the sample. Values ranging between -9 and 24 MPa were determined in this project. On average a higher pre-stress was observed

for samples cross-linked by shorter ADTs. This could result from stronger attraction of the latter films to their apertures' (gold) walls during membrane transfer, caused by their comparably high thiol and gold contents.

In the elastic regime, the biaxial stress and strain show a linear relation, with the biaxial modulus Y being the constant of proportionality. Y is related to the materials' moduli of elasticity E via the Poisson ratio ν :^[173]

$$Y = \frac{E}{1 - \nu} \quad (6.5)$$

Figure 6.6a depicts plots of stress-strain curves, computed for representative samples cross-linked with ADTs having chain lengths from 3 to 10 methylene units. To compute their biaxial moduli Y , slope functions were fitted to the stress-strain data (solid lines in figure 6.6a). Average values for Y , determined for several samples cross-linked with different ADTs, are provided in figure 6.6b. The plot suggests a nonlinear dependence of the membrane elasticity on the length of the ADT linker. An increase of alkane chain length leads to softer composites, i.e., the biaxial modulus declines from ~ 16 GPa to ~ 5 GPa when increasing the ADT alkane chain length from 4 to 10. Taking into account a Poisson ratio of $\nu = 0.33$,^[48] these values correspond to elastic moduli ranging from ~ 10 GPa to ~ 3 GPa. The comparably low elastic moduli of the GNP composites with respect to bulk gold ($E_{\text{Au}} = 78$ GPa^[224]) underline that the soft organic matrix dominates their mechanical properties. The data provide the first quantitative measure for the range in which the elastic properties of ADT cross-linked GNP membranes can be tuned by adjusting the ADT chain length, given a size of GNPs of ~ 4 nm. Besides, two GNP/BDT membrane samples were tested regarding their elastic properties. Here, an average biaxial modulus of (13 ± 1) GPa was observed, ranging between the values of Y for 4DT and 5DT cross-linked films.

6.1.7 Conclusions and Outlook

In this study, structural, optical, electronic, and mechanical properties of GNP composite membranes, fabricated via layer-by-layer spin-coating, were investigated. These investigations showed that the optical properties, i.e., the SPR absorption of the composite films could be tuned by varying the DT cross-linker. Further, by varying the DT's length, the conductivity of the films could be adjusted over several orders of magnitude. Both results indicated, that the interparticle spacing could be controlled by the choice of the cross-linker molecule. While these experiments as well as XRD showed no clear evidence for fusion and/or aggregation of GNPs, TEM indicated such processes for GNP films comprising shorter-chain ADTs. The main focus of this work was the investigation of the materials' elasticity by AFM bulge tests to study its dependence on the ADT chain-length. It was observed that the elastic modulus E of the composites is governed by the soft organic cross-linker matrix and can be adjusted in the range of ~ 3 GPa to ~ 10 GPa

by the choice of the DT chain length and structure.

In summary, the study underlines that GNP/DT composites offer a tunability of their mechanical properties, going along with tunable optical and electronic characteristics, which are highly interesting and relevant for their application as functional materials in MEMS/NEMS type devices.

6.2 Electromechanical Gold Nanoparticle Membrane Resonators: Influence of Geometry and Size on the Vibrational Characteristics

Gregor T. Dahl,[‡] Hendrik Schlicke,[‡] Clemens J. Schröter, Tobias Vossmeier

[‡]Contributed equally to this study.

The study summarized in this section, which will be submitted for publication soon, aimed at the detailed characterization of electrostatically driven ADT cross-linked GNP membrane resonators, as introduced in section 5.4. It focuses on the geometry dependence of the resonance behavior. To this end, circular resonators of different diameters as well as rectangular resonators were fabricated and thoroughly characterized. As in the preceding, published study (outlined in section 5.4),^[3] the resonators were excited using AC voltages. Vibrations of the GNP membranes were monitored using laser interferometry.

6.2.1 Device Fabrication

As in the preceding studies, membranes of 6DT cross-linked GNPs were used for resonator fabrication. The particles used in the present study had an average diameter of (3.3 ± 0.6) nm, as determined by TEM. The films were fabricated on glass substrates following the spin-coating procedure outlined in section 5.1.1, resulting in thicknesses (as determined by AFM) ranging from 41 to 45 nm.

The supporting 3D electrode microstructures had essentially the same layer arrangement (back electrode, SU-8 microcavity layer, top electrode) as in the case of the resonators investigated in the framework of the previous paper summarized in section 5.4. However, in the case of the present study, a broader variety of microcavity geometries was fabricated. The lateral geometries of the microcavities used for resonator fabrication — hence governing the shape of the freestanding membrane sections after transfer — were either circular, with diameters of $2a = 40, 50, 60, 80, 100, 120$ and $140 \mu\text{m}$, or rectangular with defined edge lengths of $a_x = 150 \mu\text{m}$ and $a_y = 50 \mu\text{m}$. The microcavity depth of $\sim 10 \mu\text{m}$ was given by the SU-8 layer thickness.

To finalize the resonator devices, GNP membranes were transferred onto the microstructures by a flotation process that was similar to that described in section 5.1.3. Again, the glass substrate supported GNP films were floated on water for approx. three days and then detached by carefully immersing the substrate into the aqueous phase, while the GNP membranes remained floating at the liquid/air interface. At this point, slight modifications of the original procedure were introduced. Instead of skimming the membranes from the water surfaces, the water carrying the membranes was slowly drained causing

the membranes to settle onto the tilted microstructures, placed below the water surfaces. This modification was intended to improve the reproducibility of the membrane transfer process.

6.2.2 Resonator Characterization

The differently shaped and sized resonators were characterized regarding their resonance spectra, fundamental resonance frequencies and quality factors. Further, *amplitude mapping* experiments were conducted, yielding lateral amplitude distributions that were employed to identify vibrational modes. All measurements were carried out under vacuum ($< 7 \times 10^{-2}$ mbar) to reduce damping. The methods used for resonator characterization are described in our previous publications. Detailed descriptions of the *frequency sweeping* spectrum acquisition procedure as well as the *ring-down* experiment for the determination of quality factors are provided in the SI of the publication on microelectromechanical chemical sensors (reprinted in section A.1.4). A description of the *amplitude mapping* procedure can be found in the ESI reprinted in section A.1.3. In the following, the procedures are briefly summarized and alterations specific to this project are described.

Spectrum acquisition

For the acquisition of amplitude spectra and determination of fundamental resonance frequencies of the resonators, the *frequency sweeping* procedure was utilized. In brief, a linearly drive frequency f_d swept sine voltage (frequency range 10 kHz to 2 MHz) with an AC component $V_{AC} = 5$ V and a DC component of $V_{DC} = 10$ V was applied to the devices. Synchronized with the time of the sweep, a deflection time trace of the membrane surface was recorded using a laser interferometer, set to a deflection measurement sampling frequency of $f_s = 5$ MHz and a data block length of $2^{16} = 65536$ points. The laserinterferometric setup is described in detail in the appendix (section A.2). The recorded deflection time traces showed pronounced oscillations when matching the resonance frequencies of the devices with the swept drive frequency. Amplitude spectra were obtained by FFT of the deflection time traces.

Determination of Q

Quality factors were determined by *ring-down* experiments,^[37] as described in sections 5.4, 5.5, as well as the respective publications.^[3,4] To this end, the fundamental resonance frequency of a membrane, measured at its central position, was determined by spectrum acquisition and evaluation. Afterwards, the membrane was excited by a sine burst, with the drive frequency adjusted to the previously measured fundamental resonance frequency. Multiple experiments were conducted for each sample, with an increasing burst length, i.e., an increasing number of sine cycles contained in the burst. Following the burst,

the excitation signal was switched off and the decay of the membrane oscillation was monitored and fitted using a damped harmonic oscillator model. The quality factor Q of the fundamental membrane vibration could then be computed by taking into account the resonance frequency and the oscillation decay time.

Amplitude Mapping

To image lateral vibrational amplitude distributions, *amplitude mapping* experiments were conducted. Resonance spectra were acquired at different positions on the membrane surface defined by a grid, using the *frequency sweeping* method with $V_{AC} = 2.5$ V and $V_{DC} = 20$ V. In contrast to earlier experiments,^[3] the x, y -positions were addressed in a random order to reduce the effects of anisotropic heating of the membrane by the incident laser. The spectra were normalized with respect to their fundamental resonance frequency. We note that this procedure to normalize the spectra was necessary, as shifts of the resonance frequencies were observed when conducting interferometric measurements at different positions on the membrane. This observation was dedicated to effects of local heating caused by the incident laser.^[3] Eventually, the maximum amplitudes observed in defined ranges of the normalized frequency spectra — acquired at different x, y positions — were extracted to generate false-colored amplitude distribution plots for the respective spectral regions.

6.2.3 Results

Circular Resonators

First, circular 6DT/GNP resonators featuring different membrane diameters $2a$ were investigated.

Resonance Spectrum. Figures 6.7a and b show two exemplary resonance spectra of a 120 μm diameter resonator, acquired at the center of the membrane and at half radius. Both spectra show a pronounced resonance peak closely above 200 kHz. It is to note that this peak, which we assign to the fundamental (0,1) vibrational mode of the circular membrane, was observed at ~ 225 kHz in the case of the spectrum recorded at the membrane center and at ~ 240 kHz in the case of the spectrum recorded at half radius. As in our earlier study,^[3] we dedicate this shift to thermal effects, caused by anisotropic heating leading to changes in the local stress of the membrane when directing the interferometer laser to the different measurement positions. As described in the introduction (section 3.3.3), frequency estimates for higher resonance modes of membrane resonators operated in vacuum can be computed with reference to the fundamental resonance frequency. These frequency estimates are denoted in the plots as vertical lines. While red lines indicate modes observable at the respective positions on the membrane (center and

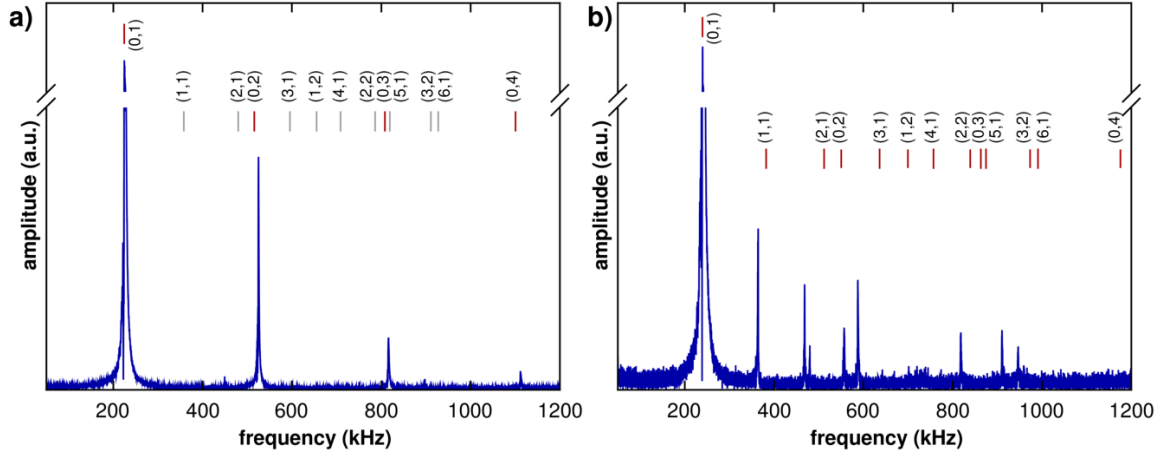


Figure 6.7: Vibrational amplitude spectra of a circular, 120 μm diameter GNP/6DT membrane resonator. The membrane had a thickness of $(43 \pm < 1)$ nm. Vertical lines denote estimate positions of vibrational modes with respect to the fundamental resonance frequencies. The red and gray colors indicate whether the modes are expected to have non-zero or zero amplitude at the given measurement positions. a) Spectrum recorded in the center of the GNP membrane ($x = 0, y = 0$). b) Spectrum recorded at half radius ($x = 0, y = 30 \mu\text{m}$).

half-radius), gray indicators represent modes that should not be observable, as the given measurement was conducted at a position that is expected to be situated on a nodal line with zero amplitude. Comparing the frequency estimates to the experimental data, the model clearly shows good agreement with the experimental results for the spectrum measured at the membrane center (figure 6.7a). Also modes having a theoretical amplitude of zero at the membrane center were not observable in the spectrum. Considering the measurement at half-radius (figure 6.7b), at most the (1, 1) and (2, 1) can be assigned to their estimate frequencies, while higher modes show strong deviations from the expected spectra positions. The observed deviations are presumably again due to local heating and hence local changes in membrane pre-stress and resulting distortions of the spectra.

Besides the acquisition of their resonance spectra, *ring down* experiments for the determination of quality factors, as well as *amplitude mapping* experiments were conducted with circular membrane resonators. These experiments gave similar results as described in section 5.4.

Dependence of the Fundamental Resonance Frequency on the Membrane's Size. Figure 6.8a depicts a plot of the averaged resonance frequencies $f_{0,1}$ of circular GNP membrane resonators with respect to their reciprocal diameters, ranging between $1/40 \mu\text{m}^{-1}$ and $1/140 \mu\text{m}^{-1}$. From theory (cf. section 3.3.3) we expect the resonance frequencies to be proportional to the inverse diameter $1/(2a)$ of the membranes (equation 6.6), assuming all membranes are uniformly pre-stressed and have the same density.^[186]

$$\frac{df_{n,m}}{d(2a)^{-1}} = \frac{\xi_{n,m}}{\pi} \sqrt{\frac{\sigma_0}{\rho}} = \frac{\xi_{n,m}}{\pi} c \quad (6.6)$$

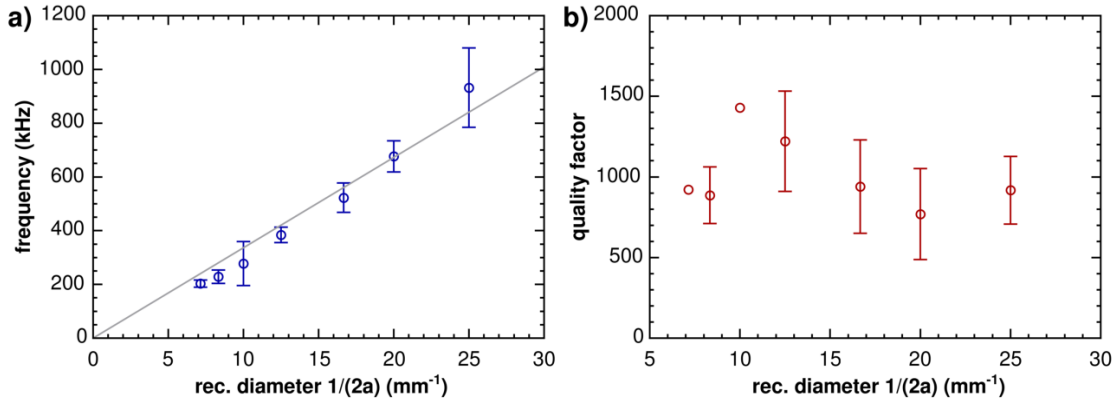


Figure 6.8: *a)* Average fundamental resonance frequencies $f_{0,1}$ of differently sized circular GNP membrane resonators, measured at the membrane center. *b)* Average quality factors determined for differently sized circular GNP membrane resonators, employing the ring-down method and 5 excitation cycles.

The error bars indicate that same-sized resonators show some scattering of their $f_{0,1}$ resonance frequencies. We assign this observation to variations in membrane pre-stress, resulting from the flotation-based membrane transfer process. Even though the process was optimized in this study, it still shows some variation of reproducibility. We assume that these issues can be improved by the application of membrane transfer processes based on contact printing or stamp transfer. Irrespective of the scattering, the resonance frequencies clearly adhere to the expected, linear trend, as indicated by a slope fit to the experimental data. From the slope of the fit function, a phase velocity $c = \sqrt{\frac{\sigma_0}{\rho}} = 44 \text{ ms}^{-1}$ was extracted.

Further, we compared the measured fundamental resonance frequencies to estimations based on the plate model (cf. section 3.3.3, equation 3.19). For the calculations, a membrane thickness of $t_m = 43 \text{ nm}$, an elastic modulus of $E = 6 \text{ GPa}$,^[2] a membrane density of 9.3 g cm^{-3} ,^[4] and a Poisson ratio of $\nu = 0.33$ ^[48] were assumed. Fundamental resonance frequencies ranging from 43 kHz to 3.5 kHz were calculated for membrane diameters ranging from 40 μm to 140 μm , respectively, using the plate model. These values are significantly lower than experimentally observed frequencies ranging between 932 kHz and 229 kHz, respectively. According to equation 3.20, the fundamental resonance frequencies are hence well-described using the membrane model.

The results of this study confirm the ability to tune the resonator frequency by alternations of the membrane’s size and the applicability of the membrane model to our devices.

As depicted in figure 6.8b the averaged quality factors of the fundamental vibration show — in contrast to the averaged resonance frequencies — very strong scattering and no clear trend concerning the resonator size. This is probably due to a low signal to noise ratio of the raw data and limited fitting accuracy using the damped harmonic oscillator model. Therefore only a rough interval for the observed quality factors, ranging from 500 to 1500 can be provided. This range is in agreement with the quality factors of GNP/6DT

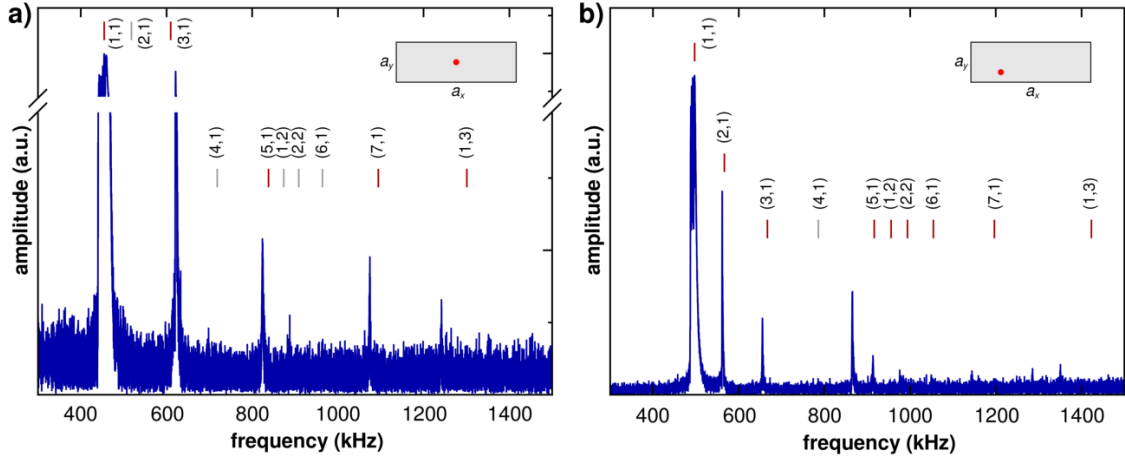


Figure 6.9: Vibrational amplitude spectra of a rectangular GNP/6DT membrane resonator with edge lengths of $a_x = 150 \mu\text{m}$ and $a_y = 50 \mu\text{m}$. The membrane had a thickness of $(44 \pm < 1) \text{ nm}$. Vertical lines denote estimate positions of vibrational modes with respect to the fundamental resonance frequencies. The red and gray colors indicate whether the modes are expected to have non-zero or zero amplitude at the given measurement positions. *a)* Spectrum recorded in the center of the membrane ($x = a_x/2, y = a_y/2$). *b)* Spectrum recorded in the center of a membrane quarter ($x = a_x/4, y = a_y/4$).

membrane resonators tested in our previous study.^[3] On average, these values are higher than quality factors reported earlier for monolayered GNP resonators (up to $Q \sim 500$ for a $\sim 9 \mu\text{m}$ diameter device).^[45] This could be due to the overall considerably larger diameters of the membranes in our study and hence reduced energy dissipation from clamping losses.

Rectangular Resonators

Besides circular geometries, a rectangular GNP membrane resonator with edge length of $a_x = 150 \mu\text{m}$ and $a_y = 50 \mu\text{m}$ was investigated regarding its resonance behavior to probe whether the experimental observations and theoretical descriptions are transferable to such anisotropic shapes.

Resonance Spectrum. As in the case of circular resonators, vibrational spectra of the rectangular membrane were acquired employing electrostatic actuation and the *frequency sweeping* method. Figure 6.9a shows the amplitude spectrum recorded at the center position $x = a_x/2, y = a_y/2$ of the membrane. The spectrum shows a pronounced resonance peak at 454 kHz. We assign this vibration to the fundamental resonance mode (1, 1) of the rectangular resonator. In this case, the fundamental resonance frequency corresponds to a phase velocity of $c = \sqrt{\sigma_0/\rho} = 43 \text{ ms}^{-1}$, which is in very good agreement with the value observed for circular resonators. Again, estimated frequencies of higher modes were computed based on this assignment. The estimated frequencies are again depicted as vertical lines in the resonance spectrum. As in the case of circular resonators, not all modes are expected to be observable at a certain measurement position. For example,

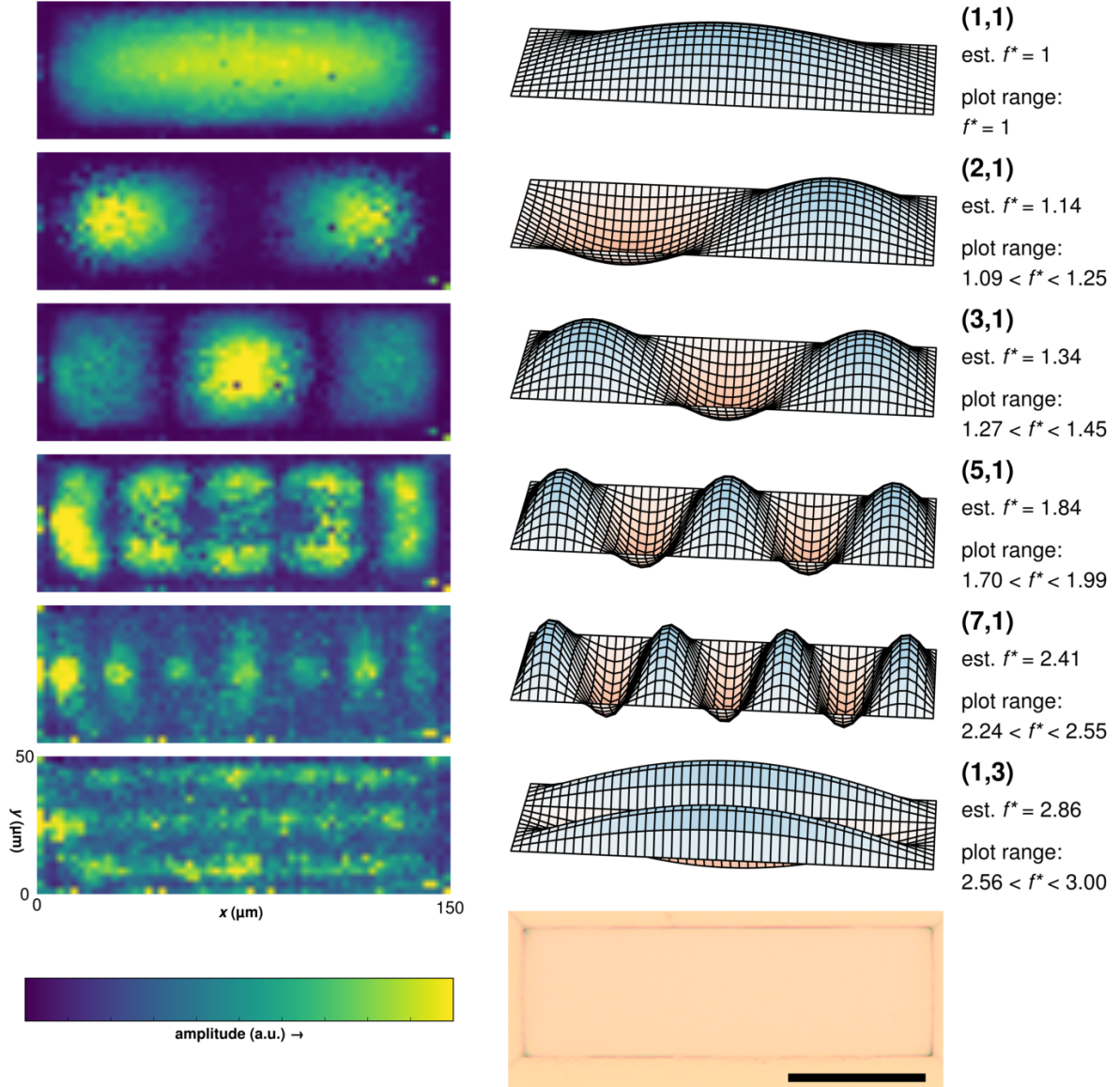


Figure 6.10: Vibrational amplitude maps of a rectangular membrane resonator (edge length $a_x = 150 \mu\text{m}$ and $a_y = 50 \mu\text{m}$, membrane thickness $(44 \pm < 1) \text{ nm}$). The left side of the figure shows the maximum amplitudes measured on the membrane surface, in different frequency ranges f^* , relative to the fundamental resonance frequency $f_{1,1}$ measured at the given position. The frequency ranges are denoted on the right side of the figure. Besides, estimated mode shapes are plotted with their theoretically estimated frequencies f^* . The lower right of the figure depicts an optical micrograph of the membrane (scale bar: $50 \mu\text{m}$).

only modes with uneven mode numbers n and m should be observed at the membrane center, as even mode numbers lead to nodal lines with zero amplitudes traversing this position. The experimental data provided in figure 6.9a show an overall good agreement with theory. However, at higher frequencies, slight deviations are visible.

An amplitude spectrum, acquired at the off-center position $x = a_x/4, y = a_y/4$, is plotted in figure 6.9b. As in the case of circular resonators, the fundamental resonance peak was

found at a higher frequency $f_{1,1} = 497$ kHz, compared to the foregoing case of the center measurement. As mentioned before, we dedicate this deviation to thermal effects induced by the incident laser beam, causing local variations of the membrane's pre-stress. The spectrum is again annotated with estimate frequencies for higher vibrational modes. Similar as in the case of circular resonators, the experimental data show good agreement with theory for the lower three vibrational modes, but strong deviations at higher frequencies. We dedicated this again to local heating of the laser causing inhomogeneous pre-stress of the membrane and distortion of its spectrum.

Amplitude Mapping. Additional to the acquisition of resonance spectra, an *amplitude mapping* experiment was conducted to verify the assignment of the observed resonance peaks to vibrational modes of the membrane. During the mapping experiment, resonance spectra were collected in a random order at different positions arranged in a grid adjusted to the membrane shape. The spectra were then normalized to their $f_{1,1}$ frequency to reduce the influence of thermally induced frequency shifts. Figure 6.10 depicts the results of this mapping experiment, showing false-colored plots of the maximum amplitudes observed in different, normalized frequency f^* ranges. Aside of the amplitude maps, images showing the expected membrane deflection of respective vibrational normal modes are provided. Further, the estimated normalized frequencies with respect to the fundamental resonance frequency $f_{n,m}^*$ are denoted. While the (1, 1), (2, 1), (3, 1) and (5, 1) modes could be clearly identified by distinct nodal lines at the expected coordinates, the overall low signal to noise ratio complicates the imaging of further modes. Still, the (7, 1) and (3, 1) modes could be identified by their amplitude maxima. We assume that, due to equal areas of oppositely phased deflections, excitation of modes with even mode numbers is hardly possible using a more or less homogeneous electric field screened by the counter electrode. We note that the frequency estimates of the modes assigned to the amplitude maps clearly fall into their spectral plot ranges. This confirms the preceding assignment of resonance peaks and underlines that the theoretical model is widely applicable, also to rectangular membrane resonators.

6.2.4 Conclusions and Outlook

Within this study, the resonance behavior of electrostatically driven GNP membranes was extensively investigated. Differently sized circular membrane resonators, as well as a rectangular resonator were probed regarding their vibrational characteristics in vacuum. The results of resonance frequency and quality factor measurements as well as amplitude mappings were presented and compared to the theoretical model of clamped membranes oscillating in vacuum. Overall, good agreement of the model with our experimental data was observed.

Future studies aim at the examination of the influence of pressure on the vibrational characteristics. This is highly interesting regarding potential applications of the resonator devices. On the one hand, the utilization of GNP membrane resonators as microelec-

tromechanical gas sensors — as reported in our recent paper^[4] (section 5.5) — requires exposure to gases, ideally at ambient pressure. Further, changes of the devices' vibrational characteristics such as the resonance frequencies or quality factors can be used to sense pressure.^[31,219]

6.3 Further Results

6.3.1 Sensor Response Kinetics of GNP Membrane Resonators

This section summarizes a study on the response kinetics of electromechanical chemical sensors based on GNP membrane resonators.

As described in section 5.5, vibrations of a circular, 120 μm freestanding GNP/6DT membrane were electrostatically excited under a nitrogen atmosphere (total pressure: 20 mbar), and shifts of its fundamental resonance frequency could be employed to detect and quantify the presence of analyte vapors at varying partial pressures. In these experiments, we observed that the sensor showed somewhat retarded responses to analyte exposures, with clearly varying response times for different analytes. This effect is shown in figure 6.11, which displays the frequency shift responses when exposing the device to vapors of toluene, 4M2P, 1-propanol and water with partial pressures of 20 Pa. The transients are normalized to the peak response. As discussed before, the response time is slowest for 4M2P, followed by toluene, water and 1-propanol. We hypothesize that due to the device design (cf. figure 5.22b, page 111) containing a microcavity sealed by the membrane, the sensor response kinetic is governed by permeation of analyte through the GNP membrane. After AG is introduced into the measurement cell, only the outer side of the membrane is exposed to the analyte, while the inner side faces the cavity volume, which initially contains pure nitrogen zero gas. Hence, the membrane experiences the maximum analyte exposure not until the analyte concentration within the microcavity has equilibrated with its exterior. This process should be dependent on the permeation rate of the analyte through the membrane, which again depends on the analyte molecule.

To test our hypothesis, we fabricated two resonators consisting of 6DT cross-linked GNP membranes, deposited onto silicon based microstructures with different geometries. On the one hand, a GNP membrane (thickness (88 ± 1) nm) was transferred onto a square, wet-etched, trapezoidal microcavity with an edge length of $\sim 87 \mu\text{m}$ and a depth of 16 μm measured at its bottom area (see figure 6.12a for a schematic and figure part c for an optical micrograph). After transfer, the membrane sealed the microcavity and the de-

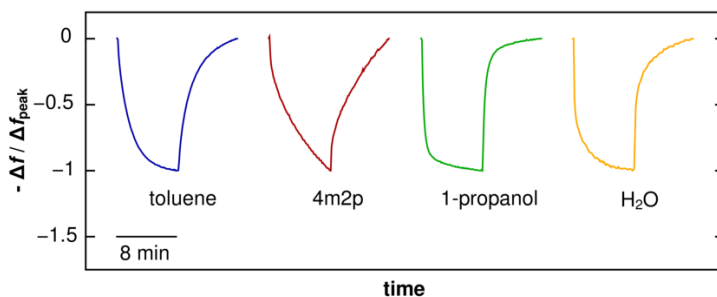


Figure 6.11: Normalized frequency shift transients of the circular GNP membrane resonator described in section 5.5, operated in a 20 mbar nitrogen atmosphere, in response to 8 min exposures to different analytes (partial pressure of 20 Pa).

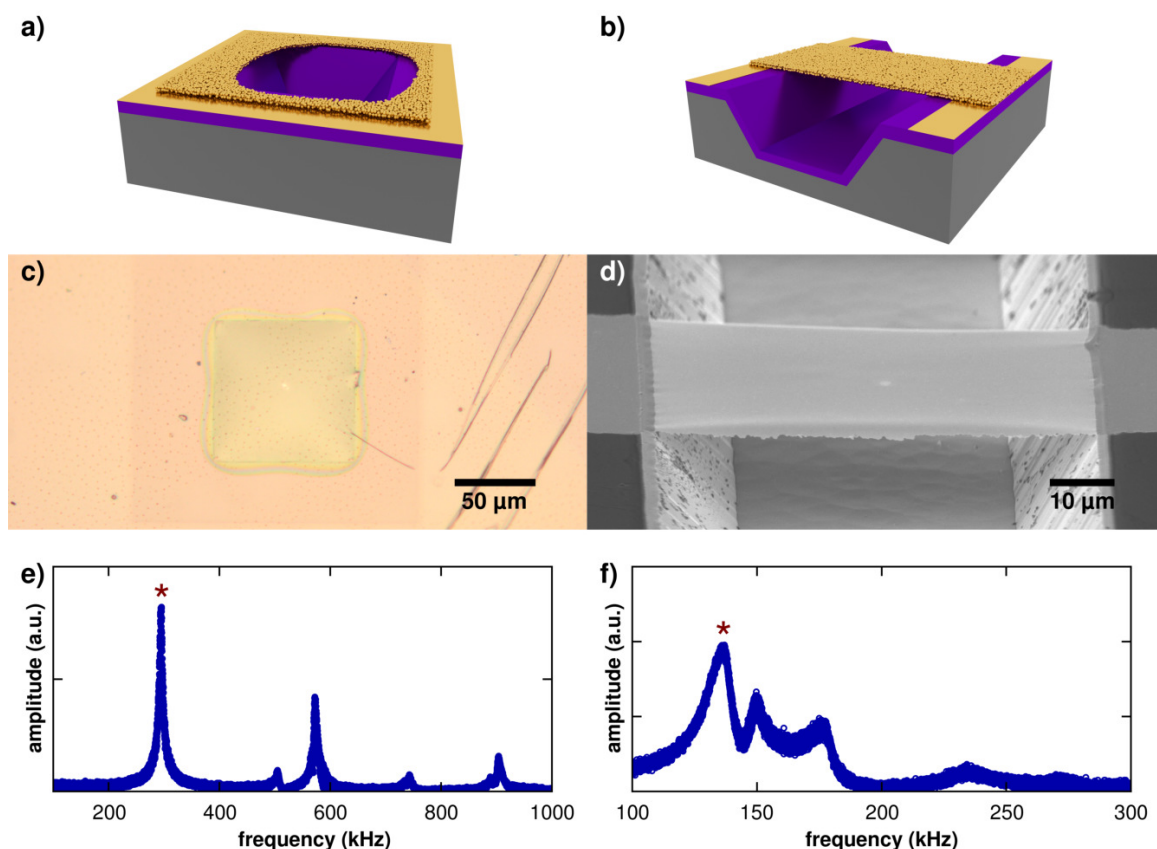


Figure 6.12: a) Schematic depicting a GNP membrane, deposited onto a trapezoidal cavity with a square aperture. The membrane is electrically connected to a gold electrode. Parts of the membrane are not depicted to visualize the cavity geometry. b) Schematic depicting a GNP membrane bridge, deposited onto a trapezoidal trench. The membrane is electrically connected to gold electrodes. c) Optical micrograph of a GNP membrane deposited onto a trapezoidal microcavity with a square aperture (completely sealed). d) Scanning electron micrograph of a GNP membrane bridge, deposited onto a microstructure featuring a trapezoidal trench. e) and f) Amplitude spectra of the resonators depicted in figure parts c and d, respectively. Measurements were conducted at a total pressure of $P_{\text{abs}} = 20$ mbar.

vice is expected to behave similarly (with relatively slow response times) to the sensor device discussed in section 5.5. On the other hand, a bridge-like resonator geometry was fabricated. Here, a stripe of a GNP membrane (thickness (45 ± 2) nm) was transferred onto a silicon microstructure, featuring a wet-etched $65 \mu\text{m}$ wide trench with a depth of $17 \mu\text{m}$ (see the schematic in figure 6.12b and a scanning electron micrograph in figure part d). In this case, the membrane transfer was conducted following a PDMS stamp based transfer process.^[6] Here, the volume below the membrane was open and could be accessed by analyte molecules. Hence, virtually immediately after the introduction of AG into the measurement chamber, the membrane experiences the same, maximum analyte concentration on its two sides. We therefore expect a significantly faster sensor response of this device.

Both resonators were excited by applying frequency-swept AC voltages between the silicon wafer and the top electrode connected to the membrane. Deflections were read out

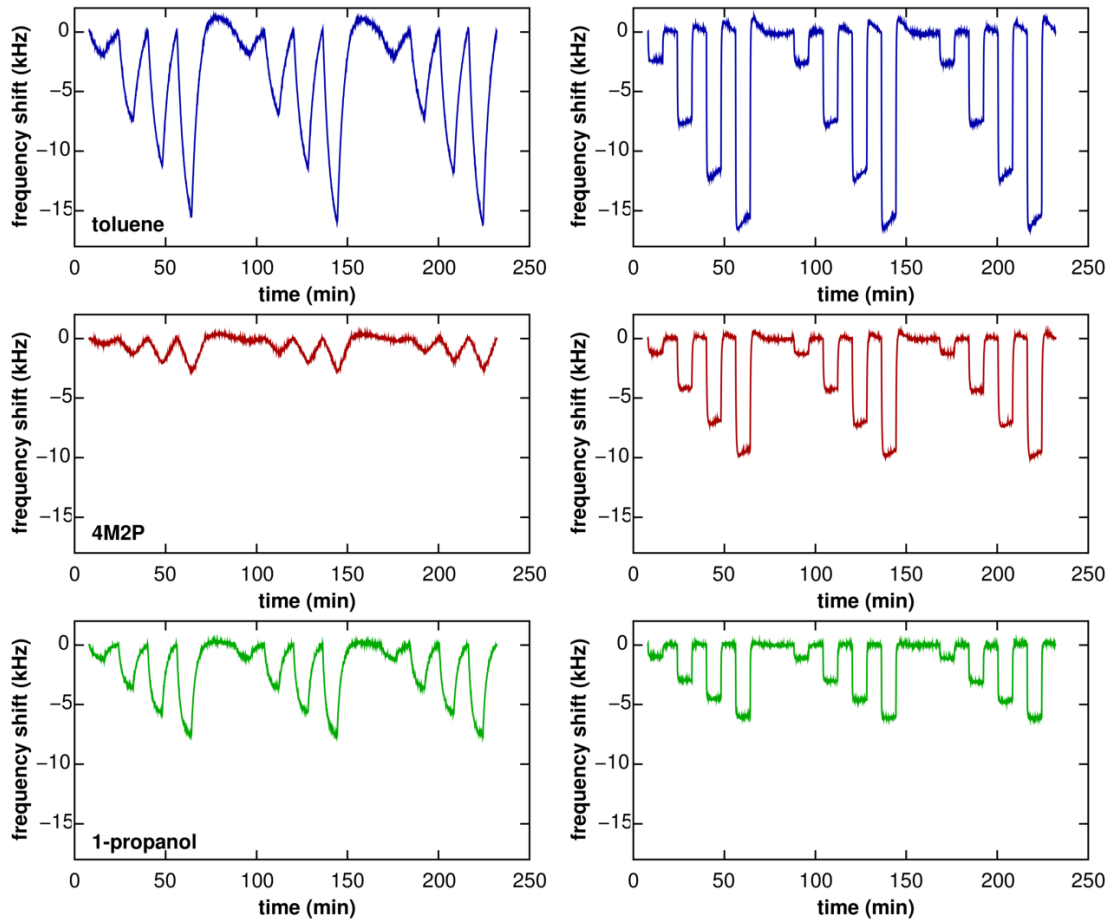


Figure 6.13: Baseline-corrected fundamental resonance frequency shift transients observed when repeatedly exposing the closed, square GNP membrane resonator (*left*), as well as the open, strip-like GNP membrane resonator (*right*) (depicted in figure 6.12a and b, respectively) to different analyte vapors (as indicated) with partial pressures of 2, 8, 14 and 20 Pa.

by means of laser interferometry. The *frequency sweeping* method (cf. section 5.4) was utilized for the acquisition of vibrational amplitude spectra. Figure 6.12e and 6.12f show the amplitude spectra of the sealed and open device, recorded under nitrogen atmosphere with a total pressure of 20 mbar, respectively. While the spectrum of the square resonator shows relatively sharp peaks, the bridge-type resonator exhibits rather broad resonances. We dedicate this observation to pronounced imperfections of its geometry, such as wrinkles at the edges of the freestanding membrane area leading to damping. These are visible in the scanning electron micrograph depicted in figure 6.12d. The fundamental resonance frequencies of both devices were assigned to the lowest peak visible in the spectrum (marked with an asterisk in figures 6.12e and f). For monitoring the fundamental resonance frequencies of the devices during the sensing experiments, spectra were continuously acquired in a range of 100 to 450 kHz (closed resonator) and 70 to 300 kHz (open resonator). The AC and DC components of the excitation signal were set to $V_{DC} = 10$ V, $V_{AC} = 5$ V (closed resonator) and $V_{DC} = 12.5$ V, $V_{AC} = 6.25$ V (open resonator).

As in the sensor test experiments described in section 5.5, both resonators were first exposed to pure nitrogen ZG, followed by AG with analyte partial pressures of 2 to 20 Pa for 8 min, spaced by applications of pure ZG (8 min). The left and right columns in figure 6.13 show exemplary frequency shift time traces of the closed and open resonator, respectively, exposed to different analytes. It is clearly visible that the resonator comprising a sealed microcavity shows slow responses to the different analytes. Compared to the circular resonator tested in section 5.5 (cf. the response time traces in the respective SI, reprinted in section A.1.4, pages 233ff) the responses were even slower. This can be attributed to the higher membrane thickness (88 nm vs. 44 nm) resulting in impeded permeability of the present GNP membrane. Regarding the transient shapes, the response towards 4M2P seems to be slowest, followed by the responses to toluene and 1-propanol. This order is in agreement with the response kinetics observed in our previous study (section 5.5, normalized transients are provided in figure 6.11). In contrast, the resonator having a bridge-like geometry responds essentially immediately to AG exposures and hence shows almost rectangular transients, independent of the analyte molecule.

The present results substantiate our assumption that the response kinetics of our closed microelectromechanical chemical sensors are governed by analyte permeation through the GNP membranes. Therefore, to accelerate the sensor response, resonators with partially open geometries should be employed. On the other hand, the retardation of the closed sensors' responses is dependent on the nature of the analyte. Hence, acquisition and suitable evaluation of the response times could be exploited to discriminate between different analytes or to obtain information about the membrane permeability. Such investigations will be the subject of more detailed studies in the near future.

6.3.2 Quasi-static Deflection of GNP Membranes for Chemical Sensing

In section 5.5, we demonstrated that GNP membrane-based resonators can be employed as microelectromechanical chemical sensors. The transduction mechanism of these devices is presumably mainly based on analyte sorption-induced changes in the membrane's pre-stress. These are reflected by variations of the resonators' fundamental frequencies, providing the sensor signal. In section 5.3, quasi-static actuation of similar, freestanding GNP membranes with DC voltages was reported. Similar to the resonance frequency determined by dynamic actuation with AC voltages, the voltage-deflection relation obtained by quasi-statically deflecting the GNP membranes with varying DC voltage pulses depends on the membrane's pre-stress. Therefore, the latter, quasi-static actuation method represents another possibility to read out changes in the membrane's pre-stress by using the voltage-deflection relation as sensing signal. Quasi-static actuation can be advantageous for chemical sensing, because membrane movements can be sufficiently slow, compared to the fast deflection changes of an oscillating membrane. While fast membrane oscillations suffer from severe damping when the resonators are operated under ambient pressure, quasi-static actuation can be readily performed.

In the following, we show that besides dynamic actuation, quasi-static electrostatic deflection of GNP membranes is a valid method to detect analyte vapors. The experiments described here were carried out using a square 6DT cross-linked GNP membrane resonator. The freestanding membrane had a thickness of (39 ± 1) nm, an edge length of ~ 100 μm , and sealed a ~ 10 μm deep cuboid microcavity. The microstructure supporting the GNP membrane (schematically depicted in figure 6.14b) was fabricated from SU-8 following the fabrication process outlined in section 5.1.2. In a typical experiment, 1 s pulses of increasing DC voltages of 20, 40, 60, 80, and 100 V, spaced by delays of 1 s with zero bias were repeatedly applied between the top and counter electrode of the device, causing inward deflections of the GNP membranes ranging up to $\sim 1 - 2$ μm . These de-

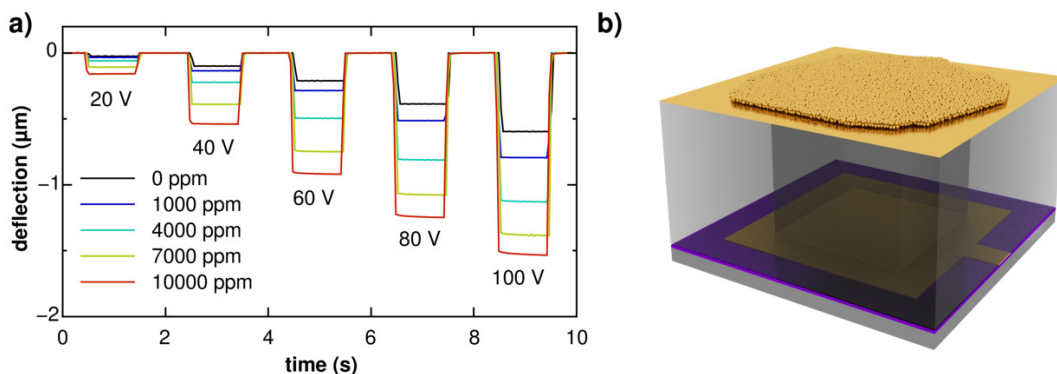


Figure 6.14: a) Central point deflection time series of a square freestanding 6DT cross-linked GNP membrane, actuated using different DC voltage pulses. Actuation was performed under exposure to an ambient pressure nitrogen atmosphere, enriched with different fractions of toluene. b) Schematic depicting the geometry of the freestanding GNP membrane placed onto a microstructure for microelectromechanical chemical sensing utilizing quasi-static actuation.

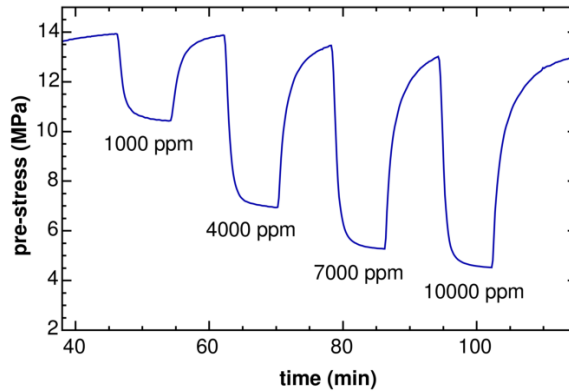


Figure 6.15: Time trace of a square GNP membrane's pre-stress, determined by quasi-static actuation at ambient pressure when exposed to 8 min AG pulses with toluene concentrations of 1000, 4000, 7000 and 10 000 ppm in nitrogen.

flections were monitored by means of laser interferometry. The first sensing experiment was conducted at ambient pressure. Here, the GNP membrane actuator was operated in a test cell under pure nitrogen (ZG) atmosphere. Afterwards, 8 min pulses of toluene were introduced, with concentrations of 1000, 4000, 7000 and 10 000 ppm, spaced by 8 min applications of ZG. Figure 6.14 provides five series showing deflection transients of the GNP membrane, recorded under exposure to the different toluene concentrations, as well as pure nitrogen ZG. The membrane deflection significantly increased when exposing the membrane to toluene vapor. Equation 5.7 (page 79) gives an estimation of a circular GNP membrane's voltage-deflection behavior under electrostatic actuation. Analogously, a similar equation can be derived for square membranes, as used in this experiment, by introducing the electrostatic force per area term into an equation for the pressure/deflection relation^[178] in bulge tests on square apertures:

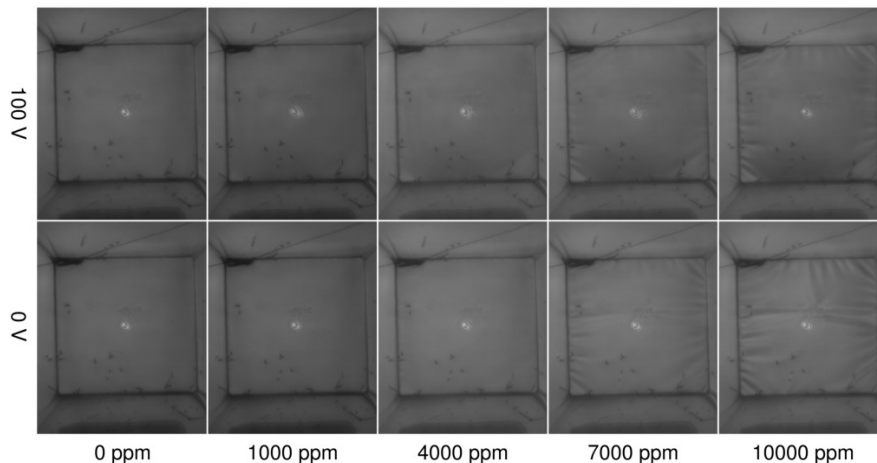


Figure 6.16: Optical micrographs of the sensor's membrane under exposure to AG with toluene fractions of 0, 1000, 4000, 7000 and 10 000 ppm (columns), and an applied voltage of 100 V and 0 V (rows). The bright spot in the membrane's center corresponds to a reflection/scattering of the interferometer laser. The edge length of the square membrane is $\sim 100 \mu\text{m}$.

$$\frac{\epsilon V^2}{2d^2} = \frac{C_1 \sigma_0 t_m}{b_x^2} h + \frac{C_2 E t_m}{b_x^4} h^3 \quad (6.7)$$

Here, V is the voltage, h is the central point deflection and $d \sim 10 \mu\text{m}$ is the distance between the membrane and the counter electrode, which is — in a first approximation — assumed to be constant. b_x represents the half membrane edge length, σ_0 the membrane pre-stress, and t_m the membrane thickness. C_1 and C_2 are constants that depend on the membrane geometry and are $C_1 = 3.393$ and $C_2 = 1/[(1 - \nu)(0.8 + 0.062\nu)^3]$ for square membranes, with ν being the Poisson ratio.^[178] The equation can be simplified for small deflections relative to the aperture width by taking into account only the first term on the right hand side of equation 6.7, scaling linearly with the central point deflection h :

$$\frac{\epsilon V^2}{2d^2} = \frac{3.393 \sigma_0 t_m}{b_x^2} h \quad (6.8)$$

The latter equation was fitted to the squared voltage-deflection $V^2(h)$ relations extracted from the continuously recorded series of deflection transients to determine the temporal evolution of pre-stress of the freestanding GNP membrane under exposure to toluene. Figure 6.15 depicts the resulting time trace of membrane pre-stress, showing pronounced transients when exposing the sensor to different toluene concentrations. The change in pre-stress is also visible in the optical micrographs of the membrane shown in figure 6.16. Along with increasing toluene concentrations the membrane — showing initially a tense structure — starts to exhibit pronounced wrinkles that are indicative for the swelling of the membrane material and a resulting decrease in pre-stress.

In a second study, a similar experiment was conducted operating the same device under a reduced total pressure of 20 mbar. Again, AG pulses with toluene concentrations of 1000, 4000, 7000 and 10 000 ppm were fed into the test cell, corresponding to considerably lower toluene partial pressures of 2, 8, 14 and 20 Pa, compared to the ambient pressure experiment. The pre-stress time trace, obtained following the quasi-static readout method, is plotted in figure 6.17. Also at these lower toluene partial pressures, a significant decrease in the membrane pre-stress was observed when exposing the membrane to AG. In a second experiment, also conducted at a total pressure of 20 mbar, the device was operated in dynamic mode, i.e., the resonator's fundamental frequency $f_{1,1}$ was continuously monitored by acquisition of amplitude spectra following the *frequency-sweeping* method, as described in section 5.5. Using the equation for a clamped square membrane (edge length $a_x = a_y$) oscillating in vacuum (cf. section 3.3.3) and assuming a mass density of 9.3 g cm^{-3} ,^[4] the pre-stress σ_0 of the GNP membrane under exposure to toluene vapor was computed:

$$\sigma_0 = \frac{4\rho a_x^2 f_{m,n}^2}{m^2 + n^2} \quad (6.9)$$

The time trace of the pre-stress computed from the membrane's fundamental resonance

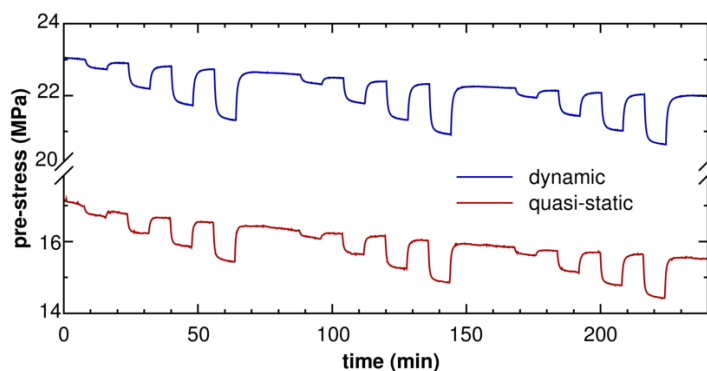


Figure 6.17: Time trace of a square GNP membrane’s pre-stress, determined by quasi-static as well as dynamic actuation at a total pressure of 20 mbar, when repeatedly exposing the device to 8 min AG pulses with toluene partial pressures of 2, 8, 14 and 20 Pa in nitrogen.

frequency is also plotted in figure 6.17. It is evident that both experiments, utilizing the different readout techniques, yield similar absolute values for the membrane’s pre-stress, as well as similar changes when exposing the device to toluene vapor. The observed differences could be caused by measurement uncertainties, e.g. regarding the cavity depth, which was estimated from the SU-8 layer thickness, or approximations made when deriving the model for the quasi-static voltage-deflection relation (see section 5.3).

The observations described in this section support our assumption that the changes in resonance frequency observed when exposing freestanding GNP membrane resonators to analyte vapors are predominantly due to variation of the membrane pre-stress. In principle — using lightweight membranes — the dynamic and quasi-static method could yield a different set of information, because the former method is sensitive to sorption-induced changes in the membrane density, which were negligible here, while the latter should solely depend on the membrane’s mechanical properties. In this case, the information could be used for advanced characterization or identification of analyte species.

Additionally, both — the dynamic and/or quasi-static — microelectromechanical chemical sensing concepts can be employed in combination with chemiresistive readout of the GNP membrane. As all three transduction principles should yield different sensitivities and selectivities, their combination could be beneficial for the realization of multivariate sensing concepts aiming at analyte recognition.

Current studies aim at the implementation of an all-electronic membrane deflection readout. This is of great interest as it would enable the facile integration of the chemical sensors into electronic circuitry, without the need for optical/interferometric detection systems.

6.4 Conference Proceeding: TechConnect Nanotech 2016

The following section reproduces a conference proceeding article, which connects to a talk held in May 2016 at the TechConnect Nanotech 2016 conference in Washington, D.C., USA. The article summarizes the fabrication of GNP membrane based MEMS/NEMS devices, such as resistive pressure sensors and electrostatic actuators as described in the synopsis section 5.

The article is reprinted with permission from “Freestanding Membranes of Cross-Linked Gold-Nanoparticles: Novel Functional Materials for MEMS/NEMS Applications”, H. Schlicke, C. J. Schröter, M. Rebber, D. Battista, S. Kunze, T. Vossmeier, *TechConnect Briefs 2016: Advanced Manufacturing, Electronics and Microsystems* **2016**, 83-86.^[5]

Freestanding Membranes of Cross-Linked Gold-Nanoparticles: Novel Functional Materials for MEMS/NEMS Applications

H. Schlicke*, C. J. Schröter*, M. Rebber*, D. Battista*, S. Kunze* and T. Vossmeier*

* Institute of Physical Chemistry, University of Hamburg,
Grindelallee 117, 20146 Hamburg, Germany
email: schlicke@chemie.uni-hamburg.de

ABSTRACT

3D cross-linking of gold-nanoparticles (GNPs) with alkylene dithiol molecules renders thin films with unique optical, mechanical and charge transport characteristics that can be tuned by variation of the GNP size and shape as well as by the nature of the dithiol molecule. So far, substrate-supported films were successfully applied as resistive strain gauges and chemiresistors. The films exhibit mechanical stability, sufficient to transfer and deposit them as freestanding membranes onto a variety of 3D structured substrates. The tunability of the material properties as well as the strain sensitivity make cross-linked GNP membranes interesting candidates for the implementation in micro- / nanoelectromechanical systems (MEMS/NEMS). Here, we report on the investigation of electromechanical properties of freestanding cross-linked GNP membranes and explore their applicability in MEMS/NEMS, i.e. as functional materials in pressure sensors or electrostatic actuators.

Keywords: gold, nanoparticle, MEMS, NEMS, membrane

1 INTRODUCTION

Recently, freestanding membranes of monothiol capped gold nanoparticle (GNP) monolayers[1, 2] as well as polymer-encapsulated GNPs[3] were fabricated and attracted interest due to their potential applications, e.g. as pressure sensors with optical readout or drumhead resonators using piezoelectric actuation. However, layers of GNPs capped with long-chain organic ligands or encapsulated in a polymer matrix commonly show low conductivity, due to the large tunneling gaps formed by the ligand shells separating the nanoparticles. Conductive GNP films can be obtained by shrinking these gaps, i.e. by ligand exchange with short-chain ligands or cross-linkage of the GNPs using e.g. short dithiol molecules. The electrical conductivity of such GNP films can be well-described by a simple semiempirical Arrhenius-type activated tunneling model (equation 1).[4, 5]

$$\sigma = \sigma_0 e^{-\beta\delta} e^{-\frac{E_A}{kT}} \quad (1)$$

Here, σ_0 is a preexponential factor, β is the tunneling decay constant, δ denotes the interparticle distance, E_A the activation energy, T the temperature and k is the Boltzmann constant. As the conductivity strongly depends on the interparticle distance, it is highly sensitive to external stimuli. For example, upon application of strain to a conductive GNP composite, it is transferred to the flexible organic matrix leading to further separation of the particles and hence a change in resistance. This leads to investigations of the applicability of substrate-supported GNP composite films as strain gauges.[6, 7, 8, 9] Gauge factors of up to 200 were measured.[6] Besides a high sensitivity to strain, the conductivity of GNP composites is influenced when exposing the material to chemical vapors or gases.[10, 11, 12, 9] This behavior is attributed to analyte uptake by the organic matrix, resulting in an increase of the interparticle distance due to swelling and changes in its dielectricity.[9] While extensive work was conducted investigating the above-mentioned characteristics of substrate-supported GNP composites, the investigation of electromechanical properties and potential applications of freestanding, conductive, cross-linked GNP composites is still in its infancy. The focus of our work is the investigation of these properties, e.g. by atomic force microscopy based micro bulge tests,[13] and the exploration of potential applications of the membranes in MEMS/NEMS.

2 FABRICATION OF GNP MEMBRANES

There are different methods reported for the fabrication of substrate-supported dithiol cross-linked gold nanoparticle composite films. Bethell et al.[14] reported on the fabrication of GNP/dithiol networks on functionalized SiO₂ surfaces. Firstly, the substrate surface was functionalized with mercaptosilanes. Upon immersion of the functionalized substrate into a solution of weakly capped gold colloids, the latter bound to the thiol groups exposed by the substrate. Afterwards, solutions of dithiols and gold colloids were applied alternately, leading to the successive formation of a GNP-dithiol network. Similar layer-by-layer self-assembly (LBL-SA) processes were used by different groups to fabricate thin films con-

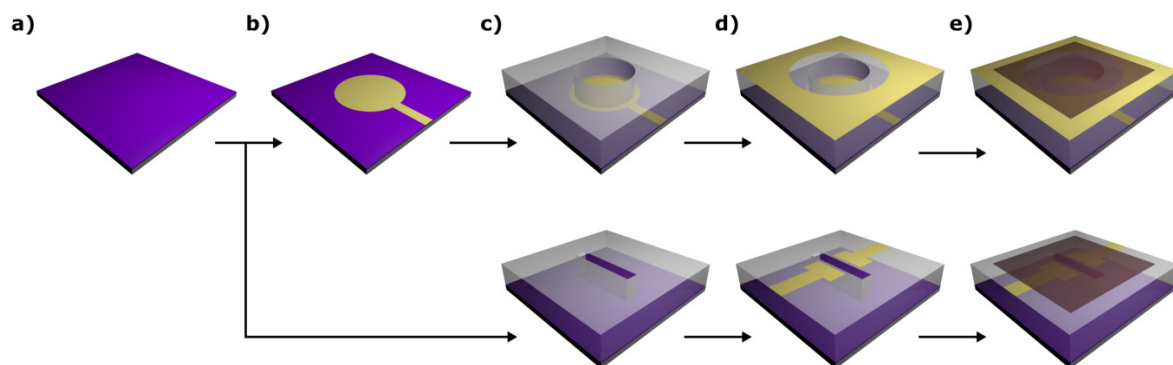


Figure 1: Fabrication process of different GNP-membrane based devices. The top row depicts the fabrication of an electrostatic actuator, while the bottom row depicts the fabrication process of a GNP membrane based ambient pressure sensor. *a)* A silicon wafer with a thermal oxide layer acts as substrate. *b)* If desired, Ti/Au back electrodes were deposited onto the substrate. *c)* SU-8 epoxy photoresist is used for fabricating 3D structures with cavities for freestanding membrane deposition. *d)* Deposition of Au top electrodes for electrically contacting the freestanding membranes. *e)* GNP membrane deposition.

sisting of GNP-dithiol networks on glass[5, 11] or polymer (polyethylene)[9, 7] substrates.

While these LBL-SA processes exhibit different advantages for the fabrication of substrate-supported GNP networks, e.g. a high degree of control and excellent particle cross-linking ratios,[11] they show major drawbacks when it comes to the fabrication of freestanding GNP membranes by lift-off and transfer procedures, as the resulting GNP networks are covalently attached to the substrate. For the fabrication of GNP membranes we follow a procedure which was published by our group in 2011.[15]

Here, a solution of GNPs with weakly bound dodecylamine (DA) ligands in heptane was spin-coated onto glass substrates. Subsequently, a methanolic solution of an alkylene dithiol was spin-coated leading to a ligand exchange and formation of a thin film of cross-linked GNPs. The two deposition steps could be repeated to obtain GNP-dithiol composite films with controlled thickness in the 20 – 100 nm range. Compared to the conventional self-assembly based processes, the spin-coating based deposition enables rapid fabrication of the thin films and - due to the absence of strong chemical binding between the film and the substrate - a lift-off of the film. This can be achieved either by alkaline underetching[16, 15] or careful immersion of the substrates into deionized water,[17] leading to detachment of the film, which then remains floating at the liquid-air interface and can be transferred to arbitrary substrates.

3 DEVICE FABRICATION AND CHARACTERIZATION

Different microstructures were used as support for the freestanding GNP membranes, depending on the target application of the final device. In this paper, we present the exploration of two different MEMS applications of dithiol cross-linked GNP membranes. On the one hand, we demonstrated the fabrication of a resistive ambient pressure sensor, employing a GNP membrane as strain sensitive transducer.[18] On the other hand, we demonstrated electrostatic actuation of freestanding GNP composite membranes.[17] These two applications will be discussed in the following. The fabrication of the devices was similar in both cases. Figure 1, top row, schematically depicts the fabrication process of an electrostatic actuator device, while the fabrication of an ambient pressure sensor is depicted in the bottom row. Commonly, 3D microstructures were fabricated onto doped silicon wafers with thermally grown oxide layers, acting as insulation barriers.

3.1 Ambient Pressure Sensor

In a recent paper, we demonstrated the applicability of dithiol cross-linked GNP membranes as strain sensitive transducers in resistive ambient pressure sensors.[18] The fabrication of such a device is schematically depicted in figure 1, bottom row. Onto a silicon wafer substrate, a layer of SU-8 photoresist was deposited and a microcavity was subsequently fabricated using photolithography. On top of this relief structure, following a lift-off procedure, gold electrodes were deposited in proximity to the cavity. Finally, a 1,6-hexanedithiol

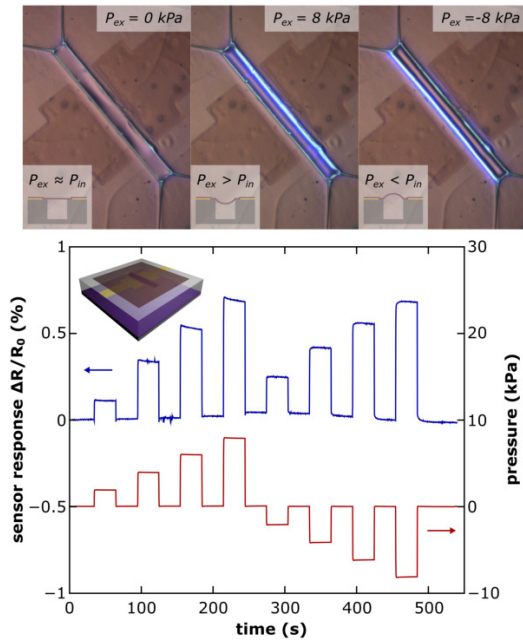


Figure 2: (top) Micrographs of a GNP membrane based resistive pressure sensor upon application of different external pressures. The device comprises a 55 nm thick 6DT cross-linked GNP membrane, sealing a $\sim 40 \mu\text{m}$ wide and $\sim 40 \mu\text{m}$ deep microcavity. (bottom) Time trace of the GNP membrane pressure sensor response (upper blue line) to applied external pressure transients (lower red line). The resistance was read out by electrodes deposited in proximity to the cavity. Adapted from Ref. [18] with permission from The Royal Society of Chemistry.

(6DT) cross-linked GNP membrane was transferred to the microstructure, as described above.

In this type of pressure sensor, the GNP membrane acts both as diaphragm, and as strain sensitive transducer. Sealing the microcavity, the membrane deflects upon variation of the external pressure, due to the pressure difference between the cavity volume and the exterior. The resulting strain causes a change in the membrane's resistance that can simply be read out by contacting the electrodes in proximity to the microcavity.

For characterization the devices were placed in a pressure cell, suitable to apply positive and negative pressures (relative to ambient) in a range of $\pm 10 \text{ kPa}$. The cell pressure as well as the resistance of the device were constantly monitored using digital reference pressure gauges (Sensortech) and a Keithley 2601A source measure unit. Figure 2 shows an exemplary resistance and pressure trace, recorded while applying pressures in a range from approximately -8 to 8 kPa to a device comprising a 55 nm thin 6DT cross-linked GNP

membrane, placed onto a $\sim 40 \mu\text{m}$ wide microcavity (depth $\sim 40 \mu\text{m}$). Upon application of positive and negative pressures up to $|P| \sim 8 \text{ kPa}$ (relative to ambient), deflections of the membrane (see figure 2, top) and a resistance change up to $\sim 0.7\%$ were observed. As expected, the sensor response was nearly independent of the applied pressure's direction. The transfer function of the device was further analyzed and could be well-described using a simple theoretical model.[18]

3.2 Electrostatic Actuator

Further, we demonstrated electrostatic actuation, a widely used principle in MEMS/NEMS, of freestanding, dithiol cross-linked GNP membranes.[17] The fabrication of electrostatic membrane actuators is depicted in figure 1, top row. Again, doped silicon wafers with thermally grown oxide layers were used as substrates. While the wafers could either be used as global counter electrodes themselves, alternatively, structured Ti/Au back electrodes were fabricated for addressing different actuators on one wafer substrate individually. On top of the back electrode structure a layer of SU-8 was deposited and structured using photolithography to yield microcavities of a desired shape. Subsequently, a structured gold top electrode, suitable for contacting a GNP membrane and used as signal ground, was deposited on top of the SU-8 layer. Finally, a 6DT cross-linked GNP membrane was transferred to the 3D electrode structure following the lift-off and transfer process described above. The membrane settled to the electrode structure and remained freestanding on the microcavity.

To demonstrate electrostatic actuation of freestanding, 6DT cross-linked GNP membranes, DC voltages were applied between the top and back electrodes. The potential difference resulted in coulomb forces, pulling the freestanding membrane into the SU-8 cavity. Deflections of the membranes were monitored using atomic force microscopy, confocal microscopy and laser interferometry.[17] Figure 3 depicts exemplary data measured investigating a 6DT cross-linked GNP membrane (thickness 46 nm) deposited onto a $\sim 150 \mu\text{m}$ diameter circular SU-8 cavity, $\sim 8 \mu\text{m}$ above the back electrode. Voltage transients up to $\pm 40 \text{ V}$ were applied between the membrane and the back electrode and deflections up to $\sim 0.8 \mu\text{m}$ were observed using laser interferometry (SIOS Nanovibration Analyzer NA). The voltage-deflection behavior of different devices was measured and approximated using a theoretical model.[17]

The results demonstrate that electrostatic actuation can be used for excitation of freestanding GNP membranes, which is an important step towards the fabrication of more advanced devices, such as electrostatically driven membrane resonators.

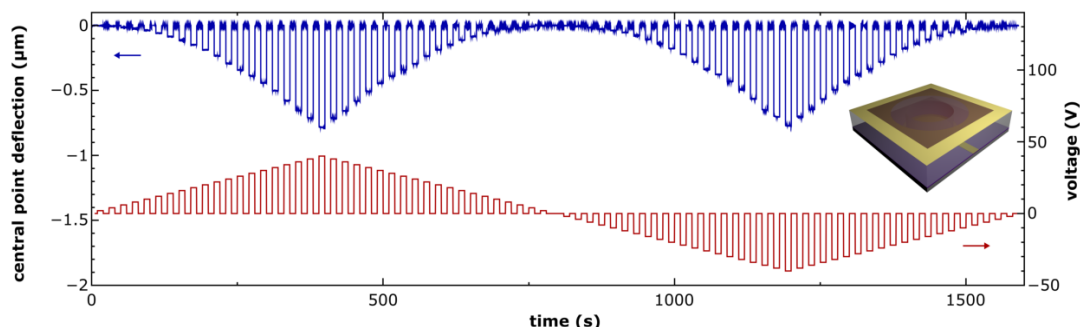


Figure 3: Deflection time trace (*upper blue line*) of a GNP membrane based electrostatic actuator upon application of voltage transients in a range of ± 40 V (*lower red line*). The device comprised a 46 nm thick 6DT cross-linked GNP membrane, deposited onto a ~ 150 μm diameter circular microcavity, ~ 8 μm above a back electrode. Deflections were measured in the center of the membrane using laser interferometry and corrected for a drift caused by the measurement setup.

4 SUMMARY

In summary, our results underline that freestanding conductive membranes of cross-linked gold nanoparticles are interesting candidates for the fabrication of MEMS/NEMS. The applicability of the composite material as strain sensitive transducer in resistive pressure sensors was demonstrated and electrostatic actuation of the membranes was shown. Current studies aim at the fabrication of electrostatically driven GNP membrane drumhead resonators for microgravimetric or pressure sensing applications.

5 ACKNOWLEDGEMENTS

The work of H.S. is supported by a scholarship of the Joachim Herz Stiftung. T.V. acknowledges financial support by the DFG, grant number VO698/3-1.

REFERENCES

- [1] Mueggenburg, K. E.; Lin, X.-M.; Goldsmith, R. H.; Jaeger, H. M. *Nat. Mater.* **2007**, *6*, 656–660.
- [2] Kanjanaboos, P.; Lin, X.-M.; Sader, J. E.; Rupich, S. M.; Jaeger, H. M.; Guest, J. R. *Nano Lett.* **2013**, *13*, 2158–62.
- [3] Jiang, C.; Markutsya, S.; Pikus, Y.; Tsukruk, V. V. *Nat. Mater.* **2004**, *3*, 721–728.
- [4] Terrill, R. H.; Postlethwaite, T. A.; Chen, C.-h.; Poon, C.-D.; Terzis, A.; Chen, A.; Hutchison, J. E.; Clark, M. R.; Wignall, G.; Londono, J. D.; Superfine, R.; Falvo, M.; Johnson Jr., C. S.; Samulski, E. T.; Murray, R. W. *J. Am. Chem. Soc.* **1995**, *117*, 12537–12548.
- [5] Wessels, J. M.; Nothofer, H.-G.; Ford, W. E.; von Wrochem, F.; Scholz, F.; Vossmeier, T.; Schroedter, A.; Weller, H.; Yasuda, A. *J. Am. Chem. Soc.* **2004**, *126*, 3349–3356.
- [6] Herrmann, J.; Müller, K.-H.; Reda, T.; Baxter, G. R.; Raguse, B.; de Groot, G. J. J. B.; Chai, R.; Roberts, M.; Wieczorek, L. *Appl. Phys. Lett.* **2007**, *91*, 183105.
- [7] Vossmeier, T.; Stolte, C.; Ijeh, M.; Kornowski, A.; Weller, H. *Adv. Funct. Mater.* **2008**, *18*, 1611–1616.
- [8] Farcau, C.; Moreira, H.; Viallet, B.; Grisolia, J.; Ciuculescu-Pradines, D.; Amiens, C.; Ressler, L. *J. Phys. Chem. C* **2011**, *115*, 14494–14499.
- [9] Olichwer, N.; Leib, E. W.; Halfar, A. H.; Petrov, A.; Vossmeier, T. *ACS Appl. Mater. Interfaces* **2012**, *4*, 6151–6161.
- [10] Wohltjen, H.; Snow, A. W. *Anal. Chem.* **1998**, *70*, 2856–2859.
- [11] Joseph, Y.; Besnard, I.; Rosenberger, M.; Guse, B.; Nothofer, H.-G.; Wessels, J. M.; Wild, U.; Knop-Gericke, A.; Su, D.; Schlögl, R.; Yasuda, A.; Vossmeier, T. *J. Phys. Chem. B* **2003**, *107*, 7406–7413.
- [12] Ibañez, F. J.; Zamborini, F. P. *Small* **2011**, *8*, 174–202.
- [13] Schlicke, H.; Leib, E. W.; Petrov, A.; Schröder, J. H.; Vossmeier, T. *J. Phys. Chem. C* **2014**, *118*, 4386–4395.
- [14] Bethell, D.; Brust, M.; Schiffrin, D. J.; Kiely, C. J. *Electroanal. Chem.* **1996**, *409*, 137–143.
- [15] Schlicke, H.; Schröder, J. H.; Trebbin, M.; Petrov, A.; Ijeh, M.; Weller, H.; Vossmeier, T. *Nanotechnology* **2011**, *22*, 305303.
- [16] Kowalczyk, B.; Apodaca, M. M.; Nakanishi, H.; Smoukov, S. K.; Grzybowski, B. A. *Small* **2009**, *5*, 1970–1973.
- [17] Schlicke, H.; Battista, D.; Kunze, S.; Schröder, C. J.; Eich, M.; Vossmeier, T. *ACS Appl. Mater. Interfaces* **2015**, *7*, 15123–15128.
- [18] Schlicke, H.; Rebber, M.; Kunze, S.; Vossmeier, T. *Nanoscale* **2016**, *8*, 183–186.

6.5 Conference Proceeding: Eurosensors 2017

The following section includes a conference proceeding article, which connects to the Eurosensors 2017 conference. The article summarizes novel electromechanical chemical sensing concepts employing freestanding GNP membrane actuators and resonators.

The article is reprinted with permission from “Electrostatically Actuated Membranes of Cross-Linked Gold Nanoparticles: Novel Concepts for Electromechanical Gas Sensors”, H. Schlicke, S. C. Bittinger, M. Behrens, M. Yesilmen, H. Hartmann, C. J. Schröter, G. T. Dahl, T. Vossmeier, *Proceedings* **2017**, 1, 301.^[6] Published under CC BY 4.0 license.

Proceedings

Electrostatically Actuated Membranes of Cross-Linked Gold Nanoparticles: Novel Concepts for Electromechanical Gas Sensors [†]

Hendrik Schlicke, Sophia C. Bittinger, Malte Behrens, Mazlum Yesilmen, Hauke Hartmann, Clemens J. Schröter, Gregor T. Dahl and Tobias Vossmeier *

Institute of Physical Chemistry, University of Hamburg, Grindelallee 117, 20146 Hamburg, Germany; schlicke@chemie.uni-hamburg.de (H.S.); sophia.caroline.bittinger@studium.uni-hamburg.de (S.C.B.); malte.behrens@uni-muenster.de (M.B.); mazlum.yesilmen@chemie.uni-hamburg.de (M.Y.); hauke.hartmann@chemie.uni-hamburg.de (H.H.); clemens.schroeter@chemie.uni-hamburg.de (C.J.S.); dahl@chemie.uni-hamburg.de; (G.T.D.)

* Correspondence: tobias.vossmeier@chemie.uni-hamburg.de; Tel.: +49-40-42838-7069

[†] Presented at the EuroSensors 2017 Conference, Paris, France, 3–6 September 2017.

Published: 29 August 2017

Abstract: We report the preparation of freestanding membranes of cross-linked gold nanoparticles (GNPs) and demonstrate their application as electromechanical sensors for volatile organic compounds (VOCs). First, we show that the fundamental vibrational mode frequency of electrostatically excited GNP-membranes shifts significantly when exposing them to solvent vapors. We attribute this effect mainly to the reduction of the membranes' pre-stress. Second, the relief in pre-stress upon analyte sorption can also be detected via quasi-static actuation of the membranes. In this case, the increase of the deflection amplitudes at constant bias voltages can be measured as the sensor signal and correlated to the analyte's concentration. Additionally, we propose a facile route to the fabrication of such hybrid MEMS/NEMS sensors using layer-by-layer spin-coating and contact printing.

Keywords: gold; nanoparticle; membrane; electrostatic; actuator; resonator; sensor; gas sensor; MEMS; NEMS

1. Introduction

Substrate-supported films of ligand-stabilized or cross-linked gold nanoparticles (GNPs) have shown great potentials for applications as chemiresistors and strain gauges. For example, their use in medical diagnosis and integration into wearable electronics has been demonstrated [1]. Recently, freestanding GNP-membranes gained considerable attention and current research activities explore their fundamental electromechanical properties as well as their application as actuators and highly sensitive sensors [2–4]. In previous works we studied the application of α,ω -alkanedithiol cross-linked GNP-membranes as electrostatically driven actuators [5] and resonators [6]. When exposing such resonators to solvent vapors at reduced total pressure we observed a significant decrease of their resonance frequency, suggesting that such devices may find applications as novel types of highly sensitive electromechanical chemical sensors [7]. Thus, the objective of our present study was to explore the responses of freestanding GNP-membranes to solvent vapors by monitoring their fundamental resonance frequency under reduced total pressure whilst applying an AC drive voltage or, alternatively, by measuring their deflection amplitudes at ambient pressure when applying DC voltages. Furthermore, we devised a facile and robust route to the fabrication of such sensors based on depositing cross-linked GNP-films by spin-coating and transferring them onto 3D-structured electrodes via contact printing.

2. Materials and Methods

Dodecylamine stabilized GNPs with core diameters of 3–4 nm were synthesized according to the literature [8]. Thin films of 1,6-hexanedithiol cross-linked GNPs were deposited by our standard spin-coating procedure onto glass substrates [9]. For the fabrication of the sensor devices these films were detached from their original substrates and transferred onto 3D-structured substrates, which were equipped with gold electrodes. These substrates were structured using standard photolithography, either to prepare square cavities within a ~10 μm thick SU-8 layer deposited onto a thermally oxidized silicon wafer (device A), or to etch trenches into a thermally oxidized silicon wafer (device B) [6,7]. In case of device A the back electrode was deposited onto the oxidized silicon wafer before depositing and structuring the SU-8 layer. The top electrode was then deposited onto the SU-8 layer. In case of device B the p-type doped silicon substrate itself was used as the back electrode and the top electrode was deposited onto the thermally grown oxide layer. For transferring the cross-linked GNP-films onto these 3D-structured substrates two different methods were used. The first approach is based on detaching the cross-linked GNP-film from the original substrate by flotation on water [5,6]. The detached film remained floating at the water surface and could be transferred onto the sensor substrate using the Langmuir-Schaefer technique. After drying, a freely suspended membrane covering the cavity in the SU-8 layer was obtained (device A). According to the second approach, the freestanding GNP-membranes were produced via contact printing. Here, the cross-linked GNP-film was first scratched to produce a stripe pattern, covered with a thin sacrificial PMMA-layer, and then detached from the original substrate using a PDMS-stamp, similar as described by Li et al. [10]. Afterwards, the GNP-film was stamped onto the sensor substrate using a procedure similar to that reported by Choi et al. [11]. After carefully removing the stamp, freely suspended GNP-membranes spanning the trench of the 3D-structured substrate were obtained (device B). Finally, the sacrificial PMMA-layer was removed by mild solvent treatment.

The morphology, thickness and conductivity of the cross-linked GNP-films were characterized by transmission electron microscopy (TEM), atomic force microscopy (AFM), and current-voltage (IV-) measurements. To study the electromechanical responses of the freestanding GNP-membrane to solvent vapors the sensor (device A) was placed into a test cell, which was connected to a rotary vane pump for adjusting the overall cell pressure and to a commercial gas calibration system (MCZ Umwelttechnik GmbH, CGM 2000) for providing solvent vapors at various concentrations. Nitrogen 5.0 was used as zero gas. During the measurements the freestanding GNP-membrane was actuated electrostatically at ambient temperature either by applying DC voltage pulses ranging from 20 to 100 V (quasi-static actuation) or by applying an AC sine function voltage with an amplitude of 5 V (dynamic actuation). During AC actuation an offset DC voltage of 10 V was applied to avoid zero-crossing of the net voltage and, hence, of the electrostatic forces acting on the freestanding membrane. The deflection amplitudes of the membrane and its resonance frequency were measured using a laser interferometer (Nanovibration Analyzer NA, SIOS GmbH) directed at the center of the membrane. The experimental setup and procedures are described in detail elsewhere [7].

3. Results

Panels (a) and (b) in Figure 1 show schematic drawings of the two sensors (devices A and B) fabricated and characterized in this study. The GNPs used for membrane preparation had average diameters of 3–4 nm. As shown by the representative TEM image in panel (c) the GNP-membranes consisted of a granular network of GNPs with feature sizes determined by the sizes of the particles. The GNP-membrane used for the fabrication of device A had a thickness of ~39 nm and a conductivity of ~0.13 $\Omega^{-1}\text{cm}^{-1}$. Panel (d) in Figure 1 shows an SEM image of device B with four GNP-membranes bridging a trench of ~35 μm width. The membranes were transferred onto the substrate using a PDMS-stamp. Thus, this result evidences the feasibility of fabricating freestanding membranes of cross-linked GNPs via facile contact printing.

Panel (e) in Figure 1 shows the shifts of the fundamental resonance frequency f_0 (~0.35 MHz) of device A when dosed with toluene vapor (1000, 4000, 7000, 10,000 ppm) at a constant total pressure of 20 mbar. The sensor responded fully reversible with a frequency decrease of up to ~11 kHz, i.e.,

–3% of f_0 . Finally, panel (f) in Figure 1 shows the central point deflection of the membrane (device A) measured under ambient pressure (~1 bar) when applying DC voltage pulses in the range 20 to 100 V. These measurements reveal that the deflection amplitudes increase significantly in the presence of toluene vapor and that this effect becomes much more pronounced when increasing the toluene concentration from 1000 to 10,000 ppm.

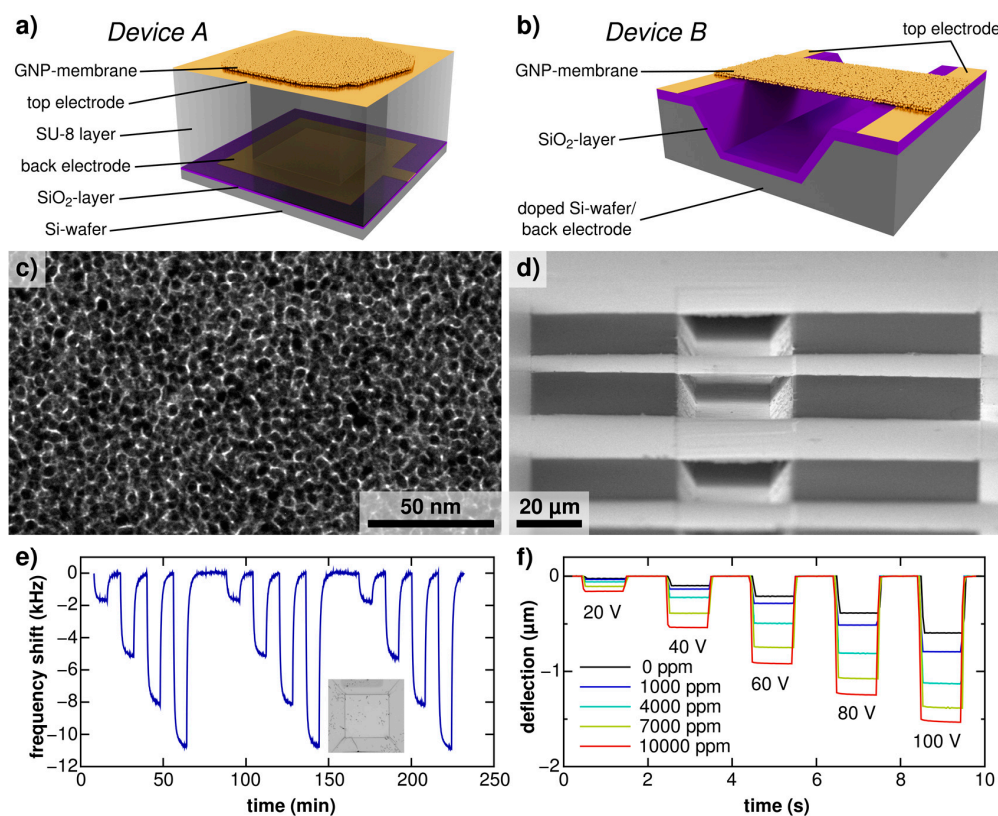


Figure 1. (a) Sensor with square cavity defined in an SU-8 resist layer (device A). The cavity is covered by the cross-linked GNP-membrane; (b) Sensor having an open bridge structure (device B). The GNP-membrane spans a trench etched into a silicon substrate; (c) Representative TEM image of the cross-linked GNP-membrane; (d) SEM image of freestanding GNP-membranes spanning a trench etched into a silicon substrate; (e) Shifts of the fundamental resonance frequency of sensor device A when dosed with toluene vapor (1000, 4000, 7000, 10,000 ppm) at a total pressure of 20 mbar. Inset: Optical microscopy image of the GNP-membrane. The edge length of the square cavity was ~100 μm; (f) Membrane deflections measured when actuating sensor device A by applying DC voltage pulses with and without the presence of toluene vapor, as indicated.

4. Discussion

In this study we demonstrated the application of an electrostatically driven actuator based on a freestanding membrane of cross-linked GNPs as electromechanical sensor for the detection of VOCs. Previously, we assigned the decrease of the fundamental resonance frequency of GNP-membrane resonators observed upon sorption of solvent molecules to the reduction of the membrane’s pre-stress and concluded that the gravimetric effect is negligible [7]. Here, we confirmed this interpretation by studying the quasi-static deflection of a GNP-membrane (device A) by applying DC voltages in the absence/presence of toluene vapor. Taking into account the membrane’s dimensions, the deflection amplitude, and the applied electric field it is possible to calculate the change in pre-stress due to analyte sorption, revealing a decrease from ~14 MPa to lower than ~5 MPa when toluene vapor was present at the highest concentration (10,000 ppm). Importantly, the quasi-static actuation mode can

be applied at ambient pressures while the dynamic operation mode, i.e., the measurement of the resonance frequency shift, can only be applied at reduced pressure in order to avoid significant damping of membrane's vibration.

Furthermore, we demonstrated a facile route to the fabrication of such sensors by transferring the GNP-membrane, which was prepared by a simple spin-coating process, onto the sensor substrate via contact printing (device B). In contrast to previously reported methods, which are based on transferring the GNP-membrane from a water surface, contact printing allows for spatial control of the transfer process and is even suited for controlling the pre-stress of the resulting freestanding GNP-membrane.

Currently, we focus on characterizing the chemical selectivity and sensitivity of membrane-based electromechanical sensors. Further, we will replace the interferometer by implementing a simplified optical or full electrical detection of the membrane's deflection. Finally, together with other previous studies [1], our findings presented above suggest the possibility of designing advanced chemical sensors based on freestanding GNP-membranes with multimode optical, resistive, and electromechanical signal transduction mechanisms.

Acknowledgments: H.S. acknowledges the Joachim Herz Stiftung for financial support. T.V. acknowledges financial support by the DFG, grant number VO698/3-1.

Conflicts of Interest: The authors declare no conflict of interest. The founding sponsors had no role in the design of the study; in the collection, analyses, or interpretation of data; in the writing of the manuscript, and in the decision to publish the results.

References

1. Segev-Bar, M.; Bachar, N.; Wolf, Y.; Ukrainsky, B.; Sarraf, L.; Haick, H. Multi-Parametric Sensing Platforms Based on Nanoparticles. *Adv. Mater. Technol.* **2017**, *2*, 1600206.
2. Wang, Y.; Kanjanaboos, P.; McBride, S.P.; Barry, E.; Lin, X.-M.; Jaeger, H.M. Mechanical properties of self-assembled nanoparticle membranes: Stretching and bending. *Faraday Discuss.* **2015**, *181*, 325–338.
3. Schlicke, H.; Rebber, M.; Kunze, S.; Vossmeier, T. Resistive pressure sensors based on freestanding membranes of gold nanoparticles. *Nanoscale* **2016**, *8*, 183–186.
4. Gauvin, M.; Grisolia, J.; Alnasser, T.; Viallet, B.; Xie, S.; Brugger, J.; Ressler, L. Electro-mechanical sensing in freestanding monolayered gold nanoparticle membranes. *Nanoscale* **2016**, *8*, 11363–11370.
5. Schlicke, H.; Battista, D.; Kunze, S.; Schröter, C.J.; Eich, M.; Vossmeier, T. Freestanding Membranes of Cross-Linked Gold Nanoparticles: Novel Functional Materials for Electrostatic Actuators. *ACS Appl. Mater. Interfaces* **2015**, *7*, 15123–15128.
6. Schlicke, H.; Schröter, C.J.; Vossmeier, T. Electrostatically driven drumhead resonators based on freestanding membranes of cross-linked gold nanoparticles. *Nanoscale* **2016**, *8*, 15880–15887.
7. Schlicke, H.; Behrens, M.; Schröter, C.J.; Dahl, G.T.; Hartmann, H.; Vossmeier, T. Cross-Linked Gold-Nanoparticle Membrane Resonators as Microelectromechanical Vapor Sensors. *ACS Sens.* **2017**, *2*, 540–546.
8. Leff, D.V.; Brandt, L.; Heath, J.R. Synthesis and Characterization of Hydrophobic, Organically-Soluble Gold Nanocrystals Functionalized With Primary Amines. *Langmuir* **1996**, *12*, 4723–4730.
9. Schlicke, H.; Schröder, J.H.; Trebbin, M.; Petrov, A.; Ijeh, M.; Weller, H.; Vossmeier, T. Freestanding films of crosslinked gold nanoparticles prepared via layer-by-layer spin-coating. *Nanotechnology* **2011**, *22*, 305303.
10. Li, H.; Wu, J.; Huang, X.; Yin, Z.; Liu, J.; Zhang, H. A Universal, Rapid Method for Clean Transfer of Nanostructures onto Various Substrates. *ACS Nano* **2014**, *8*, 6563–6570.
11. Choi, M.K.; Park, I.; Kim, D.C.; Joh, E.; Park, O.K.; Kim, J.; Kim, M.; Choi, C.; Yang, J.; Cho, K.W.; et al. Thermally Controlled, Patterned Graphene Transfer Printing for Transparent and Wearable Electronic/Optoelectronic System. *Adv. Funct. Mater.* **2015**, *25*, 7109–7118.



© 2017 by the authors. Licensee MDPI, Basel, Switzerland. This article is an open access article distributed under the terms and conditions of the Creative Commons Attribution (CC BY) license (<http://creativecommons.org/licenses/by/4.0/>).

6.6 Conference Proceeding: IEEE NMDC 2017

The following section includes a conference proceeding article, which connects to a talk scheduled in October 2017 at the 2017 IEEE Nanotechnology Materials and Devices Conference (NMDC) conference in Singapore, Republic of Singapore. The article summarizes MEMS/NEMS pressure and chemical sensor devices employing freestanding GNP membranes.

The article is reprinted with permission from “Membranes of Organically Cross-Linked Gold Nanoparticles: Novel Materials for MEMS/NEMS Sensors and Actuators”, H. Schlicke, C. J. Schröter, G. T. Dahl, M. Rebber, M. Behrens, T. Vossmeier, *2017 IEEE Nanotechnology Materials and Devices Conference (NMDC)*, in press. ©2017 IEEE.

Membranes of Organically Cross-Linked Gold Nanoparticles: Novel Materials for MEMS/NEMS Sensors and Actuators*

Hendrik Schlicke¹, Clemens J. Schröter¹, Gregor T. Dahl¹,
Matthias Rebber¹, Malte Behrens¹, Tobias Vossmeier¹

Abstract— We report the application of freestanding membranes of cross-linked gold nanoparticles (GNPs) as functional materials in novel MEMS/NEMS sensors. GNP composite films are fabricated using a facile ink-based process and transferred onto lithographically fabricated 3D microstructures, suitable to support and electronically address the resulting freestanding membranes. We show that 1,6-hexanedithiol cross-linked GNP membranes can be utilized both, as diaphragm and strain-sensitive transducer in highly sensitive gauge pressure sensors. Aside from this application, we demonstrate electrostatic actuation of such composite membranes and the fabrication of electrostatically driven GNP membrane drumhead resonators with resonance frequencies in the high kilohertz to low megahertz range. Further, these GNP membrane resonators are successfully employed as electromechanical chemical sensors for the detection of vapors and gases, using sorption-induced shifts of their fundamental resonance frequency as sensing signal.

I. INTRODUCTION

Recently, the fabrication of freestanding nanoparticle composite membranes attracted considerable scientific attention, and applications as physical or chemical sensors have been proposed.[1], [2], [3], [4] Metal nanoparticle composite membranes are interesting candidates for functional materials in MEMS and NEMS, as they offer electronic, optical and mechanical properties that can be tuned by adjusting their composition. Further, their pronounced strain sensitivity, originating from the tunneling based charge transport mechanism of the composites, as well as the ability to sorb analytes enable potential applications in novel types of sensors. In this contribution we report the utilization of freestanding membranes consisting of alkanedithiol (ADT) cross-linked GNPs in highly sensitive pressure sensors, and electromechanical chemical sensors for vapors and gases. Firstly, GNP membranes were fabricated by an ink-based spin-coating process.[5] Here, solutions of GNPs (average diameter: 3-4 nm) and 1,6-hexanedithiol (6DT) cross-linkers were alternately deposited onto rotating glass substrates, forming cross-linked, disordered GNP thin films with adjustable thickness in the 20 to 100 nm range. In a second step, freestanding GNP membranes were obtained by detaching the composite films from their initial substrates and transferring them onto 3D microstructures. A transmission

*The work of H.S. is supported by a scholarship of the Joachim Herz Stiftung. T.V. acknowledges financial support by the DFG, grant number VO698/3-1.

¹Hendrik Schlicke, Clemens J. Schröter, Gregor T. Dahl, Matthias Rebber, Malte Behrens and Tobias Vossmeier are with the Institute of Physical Chemistry, University of Hamburg, Grindelallee 117, 20146 Hamburg, Germany. schlicke@chemie.uni-hamburg.de

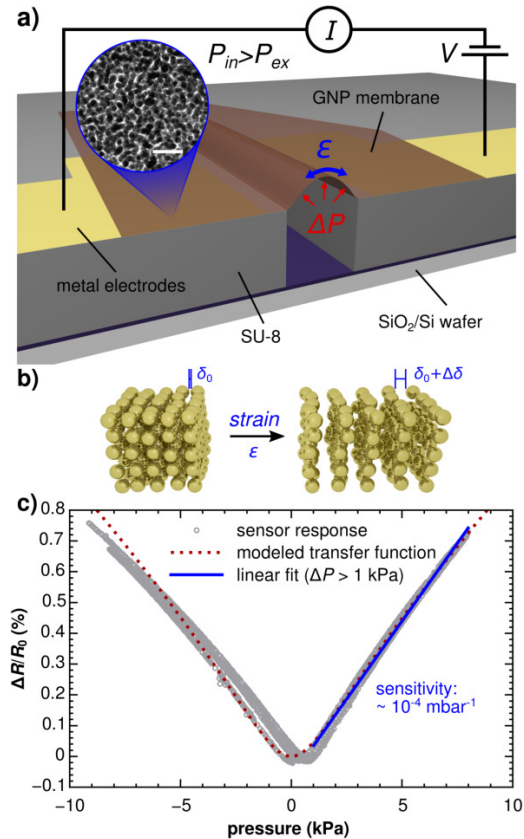


Fig. 1. a) Cross-sectional view of a GNP membrane based pressure sensor. The inset shows a transmission electron micrograph of a 6DT cross-linked GNP membrane. Scale bar: 25 nm. b) Schematic depicting the effect of strain on GNP composite materials. c) Sensor response of a GNP membrane based pressure sensor.[6]

electron micrograph displaying the granular structure of such a GNP membrane is depicted in the inset of figure 1a.

II. PRESSURE SENSING

A resistive pressure sensor was fabricated by transferring a GNP membrane onto an SU-8 based microstructure, featuring a cuboid cavity with proximal electrodes. After transfer of the membrane, it settled on the microstructure, sealing the microcavity. In this device, the membrane acts both, as diaphragm and strain-sensitive transducer. A schematic, cross-sectional view of such a GNP membrane based pressure sensor, summarizing the sensing principle, is depicted

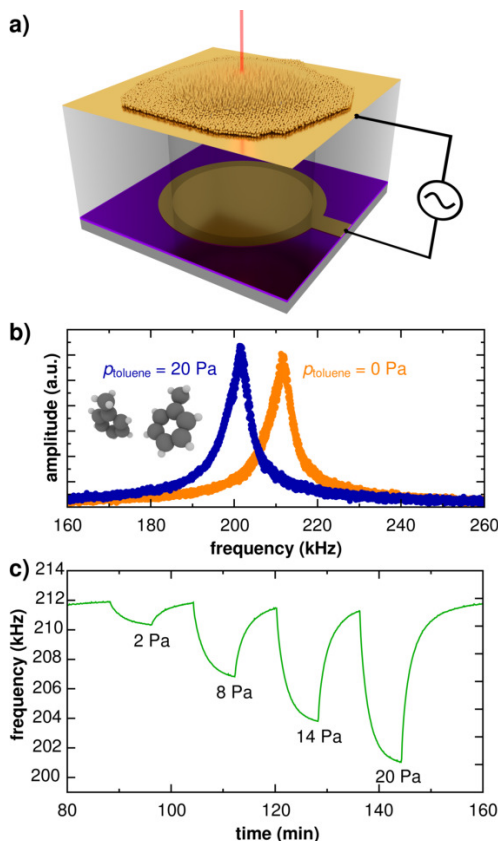


Fig. 2. a) Schematic depicting a GNP membrane based drumhead resonator with interferometric deflection readout, excited using AC voltages. b) Amplitude spectra showing the fundamental vibrational resonance of a $\sim 120 \mu\text{m}$ diameter circular GNP membrane resonator (thickness $44 \pm 1 \text{ nm}$) at 20 mbar under pure nitrogen atmosphere (orange curve) and under exposure to a toluene partial pressure of 20 Pa (blue curve). Adapted with permission from [7]. Copyright 2017 American Chemical Society.

in figure 1a. Variations of the environmental pressure cause a pressure difference between the internal microcavity volume and the exterior, which again results in inward or outward bulging of the membrane with respect to the cavity's aperture, depending on the direction of pressure variation. The bulging-induced strain translates into changes of the interparticle distances (see figure 1b). As the tunneling-based charge transport through metal composite membranes is very sensitive to changes in these interparticle distances, strain, and hence pressure variations are reflected in a strong resistive response of the device, measured between the electrodes. An exemplary sensor response trace is depicted in figure 1c. The data indicate a comparably high resistive pressure sensitivity of our sensor ($\sim 1 \times 10^{-4} \text{ mbar}^{-1}$) and could be well-described using a simple analytical model.[6]

III. RESONATORS AND CHEMICAL SENSING

Recently, our group reported electrostatically driven GNP membrane drumhead resonators. Figure 2a depicts a schematic of a device consisting of a 6DT cross-linked GNP membrane deposited onto a microstructure, featuring

a circular cavity. The cavity is equipped with a gold top electrode to electronically address the membrane and another counter electrode at its bottom. The application of AC voltages between the electrodes induces periodically varying electrostatic forces acting on the GNP membranes. Pronounced oscillations of the membranes could be excited when sweeping the drive frequency ω_d and matching one of their resonance frequencies. Using laser interferometry, vibrational spectra of GNP membrane resonators were acquired and mode shapes were imaged.[4] Here, we report the use of such GNP membrane resonators as electromechanical chemical sensors.[7] Constantly monitoring the vibrational spectrum of a resonator, it was exposed to vapors of different analytes, i.e., toluene, 4-methylpentan-2-one, 1-propanol and water. Figure 2b shows amplitude spectra of the fundamental vibrational mode of a circular, $120 \mu\text{m}$ diameter GNP membrane resonator at a total pressure of 20 mbar. The orange curve depicts a spectrum acquired in pure nitrogen atmosphere, while the blue curve was acquired when introducing toluene at a partial pressure of 20 Pa (10000 ppm). The spectra clearly show a downshift of the resonance frequency of $\sim 10 \text{ kHz}$, i.e., $\sim 5\%$. A time trace showing transients of the resonator's fundamental resonance frequency when repeatedly introducing toluene at varying partial pressures is provided in figure 2c. The data clearly indicate the reversibility of the sensor response. We assigned the strong shifts to a transduction mechanism that is based on sorption-induced changes of the membranes' pre-stress.

IV. CONCLUSIONS

In this contribution we report highly sensitive pressure sensors as well as microelectromechanical chemical sensors based on freestanding membranes of organically cross-linked GNPs, with thicknesses in the range of several tens of nanometers. Our results emphasize the potential of nanocomposites for applications as functional materials in novel MEMS/NEMS type sensors.

REFERENCES

- [1] K. E. Mueggenburg, X.-M. Lin, R. H. Goldsmith, H. M. Jaeger, "Elastic Membranes of Close-Packed Nanoparticle Arrays," *Nat. Mater.*, vol. 6, pp. 656-660, Sep. 2007.
- [2] C. Jiang, S. Markutsya, Y. Pikus, V. V. Tsukruk, "Freely Suspended Nanocomposite Membranes as Highly Sensitive Sensors," *Nat. Mater.*, vol. 3, pp. 721-728, Oct. 2004.
- [3] M. Gauvin, J. Grisolia, T. Alnasser, B. Viallet, S. Xie, J. Brugger, L. Ressler, "Electro-Mechanical Sensing in Freestanding Monolayered Gold Nanoparticle Membranes," *Nanoscale*, vol. 8, pp. 11363-11370, Jun. 2016.
- [4] H. Schlicke, C. J. Schröter, T. Vossmeier, "Electrostatically driven drumhead resonators based on freestanding membranes of cross-linked gold nanoparticles," *Nanoscale*, vol. 8, pp. 15880-15887, Sep. 2016.
- [5] H. Schlicke, J. H. Schröder, M. Trebbin, A. Petrov, M. Ijeh, H. Weller, T. Vossmeier, "Freestanding Films of Crosslinked Gold Nanoparticles Prepared via Layer-by-Layer Spin-Coating," *Nanotechnology*, vol. 22, pp. 305303, Jul. 2011.
- [6] H. Schlicke, M. Rebber, S. K. Kunze, T. Vossmeier, "Resistive Pressure Sensors Based on Freestanding Membranes of Gold Nanoparticles," *Nanoscale*, vol. 8, pp. 183-186, Jan. 2016.
- [7] H. Schlicke, M. Behrens, C. J. Schröter, G. T. Dahl, H. Hartmann, T. Vossmeier, "Cross-Linked Gold-Nanoparticle Membrane Resonators as Microelectromechanical Vapor Sensors," *ACS Sens.*, vol. 2, pp. 540-546, Apr. 2017.

7 Discussion and Outlook

Within the preceding sections 5 and 6, potential applications of DT cross-linked GNP membranes in novel types of sensors and actuators were demonstrated. Further, a number of experiments were carried out to characterize the structural, mechanical, optical, and charge transport properties of these nanostructured materials. The projects targeted in this work can be grouped in four general topics.

Pressure Sensing. In the first project outlined in section 5.2, a resistive pressure sensor employing a 55 nm thick, $\sim 40 \times \sim 500 \mu\text{m}$ sized 6DT cross-linked GNP membrane, acting both as diaphragm and strain sensitive transducer, was reported. Compared to previously reported devices based on silicon or graphene, the sensor showed a high resistive sensitivity of $\sim 1 \times 10^{-4} \text{ mbar}^{-1}$, which is presumably due to the elasticity and the inherent, tunneling-based, strongly strain sensitive charge transport mechanism of this nanocomposite. Further, the device enabled the electromechanical characterization of the GNP membrane without any perturbing substrate. Using a geometrical model, a gauge factor of $g = 7$ was estimated. Even though this value is high compared to typical gauge factors of metal foil strain gauges (~ 2), it is still relatively low for GNP composites.^[50,58,59] According to the assumed charge transport model, the use of ordered structures of larger GNPs is promising for improving the overall device sensitivity. Further improvements include the incorporation of a gas barrier layer, to prevent gases from slowly diffusing through the GNP membrane, affecting the performance and stability of the devices.

Current investigations aim at measuring the GNP membranes' resistive responses, while monitoring their deflection induced by the pressure differences. Here, AFM-based or interferometric in-situ membrane deflection measurements will be used to directly determine the geometry of the bulged membranes, which is more accurate than employing a theoretical estimation as done in this work. By directly correlating the measured membrane deflection with the resistive response, these experiments should provide valuable insights into electromechanical properties of such nanoparticle membranes.

In summary, the fabricated GNP/ADT nanomembrane based pressure sensor with its high sensitivity highlights the potential of freestanding nanocomposite membranes for electromechanical pressure/force sensing and encourages further research into this topic. Additionally, such devices are a powerful tool for the characterization of the nanomembranes' electromechanical properties.

Electrostatic Actuators and Resonators. The projects outlined in sections 5.3, 5.4 and 6.2 cover electrostatically driven GNP composite membrane actuators and resonators. Here, electrodes were placed in proximity to freestanding GNP membranes, forming ca-

capacitive structures. Applying a voltage signal to such structures leads to charging and hence to electrostatic forces, deflecting the membrane.

Section 5.3 provides the first demonstration of electrostatically actuated GNP membranes. Electrostatic actuation is a versatile transduction principle widely used in MEMS/NEMS. Quasi-static deflection of GNP membranes using DC voltages can potentially be useful in MOEMS, as it enables coupling the optical/plasmonic characteristics of the membranes to electronically controlled mechanical deflection and strain. Further, it can be used to precisely control the optical path length between a freestanding membranes and e.g. an underlying reflective electrode.

In addition, actuation of freestanding GNP membranes using AC voltages was utilized to excite resonant oscillations (section 5.4). To this end, an interferometric setup was assembled, capable of electrostatically exciting the GNP membranes and monitoring their static deflections as well as resonant oscillations in the kHz to low MHz range under ambient or reduced pressure, and under exposure to different analytes in the gas phase. The setup was used to probe a set of circular 50 μm and 100 μm sized GNP membrane resonators, which showed fundamental resonance frequencies in the high kHz range and quality factors up to ~ 2000 . Resonance spectra as well as amplitude mapping experiments were conducted and the results were interpreted using the theoretical model for tense membranes with negligible bending stiffness. Section 6.2 contains a deeper investigation of GNP membrane based resonators of different geometries.

Electrostatically actuated GNP membranes can act i.a. as sensors, as their response characteristics to electrostatic forces may depend on external parameters, such as pressure, temperature or exposure to analyte compounds. Current investigations aim at the fabrication of micro- and nanomechanical GNP membrane actuators and resonators with all-electrical excitation and readout. This is advantageous, as the devices could be directly incorporated into electronic circuitry without the need of optics for spectrum acquisition.

Electromechanical Chemical Sensing. Different projects that are part of this thesis aimed at the use of freestanding GNP membranes as microelectromechanical chemical sensors. It was demonstrated that the exposure of freestanding GNP composite membranes to vapors of toluene, 4M2P, 1-propanol or water leads to changes in their mechanical properties, which result in an altered response to imposed electrostatic forces.

Section 5.5 describes electrostatically driven GNP membrane resonators operated under reduced pressure, showing significant changes in their fundamental resonance frequency upon exposure to analyte vapors. We propose a transduction mechanism, which is based on alterations of the membranes' pre-stress upon sorption of analyte, leading to observed resonance frequency shifts.

The sorption-induced changes in the membranes' mechanical properties also influence their quasi-static deflection behavior under actuation with DC voltages. Here, the voltage-deflection relation can be used as sensing signal (section 6.3.2). The use of this measure-

ment concept is of potential interest for sensing applications requiring ambient pressures, as — in contrast to membrane oscillations — the quasi-static deflection is not prone to damping. Both electromechanical chemical sensing concepts are further summarized in a recent conference proceeding (section 6.5).

In addition, section 6.3.1 discusses the response kinetics of GNP membrane resonators forming sealed microcavities. The response time of these devices to transient analyte exposure presumably depends on the diffusion of analyte molecules through the GNP membrane, providing a metric for discriminating different analytes.

The novel sensing concepts, which were established within the framework of this thesis rendered the basis for a patent application and triggered a series of further studies. These comprise investigations regarding the achievable sensitivities and the limit of detection, as well as new approaches to analyte discrimination. Electromechanical chemical sensors using quasi-statically or dynamically actuated (resonant) GNP membranes can be used in combination with conventional GNP based chemiresistors as sensor array, because the different transduction mechanisms are expected to yield different sensitivities/selectivities. Additionally, by varying the material composition (nanoparticle sizes/shapes, matrix molecules, etc.) the sensitivities/selectivities of the devices can presumably further be adjusted. Because of the different transduction principles and their structural tunability, GNP composite membranes hence represent an interesting material system for multivariate sensing concepts.

Material Characterization. While the above-mentioned studies regarding different devices employing GNP membranes as functional components also contributed to the understanding of their properties, a further study (cf. section 6.1) focused on material characterization. Here, the structural, electronic, optical, as well as mechanical characteristics of GNP/DT composites were investigated.

Optical UV/vis absorbance spectra, as well as charge transport investigations of the GNP films showed that the use of different ADT molecules for the cross-linkage of GNPs grants control over the interparticle spacings. Besides, structural investigations were conducted. Here, TEM indicated fusion of GNPs in the composites, when cross-linked by shorter-chain ADTs.

The core element of the study was the mechanical characterization of freestanding GNP membranes using AFM bulge-tests. It provides the first report of quantitative measurements probing the elasticity of freestanding GNP membranes cross-linked using different ADTs and affirmed the tunability of their elastic properties by the selection of the ADT linker molecule. A nonlinear dependence of the elastic modulus on the ADTs' chain length was observed, with values ranging from ~ 10 GPa to ~ 3 GPa when increasing the number of methylene units from 4 to 10.

To conclude, the experiments and results summarized in this thesis underline the potential of nanocomposite membranes for the use in future hybrid MEMS/NEMS. While this thesis

is exclusively focused on GNP composites, it is to note that different concepts discussed can potentially be transferred to other nanocomposite materials. Different prototypical devices, i.e. a highly sensitive pressure sensor, novel types of chemical sensors, actuators and resonators were fabricated and their functionality was successfully demonstrated, and triggered a series of follow-up studies.

8 Bibliography

- [1] H. Schlicke, D. Battista, S. Kunze, C. J. Schröter, M. Eich, T. Vossmeier, *ACS Appl. Mater. Interfaces* **2015**, *7*, 15123–15128.
- [2] H. Schlicke, M. Rebber, S. Kunze, T. Vossmeier, *Nanoscale* **2016**, *8*, 183–186.
- [3] H. Schlicke, C. J. Schröter, T. Vossmeier, *Nanoscale* **2016**, *8*, 15880–15887.
- [4] H. Schlicke, M. Behrens, C. J. Schröter, G. T. Dahl, H. Hartmann, T. Vossmeier, *ACS Sensors* **2017**, *2*, 540–546.
- [5] H. Schlicke, C. J. Schröter, M. Rebber, D. Battista, S. Kunze, T. Vossmeier in *TechConnect Briefs 2016: Advanced Manufacturing, Electronics and Microsystems*, pp. 83–86.
- [6] H. Schlicke, S. C. Bittinger, M. Behrens, M. Yesilmen, H. Hartmann, C. J. Schröter, G. T. Dahl, T. Vossmeier, *Proceedings* **2017**, *1*, 301.
- [7] B. H. Brown, R. H. Smallwood, D. C. Barber, P. V. Lawford, D. R. Hose, *Medical Physics and Biomedical Engineering*, Taylor & Francis Group, New York, **1999**.
- [8] S. Frings, F. Müller, *Biologie der Sinne*, Springer-Verlag, Berlin/Heidelberg, **2014**.
- [9] K. L. Ekinici, *Small* **2005**, *1*, 786–797.
- [10] R. Bogue, *Sensor Rev.* **2013**, *33*, 300–304.
- [11] J. Marek, B. Hoefflinger, U.-M. Gomez in *CHIPS 2020 VOL. 2*, B. Hoefflinger (Ed.), Springer International Publishing, **2016**.
- [12] Electronic Engineering Times, *IHS MEMS Market Tracker Q3 2015; Reproduced in EE Times: MEMS Market: Ups and Upstarts (accessed August 22, 2017)*, **2015**. http://www.eetimes.com/document.asp?doc_id=1328333.
- [13] H. G. Craighead, *Science* **2000**, *290*, 1532–1535.
- [14] K. Jensen, K. Kim, A. Zettl, *Nat. Nanotechnol.* **2008**, *3*, 533–537.
- [15] B. Lassagne, D. Garcia-Sanchez, A. Aguasca, A. Bachtold, *Nano Lett.* **2008**, *8*, 3735–3738.
- [16] R. A. Barton, I. R. Storch, V. P. Adiga, R. Sakakibara, B. R. Cipriany, B. Ilic, S. P. Wang, P. Ong, P. L. McEuen, J. M. Parpia, H. G. Craighead, *Nano Lett.* **2012**, *12*, 4681–4686.

8. Bibliography

- [17] J. S. Bunch, A. M. van der Zande, S. S. Verbridge, I. W. Frank, D. M. Tanenbaum, J. M. Parpia, H. G. Craighead, P. L. McEuen, *Science* **2007**, *315*, 490–493.
- [18] J. S. Bunch, S. S. Verbridge, J. S. Alden, A. M. van der Zande, J. M. Parpia, H. G. Craighead, P. L. McEuen, *Nano Lett.* **2008**, *8*, 2458–2462.
- [19] J. S. Bunch, Dissertation, Cornell University, **2008**.
- [20] S. J. Cartamil-Bueno, P. G. Steeneken, A. Centeno, A. Zurutuza, H. S. J. van der Zant, S. Hourii, *Nano Lett.* **2016**, *16*, 6792–6796.
- [21] C. Chen, J. Hone, *Proc. IEEE* **2013**, *101*, 1766–1779.
- [22] C. Chen, S. Lee, V. V. Deshpande, G.-h. Lee, M. Lekas, K. Shepard, J. Hone, *Nat. Nanotechnol.* **2013**, *8*, 923–927.
- [23] C. Chen, S. Rosenblatt, K. I. Bolotin, W. Kalb, P. Kim, I. Kymissis, H. L. Stormer, T. F. Heinz, J. Hone, *Nat. Nanotechnol.* **2009**, *4*, 861–867.
- [24] M. Dai, C.-W. Kim, K. Eom, *Nanoscale Res. Lett.* **2012**, *7*, 499.
- [25] K. M. Milaninia, M. A. Baldo, A. Reina, J. Kong, *Appl. Phys. Lett.* **2009**, *95*, 183105.
- [26] A. D. Smith, F. Niklaus, A. Paussa, S. Vaziri, A. C. Fischer, M. Sterner, F. Forsberg, A. Delin, D. Esseni, P. Palestri, M. Östling, M. C. Lemme, *Nano Lett.* **2013**, *13*, 3237–3242.
- [27] A. M. van der Zande, R. A. Barton, J. S. Alden, C. S. Ruiz-Vargas, W. S. Whitney, P. H. Q. Pham, J. Park, J. M. Parpia, H. G. Craighead, P. L. McEuen, *Nano Lett.* **2010**, *10*, 4869–4873.
- [28] Q. Wang, W. Hong, L. Dong, *Nanoscale* **2016**, *8*, 7663–7671.
- [29] S.-E. Zhu, M. Krishna Ghatkesar, C. Zhang, G. C. A. M. Janssen, *Appl. Phys. Lett.* **2013**, *102*, 161904.
- [30] A. Castellanos-Gomez, R. van Leeuwen, M. Buscema, H. S. J. van der Zant, G. A. Steele, W. J. Venstra, *Adv. Mater.* **2013**, *25*, 6719–6723.
- [31] J. Lee, P. X.-L. Feng in *2014 IEEE International Frequency Control Symposium (FCS)*, IEEE, pp. 1–4, doi: 10.1109/FCS.2014.6859918.
- [32] J. Lee, Z. Wang, K. He, J. Shan, P. X.-L. Feng, *Appl. Phys. Lett.* **2014**, *105*, 023104.
- [33] J. Lee, Z. Wang, K. He, J. Shan, P. X.-L. Feng, *ACS Nano* **2013**, *7*, 6086–6091.
- [34] N. Morell, A. Reserbat-Plantey, I. Tsioutsios, K. G. Schädler, F. Dubin, F. H. L. Koppens, A. Bachtold, *Nano Lett.* **2016**, *16*, 5102–5108.
- [35] Z. Wang, J. Lee, K. He, J. Shan, P. X.-L. Feng, *Sci. Rep.* **2015**, *4*, 3919.

-
- [36] R. Yang, Z. Wang, P. X.-L. Feng in *2016 IEEE 29th International Conference on Micro Electro Mechanical Systems (MEMS)*, IEEE, pp. 59–62, doi: 10.1109/MEMSYS.2016.7421557.
- [37] Z. Wang, H. Jia, X. Zheng, R. Yang, Z. Wang, G. J. Ye, X. H. Chen, J. Shan, P. X.-L. Feng, *Nanoscale* **2015**, *7*, 877–884.
- [38] X. Zhang, C. Neumann, P. Angelova, A. Beyer, A. Götzhäuser, *Langmuir* **2014**, *30*, 8221–8227.
- [39] A. Turchanin, A. Beyer, C. T. Nottbohm, X. Zhang, R. Stosch, A. Sologubenko, J. Mayer, P. Hinze, T. Weimann, A. Götzhäuser, *Adv. Mater.* **2009**, *21*, 1233–1237.
- [40] X. Zhang, R. Waitz, F. Yang, C. Lutz, P. Angelova, A. Götzhäuser, E. Scheer, *Appl. Phys. Lett.* **2015**, *106*, 063107.
- [41] X. Zhang, A. Beyer, A. Götzhäuser, *Beilstein J. Nanotechnol.* **2011**, *2*, 826–833.
- [42] M. Gauvin, J. Grisolia, T. Alnasser, B. Viallet, S. Xie, J. Brugger, L. Rossier, *Nanoscale* **2016**, *8*, 11363–11370.
- [43] C. Jiang, S. Markutsya, Y. Pikus, V. V. Tsukruk, *Nat. Mater.* **2004**, *3*, 721–728.
- [44] C. Jiang, M. E. McConney, S. Singamaneni, E. Merrick, Y. Chen, J. Zhao, L. Zhang, V. V. Tsukruk, *Chem. Mater.* **2006**, *18*, 2632–2634.
- [45] P. Kanjanaboos, X.-M. Lin, J. E. Sader, S. M. Rupich, H. M. Jaeger, J. R. Guest, *Nano Lett.* **2013**, *13*, 2158–2162.
- [46] S. Markutsya, C. Jiang, Y. Pikus, V. V. Tsukruk, *Adv. Funct. Mater.* **2005**, *15*, 771–780.
- [47] Y. Wang, H. Chan, B. Narayanan, S. P. McBride, S. K. R. S. Sankaranarayanan, X.-M. Lin, H. M. Jaeger, *ACS Nano* **2017**, *11*, 8026–8033.
- [48] H. Schlicke, E. W. Leib, A. Petrov, J. H. Schröder, T. Vossmeier, *J. Phys. Chem. C* **2014**, *118*, 4386–4395.
- [49] D. Bethell, M. Brust, D. J. Schiffrin, C. Kiely, *J. Electroanal. Chem.* **1996**, *409*, 137–143.
- [50] J. Herrmann, K.-H. Müller, T. Reda, G. R. Baxter, B. Raguse, G. J. J. B. de Groot, R. Chai, M. Roberts, L. Wiczorek, *Appl. Phys. Lett.* **2007**, *91*, 183105.
- [51] H. Wohltjen, A. W. Snow, *Anal. Chem.* **1998**, *70*, 2856–2859.
- [52] H. Schlicke, J. H. Schröder, M. Trebbin, A. Petrov, M. Ijeh, H. Weller, T. Vossmeier, *Nanotechnology* **2011**, *22*, 305303.
- [53] Y. Joseph, I. Besnard, M. Rosenberger, B. Guse, H.-G. Nothofer, J. M. Wessels, U. Wild, A. Knop-Gericke, D. Su, R. Schlögl, A. Yasuda, T. Vossmeier, *J. Phys. Chem. B* **2003**, *107*, 7406–7413.

8. Bibliography

- [54] C. Jiang, S. Markutsya, V. V. Tsukruk, *Langmuir* **2004**, *20*, 882–890.
- [55] M. Brust, D. Bethell, D. J. Schiffrin, C. J. Kiely, *Adv. Mater.* **1995**, *7*, 795–797.
- [56] R. H. Terrill, T. A. Postlethwaite, C.-h. Chen, C.-D. Poon, A. Terzis, A. Chen, J. E. Hutchison, M. R. Clark, G. Wignall, J. D. Londono, R. Superfine, M. Falvo, C. S. Johnson Jr., E. T. Samulski, R. W. Murray, *J. Am. Chem. Soc.* **1995**, *117*, 12537–12548.
- [57] J. M. Wessels, H.-G. Nothofer, W. E. Ford, F. von Wrochem, F. Scholz, T. Vossmeier, A. Schroedter, H. Weller, A. Yasuda, *J. Am. Chem. Soc.* **2004**, *126*, 3349–3356.
- [58] T. Vossmeier, C. Stolte, M. Ijeh, A. Kornowski, H. Weller, *Adv. Funct. Mater.* **2008**, *18*, 1611–1616.
- [59] C. Farcau, H. Moreira, B. Viallet, J. Grisolia, D. Ciuculescu-Pradines, C. Amiens, L. Ressler, *J. Phys. Chem. C* **2011**, *115*, 14494–14499.
- [60] N. Olichwer, E. W. Leib, A. H. Halfar, A. Petrov, T. Vossmeier, *ACS Appl. Mater. Interfaces* **2012**, *4*, 6151–6161.
- [61] M. Segev-Bar, A. Landman, M. Nir-Shapira, G. Shuster, H. Haick, *ACS Appl. Mater. Interfaces* **2013**, *5*, 5531–5541.
- [62] S. D. Evans, S. R. Johnson, Y. L. Cheng, T. Shen, *J. Mater. Chem.* **2000**, *10*, 183–188.
- [63] W. H. Steinecker, M. P. Rowe, E. T. Zellers, *Anal. Chem.* **2007**, *79*, 4977–4986.
- [64] F. J. Ibañez, F. P. Zamborini, *Small* **2012**, *8*, 174–202.
- [65] N. Olichwer, A. Meyer, M. Yesilmen, T. Vossmeier, *J. Mater. Chem. C* **2016**, *4*, 8214–8225.
- [66] M. K. Nakhleh, H. Amal, R. Jeries, Y. Y. Broza, M. Aboud, A. Gharra, H. Ivgi, S. Khatib, S. Badarneh, L. Har-Shai, L. Glass-Marmor, I. Lejbkiewicz, A. Miller, S. Badarny, R. Winer, J. Finberg, S. Cohen-Kaminsky, F. Perros, D. Montani, B. Girerd, G. Garcia, G. Simonneau, F. Nakhoul, S. Baram, R. Salim, M. Hakim, M. Gruber, O. Ronen, T. Marshak, I. Doweck, O. Nativ, Z. Bahouth, D.-y. Shi, W. Zhang, Q.-l. Hua, Y.-y. Pan, L. Tao, H. Liu, A. Karban, E. Koifman, T. Rainis, R. Skapars, A. Sivins, G. Ancans, I. Liepniece-Karele, I. Kikuste, I. Lasina, I. Tolmanis, D. Johnson, S. Z. Millstone, J. Fulton, J. W. Wells, L. H. Wilf, M. Humbert, M. Leja, N. Peled, H. Haick, *ACS Nano* **2017**, *11*, 112–125.
- [67] Y. Yan, S. C. Warren, P. Fuller, B. A. Grzybowski, *Nat. Nanotechnol.* **2016**, *11*, 603–608.
- [68] M. C. Daniel, D. Astruc, *Chem. Rev.* **2004**, *104*, 293–346.

- [69] C. W. Corti, R. J. Holliday, *Gold Bull.* **2004**, *37*, 20–26.
- [70] P. Goodman, *Gold Bull.* **2002**, *35*, 21–26.
- [71] S. Eustis, M. A. El-Sayed, *Chem. Soc. Rev.* **2006**, *35*, 209–217.
- [72] L. E. Brus, *J. Chem. Phys.* **1984**, *80*, 4403–4409.
- [73] A. Henglein, *Top. Curr. Chem.* **1988**, *143*, 113–180.
- [74] C. B. Murray, D. J. Norris, M. G. Bawendi, *J. Am. Chem. Soc.* **1993**, *115*, 8706–8715.
- [75] H. Weller, *Angew. Chem. Int. Ed. Engl.* **1993**, *32*, 41–53.
- [76] M. Colombo, S. Carregal-Romero, M. F. Casula, L. Gutiérrez, M. P. Morales, I. B. Böhm, J. T. Heverhagen, D. Prospero, W. J. Parak, *Chem. Soc. Rev.* **2012**, *41*, 4306–4334.
- [77] G. Schmid, *Nanoparticles: From Theory to Application*, Wiley VCH, Weinheim, **2010**.
- [78] C. A. Mirkin, R. L. Letsinger, R. C. Mucic, J. J. Storhoff, *Nature* **1996**, *382*, 607–609.
- [79] A. G. Kanaras, Z. Wang, A. D. Bates, R. Cosstick, M. Brust, *Angew. Chem.* **2003**, *115*, 201–204.
- [80] C. J. Loweth, W. B. Caldwell, X. Peng, A. P. Alivisatos, P. G. Schultz, *Angew. Chem. Int. Ed. Engl.* **1999**, *38*, 1808–1812.
- [81] P. Alivisatos, *Nature Biotechnol.* **2004**, *22*, 47–52.
- [82] R. A. Sperling, P. Rivera Gil, F. Zhang, M. Zanella, W. J. Parak, *Chem. Soc. Rev.* **2008**, *37*, 1896.
- [83] S. K. Ghosh, T. Pal, *Chem. Rev.* **2007**, *107*, 4797–4862.
- [84] L. B. Hunt, *Gold Bull.* **1976**, *9*, 134–139.
- [85] D. J. Barber, I. C. Freestone, *Archaeometry* **1990**, *32*, 33–45.
- [86] G. Mie, *Ann. Phys.* **1908**, *25*, 377–445.
- [87] S. Link, M. A. El-Sayed, *J. Phys. Chem. B* **1999**, *103*, 8410–8426.
- [88] P. K. Jain, W. Huang, M. A. El-Sayed, *Nano Lett.* **2007**, *7*, 2080–2088.
- [89] C. Sönnichsen, B. M. Reinhard, J. Liphardt, A. P. Alivisatos, *Nat. Biotechnol.* **2005**, *23*, 741–745.
- [90] T. Ung, L. M. Liz-Marzán, P. Mulvaney, *J. Phys. Chem. B* **2001**, *105*, 3441–3452.

8. Bibliography

- [91] J. C. Maxwell Garnett, *Phil. Trans. R. Soc. Lond. A* **1904**, *203*, 237–288.
- [92] J. C. Maxwell Garnett, *Phil. Trans. R. Soc. Lond. A* **1906**, *205*, 237–288.
- [93] J. M. Thomas, *Pure Appl. Chem.* **1988**, *60*, 1517–1528.
- [94] M. Faraday, *Phil. Trans. R. Soc. Lond.* **1857**, *147*, 145–181.
- [95] J. Turkevich, P. C. Stevenson, J. Hillier, *Discuss. Faraday Soc.* **1951**, *11*, 55–75.
- [96] F. Schulz, T. Homolka, N. G. Bastús, V. Puentes, H. Weller, T. Vossmeier, *Langmuir* **2014**, *30*, 10779–10784.
- [97] G. Frens, *Nat. Phys. Sci.* **1973**, *241*, 20–22.
- [98] M. Brust, M. Walker, D. Bethell, D. J. Schiffrin, R. Whyman, *J. Chem. Soc., Chem. Commun.* **1994**, 801–802.
- [99] D. V. Leff, L. Brandt, J. R. Heath, *Langmuir* **1996**, *12*, 4723–4730.
- [100] F. Chen, X. Li, J. Hihath, Z. Huang, N. Tao, *J. Am. Chem. Soc.* **2006**, *128*, 15874–15881.
- [101] J. A. Olmos-Asar, M. Ludueña, M. M. Mariscal, *Phys. Chem. Chem. Phys.* **2014**, *16*, 15979.
- [102] G. von Freymann, V. Kitaev, B. V. Lotsch, G. a. Ozin, *Chem. Soc. Rev.* **2013**, *42*, 2528–2554.
- [103] L. Shi, Y. Zhang, B. Dong, T. Zhan, X. Liu, J. Zi, *Adv. Mater.* **2013**, *25*, 5314–5320.
- [104] D. V. Talapin, J.-S. Lee, M. V. Kovalenko, E. V. Shevchenko, *Chem. Rev.* **2010**, *110*, 389–458.
- [105] H.-L. Zhang, S. D. Evans, J. R. Henderson, R. E. Miles, T.-H. Shen, *Nanotechnology* **2002**, *13*, 439–444.
- [106] I. J. Kramer, G. Moreno-Bautista, J. C. Minor, D. Kopilovic, E. H. Sargent, *Appl. Phys. Lett.* **2014**, *105*, 163902.
- [107] V. A. Akhavan, B. W. Goodfellow, M. G. Panthani, D. K. Reid, D. J. Hellebusch, T. Adachi, B. A. Korgel, *Energy Environ. Sci.* **2010**, *3*, 1600–1606.
- [108] S. Willing, H. Lehmann, M. Volkmann, C. Klinke, *Sci. Adv.* **2017**, *3*, e1603191.
- [109] N. Garg, A. Mohanty, N. Lazarus, L. Schultz, T. R. Rozzi, S. Santhanam, L. Weiss, J. L. Snyder, G. K. Fedder, R. Jin, *Nanotechnology* **2010**, *21*, 405501.
- [110] S. Dasgupta, G. Stoesser, N. Schweikert, R. Hahn, S. Dehm, R. Kruk, H. Hahn, *Adv. Funct. Mater.* **2012**, *22*, 4909–4919.
- [111] M. Segev-Bar, H. Haick, *ACS Nano* **2013**, *7*, 8366–8378.

-
- [112] Y. Yin, A. P. Alivisatos, *Nature* **2005**, *437*, 664–670.
- [113] D. Ling, M. J. Hackett, T. Hyeon, *Nano Today* **2014**, *9*, 457–477.
- [114] G. Kalyuzhny, R. W. Murray, *J. Phys. Chem. B* **2005**, *109*, 7012–7021.
- [115] J.-S. Lee, M. V. Kovalenko, J. Huang, D. S. Chung, D. V. Talapin, *Nat. Nanotechnol.* **2011**, *6*, 348–352.
- [116] D. V. Talapin, C. B. Murray, *Science* **2005**, *310*, 86–89.
- [117] J. M. Luther, M. Law, Q. Song, C. L. Perkins, M. C. Beard, A. J. Nozik, *ACS Nano* **2008**, *2*, 271–280.
- [118] M. V. Kovalenko, M. Scheele, D. V. Talapin, *Science* **2009**, *324*, 1417–1420.
- [119] S. V. Voitekhovich, D. V. Talapin, C. Klinke, A. Kornowski, H. Weller, *Chem. Mater.* **2008**, *20*, 4545–4547.
- [120] J. Lauth, J. Marbach, A. Meyer, S. Dogan, C. Klinke, A. Kornowski, H. Weller, *Adv. Funct. Mater.* **2014**, *24*, 1081–1088.
- [121] M. Gauvin, Y. Wan, I. Arfaoui, M.-P. Pileni, *J. Phys. Chem. C* **2014**, *118*, 5005–5012.
- [122] C. Yan, I. Arfaoui, N. Goubet, M.-P. Pileni, *Adv. Funct. Mater.* **2013**, *23*, 2315–2321.
- [123] T. Andryszewski, M. Iwan, M. Hołdyński, M. Fiałkowski, *Chem. Mater.* **2016**, *28*, 5304–5313.
- [124] I. Kosif, K. Kratz, S. S. You, M. K. Bera, K. Kim, B. Leahy, T. Emrick, K. Y. C. Lee, B. Lin, *ACS Nano* **2017**, *11*, 1292–1300.
- [125] S. Kunze, *Unpublished data*, **2017**.
- [126] Y. Joseph, A. Peic, X. Chen, J. Michl, T. Vossmeier, A. Yasuda, *J. Phys. Chem. C* **2007**, *111*, 12855–12859.
- [127] Y. Joseph, B. Guse, T. Vossmeier, A. Yasuda, *J. Phys. Chem. C* **2008**, *112*, 12507–12514.
- [128] C. Shen, C. Hui, T. Yang, C. Xiao, J. Tian, L. Bao, S. Chen, H. Ding, H. Gao, *Chem. Mater.* **2008**, *20*, 6939–6944.
- [129] M. van Staveren, H. Brom, L. de Jongh, G. Schmid, *Solid State Commun.* **1986**, *60*, 319–322.
- [130] B. Abeles, P. Sheng, M. Coutts, Y. Arie, *Adv. Phys.* **1975**, *24*, 407–461.
- [131] C. A. Neugebauer, M. B. Webb, *J. Appl. Phys.* **1962**, *33*, 74–82.

8. Bibliography

- [132] W. P. Wuelfing, S. J. Green, J. J. Pietron, D. E. Cliffel, R. W. Murray, *J. Am. Chem. Soc.* **2000**, *122*, 11465–11472.
- [133] X. D. Cui, A. Primak, X. Zarate, J. Tomfohr, O. F. Sankey, A. L. Moore, T. A. Moore, D. Gust, L. A. Nagahara, S. M. Lindsay, *J. Phys. Chem. B* **2002**, *106*, 8609–8614.
- [134] X. D. Cui, X. Zarate, J. Tomfohr, O. F. Sankey, A. Primak, A. L. Moore, T. A. Moore, D. Gust, G. Harris, S. M. Lindsay, *Nanotechnology* **2002**, *13*, 5–14.
- [135] Y. Wan, N. Goubet, P.-A. Albouy, N. Schaeffer, M.-P. Pileni, *Langmuir* **2013**, *29*, 13576–13581.
- [136] T. Vossmeier, Y. Joseph, I. Besnard, O. Harnack, N. Krasteva, B. Guse, H.-G. Nothofer, Y. A. in *SPIE Vol. 5513*, pp. 202–212.
- [137] Y. Joseph, N. Krasteva, I. Besnard, B. Guse, M. Rosenberger, U. Wild, A. Knop-Gericke, R. Schlögl, R. Krustev, A. Yasuda, T. Vossmeier, *Faraday Discuss.* **2004**, *125*, 77–97.
- [138] S. K. Kim, H. Chang, E. T. Zellers, *Anal. Chem.* **2011**, *83*, 7198–7206.
- [139] G. Peng, U. Tisch, O. Adams, M. Hakim, N. Shehada, Y. Y. Broza, S. Billan, R. Abdah-Bortnyak, A. Kuten, H. Haick, *Nat. Nanotechnol.* **2009**, *4*, 669–673.
- [140] W. R. Collin, G. Serrano, L. K. Wright, H. Chang, N. Nuñovero, E. T. Zellers, *Anal. Chem.* **2014**, *86*, 655–663.
- [141] K. Persaud, G. Dodd, *Nature* **1982**, *299*, 352–355.
- [142] J. W. Gardner, P. N. Bartlett, *Sens. Actuator B Chem.* **1994**, *18*, 210–211.
- [143] R. A. Potyrailo, *Chem. Soc. Rev.* **2017**, *46*, 5311–5346.
- [144] J. Yin, P. Hu, J. Luo, L. Wang, M. F. Cohen, C.-J. Zhong, *ACS Nano* **2011**, *5*, 6516–6526.
- [145] K. S. Novoselov, A. K. Geim, S. V. Morozov, D. Jiang, Y. Zhang, S. V. Dubonos, I. V. Grigorieva, A. A. Firsov, *Science* **2004**, *306*, 666–669.
- [146] K. S. Novoselov, D. Jiang, F. Schedin, T. J. Booth, V. V. Khotkevich, S. V. Morozov, A. K. Geim, *Proc. Natl. Acad. Sci. USA* **2005**, *102*, 10451–10453.
- [147] A. Reserbat-Plantey, K. G. Schädler, L. Gaudreau, G. Navickaite, J. Güttinger, D. Chang, C. Toninelli, A. Bachtold, F. H. L. Koppens, *Nat. Commun.* **2016**, *7*, 10218.
- [148] A. Castellanos-Gomez, M. Poot, G. A. Steele, H. S. J. van der Zant, N. Agrait, G. Rubio-Bollinger, *Adv. Mater.* **2012**, *24*, 772–775.

-
- [149] D. Davidovikj, J. J. Slim, S. J. Cartamil-Bueno, H. S. J. van der Zant, P. G. Steeneken, W. J. Venstra, *Nano Lett.* **2016**, *16*, 2768–2773.
- [150] A. Castellanos-Gomez, M. Buscema, R. Molenaar, V. Singh, L. Janssen, H. S. J. van der Zant, G. A. Steele, *2D Mater.* **2014**, *1*, 011002.
- [151] S. J. Cartamil-Bueno, P. G. Steeneken, F. D. Tichelaar, E. Navarro-Moratalla, W. J. Venstra, R. van Leeuwen, E. Coronado, H. S. J. van der Zant, G. A. Steele, A. Castellanos-Gomez, *Nano Res.* **2015**, *8*, 2842–2849.
- [152] W. Eck, A. Küller, M. Grunze, B. Völkel, A. Götzhäuser, *Adv. Mater.* **2005**, *17*, 2583–2587.
- [153] A. A. Mamedov, N. A. Kotov, *Langmuir* **2000**, *16*, 5530–5533.
- [154] R. Vendamme, S.-Y. Onoue, A. Nakao, T. Kunitake, *Nat. Mater.* **2006**, *5*, 494–501.
- [155] B. Kowalczyk, M. M. Apodaca, H. Nakanishi, S. K. Smoukov, B. A. Grzybowski, *Small* **2009**, *5*, 1970–1973.
- [156] K. E. Mueggenburg, X.-M. Lin, R. H. Goldsmith, H. M. Jaeger, *Nat. Mater.* **2007**, *6*, 656–660.
- [157] K. J. Si, D. Sikdar, Y. Chen, F. Eftekhari, Z. Xu, Y. Tang, W. Xiong, P. Guo, S. Zhang, Y. Lu, Q. Bao, W. Zhu, M. Premaratne, W. Cheng, *ACS Nano* **2014**, *8*, 11086–11093.
- [158] Z. Jiang, J. He, S. a. Deshmukh, P. Kanjanaboos, G. Kamath, Y. Wang, S. K. R. S. Sankaranarayanan, J. Wang, H. M. Jaeger, X.-M. Lin, *Nat. Mater.* **2015**, *14*, 912–917.
- [159] J. He, P. Kanjanaboos, N. L. Frazer, A. Weis, X.-M. Lin, H. M. Jaeger, *Small* **2010**, *6*, 1449–1456.
- [160] M. Gauvin, T. Alnasser, E. Terver, I. Abid, A. Mlayah, S. Xie, J. Brugger, B. Viallet, L. Rossier, J. Grisolia, *Nanoscale* **2016**, *8*, 16162–16167.
- [161] X. Wang, K. J. Si, J. Yang, X. Wu, Q. Qin, W. Cheng, Y. Lu in *2016 IEEE 29th International Conference on Micro Electro Mechanical Systems (MEMS)*, IEEE, pp. 1058–1061, doi: 10.1109/MEMSYS.2016.7421816.
- [162] A. Dong, J. Chen, P. M. Vora, J. M. Kikkawa, C. B. Murray, *Nature* **2010**, *466*, 474–477.
- [163] A. Böker, J. He, T. Emrick, T. P. Russell, *Soft Matter* **2007**, *3*, 1231–1248.
- [164] B. Le Ouay, S. Guldin, Z. Luo, S. Allegri, F. Stellacci, *Adv. Mater. Interfaces* **2016**, *3*, 1600191.
- [165] D. Lee, S. Jia, S. Banerjee, J. Bevk, I. P. Herman, J. W. Kysar, *Phys. Rev. Lett.* **2007**, *98*, 026103.

8. Bibliography

- [166] P. Podsiadlo, G. Krylova, B. Lee, K. Critchley, D. J. Gosztola, D. V. Talapin, P. D. Ashby, E. V. Shevchenko, *J. Am. Chem. Soc.* **2010**, *132*, 8953–8960.
- [167] J. H. Schröder, Dissertation, Universität Hamburg, **2012**.
- [168] W. C. Oliver, G. M. Pharr, *J. Mater. Res.* **1992**, *7*, 1564–1583.
- [169] W. Cheng, M. J. Campolongo, S. J. Tan, D. Luo, *Nano Today* **2009**, *4*, 482–493.
- [170] X. W. Gu, X. Ye, D. M. Koshy, S. Vachhani, P. Hosemann, A. P. Alivisatos, *Proc. Natl. Acad. Sci. USA* **2017**, *114*, 2836–2841.
- [171] J. He, X. M. Lin, H. Chan, L. Vuković, P. Král, H. M. Jaeger, *Nano Lett.* **2011**, *11*, 2430–2435.
- [172] C. M. Stafford, C. Harrison, K. L. Beers, A. Karim, E. J. Amis, M. R. VanLandingham, H.-C. Kim, W. Volksen, R. D. Miller, E. E. Simonyi, *Nat. Mater.* **2004**, *3*, 545–550.
- [173] M. K. Small, W. Nix, *J. Mater. Res.* **1992**, *7*, 1553–1563.
- [174] J. J. Vlassak, W. D. Nix, *J. Mater. Res.* **1992**, *7*, 3242–3249.
- [175] E. Schweitzer, M. Göken, *J. Mater. Res.* **2007**, *22*, 2902–2911.
- [176] C. Jiang, S. Markutsya, V. V. Tsukruk, *Adv. Mater.* **2004**, *16*, 157–161.
- [177] C. Jiang, H. Ko, V. V. Tsukruk, *Adv. Mater.* **2005**, *17*, 2127–2131.
- [178] A. Karimi, O. R. Shojaei, T. Kruml, J. L. Martin, *Thin Solid Films* **1997**, *308-309*, 334–339.
- [179] Y. Xiang, X. Chen, J. Vlassak, *J. Mater. Res.* **2005**, *20*, 2360–2370.
- [180] *Further permissions related to this figure may be obtained from the American Chemical Society.* <http://pubs.acs.org/doi/abs/10.1021/nl401352k>.
- [181] A. M. Hurst, S. Lee, N. Petrone, J. VanDeWeert, A. M. van der Zande, J. Hone in *Transducers 2013 & Eurosensors XXVII Proceedings*, IEEE, pp. 586–589, doi: 10.1109/Transducers.2013.6626834.
- [182] H. Zhu, Y. Wang, J. Xiao, M. Liu, S. Xiong, Z. J. Wong, Z. Ye, Y. Ye, X. Yin, X. Zhang, *Nat. Nanotechnol.* **2014**, *10*, 151–155.
- [183] V. Singh, S. Sengupta, H. S. Solanki, R. Dhall, A. Allain, S. Dhara, P. Pant, M. M. Deshmukh, *Nanotechnology* **2010**, *21*, 165204.
- [184] V. Singh, S. Sengupta, H. S. Solanki, R. Dhall, A. Allain, S. Dhara, P. Pant, M. M. Deshmukh, *Nanotechnology* **2010**, *21*, 209801.
- [185] M. Tomi, A. Isacson, M. Oksanen, D. Lyashenko, J.-P. Kaikkonen, S. Tervakangas, J. Kolehmainen, P. J. Hakonen, *Nanoscale* **2015**, *7*, 14747–14751.

-
- [186] V. P. Adiga, B. Ilic, R. A. Barton, I. Wilson-Rae, H. G. Craighead, J. M. Parpia, *Appl. Phys. Lett.* **2011**, *99*, 253103.
- [187] S. S. Rao, *Mechanical Vibrations*, Addison-Wesley Publishing Company, Inc., **1986**.
- [188] K. F. Graff, *Wave Motion in Elastic Solids*, Oxford University Press, London, **1975**.
- [189] W.-M. Zhang, K.-M. Hu, Z.-K. Peng, G. Meng, *Sensors* **2015**, *15*, 26478–26566.
- [190] M. Takamura, H. Okamoto, K. Furukawa, H. Yamaguchi, H. Hibino, *J. Appl. Phys.* **2014**, *116*, 064304.
- [191] T. Lammerink, M. Elwenspoek, J. Fluitman in *1991 IEEE Micro Electro Mechanical Systems Proceedings*, IEEE, pp. 160–165, doi: 10.1109/MEMSYS.1991.114788.
- [192] S. Schmid, *Resonant MEMS*, O. Brand, I. Dufour, S. M. Heinrich, F. Jossen (Eds.), Wiley VCH, Weinheim, Germany, **2015**.
- [193] S. Schmid, M. Wendlandt, D. Junker, C. Hierold, *Appl. Phys. Lett.* **2006**, *89*, 163506.
- [194] S. Schmid, M. Wendlandt, D. Juncker, C. Hierold, *Appl. Phys. Lett.* **2007**, *90*, 039901.
- [195] S. Schmid, C. Hierold, A. Boisen, *J. Appl. Phys.* **2010**, *107*, 054510.
- [196] M. Suter, O. Ergeneman, J. Zürcher, S. Schmid, A. Camenzind, B. J. Nelson, C. Hierold, *J. Micromech. Microeng.* **2011**, *21*, 025023.
- [197] B. Lee, C. B. Prater, W. P. King, *Nanotechnology* **2012**, *23*, 055709.
- [198] R. J. Wilfinger, P. H. Bardell, D. S. Chhabra, *IBM J. Res. Dev.* **1968**, *12*, 113–118.
- [199] M. Othman, A. Brunnschweiler, *Electron. Lett.* **1987**, *23*, 728.
- [200] I. Rahneberg, Dissertation, Technische Universität Ilmenau, **2013**.
- [201] D. Dontsov, Dissertation, Technische Universität Ilmenau, **2002**.
- [202] SIOS GmbH, *Datasheet: Nano Vibration Analyzer Serie NA*, **2014**.
- [203] F. Laermer, A. Schilp, *Patent US5501893: Method of Anisotropic Etching Silicon*, **1996**.
- [204] H. Seidel, L. Csepregi, A. Heuberger, H. Baumgartel, *J. Electrochem. Soc.* **1990**, *137*, 3612–3626.
- [205] K. Williams, R. Muller, *J. Microelectromech. S.* **1996**, *5*, 256–269.
- [206] J. Melai, C. Salm, S. Smits, J. Visschers, J. Schmitz, *J. Micromech. Microeng.* **2009**, *19*, 065012.

8. Bibliography

- [207] S. Jiguet, A. Bertsch, H. Hofmann, P. Renaud, *Adv. Funct. Mater.* **2005**, *15*, 1511–1516.
- [208] S. Bae, H. Kim, Y. Lee, X. Xu, J.-S. Park, Y. Zheng, J. Balakrishnan, T. Lei, H. Ri Kim, Y. I. Song, Y.-J. Kim, K. S. Kim, B. Özyilmaz, J.-H. Ahn, B. H. Hong, S. Iijima, *Nat. Nanotechnol.* **2010**, *5*, 574–578.
- [209] L. Digianantonio, M. Gauvin, T. Alnasser, D. Babonneau, B. Viallet, J. Grisolia, G. Viau, A. Coati, Y. Garreau, L. Rossier, *J. Phys. Chem. C* **2016**, *120*, 5848–5854.
- [210] W. Cheng, M. J. Campolongo, J. J. Cha, S. J. Tan, C. C. Umbach, D. A. Muller, D. Luo, *Nat. Mater.* **2009**, *8*, 519–525.
- [211] P. Bhattacharya, R. Fornari, H. Kamimura, *Comprehensive Semiconductor Science and Technology*, Elsevier Science, Amsterdam, **2011**.
- [212] E. Kalvesten, L. Smith, L. Tenerz, G. Stemme in *1998 IEEE Micro Electro Mechanical Systems Workshop Proceedings*, IEEE, pp. 574–579, doi: 10.1109/MEMSYS.1998.659821.
- [213] C. Stampfer, T. Helbling, D. Obergfell, B. Schöberle, M. K. Tripp, A. Jungen, S. Roth, V. M. Bright, C. Hierold, *Nano Lett.* **2006**, *6*, 233–237.
- [214] C. Hierold, A. Jungen, C. Stampfer, T. Helbling, *Sens. Actuator A Phys.* **2007**, *136*, 51–61.
- [215] M. E. Motamedi, *MOEMS: Micro-opto-electro-mechanical Systems*, SPIE Press, Bellingham, Washington, **2005**.
- [216] M. Glück, *MEMS in der Mikrosystemtechnik: Aufbau, Wirkprinzipien, Herstellung und Praxiseinsatz mikroelektromechanischer Schaltungen und Sensorsysteme*, Vieweg+Teubner Verlag, **2015**.
- [217] T.-W. Yeow, K. Law, A. Goldenberg, *IEEE Commun. Mag.* **2001**, *39*, 158–163.
- [218] A. K. Pandey, O. Gottlieb, O. Shtempluck, E. Buks, *Appl. Phys. Lett.* **2010**, *96*, 203105.
- [219] D. R. Southworth, H. G. Craighead, J. M. Parpia, *Appl. Phys. Lett.* **2009**, *94*, 213506.
- [220] S. Schmid, S. Kühne, C. Hierold, *J. Micromech. Microeng.* **2009**, *19*, 065018.
- [221] K. Dransfeld, P. Kienle, G. M. Kalvius, *Physik I: Mechanik und Wärme*, Oldenbourg Wissenschaftsverlag GmbH, München, **2005**.
- [222] A. Ostendorf, C. Cramer, G. Decher, M. Schönhoff, *J. Phys. Chem. C* **2015**, *119*, 9543–9549.
- [223] A. Guinier, *X-ray Diffraction in Crystals, Imperfect Crystals, and Amorphous Bodies 7th ed.*, Dover Books on Physics, New York, **1994**.

- [224] M. Hu, X. Wang, G. V. Hartland, P. Mulvaney, J. P. Juste, J. E. Sader, *J. Am. Chem. Soc.* **2003**, *125*, 14925–14933.
- [225] Oerlikon Leyboldt Vacuum, *THERMOVAC Transmitter TTR 101N, TTR 101N S Manual*, **2016**.
- [226] Falco Systems, *WMA-300 High Voltage Amplifier Manual*, **2016**.
- [227] Institut für Arbeitsschutz der Deutschen Gesetzlichen Unfallversicherung, *GESTIS-Stoffdatenbank (accessed: September 19, 2017)*, **2017**.
- [228] TCI America, *Safety Data Sheet: 1,10-Dodecanedithiol*, **2016**.
- [229] Sigma Aldrich, *Sigma Aldrich online database (accessed: September 19, 2017)*, **2017**. <https://www.sigmaaldrich.com/>.
- [230] Sigma Aldrich, *Safety Data Sheet: 4-Methyl-2-pentanone*, **2015**.
- [231] Allresist Gesellschaft für chemische Produkte zur Mikrostrukturierung mbH, *Safety Data Sheet: AR 300-12*, **2015**.
- [232] Allresist Gesellschaft für chemische Produkte zur Mikrostrukturierung mbH, *Safety Data Sheet: AR 300-40*, **2017**.
- [233] Allresist Gesellschaft für chemische Produkte zur Mikrostrukturierung mbH, *Safety Data Sheet: AR-N 7520 Series Photoresist*, **2016**.
- [234] Merck Performance Materials GmbH, *Safety Data Sheet: AZ 726 MIF Developer*, **2015**.
- [235] Merck Performance Materials GmbH, *Safety Data Sheet: AZ ECI 3012 Photoresist*, **2015**.
- [236] Merck Performance Materials GmbH, *Safety Data Sheet: AZ 826 MIF Developer*, **2015**.
- [237] Merck Performance Materials GmbH, *Safety Data Sheet: AZ nLOF 2035 Photoresist*, **2015**.
- [238] Merck Performance Materials GmbH, *Safety Data Sheet: AZ nLOF 2070 Photoresist*, **2015**.
- [239] Merck Performance Materials GmbH, *Safety Data Sheet: AZ 1518 Photoresist*, **2016**.
- [240] TECHNIC France, *Safety Data Sheet: BOE 7-1 (AF 87.5 - 12.5) avec Surfactant*, **2017**.
- [241] micro resist technology GmbH, *Safety Data Sheet: Developer mr-Dev 600*, **2013**.
- [242] Microchem Corporation, *Safety Data Sheet: SU-8 2000 Series Resists*, **2016**.

8. Bibliography

- [243] Microchem Corporation, *Safety Data Sheet: SU-8 Series Resists*, **2016**.
- [244] Dow Corning, *Safety Data Sheet: SYLGARD 184 SILICONE ELASTOMER KIT (BASE)*, **2016**.
- [245] Dow Corning, *Safety Data Sheet: SYLGARD 184 SILICONE ELASTOMER KIT (CURING AGENT)*, **2016**.
- [246] TECHNIC France, *Safety Data Sheet: TechniEtch Cr01*, **2015**.
- [247] TECHNIC France, *Safety Data Sheet: TechniStrip NI555*, **2017**.

A Appendix

A.1 Supporting Information

This section contains the SI or ESI, relating to the publications reprinted in the synopsis, section 5.

A.1.1 Resistive Pressure Sensors Based on Freestanding Membranes of Gold Nanoparticles

Reprinted from “Resistive pressure sensors based on freestanding membranes of gold nanoparticles”, H. Schlicke, M. Rebber, S. Kunze, T. Vossmeier, *Nanoscale* **2016**, *8*, 183-186^[2] with permission from The Royal Society of Chemistry.

Electronic Supplementary Information:
Resistive pressure sensors based on freestanding
membranes of gold nanoparticles

Hendrik Schlicke, Matthias Rebber, Svenja Kunze, and Tobias Vossmeier*

*Institute of Physical Chemistry, University of Hamburg, Grindelallee 117, 20146 Hamburg,
Germany*

E-mail: tobias.vossmeier@chemie.uni-hamburg.de

*To whom correspondence should be addressed

Gold nanoparticles

Dodecylamine stabilized gold nanoparticles (GNPs) were used for membrane fabrication. The GNPs were prepared following a synthetic route published by Leff et al.¹ Transmission electron microscopy was conducted for determining the GNP sizes, using a Philips CM 300 microscope, operated at 200 kV. In order to improve the stability of the particles prior to TEM characterization, the dodecylamine ligands were exchanged by dodecanethiol, as we described previously.² Figure S1 shows a representative transmission electron micrograph and a size histogram. An average particle diameter of (3.5 ± 0.7) nm was found. Particles with diameters < 1 nm were excluded from sizing statistics.

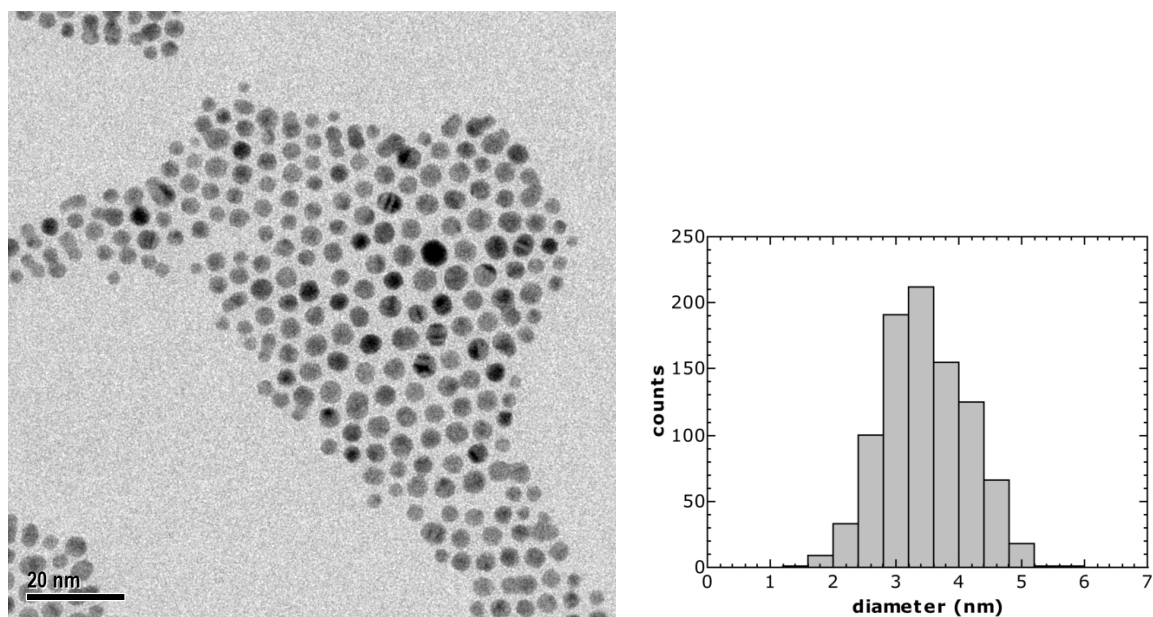


Figure S1: Transmission electron micrograph (*left*) and size histogram (*right*) of the GNP batch used for GNP membrane fabrication in this study.

UV/Vis spectroscopy of cross-linked GNP-films

A UV/Vis absorbance spectrum of the as-deposited 1,6-hexanedithiol (6DT) cross-linked GNP film on a glass substrate is depicted in Figure S2. Compared to the solution phase spectrum of the GNPs (dashed gray line), the plasmon band is red shifted due to the short interparticle distances resulting in plasmonic interactions.

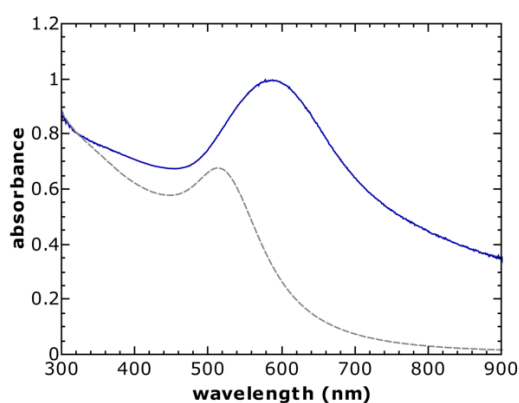


Figure S2: UV/Vis absorbance spectrum of the GNP membrane used for fabrication of the pressure sensor. A solution-phase spectrum of the GNPs is shown as dashed gray line (dilution $f = 1/600$).

Film thickness measurements (AFM)

For thickness measurements, sections of the as-deposited GNP film on a glass substrate were scratched using a cannula. Three AFM scans were conducted at different locations at the film edges using a DI Multimode AFM equipped with a Nanoscope IV controller and a 100 μm scanner. From each scan, five step-profiles were obtained and step-height values were extracted and averaged. Figure S3 shows the AFM scans recorded for film thickness measurement. An average thickness of $t = (55 \pm 1)$ nm was measured.

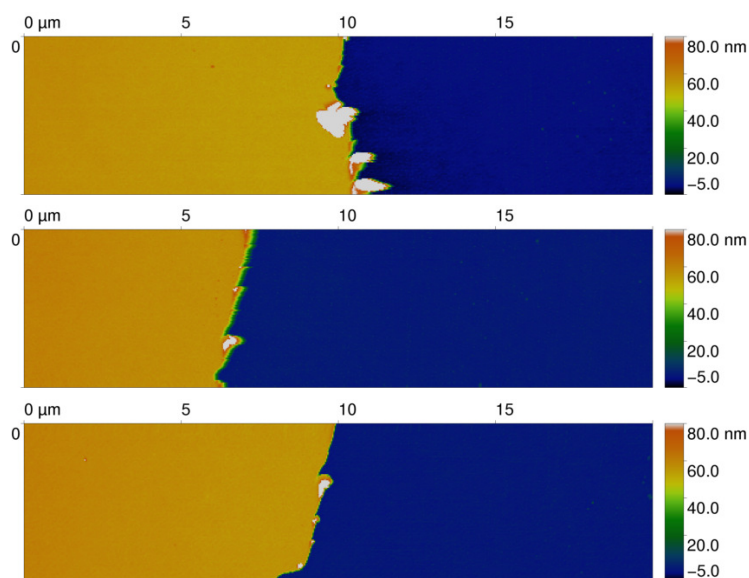


Figure S3: AFM scans ($20 \times 5 \mu\text{m}^2$) of GNP film sections used for thickness measurements.

Charge transport measurements

A section of the as-prepared substrate-supported GNP-film was investigated regarding its charge transport properties. Gold electrodes (~ 100 nm thickness) were deposited onto the film section by thermal evaporation, using a cannula (outer diameter $0.4\ \mu\text{m}$) as a shadow mask. Current-voltage (IV) data were measured by using an Agilent 4156C semiconductor parameter analyzer. The sample clearly showed ohmic behavior, see figure S4.

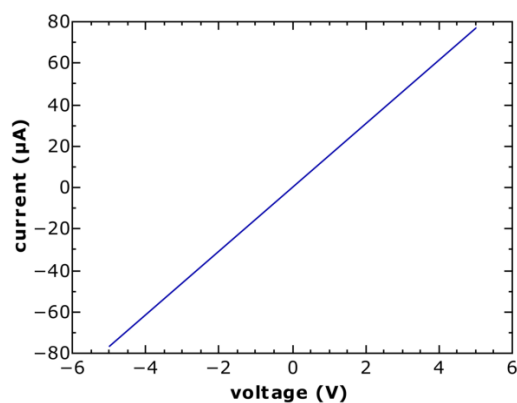


Figure S4: Current-voltage characteristics of the 55 nm thick GNP film used for fabrication of the pressure sensor (electrode geometry: $411\ \mu\text{m}$ channel length, $0.9\ \text{cm}$ channel width), corresponding to a conductivity of $0.1\ \text{S cm}^{-1}$.

Investigation of mechanical properties

For the model describing the sensor response, a biaxial modulus of 8.9 GPa for 6DT interlinked GNP membranes was used as an input parameter. This value was determined by bulge testing of 6DT interlinked GNP membranes as described in an earlier study for 1,9-nonanedithiol (9DT) interlinked GNP membranes.³

For bulge testing, sections of 6DT interlinked GNP films were transferred to substrates, having circular apertures with a diameter of $\sim 100 \mu\text{m}$. The membranes were then bulged by applying a varying nitrogen overpressure to their backside and the resulting membrane bulges were monitored using tapping mode atomic force microscopy (AFM, JPK Nanowizard). By analyzing the pressure-dependent topography data applying the “circular fit method”, stress-strain diagrams (as exemplarily shown in figure S5) were extracted. Slope fits of the stress-strain data collected from 4 membranes yielded an average biaxial modulus of (8.9 ± 0.6) GPa.⁴ A more detailed description of the bulge test procedure and data evaluation method is provided in our previous publication.³

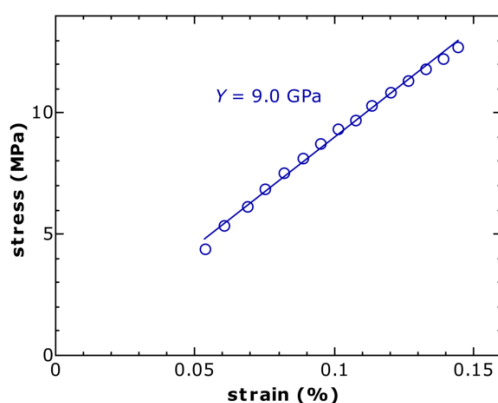


Figure S5: Representative stress-strain diagram extracted from a bulge test of a 6DT interlinked GNP membrane. The solid line depicts the slope fit yielding a biaxial modulus of $Y = 9.0$ GPa.

Pressure sweep measurements

The resistance and pressure time traces of the pressure sweeps conducted for recording the sensor's transfer function shown in figure 2 in the main document are depicted in figure S6:

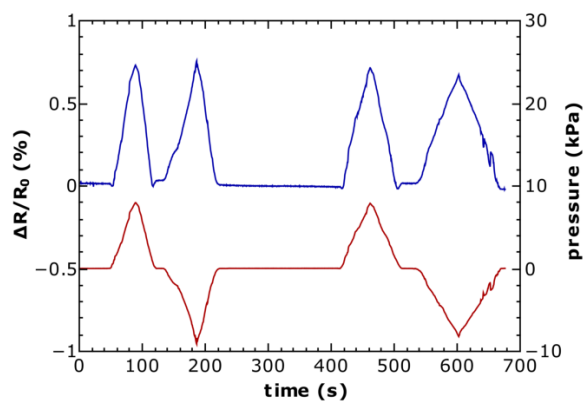


Figure S6: Resistance (*blue*) and pressure (*red*) time traces obtained by pressure sweeps for recording the sensor's transfer function.

Theoretical estimation of the sensor response

In figure 2c of the main document an estimate of the sensor response is depicted (dashed red curve). In the following, the underlying model is described.

For bulge tests on rectangular apertures, the membrane deflection at a given pressure difference can be calculated using equation 1:⁵

$$\Delta P(h) = P_{in} - P_{ex}(h) = \frac{C_1 \sigma_0 t}{a^2} h + \frac{C_2 E t}{a^4} h^3 \quad (1)$$

Here, P_{in} is the internal bulge pressure, P_{ex} is the pressure of the surrounding, h is the bulge height of the membrane's center, σ_0 is the residual stress of the membrane, t is the membrane thickness, a denotes the half width of the aperture, $E = Y(1 - \nu)$ represents the membrane material's Young's modulus and C_1 and C_2 are constants based on the bulge geometry. For bulge experiments on rectangular apertures with an aspect ratio of ≥ 4 , the constants become independent of the membrane shape and assume the following values:

$$\begin{aligned} C_1 &= 2 \\ C_2 &= \frac{4}{3(1 - \nu^2)} \end{aligned} \quad (2)$$

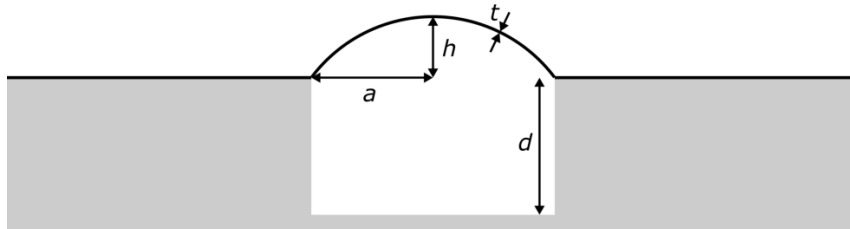


Figure S7: Schematic depicting a cross-sectional view of a membrane bulged on a rectangular cavity with annotations for the bulge height h , half aperture width a , cavity depth d and the membrane thickness t .

Here ν is the Poisson ratio of the membrane material. For all calculations we implied a cavity geometry having an aspect ratio sufficient to describe the membrane bulge section screened by the electrodes with a constant bulge height along the cavity length. This assumption applies for the device geometries used in this study.

In a bulge test, the pressure P_{in} is sourced from a large reservoir. Thus, both pressures P_{in} as well as the external pressure P_{ex} can be assumed to be constant. In our case, P_{ex} (pressure in the measurement cell) is varied in the range ± 8 kPa, resulting in a deflection of the membrane. The micrometer-range deflection of the membrane sealing the microcavity leads to changes of the cavity volume and hence to changes of the internal cavity pressure P_{in} , which can not be neglected. Thus, the internal cavity pressure P_{in} is a function of the bulge height. Equation 1 translates to:

$$P_{ex}(h) = P_{in}(h) - \frac{C_1 \sigma_0 t}{a^2} h - \frac{C_2 E t}{a^4} h^3 \quad (3)$$

$P_{in}(h)$ is expressed by the initial internal cavity pressure $P_{in,0}$ and the change in the cavity volume. The initial cavity volume (assuming a flat membrane sealing the cavity) is given by its dimensions $V_0 = ld2a$ (length l , depth d and width $2a$):

$$P_{in}(h) = P_{in,0} \frac{V_0}{V_0 + \Delta V(h)} \quad (4)$$

The volume change is given by the volume of the bulge, which is approximated as a cylindrical cap and adds or subtracts to V_0 , depending on the deflection's direction:

$$\Delta V(h) = \frac{\arctan\left(\frac{h}{a}\right) \cdot (h^2 + a^2)^2 + ah(h^2 - a^2)}{2h^2} l \quad (5)$$

By combination of equations 3, 4 and 5, an expression relating the external pressure

(pressure in the measurement cell) P_{ex} and the bulge height h can be obtained. From the bulge height h , the strain of the membrane ε (change in arc length relative to $2a$) can be approximated:

$$\varepsilon = \frac{2h^2}{3a^2} \quad (6)$$

This assumption only holds for membranes which are initially flat, i.e. having positive or zero residual stress. Imposing the gauge factor G_s , which is assumed to be constant in the observed strain range⁶ and taking into account the active area of the sensor (freestanding membrane width $2a$ vs. electrode distance c) the sensor response can be approximated as follows:

$$\frac{\Delta R}{R_0}(h) = \frac{2h^2}{3a^2} G_s \frac{2a}{c} \quad (7)$$

The transfer function depicted in the main document is obtained by parametrically plotting $\frac{\Delta R}{R_0}(h)$ against $P_{ex}(h) - P_{in,0}$ in a bulge height range of $-1.2 \mu\text{m} \leq h \leq 1.2 \mu\text{m}$. In the following, the parameters assumed for calculating the estimated transfer function depicted in figure 2c (main document) are listed:

Table S1: Parameters assumed for sensor response estimation

Cavity depth	$d =$	40 μm
Cavity width	$2a =$	40 μm
Electrode distance	$c =$	80 μm
Membrane thickness	$t =$	55 nm
Biaxial modulus	$Y =$	8.9 GPa
Poission ratio	$\nu =$	0.33 ³
Initial Cavity Pressure	$P_{in,0} =$	1×10^5 Pa
Gauge factor	$G_s =$	7 ^a
Residual membrane stress	$\sigma_0 =$	6 MPa ^a

^a These parameters were obtained by matching the estimated response with the experimental data.

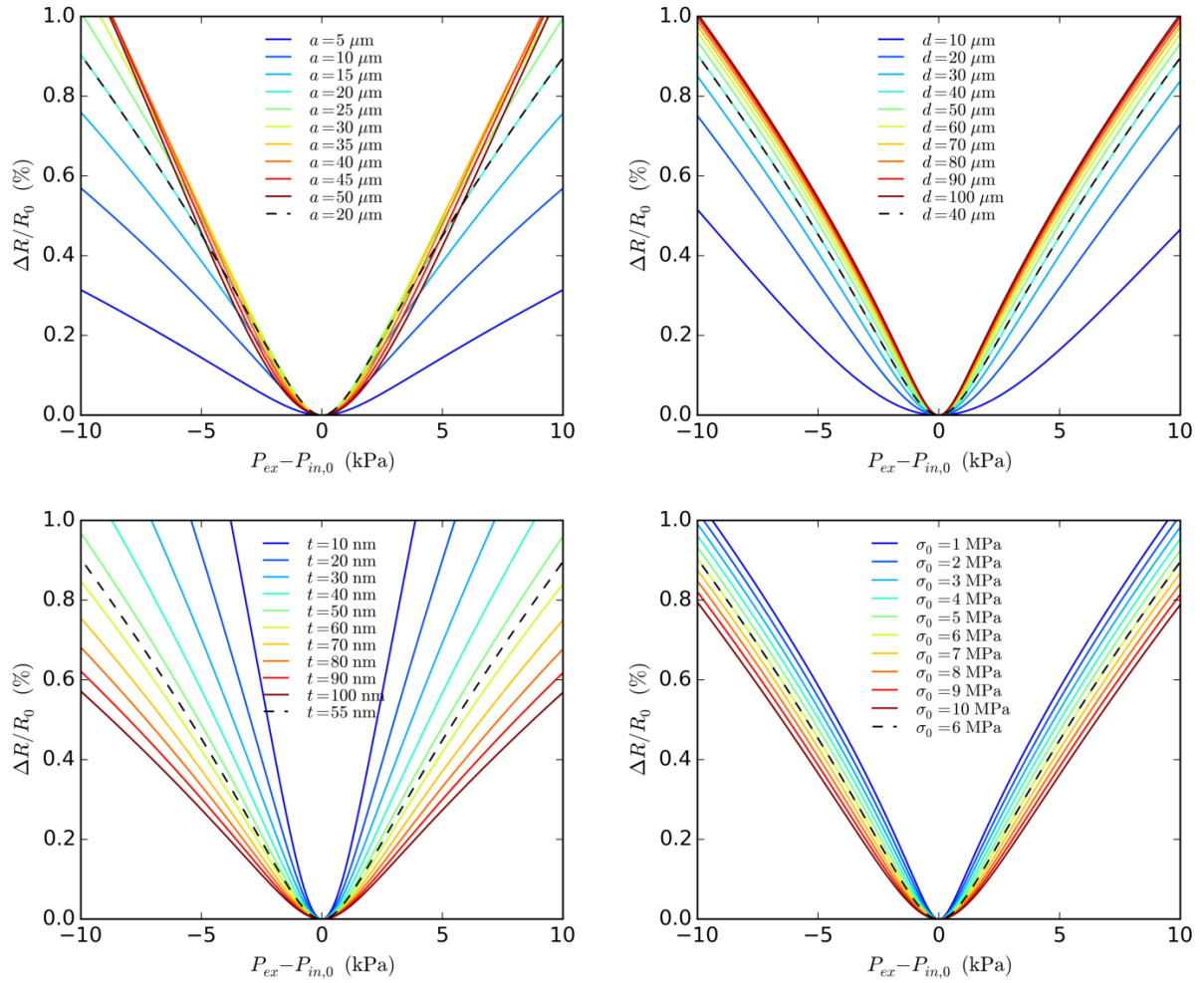


Figure S8: Predicted sensor transfer functions calculated using the parameters from table S1. The graphs show the initial transfer function (dashed black line) and curves obtained by varying the half aperture width a while scaling c proportionally to extract the influence of the bulge geometry (*top left*), varying the cavity depth d (*top right*), the membrane thickness t (*bottom left*) and the residual stress parameter σ_0 (*bottom right*).

Figure S8 depicts the estimated transfer function calculated using the parameters from table S1 as well as predicted curves under variations of different device parameters. It can be seen that the sensor response is weaker for thicker membranes or membranes having higher residual stresses after deposition, as higher pressure differences are necessary to bulge the membrane to the same extent (in terms of the change in arc length). A reduction of the aperture width $2a$ also leads to a decrease of the sensor response. Increasing the aperture width, a slight increase of sensitivity is estimated until a maximum of sensitivity could be reached. However, widening the cavity will disproportionately complicate the fabrication of larger-scale defect-free freestanding membranes. Reducing the volume of the pressure reservoir by decreasing the cavity depth d lowers the sensitivity as the pressure drop in the microcavity upon bulging is more pronounced in this case.

Pressure cell setup

Figure S9 depicts a schematic of the setup used for applying external pressures to the devices under test. It consists of a series of two needle valves, suitable to generate pressures relative to ambient from 0 to 10 kPa using a nitrogen back pressure from a gas tank or 0 to -10 kPa using a vacuum pump. The pressure, monitored by a digital pressure sensor P_2 can be adjusted and then forwarded to the pressure cell. Its pressure is monitored by another digital pressure sensor P_1 .

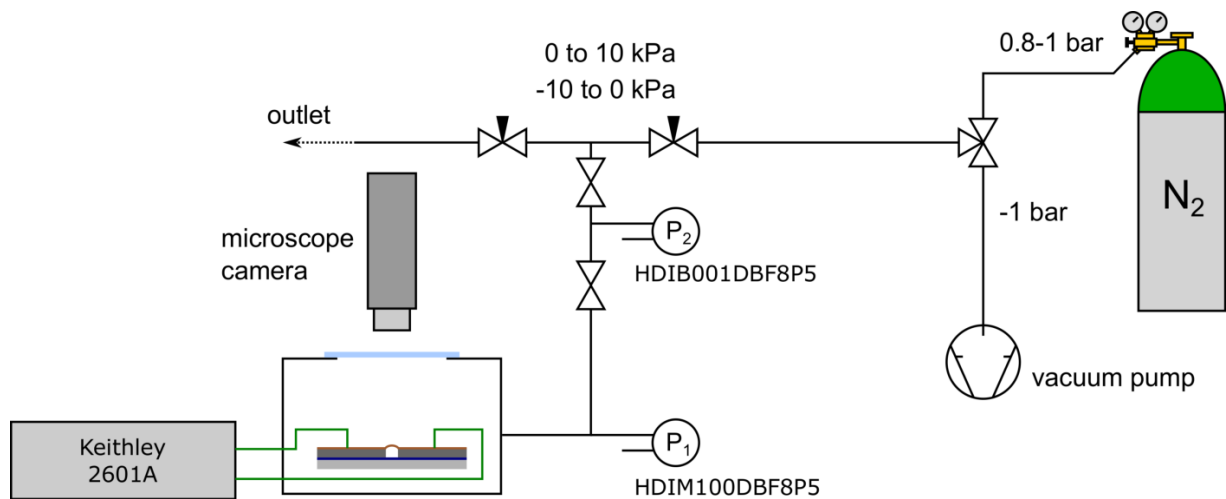


Figure S9: Setup used for characterization of the pressure sensor.

Fabrication of 3d electrode microstructures

General procedure: Optical lithography was used to fabricate 3d electrode microstructures. In a first step rectangular cavities (width ranging from $\sim 20\ \mu\text{m}$ to $\sim 80\ \mu\text{m}$ and length ranging from $\sim 500\ \mu\text{m}$ to $\sim 620\ \mu\text{m}$) were lithographically fabricated using a SU-8 50 photoresist layer on a thermally oxidized silicon wafer. Subsequently, AZ nLOF 2035 photoresist was used as a sacrificial layer in order to structure the top electrodes. In a last step either $\sim 40\ \text{nm}$ of gold were deposited by thermal evaporation or $\sim 40\ \text{nm}$ of platinum were deposited by sputtering.

Detailed description: First, a layer of SU-8 50 (MicroChem) photoresist was deposited onto a piece of thermally oxidized silicon wafer (Siegert Wafer, boron p-doped, $\langle 100 \rangle$, $675 \pm 25\ \mu\text{m}$ thickness, $300\ \text{nm} \pm 5\%$ SiO_2 thickness) by using a Spin Coater (K.L.M. SCC-200). After deposition, the photoresist was soft-baked using a hotplate at $65\ ^\circ\text{C}$ for 5 min and immediately afterward another hot plate at $95\ ^\circ\text{C}$ for 15 min. Subsequently the substrates were allowed to cool down to room temperature and were irradiated with UV light through a patterned chromium/glass mask (manufactured by Compugraphics Jena GmbH) using a long pass filter (Omega Optical PL-360P) and a Karl Suss MJB-3 mask aligner.

After exposure, the substrate was immediately post-exposure baked at $65\ ^\circ\text{C}$ for 1 min and at $95\ ^\circ\text{C}$ for 4 min. Once the sample cooled down to room temperature, the substrate was developed for 5.5 min under agitation using mr-Dev600 (micro resist technology). Following development, the substrate was rinsed with fresh mr-Dev 600 and isopropyl alcohol. After all contamination have been removed, the substrate was dried in a gentle stream of nitrogen.

In order to enhance cross-linking of the photoresist and to reduce cracks which may form during the fabrication process, the SU-8 samples were hardbaked. The hardbaking step was conducted on a hotplate, starting from $120\ ^\circ\text{C}$ up to $200\ ^\circ\text{C}$, within $\sim 10\ \text{min}$. This

temperature was held for 30 min before being cooled back to room temperature. In a second step, electrodes were deposited onto the SU-8 3d structures. To do so, one layer of AZ nLOF 2035 was spincoated at 33 rps for 60s and soft-baked for 2 min at 110 °C. After that another layer was spincoated in the same procedure. Then a third layer was spincoated at 33 rps for 60s and soft-baked for 4 min at 110 °C.

After the samples cooled down to room temperature, the photoresist was irradiated with UV light through a patterned negative chromium/glass photomask, yielding $\sim 300\ \mu\text{m}$ wide electrodes which were placed $20\ \mu\text{m}$ beside the cavity. Following exposure, the substrate was post-exposure-baked on a hotplate for 1 min at 120 °C and then cooled to ambient temperature. Dissolution of the unexposed photoresist areas was achieved by immersing the sample into AZ 726 MIF (AZ Electronic Materials) developer for 2 min. Subsequently, the substrate was rinsed briefly with fresh developer, then with ultrapure water and dried in a gentle stream of nitrogen. After the second (sacrificial) photoresist layer have been structured, $\sim 40\ \text{nm}$ of gold were deposited onto the photoresist layer by thermal evaporation (UNIVEX 350G Oerlikon Leybold Vacuum) or $\sim 40\ \text{nm}$ of Platinum were deposited onto the photoresist layer by Sputtering (GATAN Model 682 Precision Etching and Coating System (PECS)). To remove the layer of gold or platinum in the exposed areas, the substrate was immersed into TechniStrip NI555 (TECHNIC) at 80 °C for 1 hour. Due to remaining residues of gold at the edge of the SU-8 layer, the substrate was placed in an ultrasonic bath (Bandelin Sonorex RK 255 H) for a few seconds. Subsequently, the structure was rinsed in acetone, isopropanol, ultrapure water and dried in a gentle stream of nitrogen.

References

- (1) Leff, D. V.; Brandt, L.; Heath, J. R. Synthesis and Characterization of Hydrophobic, Organically-Soluble Gold Nanocrystals Functionalized with Primary Amines. *Langmuir* **1996**, *12*, 4723–4730.
- (2) Schlicke, H.; Schröder, J. H.; Trebbin, M.; Petrov, A.; Ijeh, M.; Weller, H.; Vossmeier, T. Freestanding Films of Crosslinked Gold Nanoparticles Prepared via Layer-by-Layer Spin-Coating. *Nanotechnology* **2011**, *22*, 305303.
- (3) Schlicke, H.; Leib, E. W.; Petrov, A.; Schröder, J. H.; Vossmeier, T. Elastic and Viscoelastic Properties of Cross-Linked Gold Nanoparticles Probed by AFM Bulge Tests. *J. Phys. Chem. C* **2014**, *118*, 4386–4395.
- (4) Schlicke, H.; Battista, D.; Kunze, S.; Schröter, C. J.; Eich, M.; Vossmeier, T. Free-standing Membranes of Cross-Linked Gold Nanoparticles: Novel Functional Materials for Electrostatic Actuators. *ACS Appl. Mater. Interfaces* **2015**, *7*, 15123–15128.
- (5) Schweitzer, E.; Göken, M. In Situ Bulge Testing in an Atomic Force Microscope: Microdeformation Experiments of Thin Film Membranes. *J. Mater. Res.* **2011**, *22*, 2902–2911.
- (6) Vossmeier, T.; Stolte, C.; Ijeh, M.; Kornowski, A.; Weller, H. Networked Gold-Nanoparticle Coatings on Polyethylene: Charge Transport and Strain Sensitivity. *Adv. Funct. Mater.* **2008**, *18*, 1611–1616.

A.1.2 Freestanding Membranes of Cross-Linked Gold Nanoparticles: Novel Functional Materials for Electrostatic Actuators

Reprinted with permission from “Freestanding Membranes of Cross-Linked Gold Nanoparticles: Novel Functional Materials for Electrostatic Actuators”, H. Schlicke, D. Battista, S. Kunze, C. J. Schröter, M. Eich, T. Vossmeier, *ACS Appl. Mater. Interfaces* **2015**, *7*, 15123-15128.^[1] Copyright ©2015 American Chemical Society.

Supporting Information:

Freestanding Membranes of Cross-Linked Gold Nanoparticles: Novel Functional Materials for Electrostatic Actuators

Hendrik Schlicke,[†] Daniela Battista,^{†,¶} Svenja Kunze,[†] Clemens J. Schröter,[†]
Manfred Eich,[‡] and Tobias Vossmeier^{*,†}

Institute of Physical Chemistry, University of Hamburg, Grindelallee 117, 20146 Hamburg, Germany, and Institute of Optical and Electronic Materials, Hamburg University of Technology, Eissendorfer Strasse 38, 21073 Hamburg, Germany

E-mail: tobias.vossmeier@chemie.uni-hamburg.de

*To whom correspondence should be addressed

[†]Institute of Physical Chemistry, University of Hamburg, Grindelallee 117, 20146 Hamburg, Germany

[‡]Institute of Optical and Electronic Materials, Hamburg University of Technology, Eissendorfer Strasse 38, 21073 Hamburg, Germany

[¶]Present Address: Chemical Sciences and Technologies, University of Milano-Bicocca, Milano, Italy

Gold Nanoparticles

In this study, three batches of dodecylamine stabilized gold nanoparticles (GNPs) were used for membrane fabrication. The GNPs were prepared following a synthetic route published by Leff et al.¹ and showed typical UV/Vis absorbance spectra (figure S1) with surface plasmon resonance peaks at 503 nm (batch 1, figure S1, red curve), 513 nm (batch 2, figure S1, blue curve) and 512 nm (batch 3, figure S1, green curve).

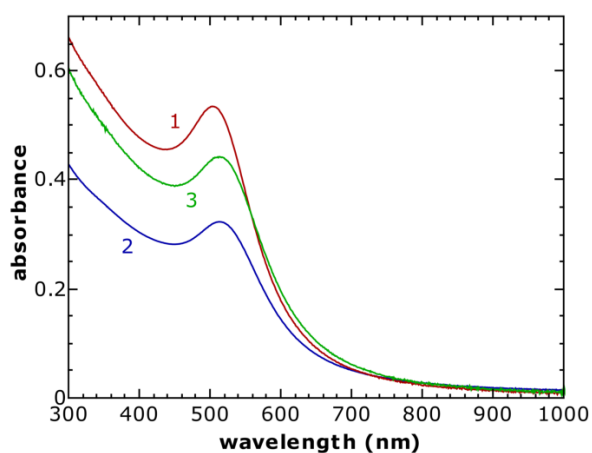


Figure S1: UV/Vis absorbance spectra (dilution factor $f = 1/600$) of the GNP solution 1, 2 and 3 used for fabrication of the actuator devices.

Transmission electron microscopy was conducted for determining the GNP sizes, using a JEOL JEM-1011 microscope, equipped with a LaB₆ cathode and operated at 100 kV. In order to improve the stability of the particles prior to TEM characterization, the dodecylamine ligands were exchanged by dodecanethiol, as we described previously.² Figure S2 shows representative transmission electron micrographs and size histograms of the GNP batches 1, 2 and 3. For these samples average particle diameters of (3.5 ± 0.5) nm, (3.5 ± 0.8) nm and (3.6 ± 0.6) nm were found, respectively. Particles with diameters < 1 nm were excluded from sizing statistics.

While device A and B were fabricated using GNP batch 1 and 2, respectively, devices C and D were fabricated using GNP batch 3.

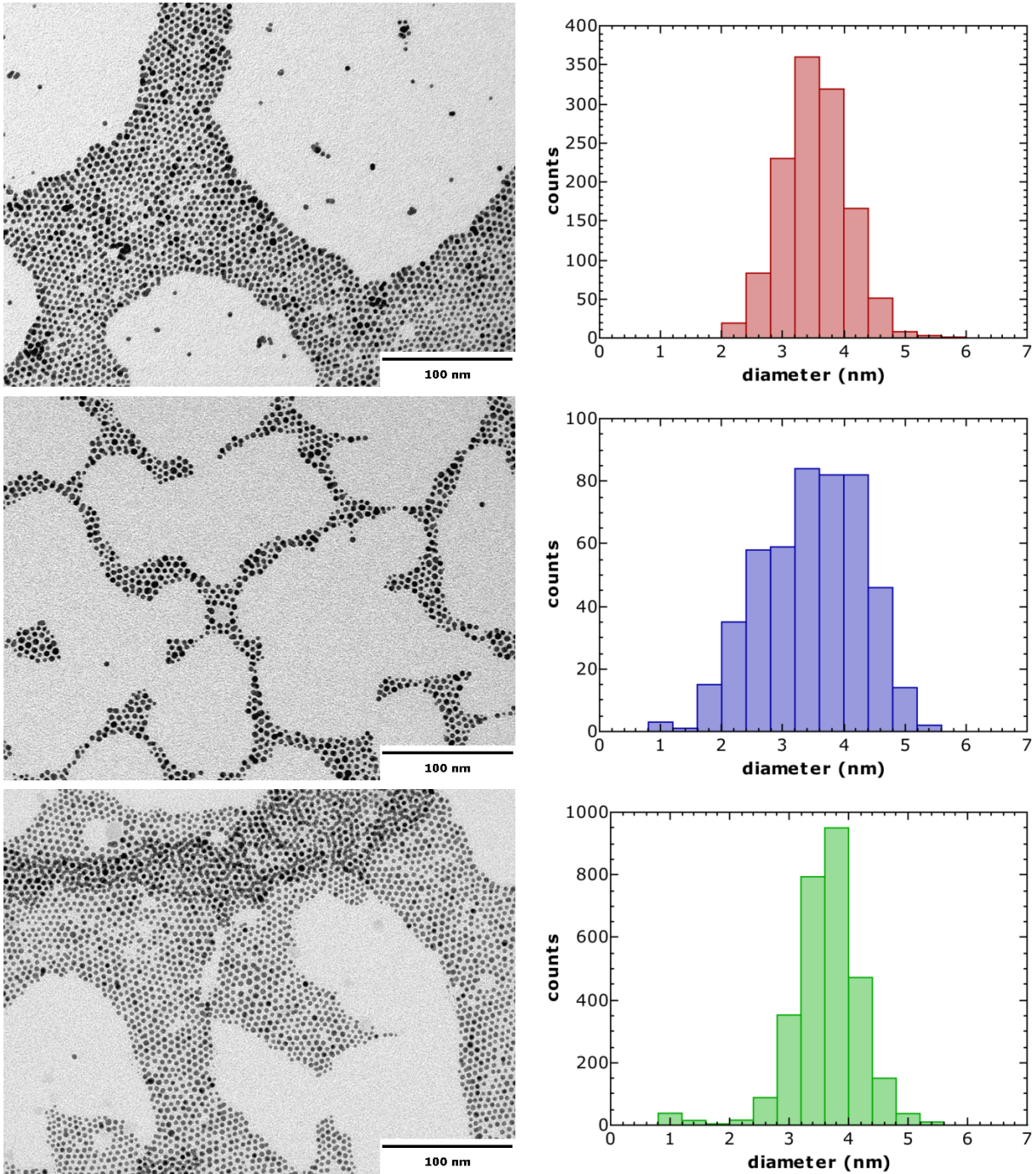


Figure S2: Transmission electron micrographs (*left*) and size histograms (*right*) for GNP particle batch 1 (*top*), 2 (*middle*) and 3 (*bottom*).

UV/Vis Spectroscopy of Crosslinked GNP-Films

Figure S3 shows UV/Vis absorption spectra of the as-deposited 1,6-hexanedithiol (6DT) cross-linked GNP films prior to lift-off and transfer. The spectra show a pronounced plasmon absorbance band originating from the GNPs incorporated in the membranes. Compared to the solution phase spectra shown in figure S1, the plasmon band is red shifted due to the short interparticle distances resulting in plasmonic interactions.

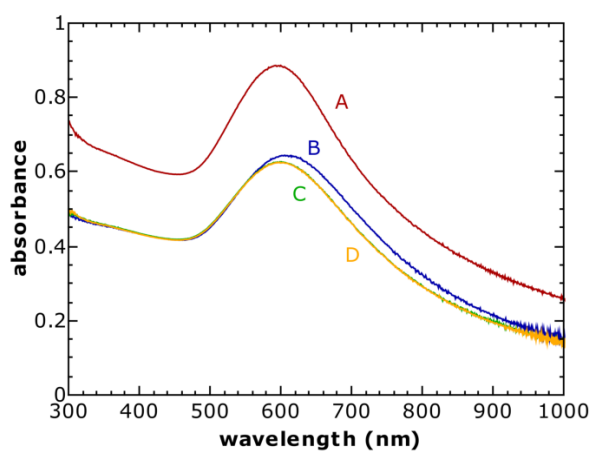


Figure S3: UV/Vis absorbance spectra of the GNP membranes used in the actuator devices A, B, C and D.

Film Thickness Measurements (AFM)

For thickness measurements, sections of the as-deposited GNP films on glass substrates were scratched using a cannula. For each film sample, two AFM scans were conducted at different locations at the film edges using a DI Multimode AFM equipped with a Nanoscope IV controller and a 100 μm scanner. From each scan, at least four step-profiles were obtained and step-height values were extracted and averaged. Figure S4 shows the AFM scans recorded for film thickness measurements of the films used for the fabrication of the devices A, B, C and D.

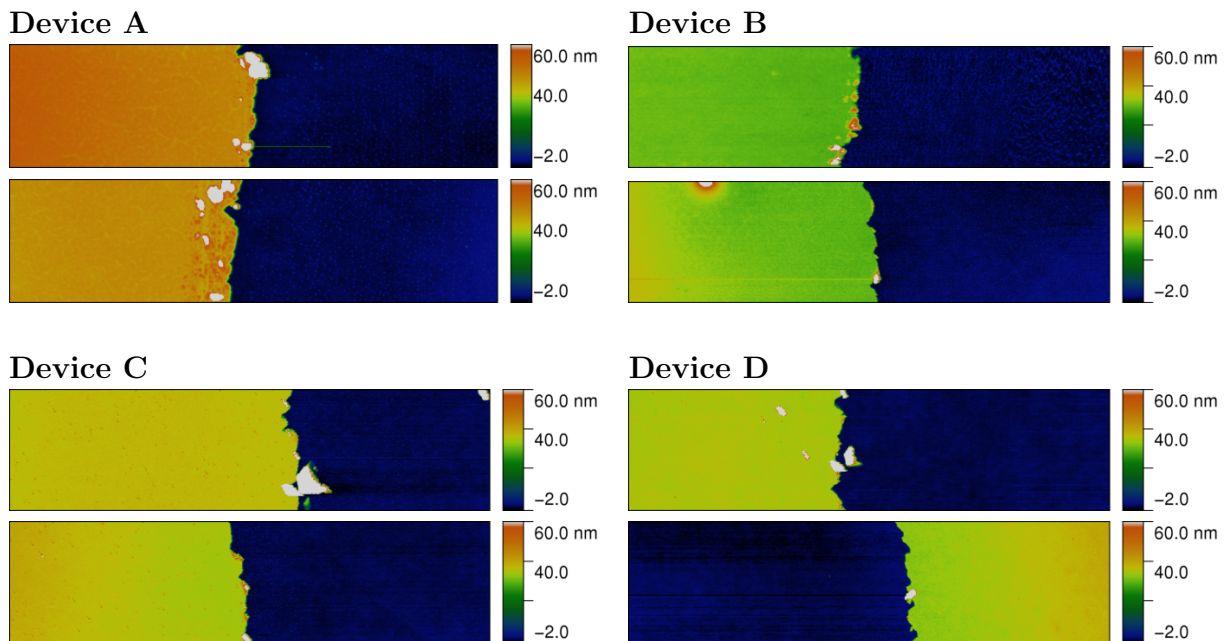


Figure S4: AFM scans ($20 \times 5 \mu\text{m}^2$) of GNP film sections used for thickness measurements. The films showing the depicted data were used for the fabrication of the actuator devices A, B, C and D. Film thicknesses of $(45 \pm 1) \text{ nm}$, $(29 \pm 1) \text{ nm}$, $(37 \pm 1) \text{ nm}$ and $(33 \pm 1) \text{ nm}$ were extracted, respectively.

Charge Transport Measurements

Sections of the as-prepared substrate-supported GNP-films were investigated regarding their charge transport properties. Gold electrodes (~ 100 nm thickness) were deposited onto sections of the films by thermal evaporation using a cannula ($0.4 \mu\text{m}$) as a shadow mask. Current-voltage (IV) data were measured by applying a varying voltage to the samples and measuring the resulting current using an Agilent 4156C semiconductor parameter analyzer. The samples showed ohmic behavior.

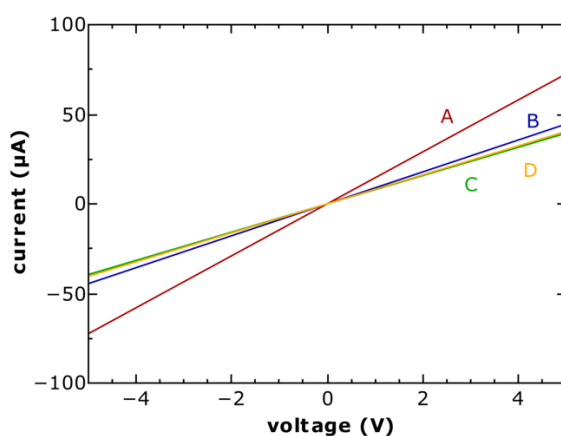


Figure S5: Current-voltage characteristics of the GNP films used for fabrication of the actuators A, B, C and D, normalized to a standard electrode geometry with a width of 1 cm and a channel length of $400 \mu\text{m}$. Taking into account the electrode geometry and film thickness, conductivities of 13 S m^{-1} , 12 S m^{-1} , 8.6 S m^{-1} and 9.7 S m^{-1} were calculated, respectively.

Investigation of Mechanical Properties

For the electrostatic model describing the voltage-deflection $V(h)$ relation of the presented actuator devices, a biaxial modulus of 8.9 GPa for 6DT interlinked GNP membranes was used as an input parameter. This value was determined by bulge testing of 6DT interlinked GNP membranes as described in an earlier study for 1,9-nonanedithiol (9DT) interlinked GNP membranes.³

For bulge testing, sections of 6DT interlinked GNP films were transferred to substrates, having circular apertures with a diameter of $\sim 100 \mu\text{m}$. The membranes were then bulged by applying a varying nitrogen overpressure to their backside and the resulting membrane bulges were monitored using tapping mode atomic force microscopy (AFM, JPK Nanowizard). By analyzing the pressure-dependent topography data applying the “circular fit model”, stress-strain diagrams (as exemplarily shown in figure S6) were extracted. Slope fits of the stress-strain data collected from 4 membranes yielded an average biaxial modulus of (8.9 ± 0.6) GPa. A more detailed description of the bulge test procedure and data evaluation method are provided in our previous publication.³

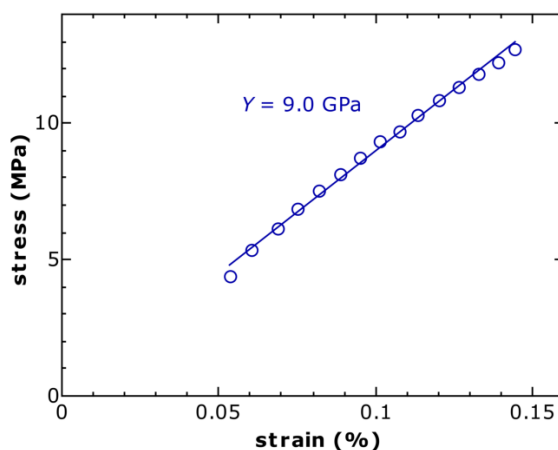


Figure S6: Representative stress-strain diagram extracted from a bulge test of a 6DT interlinked GNP membrane. The solid line depicts the slope fit yielding a biaxial modulus of $Y = 9.0$ GPa.

Interferometric Deflection Measurements

The voltage-deflection $V(h)$ responses of device C and D were investigated using a MEMS analyzer (Nanovibration Analyzer NA, SIOS Messtechnik GmbH). For this purpose, voltage pulses of 10 s, spaced by a 10 s delay within the range of $V = \pm 40$ V and $V = \pm 30$ V in 2 V steps were applied to the devices using a Keithley 2601A source measure unit, respectively. For device D the voltage range was limited to ± 30 V, as the actuator showed comparably large deflections of ~ 1.5 μm at $|V| = 30$ V. In other experiments destruction of actuator devices was observed for deflections exceeding ~ 2 μm due to an irreversible “snap down” of the membrane to the wafer back-electrode. Figures S7 and S8 show voltage transients applied to the devices (blue) and the respective deflection transients (green/orange). As a slight baseline drift was caused by the mechanical instability of the experimental setup, each transient was baseline corrected by subtracting a linear fit to the baseline data.

Device C

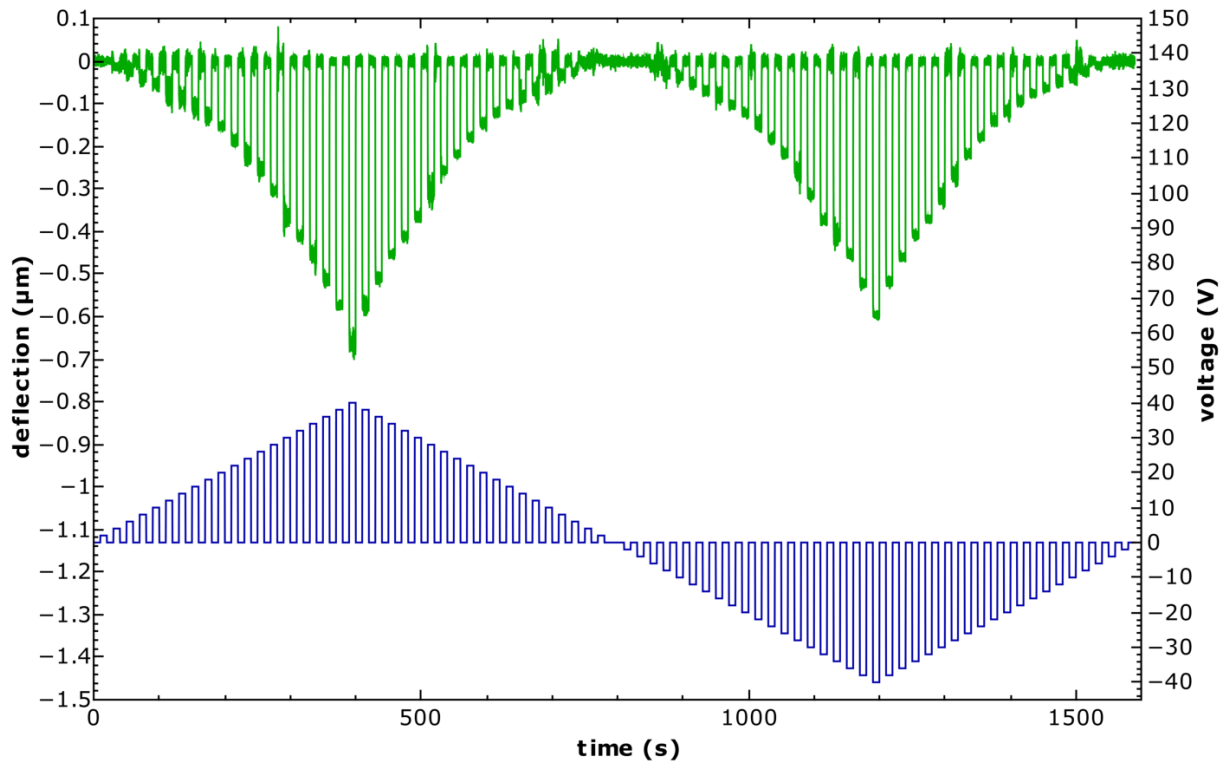


Figure S7: Result of the interferometric measurement of actuator C. The plot shows the applied voltage (blue) and baseline-corrected deflection (green) transients.

Device D

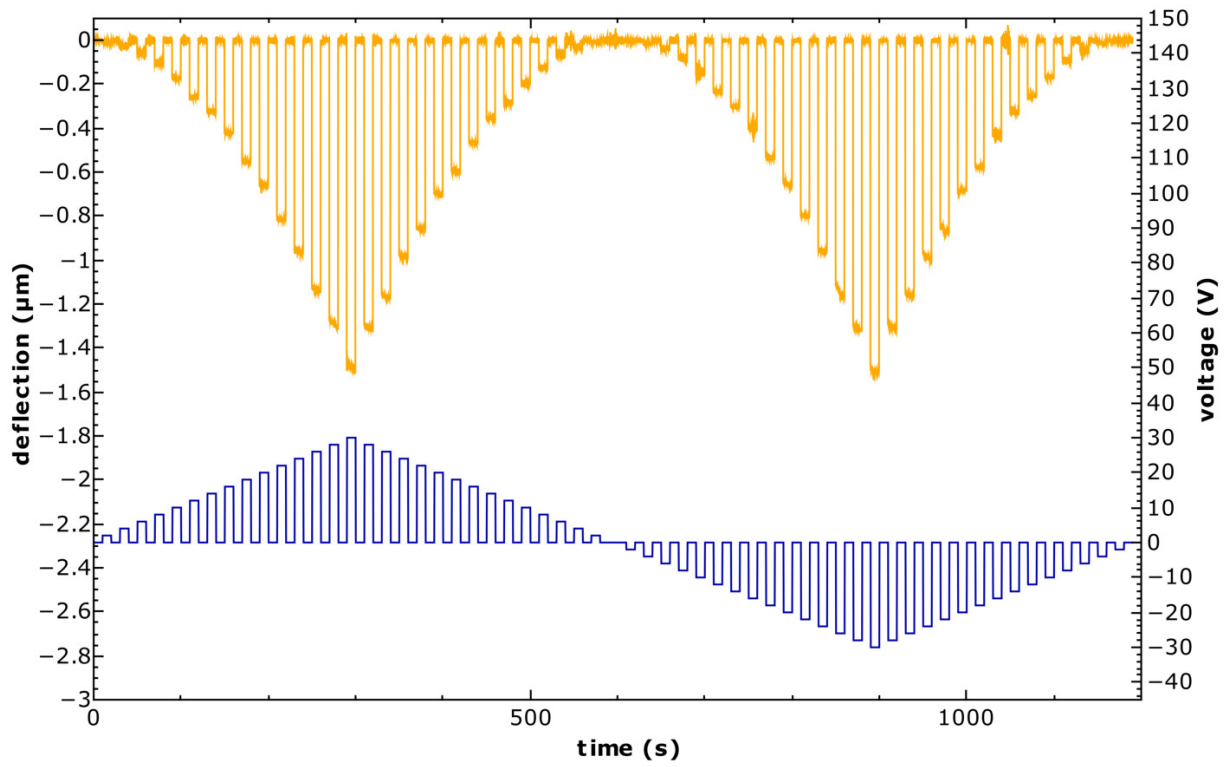


Figure S8: Result of the interferometric investigation measurement of actuator D. The plot shows the recorded voltage (blue) and baseline-corrected deflection (orange) transients.

Optical Micrographs

Figure S9 depicts optical micrographs of device C and D.

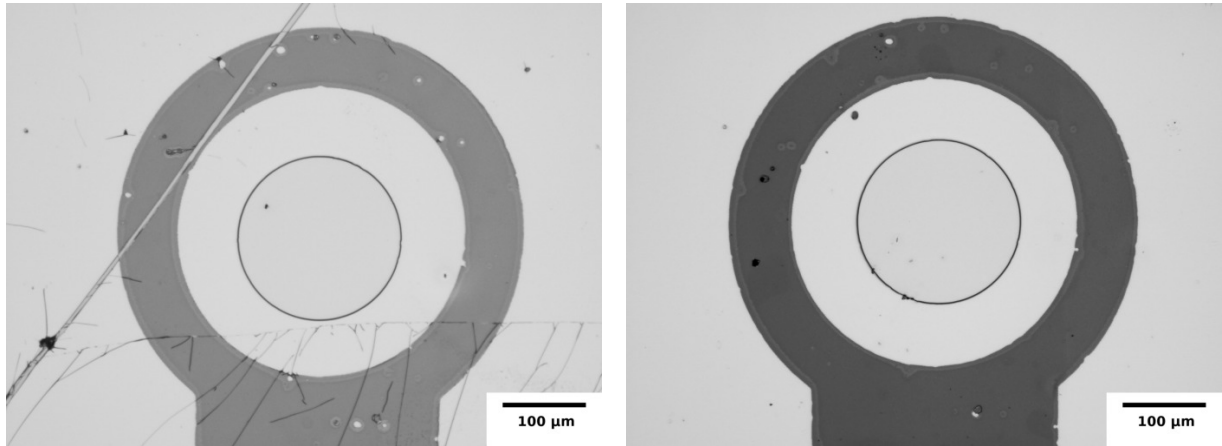


Figure S9: Optical micrographs of device C (*left*) and D (*right*).

Fabrication of 3d Electrode Microstructures

General procedure: Electrode microstructures were fabricated lithographically following a multi-step process. First, cylindrical 200 μm wide, $\sim 8 - 15 \mu\text{m}$ deep cavities were lithographically fabricated on a silicon wafer in a SU-8 photoresist layer. Subsequently the negative AZ nLOF 2070 photoresist was used as sacrificial layer for preparing the top electrodes. The resist was deposited onto the 3d structures, and a negative image of the ring electrodes was prepared. Afterwards, gold was deposited by thermal evaporation ($\sim 100 \text{ nm}$) and lifted off by removal of the sacrificial photoresist layer.

Detailed description: First, a layer of SU-8 2015 (MicroChem) photoresist was deposited onto a piece of a silicon wafer (Siegert Wafer, boron p-doped, $(380 \pm 15) \mu\text{m}$ thickness, $1 - 10 \Omega \text{ cm}$ resistivity) or thermally oxidized silicon wafer (Addison, antimony n-doped, $(625 \pm 25) \mu\text{m}$ thickness, $300 \text{ nm} \pm 5\%$ oxide thickness, $0.005 - 0.025 \Omega \text{ cm}$ resistivity and Siegert Wafer, boron p-doped, $(675 \pm 25) \mu\text{m}$ thickness, $300 \text{ nm} \pm 5\%$ oxide thickness, $< 0.005 \Omega \text{ cm}$ resistivity) using a Spin Coater (K.L.M. SCC-200) for 60 s at 68 to 200 rps, depending on the desired layer thickness. After deposition, the photoresist was soft-baked for 3.5 min at 110°C . Once the sample was cooled to room temperature, it was irradiated with UV light through a patterned chromium/glass mask using a WG360 long pass filter and a Karl Suss MJB-3 mask aligner.

Following exposure, the substrate was post-exposure-baked for 4.5 min at 110°C and then cooled down to ambient temperature. Dissolution of the unexposed photoresist areas was achieved by immersing the sample in mr-Dev600 (micro resist technology) developer under agitation for 3.5 min. Following development, the substrate was rinsed briefly first with fresh developer, then with isopropyl alcohol (IPA) and eventually dried in a gentle stream of nitrogen. If necessary, the rinsing process in fresh developer and IPA was repeated to remove residual contaminations.

In order to enhance cross-linking of the photoresist and thus improving its stability, the

SU-8 samples were hardbaked. The hardbaking step was conducted on a hotplate, starting from 120 °C ramping up to 200 °C, within \sim 10 min. The SU-8 layer was held at the hard-bake temperature for about 10 min before being cooled back to room temperature.

In a second step, electrodes were deposited onto the 3d structures. For this purpose a layer of the negative AZ nLOF 2070_3.5 μ m (AZ Electronic Materials) photoresist was spin-coated at 68 rps for 60 s on the relief SU-8 structures and then soft-baked for 1.5 min at 120 °C. Afterwards, a second layer of AZ nLOF 2070_3.5 μ m resist was spin-coated again at 68 rps for 60 s and soft-baked for 3 min at 120 °C to fully cover the 3d-microstructure. Once the sample was cooled to room temperature, the photoresist was irradiated with UV light through a patterned negative chromium/glass photomask, yielding structures with a ring-pad electrode (inner ring diameter: 400 μ m; outer ring diameter: 600 μ m, see figure 1 in the main document). Following exposure, the substrate was post-exposure-baked for 1 min at 120 °C and then cooled to ambient temperature. Dissolution of the unexposed photoresist areas was achieved by immersing the post-exposure-baked sample into AZ 726 MIF (AZ Electronic Materials) developer or aqueous sodium hydroxide solution (0.1%) for 2 min. Following development, the substrate was rinsed with fresh developer, then with ultrapure water and dried in a gentle stream of nitrogen.

After structuring the second (sacrificial) photoresist layer, \sim 100 nm of gold were deposited onto the surface of the microstructures by thermal evaporation (Pfeiffer Classic 250 vacuum evaporation system). The electrodes were patterned by stripping the sacrificial AZ nLOF 2070_3.5 μ m photoresist topped with the gold layer by immersion into TechniStrip NI555 (TECHNIC) at 80 °C for about 20-30 minutes. Subsequently, the structures were rinsed in acetone, isopropanol, ultrapure water and dried in a stream of nitrogen.

References

- (1) Leff, D. V.; Brandt, L.; Heath, J. R. Synthesis and Characterization of Hydrophobic, Organically-Soluble Gold Nanocrystals Functionalized with Primary Amines. *Langmuir* **1996**, *12*, 4723–4730.
- (2) Schlicke, H.; Schröder, J. H.; Trebbin, M.; Petrov, A.; Ijeh, M.; Weller, H.; Vossmeier, T. Freestanding Films of Crosslinked Gold Nanoparticles Prepared via Layer-by-Layer Spin-Coating. *Nanotechnology* **2011**, *22*, 305303.
- (3) Schlicke, H.; Leib, E. W.; Petrov, A.; Schröder, J. H.; Vossmeier, T. Elastic and Viscoelastic Properties of Cross-Linked Gold Nanoparticles Probed by AFM Bulge Tests. *J. Phys. Chem. C* **2014**, *118*, 4386–4395.

A.1.3 Electrostatically driven drumhead resonators based on freestanding membranes of cross-linked gold nanoparticles

Reprinted from “Electrostatically driven drumhead resonators based on freestanding membranes of cross-linked gold nanoparticles”, H. Schlicke, C. J. Schröter, T. Vossmeier, *Nanoscale* **2016**, *8*, 15880-15887^[3] with permission from The Royal Society of Chemistry.

**Electronic Supplementary Information:
Electrostatically Driven Drumhead Resonators
Based on Freestanding Membranes of
Cross-Linked Gold Nanoparticles**

Hendrik Schlicke,^{†,‡} Clemens J. Schröter,^{†,‡} and Tobias Vossmeier^{*,†}

*Institute of Physical Chemistry, University of Hamburg, Grindelallee 117, 20146 Hamburg,
Germany*

E-mail: tobias.vossmeier@chemie.uni-hamburg.de

*To whom correspondence should be addressed

[†]Institute of Physical Chemistry, University of Hamburg, Grindelallee 117, 20146 Hamburg, Germany

[‡]Contributed equally to this work.

Gold Nanoparticles

Transmission electron microscopy was used for the determination of the GNPs' average size and size distribution. As the 1-dodecylamine stabilized particles were not stable under TEM conditions, the amine ligands were exchanged with stronger binding 1-dodecanethiol (12T) ligands, as described earlier.¹ The 12T stabilized particles were drop-casted onto a carbon coated TEM substrate and investigated using a JEOL JEM-1011 transmission electron microscope, equipped with a LaB₆ cathode operated at 100 kV.

Figure S1 shows a representative transmission electron micrograph of the particle batch used for preparing the GNP membranes, as well as a size histogram. An average diameter of 3.6 ± 0.6 nm was determined. Particles with diameters < 1 nm were excluded from the sizing statistics.

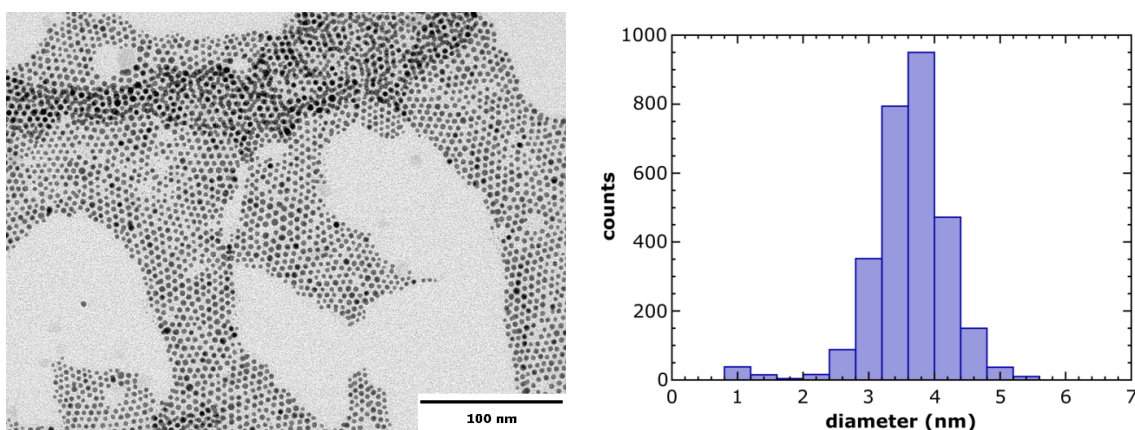


Figure S1: Transmission electron micrograph (*left*) and size histogram (*right*) of the GNP batch used for membrane fabrication.

UV/vis Spectroscopy

All membranes used for device fabrication were characterized regarding their UV/vis absorption. Figure S2 shows UV/vis absorbance spectra of the diluted GNP stock solution in n-heptane (dilution factor $f = 1/600$) and the as-deposited 6DT cross-linked GNP films on glass substrates prior to lift-off and transfer. A pronounced surface plasmon absorbance band originating from the GNPs within the membranes is observed. Compared to the solution phase spectrum, the plasmon band is red shifted due to the short interparticle distances resulting in plasmonic interactions.

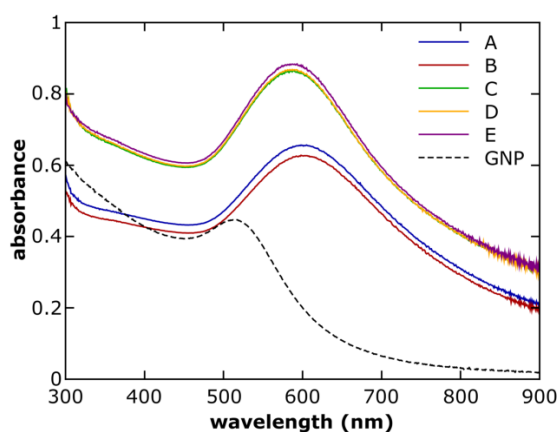
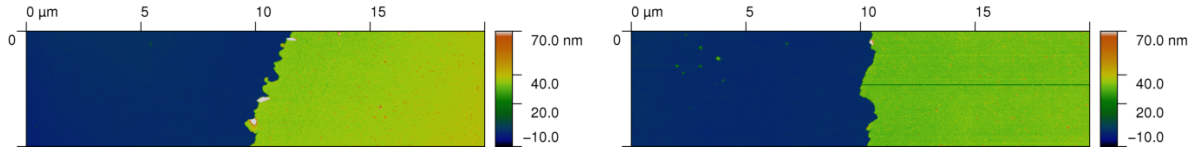


Figure S2: UV/vis absorbance spectrum of the GNP stock solution in n-heptane (dilution factor $f = 1/600$, dashed black line) and UV/vis absorbance spectra of the GNP films used for fabrication of devices A, B, C, D and E (see table S1).

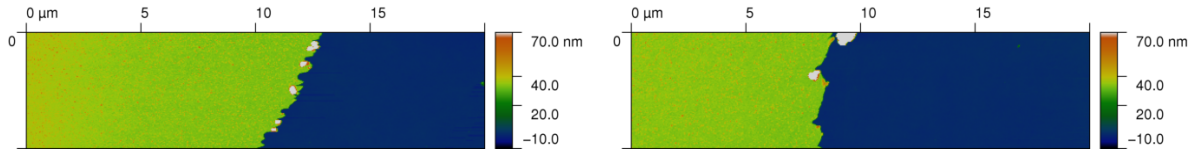
Film Thickness Measurements (AFM)

Five 6DT cross-linked GNP membranes were used for device fabrication in this study. The thickness of the membranes was determined by atomic force microscopy (AFM). Sections of the as-deposited films on glass substrates were scratched using a cannula and AFM scans ($5 \times 20 \mu\text{m}^2$, $128 \times 512 \text{px}^2$) were recorded at the edges of the resulting scratches. Two AFM scans were recorded at different positions on each sample. The scans are depicted in figure S3. From each scan, 4 line profiles were extracted and the step heights were averaged. Table S1 presents the thicknesses of the membranes used for resonator fabrication.

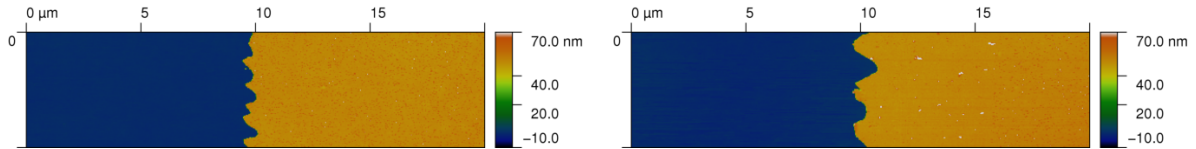
Membrane A



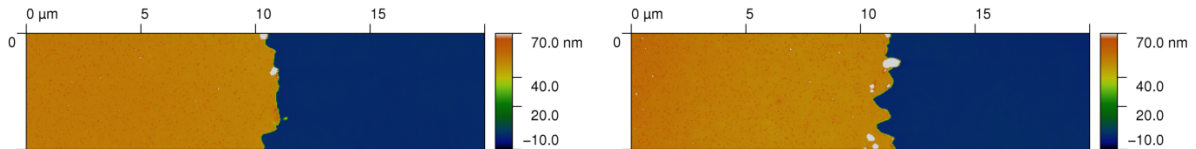
Membrane B



Membrane C



Membrane D



Membrane E

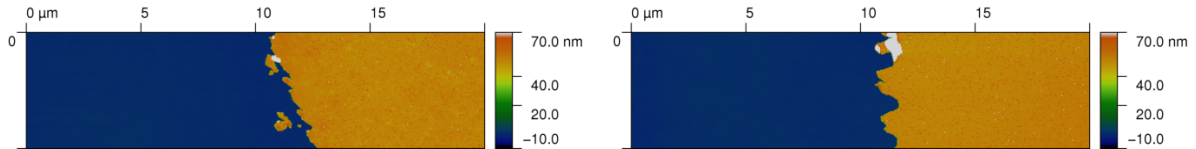


Figure S3: AFM scans ($20 \times 5 \mu\text{m}^2$) of GNP film sections used for thickness measurements. These films were used for fabricating the resonator devices A, B, C, D and E. The extracted film thicknesses are provided in table S1.

Charge Transport Measurements

Sections of the substrate-supported GNP-films were investigated regarding their charge transport properties. For this purpose, gold electrodes (thickness: ~ 100 nm) were deposited onto the as-prepared GNP films by vacuum evaporation using a cannula (0.4 mm diameter) as a shadow mask. Current-voltage (IV) curves were recorded by contacting the samples using microprobes in a custom-built probe station and sweeping the voltage in a range between -5 and 5 V using an Agilent 4156C semiconductor parameter analyzer. All samples showed ohmic behavior. IV data (normalized to a channel width of 1 cm and channel length of $400 \mu\text{m}$) of the membranes used for device fabrication in this study are plotted in figure S4. The higher currents measured for the films C, D and E with respect to A and B result from their higher thickness. Taking into account the film thickness, all films showed a conductivity of 0.1 S cm^{-1} , which is in good agreement with earlier studies.¹⁻³

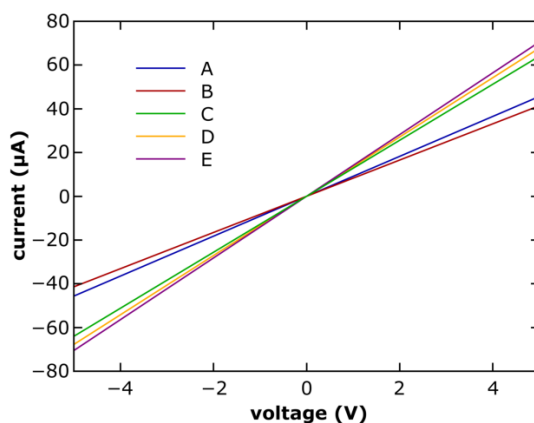


Figure S4: Current-voltage (IV) data of the as-deposited 6DT cross-linked GNP films A, B, C, D and E. The data are normalized to an electrode geometry with a channel length of $400 \mu\text{m}$ and channel width of 1 cm.

Resonator Microstructure

The left hand side of Figure S5 depicts a schematic of the electrode microstructure used for device fabrication prior to membrane transfer. The image shows the global top electrode (signal ground) and the local back electrodes suitable for addressing each of the 16 resonator devices individually. The right hand side of Figure S5 shows a photograph of a resonator contacted using wire bonding (back electrodes) and silver paint (top electrode).

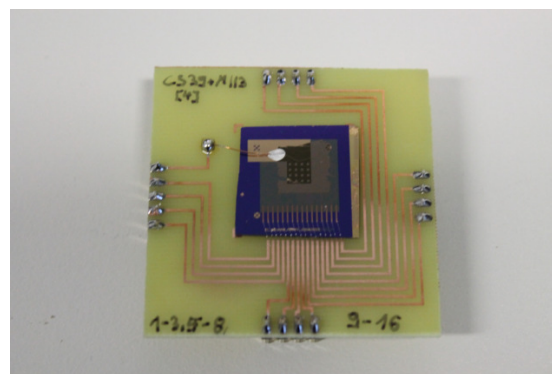
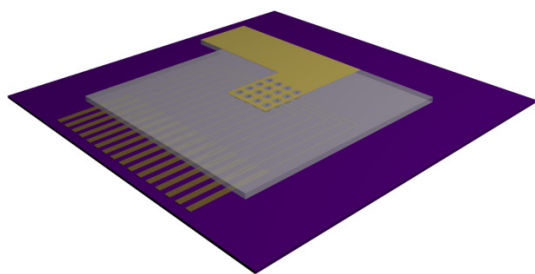


Figure S5: (*left*) Schematic showing a 3D electrode microstructure prior to GNP membrane deposition. (*right*) Photograph of a resonator microstructure, after depositing the cross-linked GNP membrane, mounted onto a printed circuit board.

Data Acquisition Procedures

Interferometry

Time dependent deflection series were recorded using a SIOS Nanovibration Analyzer NA (SIOS GmbH, Germany). This instrument is a commercially available, modified Michelson interferometer, working with a 632.8 nm HeNe laser, combined with an optical microscope. The interferometer's optics and detection system provide two electronic signals to the evaluation electronics, representing the sample's deflection as a sine as well as a cosine modulated voltage V_x and V_y , with a periodicity of $\lambda/2$, each. This principle enables the computation of the angle $\theta = \arctan(\frac{V_y}{V_x})$, which linearly corresponds to the sample deflection h . Employing this measurement principle with a precise 90° phase shift between V_x and V_y obtained by waveplates and using matched preamplification and evaluation circuitry, the interferometer enables highly linear deflection measurements. Under the worst conditions the manufacturer expects a cyclic linearity error of less than 3 nm. Typical errors are smaller.

Typically, a laser power of roughly $\sim 5 \mu\text{W}$ was used for the interferometric measurements (spot diameter $< 2 \mu\text{m}$) to avoid destruction of the GNP membranes.

”Frequency Scanning” Spectrum Acquisition

The ”frequency scanning” acquisition method was used to record vibrational spectra of the resonator devices. Here the vibration's amplitudes at continuous drive signals were measured using an interferometric vibration analyzer (SIOS Nanovibration Analyzer NA). Using an Agilent 33521B function generator, a sine voltage signal was generated and amplified by a high-voltage amplifier (Falco Systems WMA-300) with a gain of $G \sim 50$ (eq. S1). The output of the amplifier was connected to the resonator device, which was placed in a vacuum cell. The signal used for driving the resonators was characterized by the drive frequency f_d ,

an amplitude V_{AC} and offset voltage V_{DC} .

$$V(t) = V_{DC} + V_{AC} \sin(2\pi f_d t) \quad (\text{S1})$$

After setting the function generator to the first drive frequency f_d , the interferometer was armed and triggered by the sync signal of the function generator. Receiving a trigger signal, a deflection-time trace $h_{f_d}(t)$ containing 8192 data points measured at a sample rate of 12.5 MHz was recorded. After the measurement was finished, the data were transferred to the measurement computer and the function generator was set to the next drive frequency f_d and the next deflection time trace was recorded. Common vibrational spectra were acquired in a spectral range of 10 kHz to 2 MHz in 1000 steps.

For data analysis, the complex Fourier components at the drive frequencies $C(f_d)$ were computed from the deflection-time traces $h_{f_d}(t)$ acquired at the respective drive frequencies following equation S2:

$$C(f_d) = \frac{1}{T} \int_0^T h_{f_d}(t) e^{i2\pi f_d t} dt \quad (\text{S2})$$

Here, T denotes the length of the $h(t)$ time trace. The data analysis was conducted using Python, and for the numerical integration numpy's `trapz` algorithm was applied. Finally, the amplitude spectrum was obtained by computing the magnitudes of the complex Fourier components:

$$h_0(f_d) = 2|C(f_d)| \quad (\text{S3})$$

Also the phase spectrum of the vibration could be extracted by computing the phase of the complex Fourier coefficients:

$$\phi(f_d) = \angle C(f_d) \quad (\text{S4})$$

However, an interpretation of the phase data was omitted as the phase spectrum was affected by phase shifts caused by the high voltage amplifier.

”Frequency Sweeping” Spectrum Acquisition

The ”frequency sweeping” spectrum acquisition method enables a fast spectrum acquisition, e.g. for determination of the fundamental resonance frequencies or amplitude mappings. Here, the devices are again driven using a sine voltage signal as described in the preceding section. However, in case of the ”frequency sweeping” acquisition, the frequency of the drive signal f_d is linearly swept through the frequency range of interest by the function generator while a deflection time trace is recorded by the interferometer, synced with the beginning of the sweep. Commonly, deflection time traces $h(t)$ with 65536 points were recorded at a sampling frequency of 5 MHz. This resulted in a sweep time of $t_s \sim 13.1$ ms. The recorded time traces $h(t)$ were then transformed to the frequency domain by a custom Python routine employing numpy’s `fft` algorithm to yield the amplitude spectrum.

Amplitude Mapping Acquisition

GNP membrane resonators with a diameter of $100\ \mu\text{m}$ were investigated regarding the spatial deflection amplitude distributions of the membrane during the excitation of different vibrational modes. As the mode frequencies slightly shifted absolutely and relatively upon scanning the membrane with the interferometer laser, vibrational spectra of the membrane were acquired at each x, y mapping position. Usually, the membranes were scanned following a 41×41 grid, spanning $110 \times 110\ \mu\text{m}^2$ around the center of the membrane. To avoid scanning large portions of the substrate, data points were only recorded at grid positions having a distance of $\leq 55\ \mu\text{m}$ to the membrane center.

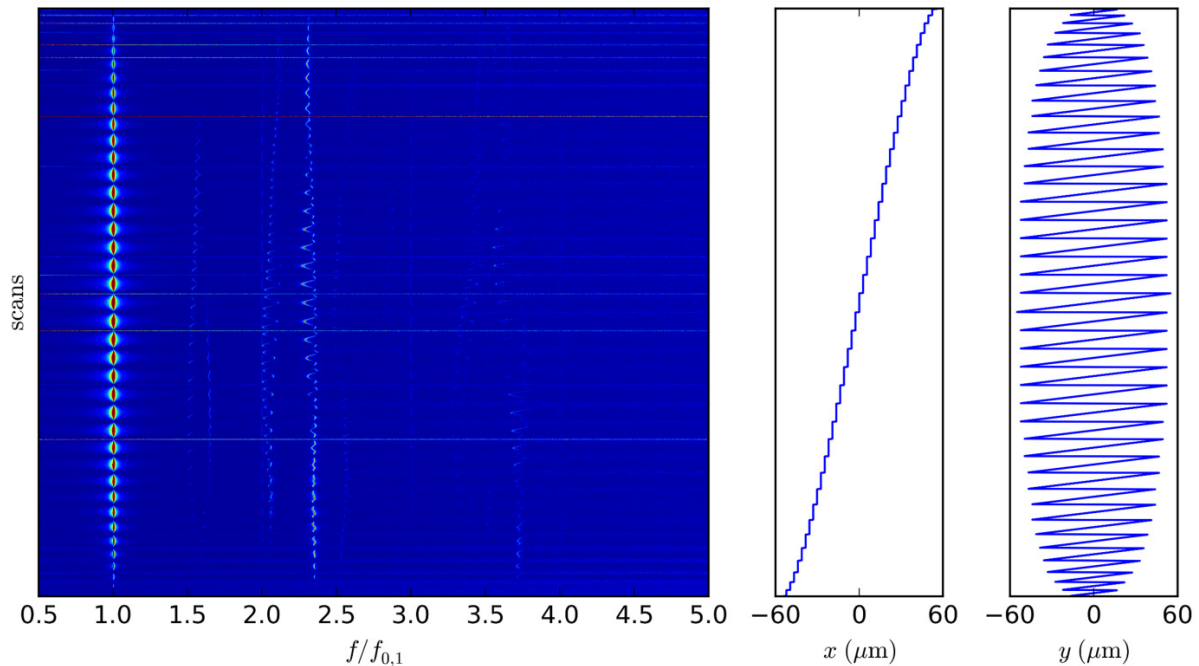


Figure S6: Normalized membrane vibration amplitude spectra recorded at different coordinates ($x = 0, y = 0$ represents the center of the membrane), normalized to the fundamental resonance frequency $f_{0,1}$. Each line represents a scan at the x, y position given in the plots on the right hand side of the figure.

At each position, an amplitude spectrum of the membrane's oscillation in a frequency range of 0.1 to 2 MHz was recorded applying the "frequency sweeping" spectrum acquisition method. The spectra were then normalized to the fundamental resonance frequency $f_{0,1}$.

Figure S6 depicts the normalized vibration spectra recorded for computing the amplitude maps shown in Figure 4 of the main document. Each line in figure S6 represents the spectrum recorded at the x, y -position given by the plots on the right hand side of the figure. For generating the amplitude maps, the peak amplitudes measured at $f_{0,1}$ and in the ranges $2.20f_{0,1} < f < 2.40f_{0,1}$ as well as $3.50f_{0,1} < f < 3.80f_{0,1}$ were plotted at their respective spatial coordinates as false-color images (figure 4). The frequency ranges used for this purpose were chosen around the estimated mode frequencies $f_{0,2;est} = 2.30f_{0,1}$ and $f_{0,3;est} = 3.60f_{0,1}$.

Ring Down Experiments

For determining the resonators quality factors Q , the devices were excited with a burst of a sine voltage signal as described by equation S1 extending over 10, 20, 30, 40, 50 and 80 cycles. The interferometric deflection measurement was synced with the beginning of the excitation burst. Usually, 65536 $h(t)$ datapoints were recorded with a sampling frequency of 12.5 MHz, 10 MHz or 5 MHz.

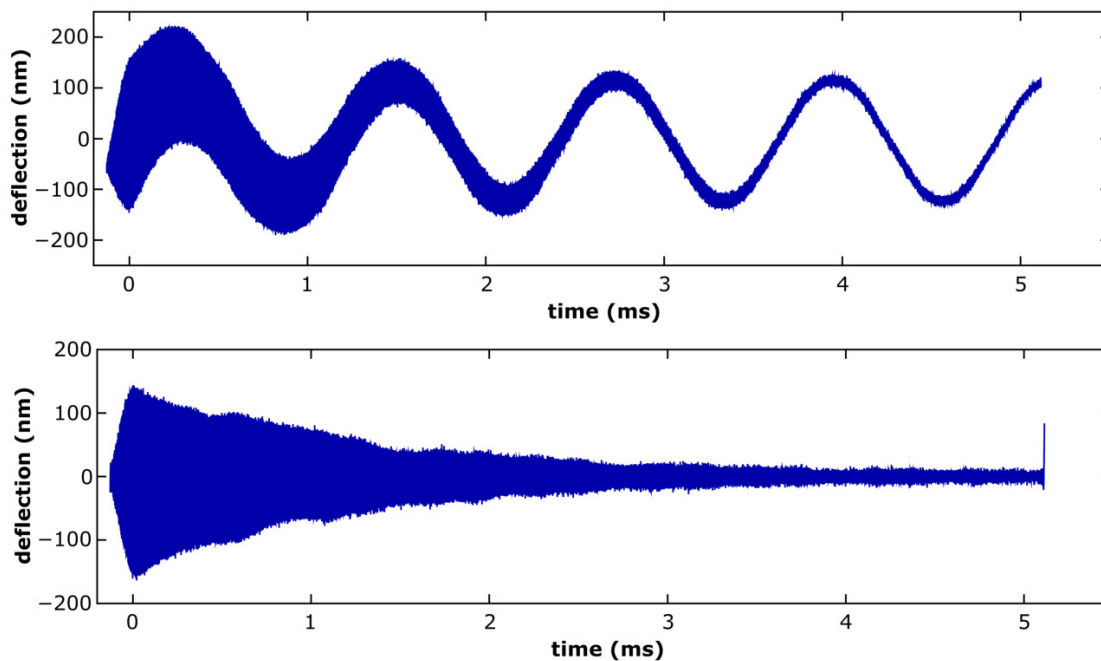


Figure S7: (*top*) Raw deflection data obtained from a ring-down experiment. (*bottom*) Deflection data after removal of the modulation caused by the oscillation of the the interferometer’s reference mirror.

Figure S7, top, depicts the raw deflection data used for plotting the deflection time traces shown in figure 5 (excitation ends at $t = 0$). A modulation of the data with a frequency of ~ 800 Hz, which is caused by the periodic movement of the interferometer’s reference mirror, is clearly visible. This low-frequency modulation was removed by Fourier transformation of the data to the frequency domain using a Python routine employing numpy’s `rfft` algorithm, setting the Fourier components in the frequency range ≤ 100 kHz to zero and back-transformation to the time domain applying numpy’s `irfft` routine. The result-

ing high-pass filtered deflection trace is depicted in figure S7, bottom. The excitation of the resonator until $t = 0$ is clearly visible, followed by a decay of the oscillation. We note that after the major decay of the vibration, low amplitude vibrations slowly running out of phase, presumably due to thermal excitation, could be observed. These oscillations did not affect our quality factor determinations within the given error margin of sample-to-sample fluctuations. The processed deflection data were fitted with equation S5 as described in the main document using `scipy's optimize.curve_fit` algorithm. As initial optimization parameters, f_{res} was set to the excitation frequency, h_0 and τ were chosen as 10 nm and 1 ms, respectively. A phase value of $\phi = 3.14$ was chosen. In rare cases, ϕ had to be adjusted to achieve convergence of the fitting procedure.

$$h(t) = h_0 \sin(2\pi f_{res}t + \phi) \exp\left(-\frac{t}{\tau}\right) \quad (\text{S5})$$

Variation of DC and AC Voltages

In general, the "frequency sweeping" spectrum acquisition was used for the determination of the resonator's fundamental resonance frequencies. DC offset voltages of $V_{DC} = 5\text{ V}$ with an AC drive voltage of $V_{AC} = 2.5\text{ V}$ were applied for devices consisting of a $100\text{ }\mu\text{m}$ resonator and $V_{DC} = 10\text{ V}$ and $V_{AC} = 5\text{ V}$ were used for driving $50\text{ }\mu\text{m}$ resonators.

In order to investigate the dependence of the resonance frequency on the offset voltage a $100\text{ }\mu\text{m}$ resonator was examined at a constant AC drive voltage of $V_{AC} = 5\text{ V}$ and a varying DC offset voltage V_{DC} in the range from 5 V to 20 V .

Also, the possible variation of the resonance frequency in relation to a varying AC drive voltage was studied. For a $100\text{ }\mu\text{m}$ resonator the AC drive voltage V_{AC} was varied in a range from 1.25 V to 3.75 V at a constant DC offset voltage of $V_{DC} = 6.25\text{ V}$. Analogously, for a $50\text{ }\mu\text{m}$ resonator an AC drive voltage V_{AC} ranging from 1.25 V to 5 V with a DC offset voltage of $V_{DC} = 6.25\text{ V}$ was applied.

Neither the variation of the DC offset voltage nor the AC drive voltage in the given ranges resulted in a resonance frequency shift distinguishable from the frequency drifts due to thermal effects caused by the incident laser beam.

Summary of the Resonator Characteristics

26 resonators built from 6DT cross-linked GNP membranes were investigated in this study.

The membrane diameters $2a$, membrane thicknesses t , fundamental resonance frequencies $f_{0,1}$ and quality factors Q are listed in table S1.

Table S1: Parameters of resonators investigated in this study. a is the resonator's membrane radius, t denotes the membrane thickness as determined by AFM, $f_{0,1}$ is the fundamental resonance frequency as measured using the "frequency sweeping" spectrum acquisition method and Q denotes the quality factor measured by ring-down experiments.

device	$2a/\mu\text{m}$	t/nm	$f_{0,1}/\text{kHz}$	Q
A1	100	33 ± 2	403.5	2068
A2	100		351.6	779
A3	50		732.2	802
B1	100	35 ± 1	356.4	1769
B2	100		381.9	1737
B3	100		385.3	1491
B4	100		382.7	1371
B5	100		371.8	543
B6	50		738.4	926
C1	100	51 ± 1	325.2	1433
C2	50		625.2	441
C3	50		728.5	850
C4	50		733.7	692
C5	50		617.8	931
C6	50		638.4	1028
C7	50		740.5	1017
C8	50		727.6	927
D1	100	52 ± 1	374.5	1385
D2	100		330.7	803
D3	100		362.7	1164
D4	50		697.2	737
D5	50		691.0	634
D6	50		769.0	584
E1	100	51 ± 1	353.2	1265
E2	100		310.4	1101
E3	100		298.2	1125

References

- (1) Schlicke, H.; Schröder, J. H.; Trebbin, M.; Petrov, A.; Ijeh, M.; Weller, H.; Vossmeier, T. Freestanding films of crosslinked gold nanoparticles prepared via layer-by-layer spin-coating. *Nanotechnology* **2011**, *22*, 305303.
- (2) Schlicke, H.; Battista, D.; Kunze, S.; Schröter, C. J.; Eich, M.; Vossmeier, T. Freestanding Membranes of Cross-Linked Gold Nanoparticles: Novel Functional Materials for Electrostatic Actuators. *ACS Appl. Mater. Interfaces* **2015**, *7*, 15123–15128.
- (3) Joseph, Y.; Besnard, I.; Rosenberger, M.; Guse, B.; Nothofer, H.-G.; Wessels, J. M.; Wild, U.; Knop-Gericke, A.; Su, D.; Schlögl, R. et al. Self-Assembled Gold Nanoparticle/Alkanedithiol Films: Preparation, Electron Microscopy, XPS-Analysis, Charge Transport, and Vapor-Sensing Properties. *J. Phys. Chem. B* **2003**, *107*, 7406–7413.

A.1.4 Cross-Linked Gold-Nanoparticle Membrane Resonators as Microelectromechanical Vapor Sensors

Reprinted with permission from “Cross-Linked Gold-Nanoparticle Membrane Resonators as Microelectromechanical Vapor Sensors”, H. Schlicke, M. Behrens, C. J. Schröter, G. T. Dahl, H. Hartmann, T. Vossmeier, *ACS Sens.* **2017**, *2*, 540-546.^[4] Copyright ©2017 American Chemical Society.

Supporting Information: Cross-Linked Gold-Nanoparticle Membrane Resonators as Microelectromechanical Vapor Sensors

Hendrik Schlicke, Malte Behrens, Clemens J. Schröter, Gregor T. Dahl, Hauke
Hartmann, and Tobias Vossmeier*

*Institute of Physical Chemistry, University of Hamburg, Grindelallee 117, 20146 Hamburg,
Germany*

E-mail: tobias.vossmeier@chemie.uni-hamburg.de

Contents

Gold Nanoparticles	S-3
UV/vis Spectroscopy	S-4
Atomic Force Microscopy	S-5
Current-Voltage Measurement	S-6
Fabrication of Electrode Microstructures	S-7
Interfacing of the Samples	S-9
Determination of the Fundamental Resonance Frequency	S-10
Determination of Q	S-12
Response Transients and Baseline Correction	S-15
Toluene	S-16
4M2P (4-methylpentan-2-one)	S-17
1-Propanol	S-18
Water	S-19
Resonator on a Non-Polymeric Supporting Structure	S-20
References	S-22

Gold Nanoparticles

For gold nanoparticle thin film fabrication a solution of dodecylamine (12A) capped gold nanoparticles (GNPs) in heptane was used. The particles were obtained following the synthesis route by Leff et al.¹ and characterized using UV/vis spectroscopy (see the absorbance spectrum in figure S2) and transmission electron microscopy (TEM). As the 12A stabilized GNPs are not stable under TEM conditions, a ligand exchange with 1-dodecanethiol (12T) was performed before depositing the particles onto carbon-coated TEM substrates.²

TEM was conducted using a Philips CM 300 machine, operated at 200 kV. A representative transmission electron micrograph as well as a size histogram are provided in figure S1. An average diameter of (3.4 ± 0.6) nm was found for the particles. Particles with a diameter of < 1 nm were excluded from the sizing statistics.

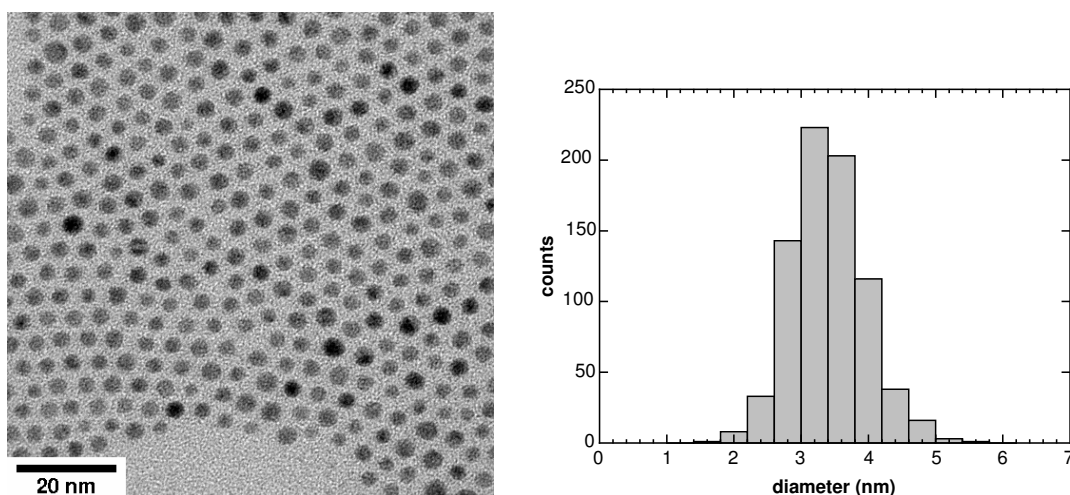


Figure S1: *(left)* Representative transmission electron micrograph of the GNPs used for resonator fabrication in this study. *(right)* Size histogram of the GNP batch.

UV/vis Spectroscopy

Prior to lift-off and transfer of the GNP thin film to the microelectrode structure for resonator fabrication, a UV/vis absorbance spectrum was recorded. The spectrum, as well as an absorbance spectrum of the GNP stock solution used for film fabrication are depicted in figure S2. A red-shift of the surface plasmon resonance band of the GNPs incorporated in the 6DT cross-linked film with respect to the peak position observed for the isolated particles in the stock solution can clearly be seen. This is due to plasmonic interactions resulting from the small interparticle spacings in the thin film.

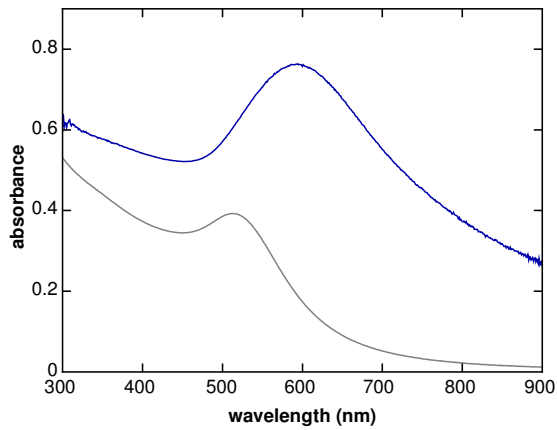


Figure S2: UV/vis absorbance spectrum of the GNP stock solution used for membrane fabrication, dilution factor $f = 1/600$, optical path length $D = 10$ mm (*gray line*) and UV/vis absorbance spectrum of the 6DT cross-linked GNP film used for resonator fabrication (*blue line*).

Atomic Force Microscopy

The thickness of the cross-linked GNP film was measured as described earlier.² A section of the substrate-supported GNP film was scratched using a cannula and two AFM scans ($20 \times 5 \mu\text{m}^2$, $512 \times 128 \text{px}^2$) were acquired at different positions at the edges of the scratches. The topographic AFM data are depicted in figure S3. From each scan five step profiles were extracted and the step heights were averaged to yield the GNP film thickness. For the 6DT cross-linked GNP film used for resonator fabrication, a thickness of $(44 \pm 1) \text{ nm}$ was determined.

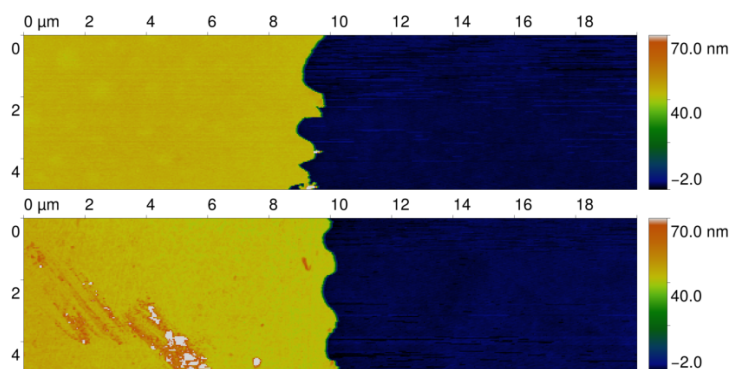


Figure S3: Atomic force microscopy scans acquired at the edges of scratches applied to a section of the substrate-supported GNP film.

Current-Voltage Measurement

Current-voltage data of the GNP film chemiresistor were acquired using an Agilent 4156C semiconductor parameter analyzer. Figure S4 depicts a current-voltage curve of the 6DT cross-linked GNP film chemiresistor investigated in this study. The device shows ohmic conductivity and taking into account the channel geometry, a conductivity of 0.1 Scm^{-1} was calculated. This agrees well with values reported earlier for 6DT cross-linked GNP films.^{2,3}

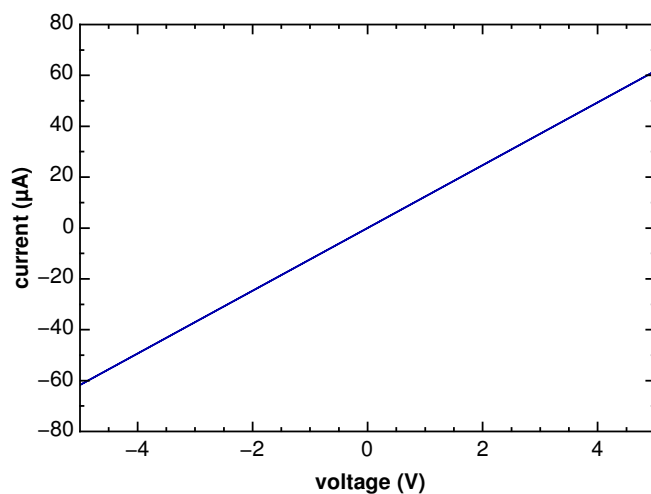


Figure S4: Current-voltage characteristic of the GNP film chemiresistor investigated in this study. Conductive channel dimensions: length: $l \sim 400 \mu\text{m}$, width: $w \sim 11 \text{ mm}$, thickness: $t = 44 \text{ nm}$.

Fabrication of Electrode Microstructures

The 3D electrode microstructures acting as support for the freestanding GNP membranes were fabricated in a three-layer photolithographic process. Firstly, a Ti/Au back-electrode layer was deposited onto an oxidized silicon wafer. Afterwards, an SU-8 layer containing cylindrical microcavities acting as support for the freestanding membranes was fabricated. In a third step, gold electrodes were deposited on top of the SU-8 layer for electrically contacting the freestanding membranes.

Fabrication of the Back Electrodes Firstly, layers of titanium and gold (~ 10 nm and ~ 40 nm, respectively) were deposited onto a thermally oxidized silicon wafer (University Wafer, thickness: $380\ \mu\text{m}$, $n(\text{P})$ -doped, $1\text{-}10\ \Omega\text{cm}$, $\langle 100 \rangle$ orientation, $1\ \mu\text{m}$ thermal oxide) by thermal evaporation (oerlikon leybold UNIVEX 350G). Afterwards, a layer of AZ ECI 3012 (MicroChemicals) positive photoresist was deposited via spin-coating (3000 rpm). The coated wafer was then soft-baked at $90\ ^\circ\text{C}$ for 90 s and exposed using a Karl Süss MJB-3 mask aligner and a photomask providing the back electrode structure. The resist layer was post-exposure baked at $110\ ^\circ\text{C}$ for 90 s and developed using AZ 726 MIF (MicroChemicals) developer for 1 min. The wafer was eventually rinsed in demineralized water and dried in a nitrogen flow. Exposed sections of the gold layer were then etched using a $\text{KI}:\text{I}_2:\text{H}_2\text{O}$ mixture (4:1:200, m:m:m). The titanium adhesive layer was afterwards removed by immersion of the wafer in concentrated hydrochloric acid (37%) at $42\ ^\circ\text{C}$ for 60 min. Residual photoresist was removed using N-methyl-2-pyrrolidone or acetone and water.

Fabrication of the SU-8 microcavities The wafer supporting the back electrode structures was coated with SU-8 2015 (MicroChem) negative photoresist by spin-coating (3000 rpm) and soft-baked at $65\ ^\circ\text{C}$ for 60 s and at $90\ ^\circ\text{C}$ for 120 s. Exposure of the resist layer was performed using a Karl Süss MJB-3 mask aligner after aligning a photomask providing the cavity structures with the respective back electrode structures and applying an optical 360 nm long-

pass filter (Laser Components LC-PL-360LP). The wafer was post-exposure baked for 60 s at 65 °C and for 120 s at 90 °C. Development of the SU-8 layer was performed using mr-Dev 600 (micro resist technology) developer solution for 3 min and stopped by rinsing the structure in isopropyl alcohol and water. Afterwards the samples were treated with an oxygen plasma (Harrick Plasma PDC-002) to clean the SU-8 surface. Finally, the resist layer was hard-baked by ramping the sample temperature from 120 °C to 200 °C and holding it for 20 min.

Fabrication of the Top Electrodes Gold top electrodes were fabricated following a lift-off process. Firstly, a layer of AZ nLof 2035 (MicroChemicals) negative photoresist was deposited onto the wafer containing the back electrodes and SU-8 microcavity structures by spin-coating (2000 rpm) and soft-baked for 90 s at 120 °C. The deposition step was repeated to fully cover the 3D structures with photoresist. Following the second deposition, the samples were again soft baked for 120 s at 120 °C. Exposure of the resist layer was then performed using a Karl Süss MJB-3 mask aligner by aligning a photomask providing the top electrode structures with the respective back electrode structures. After a post-exposure bake for 60 s at 120 °C, the resist layer was developed using AZ 726 MIF developer for 120 s and rinsed using demineralized water. Afterwards, the exposed SU-8 regions were cleaned in an oxygen plasma (Harrick Plasma PDC-002). A gold layer (~40 nm thickness) was deposited onto the wafer by thermal evaporation (oerlikon leybold UNIVEX 350G) and structured by a lift-off process, removing the gold layer from the sample sections covered with AZ 2035 photoresist by dissolving the latter in TechniStrip NI555 (MicroChemicals) at 60 °C for 60 min. Eventually the finalized microstructures were rinsed with demineralized water and dried in a nitrogen flow.

Interfacing of the Samples

The GNP membrane resonator structure was mounted on a custom-designed printed circuit board (PCB) as shown in figure S5a. Electric contacts to the top electrode and the back electrodes were made using silver paint or wire bonding, respectively.

The PCB was equipped with contacts, suitable for addressing a quartz crystal microbalance as well as a GNP thin film chemiresistor on its backside, as shown in figure S5b. The assembled PCB was mounted onto a matching socket in the vacuum cell.

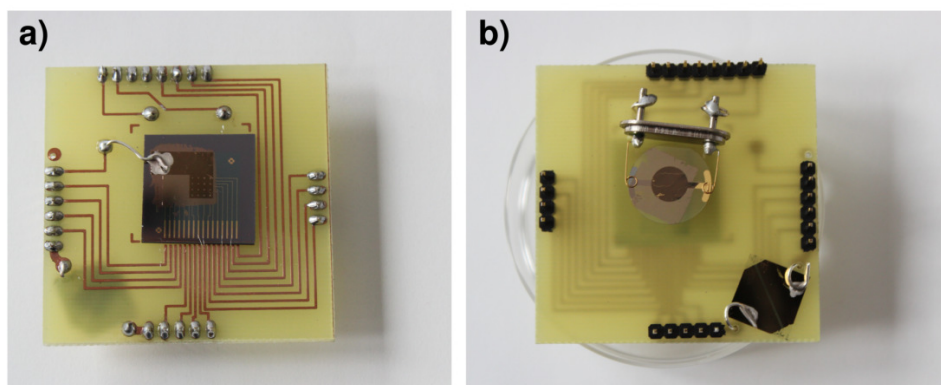


Figure S5: Photographs of the fully assembled printed circuit board, containing a GNP membrane resonator structure on the front side *a)* and a quartz crystal microbalance as well as a GNP thin film chemiresistor on the backside *b)*.

Determination of the Fundamental Resonance Frequency

Vibrational spectra for the determination of the GNP membrane resonator’s fundamental resonance frequency were acquired following the “frequency sweeping” protocol, as described in an earlier publication.⁴ The GNP membrane resonator was excited using a voltage sine function with a linearly swept drive frequency f_d , an AC component V_{AC} and a DC component V_{DC} (equation S1). Here, the DC component was set to a larger value than the AC component, to avoid a zero-crossing of the net voltage and hence of the electrostatic forces acting on the freestanding membrane.⁴ The drive frequency was swept in the spectral range of interest.

$$V(t) = V_{DC} + V_{AC} \sin(2\pi f_d t) \quad (\text{S1})$$

Synchronized with the duration of the sweep, a deflection time trace of the membrane was acquired using a Nanovibration Analyzer NA laser interferometer (SIOS GmbH). A total of 65536 datapoints was recorded with a sampling frequency of several MHz, depending on the maximum drive frequency. Figure S6 exemplarily depicts the deflection time trace corresponding to the membrane vibrational spectrum shown in figure 3b of the main document. Here, the excitation voltages were set to $V_{DC} = 10 \text{ V}$ and $V_{AC} = 5 \text{ V}$, and membrane deflections were recorded with a sampling frequency of 5 MHz. The drive frequency range was set between 10 kHz and 2 MHz. Clearly visible, the time trace is superimposed by a low-frequency oscillation, corresponding to an intended vibration of the interferometer’s reference mirror. The deflection time trace shows oscillations of the GNP membrane as the swept drive frequency matches with resonant frequencies of the resonator. We dedicate the beats observed after maximum excitation of the fundamental resonance mode to slight distortions. A frequency spectrum was obtained by computing the Fast Fourier Transform (FFT) of the deflection time trace.

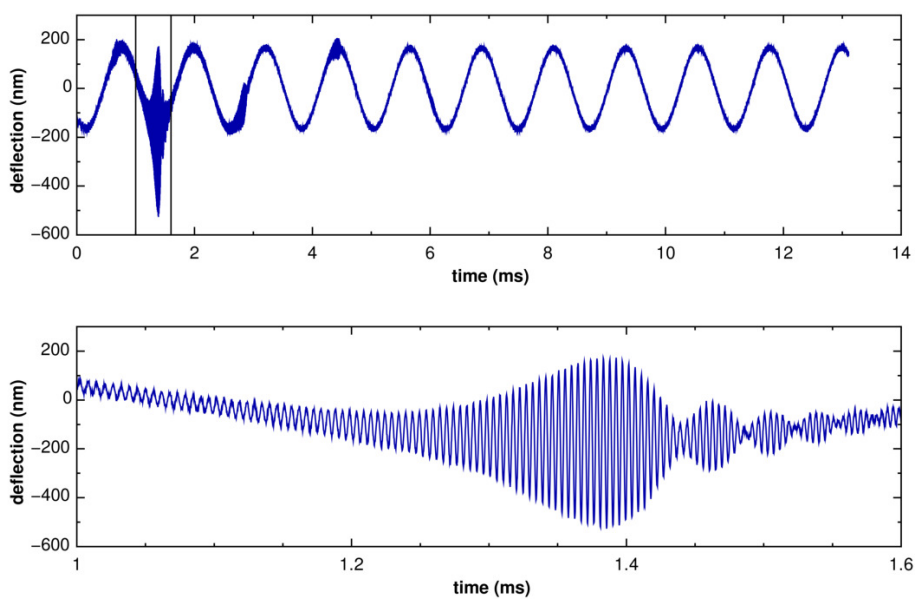


Figure S6: Deflection time trace of the "frequency sweeping" spectrum acquisition procedure, corresponding to the vibrational spectrum depicted in figure 3b of the main document. The lower graph shows a zoom-in into the time interval delimited by the vertical lines depicted in the upper graph.

Determination of Q

The quality factor of the GNP membrane resonator in a 20 mbar nitrogen atmosphere was determined by ring-down experiments, as described earlier.^{4,5}

Firstly, the fundamental resonance frequency of the resonator was determined as described in the previous section. The resonator was excited with bursts of a sine function ($V_{AC} = 5$ V, $V_{DC} = 10$ V) at its fundamental resonance frequency, containing each 5, 10, 20, 30 or 40 cycles. Synchronized with the beginning of the sine burst, the deflection of the GNP membrane center was recorded interferometrically, at a sampling frequency of 12.5 MHz. To remove a low-frequency modulation of the deflection data caused by oscillations of the reference mirror, a Fast Fourier Transform (FFT) of the data was performed and spectral components below 100 kHz were set to zero. Afterwards, the data were transformed back to the time domain using an inverse FFT. FFTs were performed using numpy's `rfft` and `irfft` algorithms.

The high-pass filtered deflection data for the 5 ring-down experiments are depicted in figure S7. The graphs also show a fit of a damped harmonic oscillator function (eq. S2) to the deflection data, beginning right after the end of the excitation burst.

$$h(t) = h_0 \sin(2\pi f_0 t) \exp\left(-\frac{t}{\tau}\right) \quad (\text{S2})$$

From the optimized fit functions, the resonance frequency f_0 , initial amplitude h_0 and oscillation decay time τ were extracted. Figure S8 shows the observed initial amplitude as well as the decay time as a function of the number of excitation cycles. An average quality factor $Q = 45 \pm 1$ was computed from the fit parameters following equation S3.

$$Q = f_0 \pi \tau \quad (\text{S3})$$

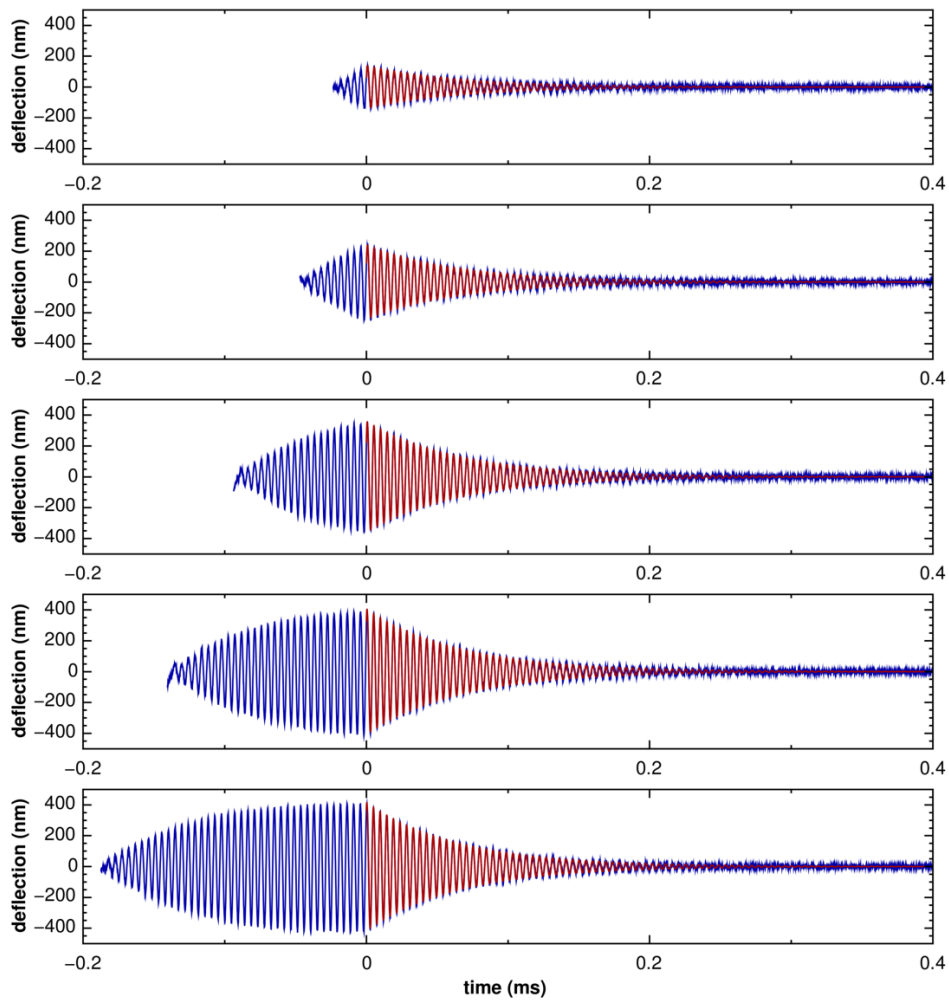


Figure S7: Deflection time traces $h(t)$ of ring-down experiments recorded for determining the quality factor Q of the GNP membrane resonator with (from top to bottom) 5, 10, 20, 30 and 40 excitation cycles (*blue*). Fits of the damped harmonic oscillator model (equation S2, *red*).

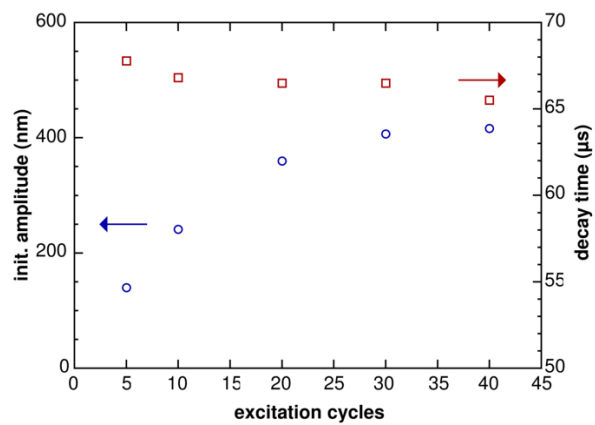


Figure S8: Fit parameters as a function of excitation cycle count: Initial amplitude h_0 (*blue*) and decay time τ (*red*).

Response Transients and Baseline Correction

Below, the time traces for the different measurements are provided (figures S9 to S12). Here, figure parts *a*) show the fundamental resonance frequency $f_0(t)$ of the GNP membrane resonator extracted from fitting lorentzians to the resonance peaks in the amplitude spectra, recorded at different times, as described above. The plots further show the fitted baselines $f_{0,baseline}(t)$ (dashed red lines). Baseline correction was performed by computing the average of the last three frequency datapoints at the end of each 8 min nitrogen (ZG) application. The averaged datapoints were subsequently connected using linear functions to yield the baselines. The baselines were then subtracted from the original frequency data, yielding curves in figure parts *b*), i.e. the frequency shifts $\Delta f_0(t)$ of GNP membrane resonator. The magnitudes of the transients were then computed by averaging the last three frequency shift datapoints at the end of each analyte gas AG exposure. These averages are indicated by the red crosses shown in figure parts *b*).

Figure parts *c*) depict the resistance $R(t)$ of the GNP thin film chemiresistor. The same method as described above was applied to find suitable baselines $R_{baseline}(t)$ (dashed red lines). The relative resistance changes shown in figure parts *d*) were computed by calculating $\frac{R(t)}{R_{baseline}(t)} - 1$. The magnitudes of the transients were again computed by calculating the average of the last three $\Delta R/R_0$ datapoints at the end of each AG application and are indicated by red crosses. Figure parts *e*) depict the frequency shifts of the GNP membrane loaded QCM (10 MHz, electrode diameter 6 mm, one side coated). Here, the raw data are represented by the gray lines and the orange lines depict the data after application of a median filter with a window size of 5. The absolute pressure and the temperature measured in the vacuum cell during the experiments are shown in graph *f*) and *g*), respectively.

Toluene

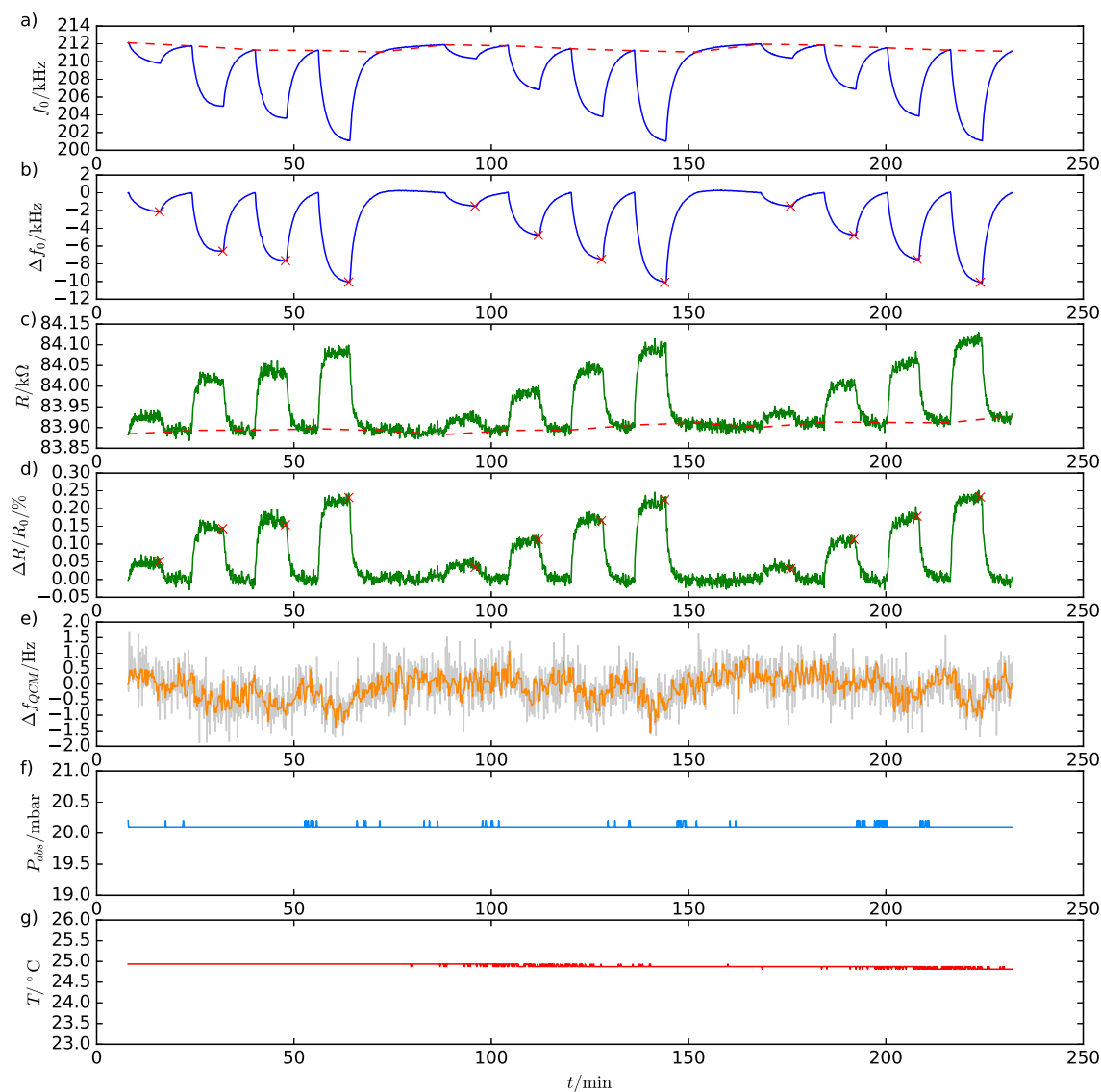


Figure S9: a) Fundamental resonance frequency f_0 of the GNP membrane resonator (blue line). The dashed red line shows the baseline used for baseline subtraction. b) Shift of the resonance frequency Δf_0 of the membrane resonator. The red crosses indicate the maximum response for a given analyte concentration (see below). c) Resistance R of the GNP thin film chemiresistor (green line). The dashed red line shows the baseline used for baseline subtraction. d) Relative resistance change $\frac{\Delta R}{R_0}$ of the chemiresistor. The red crosses indicate the maximum response for a given analyte concentration (see below). e) Frequency shift Δf_{QCM} of the GNP film loaded QCM device. f) Absolute pressure P_{abs} measured within the sensor cell. g) Temperature T measured within the sensor cell. The observed transients are the responses to three consecutive trains of 8 min pulses of toluene vapor with increasing partial pressure of 2 Pa, 8 Pa, 14 Pa, and 20 Pa.

4M2P (4-methylpentan-2-one)

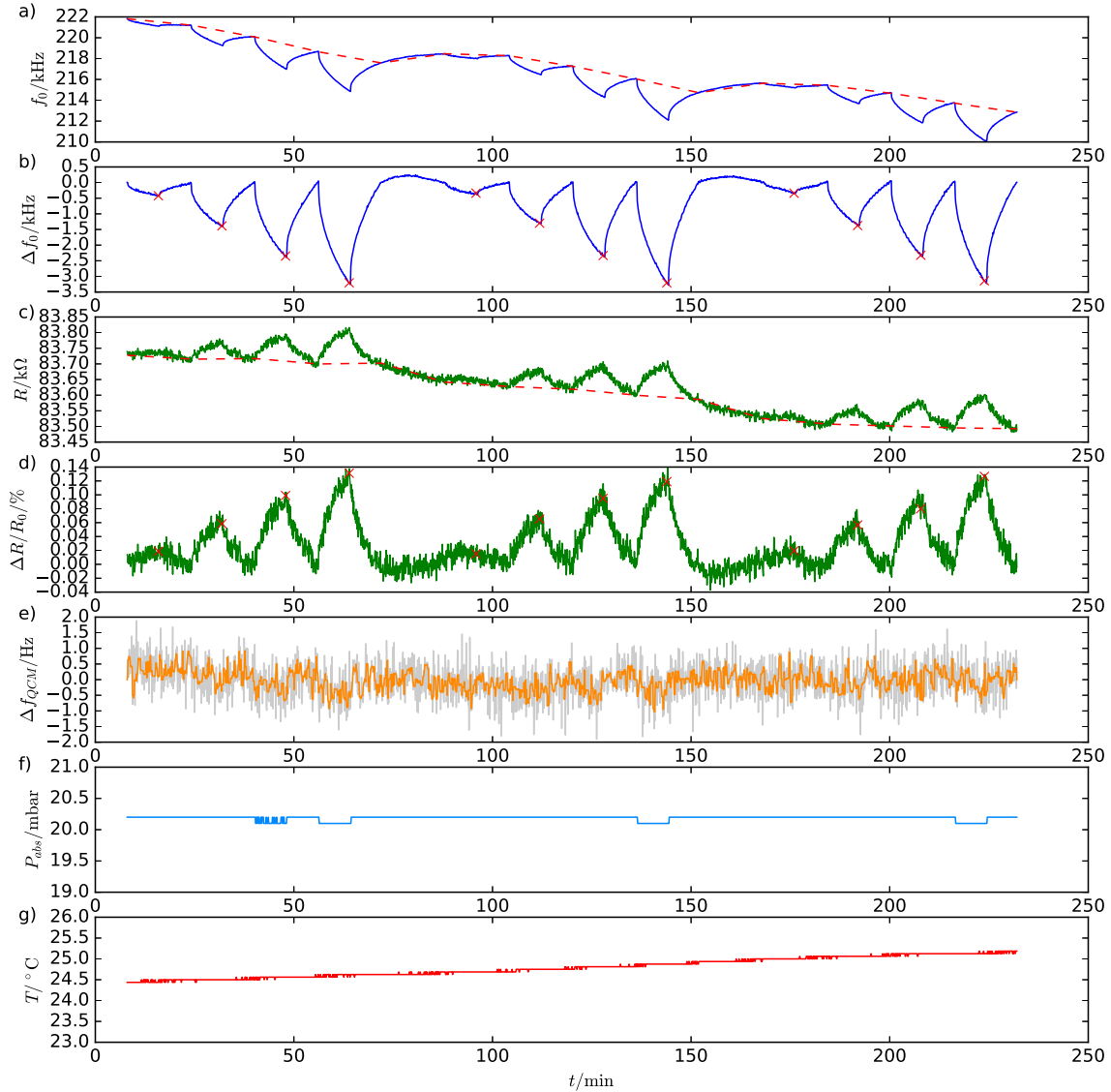


Figure S10: a) Fundamental resonance frequency f_0 of the GNP membrane resonator (blue line). The dashed red line shows the baseline used for baseline subtraction. b) Shift of the resonance frequency Δf_0 of the membrane resonator. The red crosses indicate the maximum response for a given analyte concentration (see below). c) Resistance R of the GNP thin film chemiresistor (green line). The dashed red line shows the baseline used for baseline subtraction. d) Relative resistance change $\frac{\Delta R}{R_0}$ of the chemiresistor. The red crosses indicate the maximum response for a given analyte concentration (see below). e) Frequency shift Δf_{QCM} of the GNP film loaded QCM device. f) Absolute pressure P_{abs} measured within the sensor cell. g) Temperature T measured within the sensor cell. The observed transients are the responses to three consecutive trains of 8 min pulses of 4M2P (4-methylpentan-2-one) vapor with increasing partial pressure of 2 Pa, 8 Pa, 14 Pa, and 20 Pa.

1-Propanol

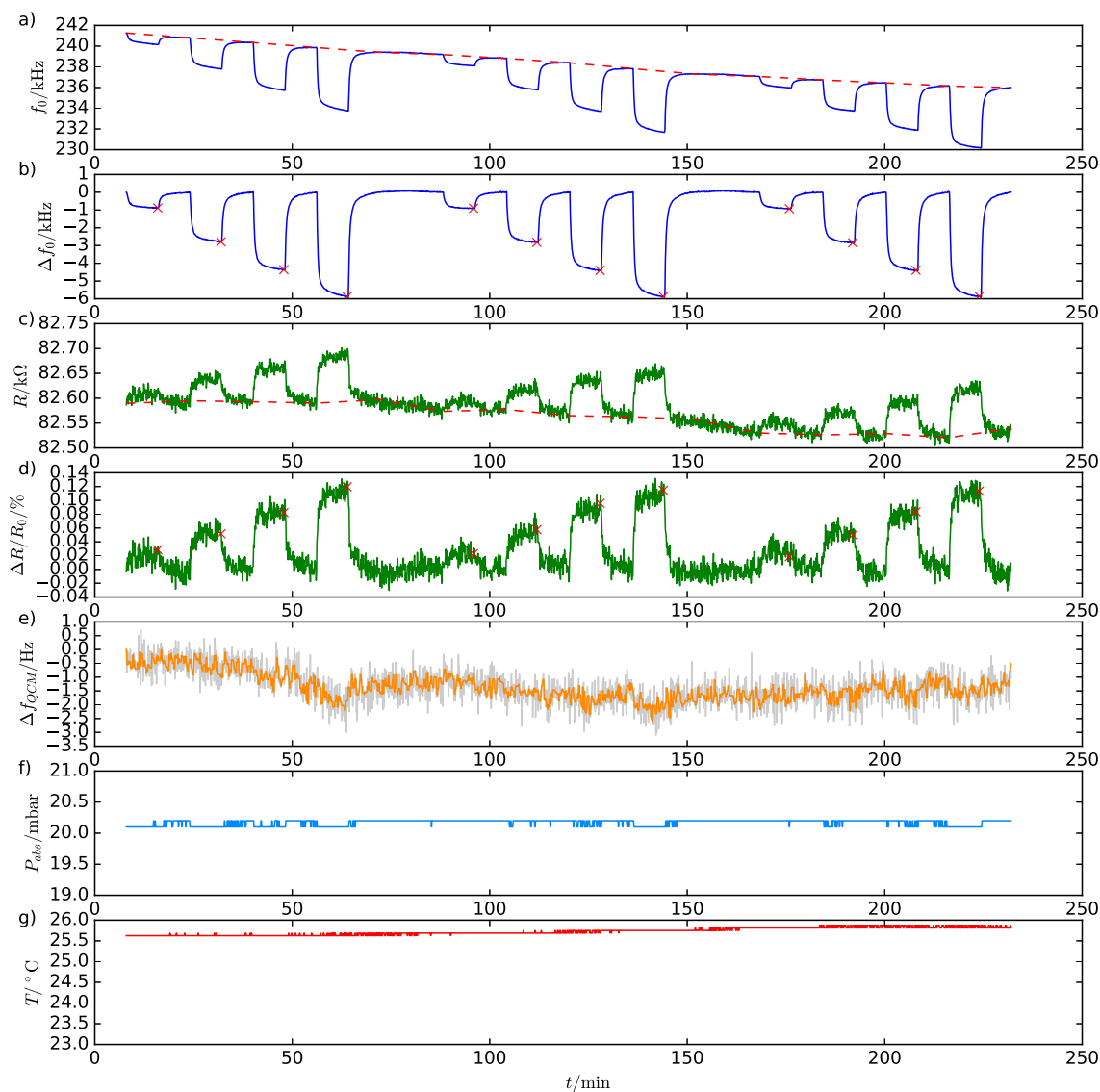


Figure S11: a) Fundamental resonance frequency f_0 of the GNP membrane resonator (blue line). The dashed red line shows the baseline used for baseline subtraction. b) Shift of the resonance frequency Δf_0 of the membrane resonator. The red crosses indicate the maximum response for a given analyte concentration (see below). c) Resistance R of the GNP thin film chemiresistor (green line). The dashed red line shows the baseline used for baseline subtraction. d) Relative resistance change $\frac{\Delta R}{R_0}$ of the chemiresistor. The red crosses indicate the maximum response for a given analyte concentration (see below). e) Frequency shift Δf_{QCM} of the GNP film loaded QCM device. f) Absolute pressure P_{abs} measured within the sensor cell. g) Temperature T measured within the sensor cell. The observed transients are the responses to three consecutive trains of 8 min pulses of 1-propanol vapor with increasing partial pressure of 2 Pa, 8 Pa, 14 Pa, and 20 Pa.

Water

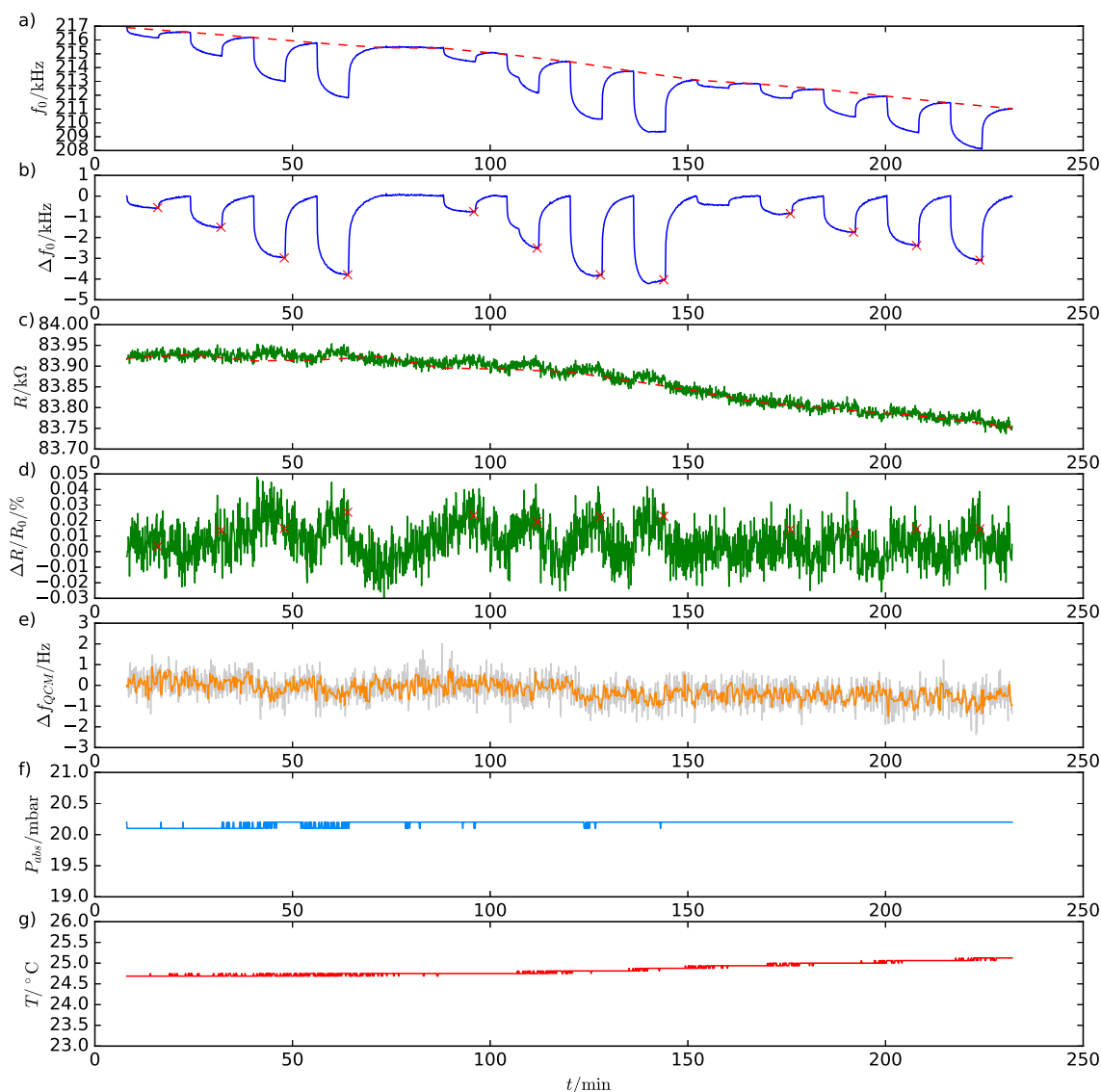


Figure S12: a) Fundamental resonance frequency f_0 of the GNP membrane resonator (blue line). The dashed red line shows the baseline used for baseline subtraction. b) Shift of the resonance frequency Δf_0 of the membrane resonator. The red crosses indicate the maximum response for a given analyte concentration (see below). c) Resistance R of the GNP thin film chemiresistor (green line). The dashed red line shows the baseline used for baseline subtraction. d) Relative resistance change $\frac{\Delta R}{R_0}$ of the chemiresistor. The red crosses indicate the maximum response for a given analyte concentration (see below). e) Frequency shift Δf_{QCM} of the GNP film loaded QCM device. f) Absolute pressure P_{abs} measured within the sensor cell. g) Temperature T measured within the sensor cell. The observed transients are the responses to three consecutive trains of 8 min pulses of water vapor with increasing partial pressure of 2 Pa, 8 Pa, 14 Pa, and 20 Pa.

Resonator on a Non-Polymeric Supporting Structure

To exclude a significant influence by swelling of the polymeric SU-8 structured microelectrode on the resonator's frequency response to solvent vapors, control experiments were conducted employing silicon based supporting structures. Using lithographic methods, a square microcavity ($\sim 87 \mu\text{m}$ edge length) was etched into a thermally oxidized, doped silicon wafer (Siegert Wafer, p/B-Si, $1 - 30 \Omega\text{cm}$, 500 nm wet thermal oxide, $\langle 100 \rangle \pm 0.5^\circ$), providing the back electrode of the resonator. On top of said structure, a 6DT cross-linked GNP ($3.9 \pm 0.6 \text{ nm}$) membrane (thickness: $88 \pm 1 \text{ nm}$) was deposited, remaining freestanding over the microcavity. Before depositing the GNP membrane onto the cavity, the microstructure was equipped with a top electrode for electrically contacting the membrane. A micrograph of the device is depicted in figure S13. The frequency responses of the square GNP membrane resonator to toluene vapor of different partial pressures (2 Pa, 8 Pa, 14 Pa, 20 Pa) were investigated as described for the SU-8 structured resonator. A representative frequency time trace of the silicon based resonator is depicted in Figure S13. Because the device shows similar responses as the SU-8 based resonator significant influences caused by swelling of the supporting microelectrode structure due to sorption of analyte can be excluded. Compared to the SU-8 structured resonator the silicon structured resonator shows somewhat slower responses to toluene vapor. We attribute this finding to the thicker GNP membrane used in the case of the silicon structured device, which retards the diffusion of the analyte across the membrane and, thus, equilibrium conditions requiring the same analyte concentration on both sides of the membrane are reached more slowly.

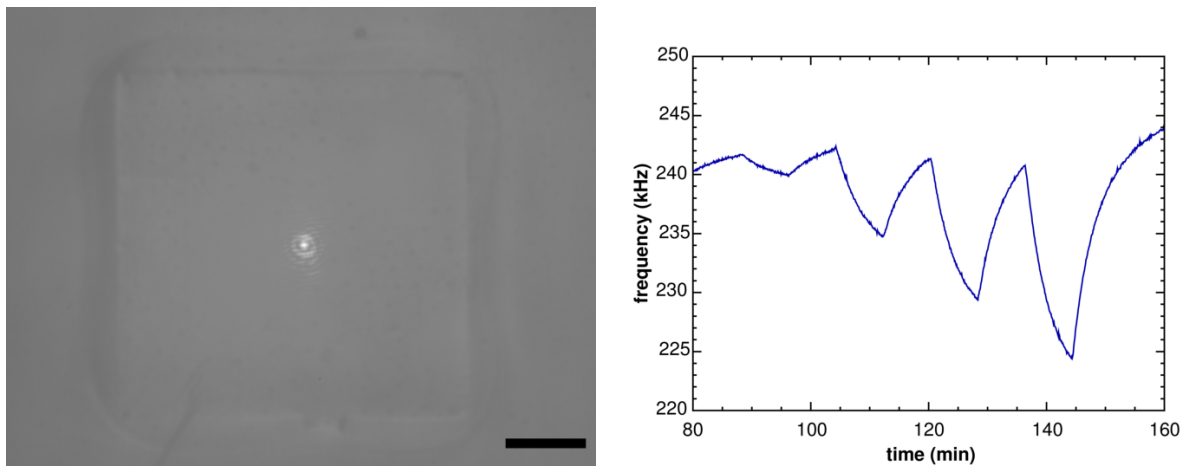


Figure S13: (*left*) Micrograph of a 6DT cross-linked GNP membrane resonator, which was fabricated by depositing an ~ 88 nm thick 6DT cross-linked GNP membrane onto a square cavity (~ 87 μm edge length) etched into the surface of an SiO_2/Si substrate. Scale bar: 20 μm . The bright spot at the membrane's center represents a reflection of the interferometer's laser. (*right*) Fundamental resonance frequency f_0 time trace of the GNP membrane resonator. The observed transients are the responses to 8 min pulses of toluene vapor with increasing partial pressure of 2 Pa, 8 Pa, 14 Pa, and 20 Pa.

References

- (1) Leff, D. V.; Brandt, L.; Heath, J. R. Synthesis and Characterization of Hydrophobic, Organically-Soluble Gold Nanocrystals Functionalized with Primary Amines. *Langmuir* **1996**, *12*, 4723–4730.
- (2) Schlicke, H.; Schröder, J. H.; Trebbin, M.; Petrov, A.; Ijeh, M.; Weller, H.; Vossmeier, T. Freestanding films of crosslinked gold nanoparticles prepared via layer-by-layer spin-coating. *Nanotechnology* **2011**, *22*, 305303.
- (3) Schlicke, H.; Rebber, M.; Kunze, S.; Vossmeier, T. Resistive pressure sensors based on freestanding membranes of gold nanoparticles. *Nanoscale* **2016**, *8*, 183–186.
- (4) Schlicke, H.; Schröter, C. J.; Vossmeier, T. Electrostatically driven drumhead resonators based on freestanding membranes of cross-linked gold nanoparticles. *Nanoscale* **2016**, *8*, 15880–15887.
- (5) Wang, Z.; Jia, H.; Zheng, X.; Yang, R.; Wang, Z.; Ye, G. J.; Chen, X. H.; Shan, J.; Feng, P. X.-L. Black phosphorus nanoelectromechanical resonators vibrating at very high frequencies. *Nanoscale* **2015**, *7*, 877–884.

A.2 Interferometer Setup

Figure A.1 provides an overview of the major components incorporated within the experimental setup used for electrostatic excitation of GNP membrane actuators and resonators as well as monitoring their responses by interferometric deflection measurements. As the figure depicts the setup's latest condition, modifications may have been applied during the course of the individual studies included in this thesis.

The setup includes a custom-built test cell placed on an x, y -cross table, which is attached to a rotary vane pump via a cooling trap. Further, the cell is connected to a calibration system (Umwelttechnik MCZ GmbH CGM 2000), providing nitrogen (ZG) as well as nitrogen enriched with different analyte vapors (AG). The test cell pressure can be controlled by adjusting the ZG/AG feed using a needle valve. The pressure as well as the temperature are continuously monitored by a Raspberry Pi single-board computer and accessible via local area network (LAN). The system uses an Oerlikon TTR 101N THERMOVAC pressure sensor, featuring a MEMS Pirani gauge for accurately measuring low pressures in the sub-mbar range as well as a piezoresistive membrane sensor that is capable of measuring pressures in the mbar to ambient pressure range independently of the gas type present.^[225] Further, a DS18B20 temperature sensor is incorporated into the test cell.

A Keysight 33521B waveform generator provides the GNP resonator's excitation signal, which is amplified using a Falco Systems WMA-300 amplifier (gain ~ 50 , DC to 5 MHz(@ -3 dB), max. ± 150 V/300 mA).^[226] Deflection/vibration readout is performed using a fiber coupled HeNe laser interferometer, incorporated into a technical microscope (SIOS Nanovibration Analyzer NA). The device features a maximum sampling rate of 12.5 MHz, a maximum z -resolution of 20 pm and a laser spot size of < 2 μm .^[202] The interferometer is controlled by a computer (PC2) running a commercial software (SIOS InfasVibro), providing a transmission control protocol (TCP) interface.

Besides the characterization of GNP membrane resonators, the setup enables simultaneous chemiresistive measurements. Here, the resistance of chemiresistors placed within the test cell can be monitored and recorded using a Keithley 2601A SMU.

Further, QCM measurements can be performed, e.g. for monitoring the analyte mass sorbed by a GNP film deposited onto a quartz crystal resonator. Here, an Agilent E5100A network analyzer can be used to record impedance spectra or monitor the resonance frequencies of quartz crystals.

PC1 is employed to control the experiments and collect measurement data. For this purpose custom python routines were developed, which interface with the different components of the experimental setup via the respective data connections.

A.3 Chemicals and Safety

Table A.1 lists all chemicals used within the framework of this thesis as well as their classification according to globally harmonized system (GHS).

Table A.1: List of chemicals and GHS classifications.








Substance	GHS Symbols	Hazard Statements	Precautionary Statements	Ref.
1-Dodecanethiol		H314, H317, H410	P273, P280, P301 + P330 + P331, P303 + P361 + P353, P305 + P351 + P338, P315, P405, P501	[227]
1-Dodecylamine		H304, H314, H335, H373, H410	P261, P273, P280, P301 + P310, P305 + P351 + P338, P310	[227]
1-Propanol		H225, H318, H336	P210, P240, P280, P305 + P351 + P338, P313, P403 + P233	[227]
1,10-Decanedithiol		H315, H319	P264, P280, P302 + P352 + P332 + P313 + P362 + P364, P305 + P351 + P338 + P337 + P313	[228]
1,3-Propanedithiol		H315, H319, H335	P305 + P351 + P338	[229]
1,4-Benzenedithiol	Not a hazardous substance or mixture according to Regulation (EC) No. 1272/2008.			[229]
1,4-Butanedithiol	Not a hazardous substance or mixture according to Regulation (EC) No. 1272/2008.			[229]
1,5-Pentanedithiol	Not a hazardous substance or mixture according to Regulation (EC) No. 1272/2008.			[229]
1,6-Hexanedithiol	Not a hazardous substance or mixture according to Regulation (EC) No. 1272/2008.			[229]
1,8-Octanedithiol		H302	-	[229]
1,9-Nonanedithiol		H315, H319, H335	P261, P305 + P351 + P338	[229]

Table A.1: List of chemicals and GHS classifications.












Substance	GHS Symbols	Hazard Statements	Precautionary Statements	Ref.
2-Propanol		H225, H318, H336	P210, P240, P280, P305 + P351 + P338, P313, P403 + P233	[227]
4-Methylpentan-2-one		H255, H319, H332, H335, EUH066	P210, P261, P305 + P351 + P338	[230]
Acetone		H225, H319, H336, EUH066	P210, P240, P305 + P351 + P338, P403 + P233	[227]
AR 300-12 Thinner		H226	P210, P233, P243, P303 + P361 + P353, P403 + P235	[231]
AR 300-40 Series Developer		H290, H302, H312, H314, H371, H373	P260, P280, P301 + P330 + P331, P303 + P361 + P353, P305 + P351 + P338, P310, P390	[232]
AR-N 7520 Series Photoresist		H226	P210, P233, P243, P303 + P361 + P353, P403 + P235	[233]
AZ 726 MIF Developer		H290, H302 + H312, H314, H371, H373	P260, P280, P308 + P311, P362 + P364	[234]
AZ ECI 3012 Photoresist		H226, H318, H335	P210, P261, P303 + P361 + P353, P304 + P340 + P312, P305 + P351 + P338 + P310, P370 + P378	[235]
AZ MIF 826 Developer		H290, H302 + H312, H314, H371, H373	P260, P280, P308 + P311, P362 + P364	[236]
AZ nLOF 2035 Photoresist		H226	P210, P233, P280, P303 + P361 + P353, P370 + P378, P403 + P235	[237]
AZ nLOF 2070 Photoresist		H226	P210, P233, P280, P303 + P361 + P353, P370 + P378, P403 + P235	[238]

Table A.1: List of chemicals and GHS classifications.






















Substance	GHS Symbols	Hazard Statements	Precautionary Statements	Ref.
AZ1518 Photoresist		H226	P210, P233, P280, P303 + P361 + P353, P370 + P378, P403 + P235	[239]
BOE 7-1 (AF 87.5 – 12.5) with surfactants Etchant	  	H301 + H331, H310, H314	P260, P301 + P310, P303 + P361 + P353, P305 + P351 + P338, P405, P501	[240]
Chlorobenzene	  	H226, H332, H315, H411	P260, P262, P273, P403	[227]
Ethanol	 	H225, H319	P210, P240, P305 + P351 + P338, P403 + P233	[227]
Gold (bulk)	Not a hazardous substance or mixture according to Regulation (EC) No. 1272/2008.			[229]
Gold nanoparticles (3-4 nm)	Substance not yet fully tested.			
Hydrochloric acid	 	H290, H314, H335	P260, P280, P303 + P361 + P353, P304 + P340 + P310, P305 + P351 + P338	[227]
Hydrogen Peroxide	  	H271, H302, H314, H332, H335, H412	-	[227]
Iodine	  	H312 + H332, H315, H319, H335, H372, H400	P273, P302 + P352, P305 + P351 + P338, P314	[227]
Methanol	  	H225, H331, H311, H301, H370	P210, P233, P280, P302 + P352, P304 + P340, P308 + P310, P403 + P235	[227]
mr-dev 600 Developer		H226	P210, P233, P240, P241, P242, P243, P280, P303 + P361 + P353, P370 + P378, P403 + P235	[241]

Table A.1: List of chemicals and GHS classifications.








Substance	GHS Symbols	Hazard Statements	Precautionary Statements	Ref.
n-Heptane		H225, H304, H315, H336, H410	P210, P240, P273, P301 + P330 + P331, P302 + P352, P403 + P233	[227]
N-Methylpyrrolidone		H315, H319, H335, H360D	P201, P261, P305 + P351 + P338, P308 + P313	[229]
Oxygen		H270, H280	P244, P220, P370 + P376, P403	[227]
Poly (methyl methacrylate)	Not a hazardous substance or mixture according to Regulation (EC) No. 1272/2008.			[229]
Potassium hydroxide		H290, H302, H314	P280, P301 + P330 + P331, P305 + P351 + P338, P308 + P310	[227]
Potassium iodide	Not a hazardous substance or mixture according to Regulation (EC) No. 1272/2008.			[227]
Sodium borohydride		H260, H301, H314, H360F, EUH014	P201, P231 + P232, P280, P308 + P313, P370 + P378, P402 + P404	[227]
Sodium hydroxide		H290, H314	P280, P301 + P330 + P331, P305 + P351 + P338, P308 + P310	[227]
SU-8 2015 Photoresist		H226, H302, H332, H319, H315, H317, H411	P210, P261, P280, P233, P273, P305 + P351 + P338, P312, P363, P333 + P313, P337 + P313, P370 + P378, P370 + P378, P391, P403 + P235, P501	[242]

Table A.1: List of chemicals and GHS classifications.





Substance	GHS Symbols	Hazard Statements	Precautionary Statements	Ref.
SU-8 50 Photoresist		H302, H319, H315, H317, H411	P261, P273, P280, P301 + P310, P303 + P361 + P353, P333 + P313, P305 + P351 + P338, P337 + P313, P363, P391, P403 + P233, P501	[243]
SYLGARD 184 SILICONE ELASTOMER KIT (BASE)	Not a hazardous substance or mixture according to Regulation (EC) No. 1272/2008.			[244]
SYLGARD 184 SILICONE ELASTOMER KIT (CURING AGENT)	Not a hazardous substance or mixture according to Regulation (EC) No. 1272/2008.		P210, P234, P403	[245]
TechniEtch Cr01 Etchant		H314, H318	P260, P303 + P361 + P353, P305 + P351 + P338, P310, P405, P501	[246]
Technistrip NI 555 Remover/Stripper	The product is not classified according to the CLP regulation.			[247]
Tetrachloroauric(III) acid		H302, H314, H317	P280, P305 + P351 + P338, P310	[229]
Tetraoctylammonium bromide	Not a hazardous substance or mixture according to Regulation (EC) No. 1272/2008.			[229]
Titanium (bulk)	Not a hazardous substance or mixture according to Regulation (EC) No. 1272/2008.			[229]
Toluene		H225, H361d, H304, H373, H315, H336	P210, P240, P301 + P310 + P330, P302 + P352, P308 + P313, P314, P403 + P233	[227]
Water	Not a hazardous substance or mixture according to Regulation (EC) No. 1272/2008.			[227]

Table A.2 lists all substances classified as carcinogenic, mutagenic or toxic to reproduction (CMR).

Table A.2: List of CMR classified substances.

Substance	CMR classification	Usage and amount
N-Methylpyrrolidone	R _D category 1B	solvent, 200 mL
Sodium borohydride	R _F category 1B	reductant, 6 g
Toluene	R _D category 2	solvent, 2 L

B Danksagung

Herrn Prof. Dr. Horst Weller danke ich für die freundliche Aufnahme in den Arbeitskreis und die Bereitstellung exzellenter Arbeitsbedingungen.

Mein besonderer Dank gilt Dr. Tobias Vossmeier, für die hervorragende Betreuung meiner Doktorarbeit, zahlreiche wertvolle Diskussionen und Anregungen, viele nette Gespräche, sowie die fortwährende Unterstützung. Außerdem bedanke ich mich für die Übernahme des Gutachtens.

Prof. Dr. Alf Mews danke ich für die Übernahme des Zweitgutachtens.

Der Joachim Herz Stiftung danke ich für die finanzielle Unterstützung während meiner Doktorarbeit, sowie für die Bereitstellung von Sach- und Reisemitteln. Besonders danken möchte ich Dr. Eva Ackermann und dem Team der PIER Helmholtz Graduate School, Stefanie Tepass, Maren Arnold-Vargen und Mirko Siemssen. Weiterhin bedanke ich mich bei meinen Kollegen Max Rose, Maria Kokkinidou, Rajkiran Tholapi und Zhipeng Huang aus dem zweiten JHS-Stipendiatenjahrgang für eine schöne gemeinsame Zeit.

Beate Kreutzer, Martina Krasa, Sigrid Zeckert und Marion Manin danke ich für die stete Hilfsbereitschaft bei organisatorischen Fragen.

Meinen Diplom- und Masterstudenten Svenja Kunze, Maik Finsel, Clemens Schröter, Gregor Dahl, Hauke Hartmann und Matthias Rebber, meinen Bachelorstudenten Alexander Haas, Daniela Battista, Hauke Hartmann, Matthias Rebber, Sophia Bittinger und Malte Behrens, sowie meinen Praktikanten danke ich für ihre tatkräftige Unterstützung.

Weiterhin danke ich dem gesamten “Sensor-Team” — neben den oben genannten — Dr. Natalia Olichwer, Mazlum Yesilmen und Bendix Ketelsen für die tolle Zusammenarbeit.

Bedanken möchte ich mich bei dem Team der Forschungswerkstatt der Physikalischen Chemie um Siegfried Uselis, für die Anfertigung zahlreicher Apparaturen und Komponenten, ohne die diese Arbeit so nicht möglich gewesen wäre.

Prof. Dr. Manfred Eich (TUHH) danke ich für die Bereitstellung eines konfokalen Mikroskops.

Für eine Einführung in die Elektronenstrahlolithographie und technische Unterstützung beim SEM bedanke ich mich bei PD Dr. Christian Klinke, Dr. Hauke Lehmann und Robert Schön.

Für die Anfertigung transmissionselektronenmikroskopischer Aufnahmen und Röntgendiffraktogrammen danke ich Stefan Werner und Almut Barck.

B. Danksagung

Für interessante Diskussionen zum Thema Elektronik und das ein oder andere Bauteil danke ich Jan Flügge.

Dr. Andreas Meyer danke ich für die Bereitstellung des AFMs.

Weiterhin danke ich Dr. Ralf Schüler (SIOS) sowie Dr. Christian Strelow für hilfreiche Diskussionen zur Laserinterferometrie und Schwingungsmessung.

Für die Durchsicht dieser Arbeit möchte ich mich bei Jannis Schlicke, Matthias Rebber, Clemens Schröter, Hauke Hartmann und Svenja Kunze bedanken.

Meinen ehemaligen Kolleginnen Natalia und Lisa danke ich für eine schöne Zeit in Büro 347.

Clemens, Gregor, Maik, Mazlum, Robert, Maxi, Thai, Ceyla, Indi, Chandra, Farha, Omysha und Ruwani danke ich für tolle und unterhaltsame Tage in Büro P(253).

Für jede Menge Spaß und Vergnügen in und um die Uni danke ich dem Verein, sowie Robert, Anna, Sarah, Jerry, Svenja, Natalia, Friederieke, Maik, Mazlum, Gregor, Clemens, Lisa, Hauke, Matthias, Bendix und dem gesamten AK Weller.

Schließlich möchte ich mich für die immerwährende, liebevolle Unterstützung und Geduld bei meiner Familie, besonders bei meinen Eltern Dörte und Georg, bei meinem Bruder Jannis, bei meiner Freundin Svenja und meinem Sohn Noah bedanken.

C Eidesstattliche Versicherung

Hiermit versichere ich an Eides statt, die vorliegende Dissertation selbst verfasst und keine anderen als die angegebenen Hilfsmittel benutzt zu haben. Die eingereichte schriftliche Fassung entspricht der auf dem elektronischen Speichermedium. Ich versichere, dass diese Dissertation nicht in einem früheren Promotionsverfahren eingereicht wurde.

Hendrik Schlicke

Hamburg, den 29. September 2017